Studies of Multihadronic Final States in Electron Positron Annihilation

by

O. Podobrin

Studies of Multihadronic Final States in Electron Positron Annihilation
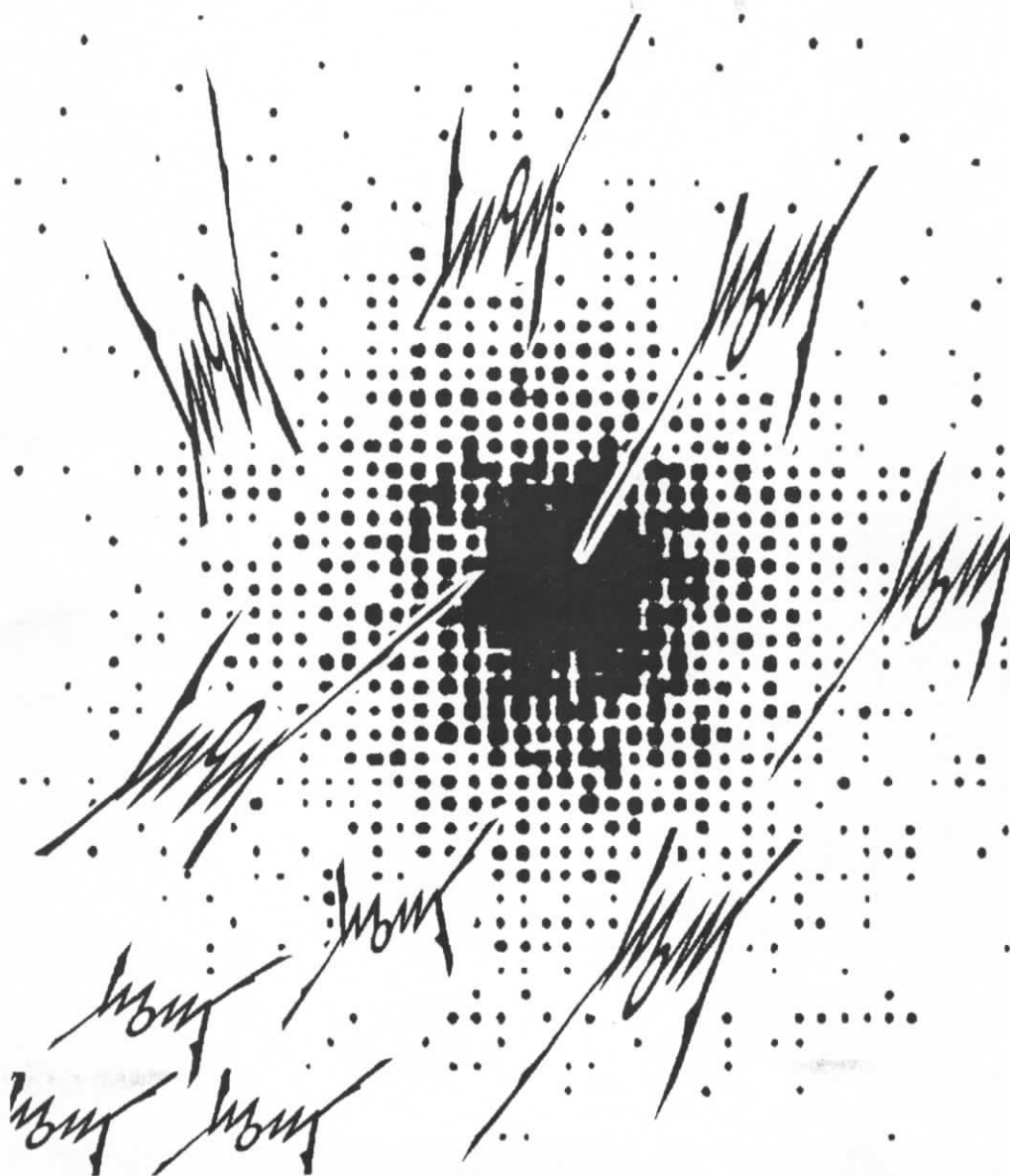
Oliver Podobrin
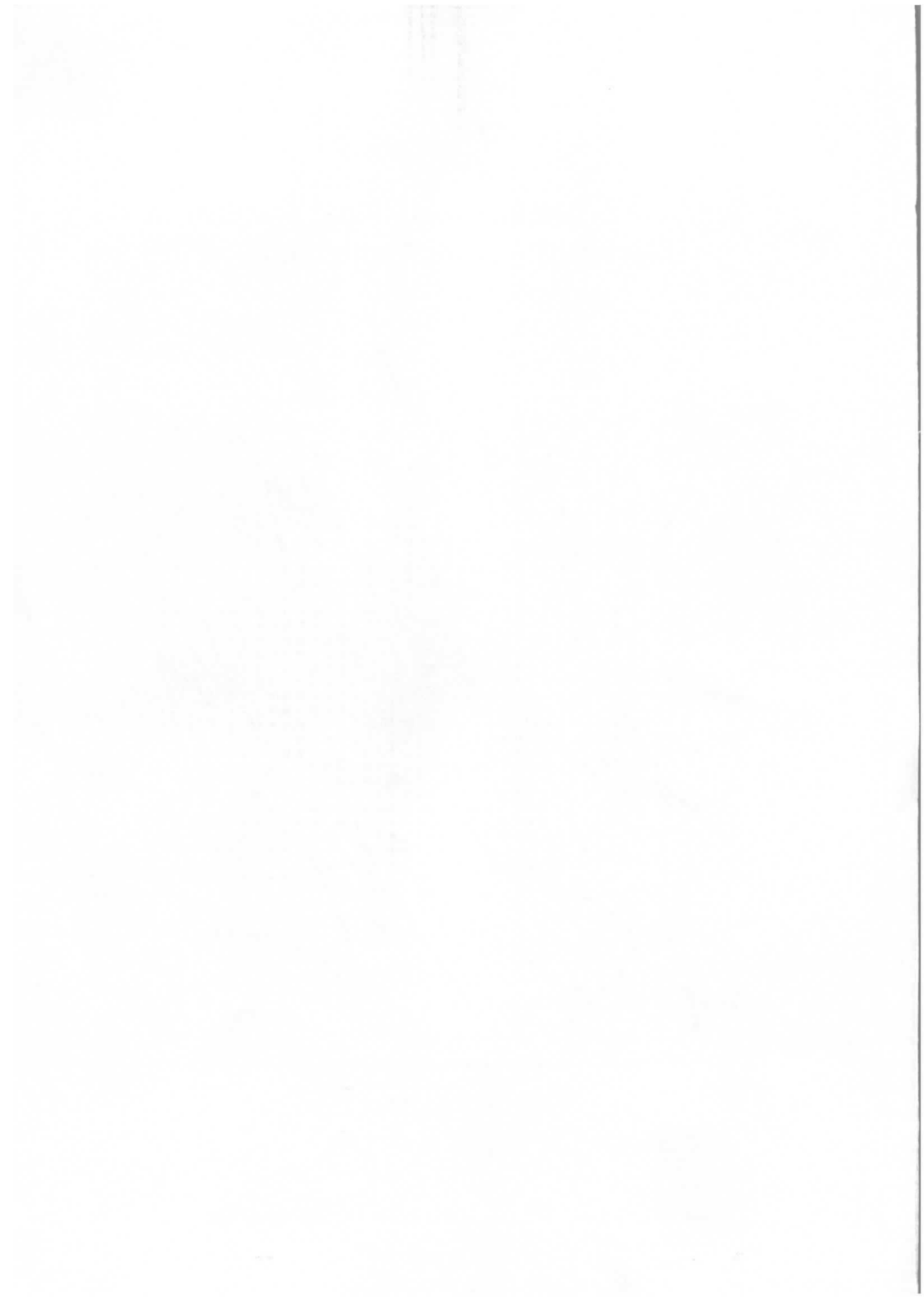
Studies of Multihadronic Final States in Electron Positron Annihilation

Dissertation
zur Erlangung des Doktorgrades
des Fachbereichs Physik
der Universität Hamburg

vorgelegt von
Oliver Podobrin
aus Münster

Hamburg
1992

To Steffi

Abstract

This thesis presents investigations of particle production in electron positron annihilation, based on data taken with the CELLO detector at the PETRA storage ring at 35 GeV centre of mass energy.

The analysis comprises general aspects of e^+e^- annihilation, such as global event shapes and inclusive cross sections, and extends to fluctuations and correlations in the multihadronic final state. Various topics are covered in this analysis, among these are multiplicity distributions, intermittency, Bose-Einstein correlations and two-particle correlations. These studies give access to the perturbative and non-perturbative phase of multiparticle production, and thereby not only assist tests of Monte Carlo models, but also provide information necessary for future improvements. The data strongly support the concept of a local transition from the parton to the hadron phase, as is realized in cluster fragmentation models.

In addition to the well-known Bose-Einstein effect, an apparent shift of the ρ^0 meson mass is observed. It is shown that the two effects have a common origin in the interference of identical pions in $\rho^0 \pi^\pm X^\mp$ final states.

Contents

List of Figures

List of Tables

≫Einer hat immer unrecht: aber mit zweien
beginnt die Wahrheit. – Einer kann sich nicht
beweisen: aber zweie kann man bereits nicht
widerlegen.≪
Friedrich Nietzsche, Die fröhliche Wissenschaft
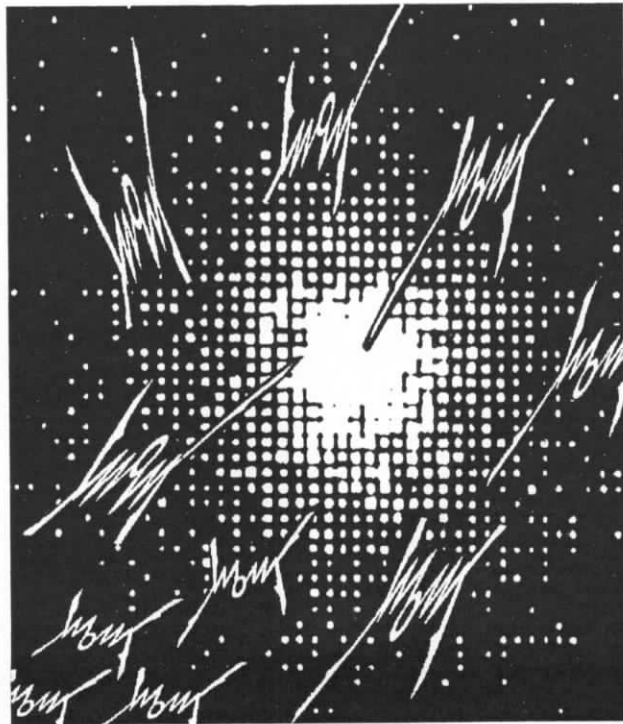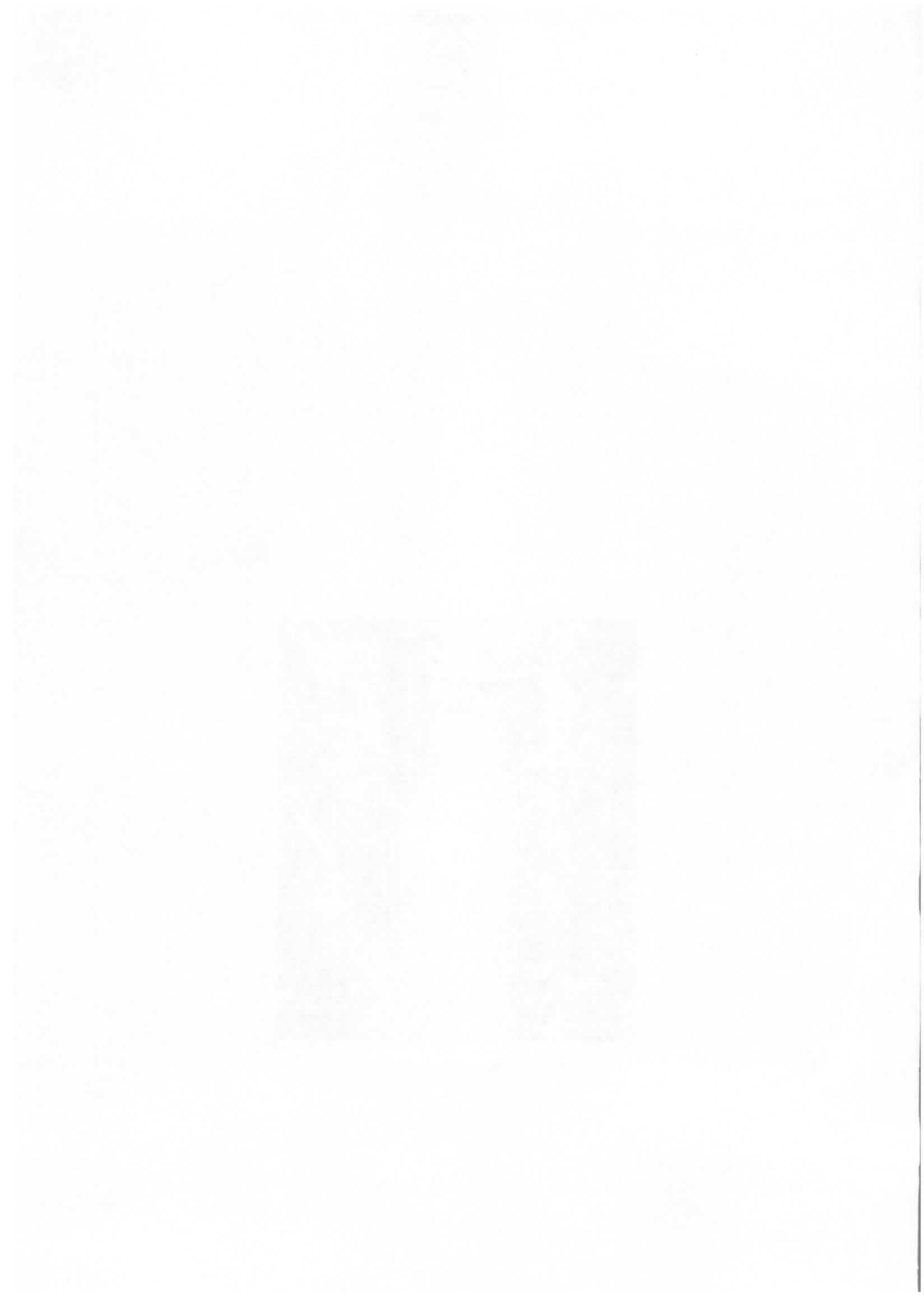
Part I

Theory and Experiment

Chapter 1

Introduction

In 1964 quarks made their appearance in particle physics: Gell-Mann and Zweig developed a group theoretical scheme to order mesons and baryons into supermultiplets of $SU(3)$ in which the u, d and s quarks are the basic flavour triplet units. The name *quarks* originates from the novel ≫Finnegans Wake≪ by James Joyce, where on page 383 the following poem is found:

> — Three quarks for Muster Mark!
> Sure he hasn't got much of a bark
> And sure any he has it's all beside the mark.

At that time the general belief was that of quarks as fictitious mathematical objects rather than as real physical states – this changed during the sixties when experimenters working with bubble chambers were discovering new particles which fitted into the predicted $SU(3)$ supermultiplets. Since about 1968 the structure of the nucleon has been studied by observing deep inelastic lepton-nucleon scattering. Such investigations have provided a large body of information on the dynamics of quark-quark interaction; in particular the results suggested the existence of point-like constituents inside the nucleon. Based on these observations Feynman developed the parton model – later on it was recognized that the static quarks of Gell-Mann and Zweig and the dynamic partons of Feynman are in fact the same objects. Since then many experiments have been devoted to the analysis of quarks and the strong forces acting between them. In particular, experiments at e^+e^- colliding beam machines gave deep insight into this area of physics.

The present thesis attempts to investigate the transition from colour triplet quarks to colour singlet hadrons – a process governed by the strong interaction, which is described by a field theory called Quantum Chromo Dynamics (QCD).

The strength of the interaction implies that already 10^{-23} seconds after the annihilation of electron and positron has created a coloured quark-antiquark pair, these transform into colour singlet metastable objects, which themselves undergo various transitions until finally stable particles emerge and are eventually observed in the CELLO detector – the extrapolation to the early stage of the event is thus difficult. A similar problem is encountered in astrophysics, where extrapolations are made from the present state of the universe to the initial big-bang: and, to a certain extent the same methods are used in the two areas of physics, e.g. quantum interferometry, factorial moment analyses etc. A great advantage of e^+e^- physics is, of course, its larger event rate.

This thesis is divided into two main sections: the present section (chapters 1-4) contains general aspects of e^+e^- annihilation, while the second section (chapters 5-10) is devoted to

3

multiparticle production. Chapter 2 gives a theoretical introduction to the physics relevant for the subsequent analyses; in particular it covers commonly used hadronization models. This is followed in chapter 3 by a description of the experiment, which has been adapted from [16]. Global properties of annihilation events and inclusive cross sections are treated in chapter 4. Chapter 5 contains basic information for the subsequent analyses of multiparticle production. In chapter 6 multiplicity distributions are analysed in great detail, including investigations of Monte Carlo models. Chapters 7 and 8 are dedicated to intermittency, the former covering more general aspects and the latter describing some experimental analyses. Bose-Einstein and two-particle correlations are analysed in chapter 9 and finally the results are summarized in chapter 10. The more extensive numerical results are presented in tabular form in the appendices A-C.

Chapter 2

Theory

The main concern of this thesis is to investigate the mechanism of particle production in e^+e^- annihilation; in particular those aspects related to the very early stage of the event. Experimental and theoretical limitations are encountered in this attempt: firstly, information on the primary event is only indirectly available through the observed final state particles; and then, the application of the basic theory (QCD) is limited by theoretical difficulties. For these reasons phenomenological models are of vital importance for the present investigations, and therefore we shall discuss them here in some detail, a more complete survey is given in [48,49].
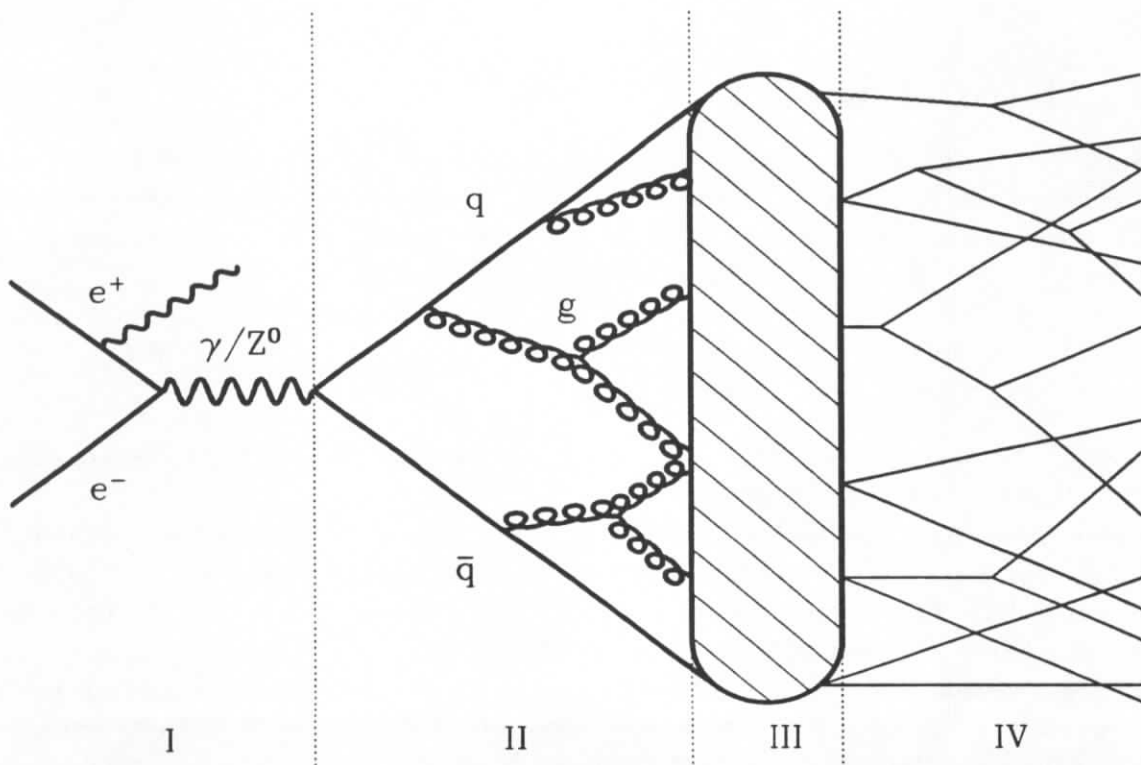
Figure 2.1: The four phases of e^+e^- annihilation: I. electro-weak phase with initial state radiation, II. perturbative QCD phase with gluon radiation off the leading quarks, III. confinement phase where colour singlet hadrons emerge and IV. decay into final state particles.

Various models of this kind exist, and can all be divided into four steps as depicted in figure 2.1. e^+e^- annihilation into $q\bar{q}$ pairs proceeds via virtual γ/Z^0 exchange, with

possible photon radiation off the initial state. This first step is purely electro-weak and therefore calculable to high precision. In the second phase the leading quarks emit gluons, which eventually split into pairs of quarks or gluons. The simulation of this process relies on approximations to QCD, of which different types are used in the corresponding models. In the third step the parton state is transformed into a system of colour-singlet hadrons. This process is governed by low momentum transfer, implying large values of α_S, which makes a perturbative description impossible, and therefore requires the use of fragmentation models. Among these the string and cluster models are most successful. In the final step matrix elements or simple phase space decays are used to transform primary hadrons into stable particles. These decays proceed through measured decay channels with their respective branching ratios.

2.1   Perturbative QCD

Two different approaches are commonly used to approximate the perturbative hadronization phase: these are the matrix element (ME) approach in $\mathcal{O}(\alpha_S^2)$ (available in the Jetset program [9]), and the parton shower (PS) approach in leading log approximation. The latter comes in three different versions: the original one due to Marchesini and Webber implemented into the Herwig program [5], the Lund version due to Sjöstrand and Bengtsson in Jetset [9] and a fairly new one from the Lund group – the colour dipole (CD) approach available in Ariadne [4].

2.1.1   Matrix elements

The Born term annihilation process $e^+e^- \rightarrow q\bar{q}$ is modified through possible gluon radiation of the coloured quarks: in $\mathcal{O}(\alpha_S)$ this yields $e^+e^- \rightarrow q\bar{q}g$ events. The cross section for the latter process can be expressed in terms of the scaled energies $x_i = 2E_i/E_{cm}$, $i = q, \bar{q}, g$, satisfying $\sum_i x_i = 2$. For massless partons the matrix element is:

$$\frac{1}{\sigma_0} \frac{d\sigma}{dx_1 dx_2} = \frac{\alpha_S}{2\pi} C_F \frac{x_1^2 + x_2^2}{(1 - x_1)(1 - x_2)} , \qquad 0 \leq x_i \leq 1, \; i = 1, 2, 3 \qquad (2.1)$$

where σ_0 is the lowest order Born term cross section and $C_F = 4/3$ is the colour factor corresponding to the transition $q \rightarrow qg$.

Energy-momentum conservation implies $y_{ij} \equiv m_{ij}^2/E_{cm}^2 = 1 - x_k$, and this relation is used to classify a three-parton system: if $\min(y_{ij}) < y_{cut}$ for any of the three possible combinations, the corresponding three-parton system is called a two-jet event. Of course, the cross sections for two- and three-jet production are then functions of y_{cut}.

The cross section (2.1) is divergent for $x_1 \rightarrow 1$ or $x_2 \rightarrow 1$; however, this is compensated by a corresponding singularity in the $q\bar{q}$ cross section, provided propagator and vertex corrections are included. The total cross section is therefore finite and amounts to $\sigma_{tot} = \sigma_0(1 + \alpha_S/\pi)$. In Monte Carlo models it is necessary to apply a non-zero y_{cut} in the three-jet phase space, since these models are based on probabilistic rules and therefore could not handle a negative total two-jet cross section.

In $\mathcal{O}(\alpha_S^2)$ two further parton states can occur: $e^+e^- \rightarrow q\bar{q}gg$ and $e^+e^- \rightarrow q\bar{q}q'\bar{q}'$, the latter is relatively uncommon and contributes only $\approx 5\%$ to the total four-jet rate. As in the previous case the Monte Carlo simulation requires the specification of a y_{cut}, such that only

positive total cross sections occur. Several schemes exist, which regulate the classification of an n-parton system as either two-jet, three-jet or four-jet (see [49] for a discussion).

2.1.2 Parton showers

Owing to the vast number of Feynman diagrams contributing to multi-parton cross sections these have not been calculated yet. An alternative to these excessive calculations is available in terms of the leading logarithm approximation (LLA). In this approach only the leading terms of the perturbative expansion are kept, thus neglecting non-leading corrections. This provides the basis for parton shower programs, since it is possible to give a probabilistic interpretation to the LLA if certain kinematical simplifications are made. In parton showers the essential features of coherence are retained [7]. Furthermore, parton showers contain the correct Sudakov damping, which is missing in lowest orders matrix elements; and, they generate multi-parton final states with "jets within jets". It is therefore expected that parton showers provide a superior description of the internal jet structure, but are inferior to the $\mathcal{O}(\alpha_S^2)$ matrix element calculation, with respect to wide-angle hard parton emission.

Parton shower models are based on the iterative use of the Altarelli-Parisi equations which determine the probability $\mathcal{P}$ that a branching $a \rightarrow bc$ occurs during a small change dt of the evolution parameter $t = \ln(Q_{evol}^2/\Lambda^2)$:

$$\frac{d\mathcal{P}_{a \rightarrow bc}}{dt} = \int dz \frac{\alpha_S(Q^2)}{2\pi} P_{a \rightarrow bc}(z) \ . \tag{2.2}$$
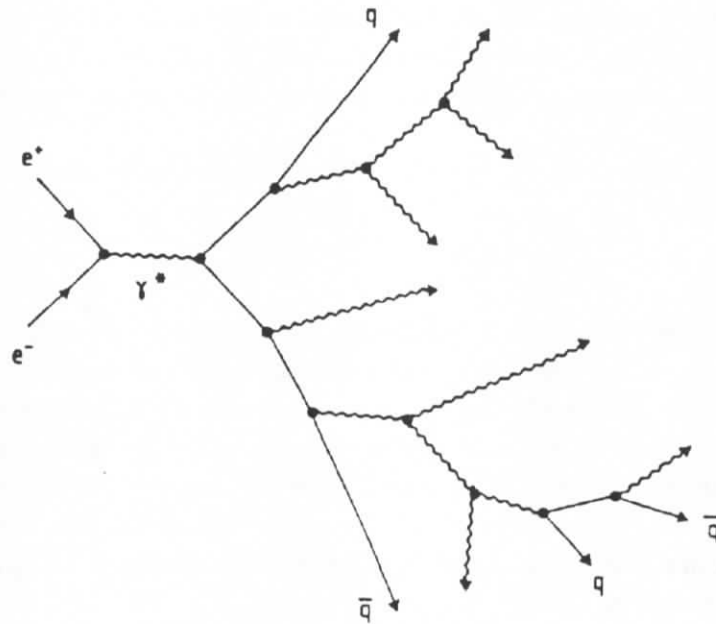
Figure 2.2: Parton shower in e^+e^- annihilation [6].

Theoretical considerations suggest that the Q^2 scale of α_S is $p_\perp^2$, i.e. approximately the transverse momentum of the branching, and this is the scale actually used in programs such as Herwig and Jetset. The $P_{a \rightarrow bc}$ in (2.2) are the Altarelli-Parisi splitting kernels:

$$P_{q \rightarrow qg}(z) = C_F \frac{1+z^2}{1-z} \ , \tag{2.3}$$

$$P_{g \to gg}(z) = N_C \frac{(1 - z(1 - z))^2}{z(1 - z)} , \tag{2.4}$$

$$P_{g \to q\bar{q}}(z) = T_R(z^2 + 1(-z)^2) , \tag{2.5}$$

which determine the distribution in energy-momentum in the transition $a \to bc$, such that b takes a fraction z and c a fraction $1 - z$ of the energy-momentum carried by parton a. The $C_F = 4/3$, $N_C = 3$ and $T_R = n_f/2$ ($n_f = 5$ is the number of active quark flavours) are colour factors determined by the gauge structure of QCD.

The evolution process starts at the maximum allowed virtuality t_{max} for a parton (depending on the available phase space) and stops whenever it is below the threshold t_{min}. Partons emerging in this process may themselves branch, so that eventually a tree-like structure develops (cf. figure 2.2).

Shower algorithms: Different interpretations of the quantities Q^2_{evol}, Q^2 and z are possible, insofar as the resulting physical differences are of non-leading character and are thus not accessible by leading log calculations. The shower algorithms in Herwig and Jetset differ in the choice of Q^2_{evol}, but both use the $p^2_\perp$ of the branching for the scale in $\alpha_S(Q^2)$.

In the Herwig model angular ordering is accomplished by the choice of an angular variable for the evolution process: $Q^2_{evol} = E^2\zeta$ with $\zeta \approx 1 - \cos\theta$. Since the energy E of the branching parton is constant, a decrease in Q^2_{evol} automatically leads to decreasing opening angles in successive branchings.

The Jetset parton shower develops in the centre of mass frame, with z defined as the energy fraction in this frame. The evolution variable t is chosen to be $t = \ln(m^2/\Lambda^2)$, implying that angular ordering must be imposed as an additional constraint on the m and z values of each branching. A special feature of this approach is that it matches the first branching, which is not constrained by the angular ordering requirement, onto the first order matrix element (2.1) for $q\bar{q}g$ production.

The colour dipole approach [3,4], realized in the Ariadne program, starts from (2.1), which can be rewritten as:

$$dn = \frac{3\alpha_S}{4\pi} \frac{dk^2_\perp}{k^2_\perp} dy d\varphi , \tag{2.6}$$

where $k_\perp$, y and φ are the transverse momentum, rapidity and azimuth of the radiated gluon. The physical picture is that of a colour dipole formed by the $q\bar{q}$ pair: this dipole radiates gluons according to (2.6). Once the first gluon has been emitted the system consists of two dipoles; one between the quark and the gluon and the other between the antiquark and the gluon. Subsequent gluon radiation is assumed to occur independently from the two dipoles; in this way the procedure is generalized to multi-gluon radiation. Because the gluon with the largest $p_\perp$ is radiated first the angular ordering condition, arising from soft gluon interference, is automatically taken into account.

2.2   Fragmentation

2.2.1   Independent fragmentation

In this section the fragmentation model of Field and Feynman [2] is discussed. This model is actually not used in the present analysis; however, it contains a number of basic features which still can be found in more recent models.

The intention of the authors was to give a parameterization of the properties of quark jets, as a reference standard for the experiments.

The model involves the following assumptions:

- The probability that the hadron containing the original quark leaves the remaining jet a fraction η of its momentum is given by an arbitrary function $f(\eta)$. This ultimately determines the momentum distribution of hadrons, and hence $f(\eta)$ is constrained by experimental data.

- New quark-antiquark pairs are produced according to the degree that flavour $SU(3)$ is broken, such that $s\bar{s}$ is half as probable as $u\bar{u}$. This particular choice was suggested by experimental data, rather than as a theoretical prediction.

- The spin of primary mesons corresponds to vector and pseudoscalar states with equal probability. This was inferred from $\rho^0/\pi^0 \approx 1$ at large $p_\perp$ in pp collisions.

- The transverse momentum of primary quarks is Gaussian distributed, according to $\exp(-p_\perp^2/2\sigma_q^2)d^2p_\perp$. This implies $\langle p_\perp^2 \rangle = 4\sigma_q^2$ for primary mesons, for firstly primary mesons receive contributions from two quarks, and secondly $p_\perp$ is a two-dimensional vector. The quark-antiquark pair $q_i\bar{q}_i$ has zero transverse momentum; i.e. transverse momentum is conserved locally in a pairwise fashion.

A severe shortcoming of this approach is that the fragmentation of jets proceeds independently for each primary quark, such that total flavour, energy and momentum are not exactly conserved in this process. Special procedures were developed which adjust these quantities at the end of the fragmentation process and thereby enforce conservation. The model does not include baryon production, and the character of the model does not make a clear suggestion of what baryons to expect. Similarly, the treatment of transverse momentum is arbitrary to some extent (see the discussion below). The separation of longitudinal and transverse fragmentation is, of course, an idealization. The particular simple ansatz for the transverse part reflects the dominance of longitudinal degrees of freedom in colour confinement.

The underlying physical picture is as follows: a quark q_0 produced at some light-cone energy-momentum $W^+ = E + p_\parallel$ in the z direction creates a colour field in which new quark-antiquark pairs are formed to discharge this field. In this process the production of particles with mass m is suppressed by a factor $\exp(-\pi m^2/F)$, where F is the field force acting on the colour charges. Thus it is more difficult to create $s\bar{s}$ pairs, for s quarks may have a larger mass than u and d quarks. The quark q_0 then combines with the antiquark $\bar{q}_1$ to form the rank-1 meson $q_0\bar{q}_1$, carrying a fraction z_1 of the original W^+ and leaving a fraction of $1 - z_1 = \eta_1$ to the remaining jet. In the next step a $q_2\bar{q}_2$ pair may emerge from the field to give the rank-2 meson $q_1\bar{q}_2$ with a fraction $z_2(1 - z_1)$ of W^+ etc. This process is iterated until finally the energy is used up (see figure 2.3).

Longitudinal fragmentation: It should be noted that the order in rank reflects the flavour relationship and does not necessarily coincide with the order in momentum; i.e. the rank-2 primary meson may have a larger momentum than the rank-1 meson. The degree of agreement between ordering in rank and momentum depends on the function $f(\eta)$; e.g. if $f(\eta)$ is a delta-function ($f(\eta) = \delta(\eta - a)$), such that every hadron would leave the same fraction a of its energy to the remaining jet, the hadrons later in rank have to have smaller momenta than those earlier in rank, corresponding to strict ordering.
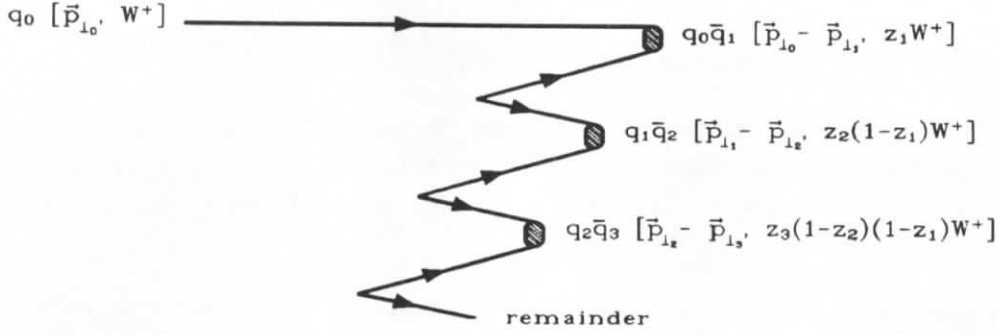
Figure 2.3: Iterative jet production: indicated are flavour, transverse momentum and light-cone energy-momentum relationship.

In determining the splitting of the original W^+ the function $f(\eta)$ is assumed to be the same at each step independent of the remaining energy: i.e. the remainder q_1 jet fragments exactly like the original q_0 jet, only scaled down by a factor $1 - z_1$ in energy. The choice of the function $f(\eta)$ is constrained by the fact that the resulting particle distributions fit the experimental data. Usually a parabola is chosen:

$$f(z) = 1 - a + 3a(1 - z)^2 \,, \tag{2.7}$$

where $a = 0.77$ is the recommended default value. The identification of z with the fraction of the jet's W^+ yields a flat central rapidity plateau for mesons produced deep in the cascade. For small z values the mean loss of rapidity per primary meson is then given by:

$$\delta y = -\int_0^1 \ln(\eta) f(\eta) d\eta \,, \tag{2.8}$$

and amounts to 0.56 units per primary meson, for $f(\eta)$ according to (2.7) with $a = 0.77$.

Transverse fragmentation: The assumption that $q\bar{q}$ pairs emerge with zero transverse momentum from the colour field leads to strong anti-correlations between mesons neighbouring in rank. As indicated in figure 2.3 the rank-i meson $q_{i-1}\bar{q_i}$ has $\vec{p}_\perp(i) = \vec{p}_{\perp i-1} - \vec{p}_{\perp i}$. From this it is immediately seen that mesons adjacent in rank have a strong tendency to appear at opposite azimuthal angles with respect to the jet axis. The correlation coefficient;

$$C_{ij} = \langle \vec{p}_{\perp i} \cdot \vec{p}_{\perp j} \rangle / \sqrt{\langle p_{\perp i}^2 \rangle \langle p_{\perp j}^2 \rangle} \,, \tag{2.9}$$

has the value $-\frac{1}{2}$ for $j = i + 1$, i.e. for mesons adjacent in rank and is zero otherwise. This is certainly a very particular choice and is considered as a pure guess by Feynman and Field [2]. In general it is also possible to give the centre of mass of the emerging $q\bar{q}$ pairs a Gaussian distribution. This would change the correlation coefficient (2.9) from the value $-\frac{1}{2}$ to any value between $-\frac{1}{2}$ and $+\frac{1}{2}$. Furthermore, it is not unreasonable to expect $p_\perp$ correlations between different $q\bar{q}$ pairs. Usually, not much attention is given to transverse fragmentation properties. It will become clear in the course of this thesis that the models are indeed too simple in this respect, and do not provide an adequate description of nature.

2.2.2 String fragmentation

In this section string fragmentation according to the Lund model is discussed; a detailed description of this model is given in [8].

The concept underlying string fragmentation is that of linear QCD confinement at large distances. The process of hadron production in e^+e^- annihilation is assumed to occur in a colour flux tube which evolves in a volume of approximately $1 \times 1 \times 30$ fm^3, at the energy of this experiment. The transverse extension of this string is of a typical hadronic size (1 fm) and the longitudinal extension is determined by the energy density $\kappa \approx 1$ GeV/fm on the string, as inferred from hadron spectroscopy.

A Lorentz covariant and causal description of particle production off this flux tube is possible in terms of the massless relativistic string, with its particular kinematics. In the model it is assumed that the flux tube may break into two colour singlet pieces via spontaneous formation of $q\bar{q}$ pairs in the colour field. On average, these breaks occur when the quark and antiquark are $1 - 5$ fm apart in their rest frame. This pair production is considered as a quantum mechanical tunneling process, such that quarks with transverse mass $m_\perp^2 = m^2 + p_\perp^2$ are produced in one space-time point and then tunnel out to the classical allowed region. Classically, quarks with transverse mass cannot be produced in one point, but must be produced at a certain distance to provide the field energy which is necessary to generate the transverse mass. The probability for the tunneling of a quark is proportional to:

$$\exp(-\pi m_\perp^2/\kappa) = \exp(-\pi m^2/\kappa)\exp(-\pi p_\perp^2/\kappa) . \tag{2.10}$$

This formula has two important implications:

- The factorization of transverse momentum and mass implies a Gaussian $p_\perp$ spectrum for the emerging quarks, independent of the quark flavour.

- Heavy quark production is suppressed in the fragmentation ($u : d : s : c \approx 1 : 1 : 0.3 : 10^{-11}$), thus charm and bottom quarks are not expected to be produced during fragmentation.

Hadrons are then formed from a quark from one break and an antiquark from an adjacent break; this is very similar to the independent fragmentation scheme, and therefore the concept of rank applies also here. However, while the iterative structure of the independent fragmentation model was just an ad hoc assumption, the string model is based on a particular space-time structure.

Space-time structure: In an iterative process the original string, stretched between the q_0 quark and the $\bar{q}_0$ antiquark, may break into two colour singlet pieces via the formation of a $q_1\bar{q}_1$ pair at (x_1, t_1) in space-time. Further breaks may then occur at later times (x_i, t_i) (see figure 2.4). Quarks and antiquarks from adjacent breaks combine to form subsystems, which are either hadrons or fragment further. Energy and momentum of the $\bar{q}_i q_{i+1}$ hadron are given by $\kappa(x_{i+1} - x_i)$ and $\kappa(t_{i+1} - t_i)$ respectively. The mass m of the hadron $\bar{q}_i q_{i+1}$ thus constrains the production points to lie on the hyperbola:

$$(x_{i+1} - x_i)^2 - (t_{i+1} - t_i)^2 = \frac{m^2}{\kappa^2} , \tag{2.11}$$

which can be parameterized as:

$$(x_{i+1} - x_i, t_{i+1} - t_i) = \frac{m}{\kappa}(\cosh y, \sinh y) , \tag{2.12}$$
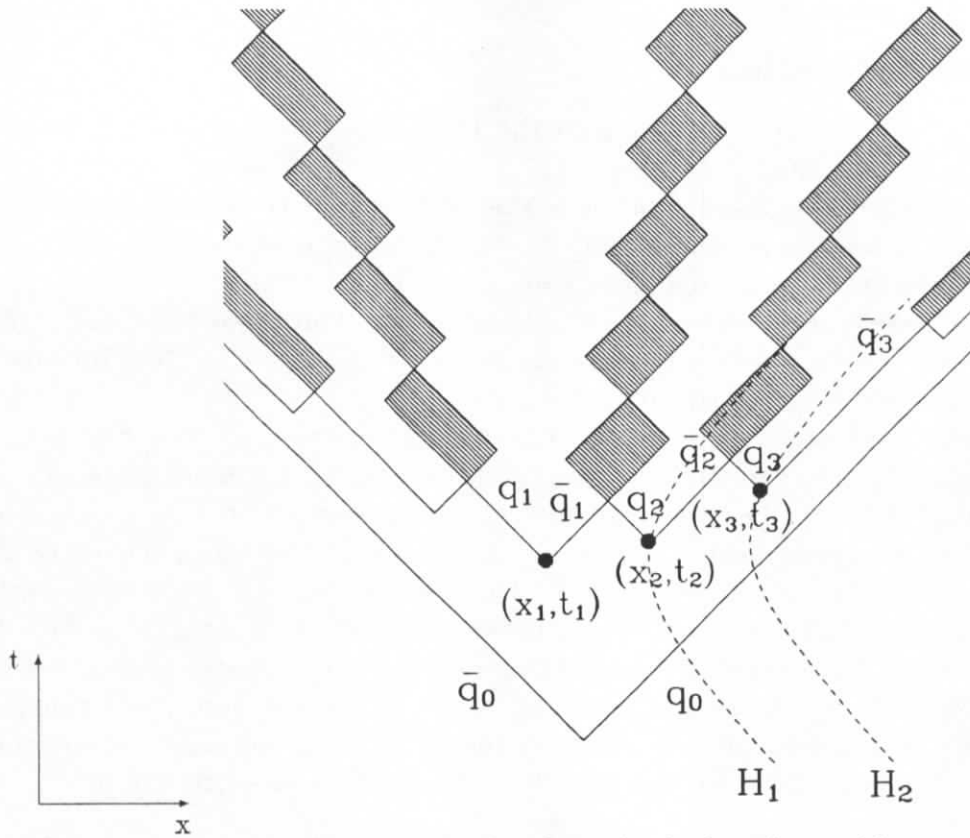
Figure 2.4: Hadron formation in the string model.

where y is the rapidity of the hadron in the $q_0\bar{q}_0$ rest frame.

The splitting of the original W^+ is done according to the left-right symmetric fragmentation function:

$$f(z) = \frac{(1-z)^a}{z} \exp\left(\frac{-bm_\perp^2}{z}\right) , \qquad (2.13)$$

where a and b are free parameters. Equation 2.13 is the most general fragmentation function (with some simplifications) obeying left-right symmetry. This property refers to the fact that, in principle, it should be impossible to distinguish whether a fragmentation process started from the quark or the antiquark end of the string. This requirement is not fulfilled in the independent fragmentation model, described in section 2.2.1.

As an alternative to (2.13) the so-called Peterson function [10] may be used for heavy charm and bottom quarks:

$$f(z) = \frac{1}{z(1 - \frac{1}{z} - \frac{\varepsilon_q}{1-z})^2} , \qquad (2.14)$$

where $\varepsilon_q = (m_0/m_q)^2$ and m_0 is a mass scale related to light hadrons.

As in independent fragmentation, string models separate the fragmentation process into longitudinal and transverse parts, although these do not decouple completely since the transverse mass enters in (2.13). Transverse fragmentation is handled the same way as in the independent fragmentation model; i.e. it is locally compensated and Gaussian distributed, implying strong correlation effects as discussed above.

The probability distribution of $q\bar{q}$ production vertices in invariant time $\tau^2 = t^2 - x^2$ is given by:

$$P(\Gamma)d\Gamma \propto \Gamma^a \exp(-b\Gamma)d\Gamma, \qquad (2.15)$$

where $\Gamma = (\kappa\tau)^2$ and a and b are the parameters of the symmetric fragmentation function (2.13). Thus, the $q_i\bar{q}_i$ production vertices are not randomly distributed in space-time, but kinematical boundary conditions require:

$$\Gamma_i = (1 - z_i) \left(\Gamma_{i-1} + \frac{m_i^2}{z_i} \right) , \qquad (2.16)$$

for adjacent breaks, with $\Gamma_0 = 0$ for the initial values at the quark and antiquark ends respectively. For large i, i.e. for particles produced in the central plateau away from the ends of the jet system the production points will, on average, lie on the hyperbola $\Gamma = (1 + a)/b$.

In the Monte Carlo model the string breaks alternate between the quark and the antiquark end of the string system. A special procedure is adopted to handle the production of the last two hadrons: when the remaining energy falls below a threshold (≈ 2 GeV) the iterative process is stopped and a final $q\bar{q}$ pair is formed to join the quark and antiquark ends of the string via the formation of two final hadrons.

Gluon radiation: The Lund string model can cope with both collinear and soft gluon radiation and this is why the model is said to be "infrared safe". Basically, this is because
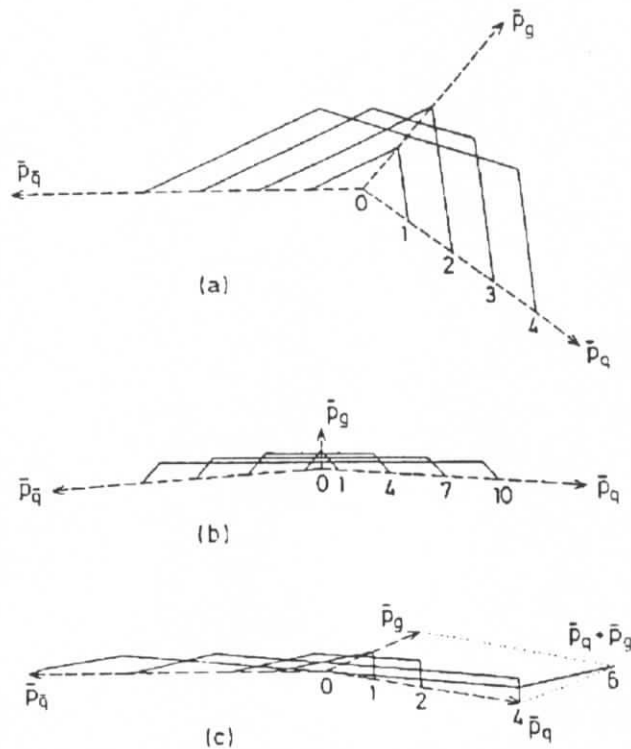
Figure 2.5: Strings with attached gluons [48]: a) an ordinary three-jet event, b) a three-jet event with a soft gluon and c) a three-jet event with a collinear gluon. The dashed lines indicate the trajectories of the partons and the solid lines show the evolving string at different times.

every emitted gluon just adds a kink to the string and thereby only changes the direction of energy-momentum flow, figure 2.5 shows the time evolution of the string for three typical cases. For this reason the model can be used in connection with both parton showers and matrix elements.

2.2.3   Cluster fragmentation

The central idea of cluster fragmentation is that of *preconfinement* [1], which means those properties of QCD, which are responsible for the local formation of colour singlet clusters, once the perturbative jet development has come to its end.

In this section we shall briefly discuss the cluster model implemented into the Herwig program [5]; a complete description of this model can be found in [5,6].

A basic requirement for any cluster model, in order to conform with the idea of preconfinement is that it does not disrupt too much the connection between colour and momentum flow. This is realized as follows: when the perturbative branching process approaches the scale $Q_0 = 2m_u = 2m_d$ the fictitious gluon mass $m_g = Q_0$ prevents further branchings of the type $g \rightarrow gg$, such that all outgoing gluons eventually decay into light (u or d) (di)quark-anti(di)quark pairs. The latter process is relatively uncommon in the perturbative phase and is enforced by a suitable modification of the $g \rightarrow q\bar{q}$ form factor. The relative abundances of different quark flavours are regulated by the quark mass assignments. In addition, the production of diquark pairs is controlled by two parameters: the scale Q_d below which diquark pair production may occur, and a probability P_d (constant per unit $\log Q$) that it will occur. This diquark scheme was introduced to account for baryon-antibaryon correlations [11], which require a relative diquark production rate of approximately 5 %; by default it is switched off.
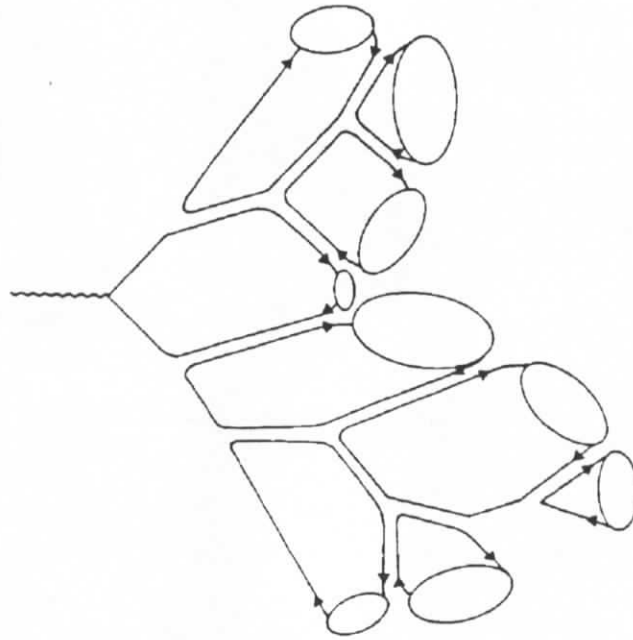
Figure 2.6: Colour structure in cluster fragmentation [6]: the blobs represent colour singlet clusters which subsequently decay.

At this stage the event consists solely of (di)quark-anti(di)quark pairs, and the dominant colour structure may be presented in a planar form as shown in figure 2.6. Neighbouring quarks and antiquarks are then combined to give colour neutral clusters. It is to note that these clusters have a distribution in mass and spatial size concentrated at low values which is approximately independent of the scale of the hard scattering process, reflecting the basic properties of preconfinement. The average mass of these clusters is actually about $3m_g$ (cf.

figure 6.17 on page 77).

Clusters, on the average, are supposed to represent the spectrum of primordial resonances occuring in the early stages of confinement. With this in mind, it appears reasonable that their decay should be a kind of averaged resonance decay. In the model it is thus assumed that most clusters disintegrate into two hadrons. This decay is isotropic in the rest frame of the pair and proceeds via the production of (di)quark-anti(di)quark pairs with one of the following flavours: $u\bar{u}$, $d\bar{d}$, $s\bar{s}$, $c\bar{c}$, $uu\overline{uu}$, $dd\overline{dd}$, $ss\overline{ss}$ $ud\overline{ud}$, $us\overline{us}$ or $ds\overline{ds}$, such that a cluster decays either into two mesons or into two baryons. The decay products are selected from the following multiplets: $0^-, 1^\pm$ or 2^+ for mesons and $\frac{1}{2}^+$ or $\frac{3}{2}^+$ for baryons. Each decay with the appropriate flavour is weighted according to the spin degeneracy $(2S + 1)$ and the available phase space.

An appealing property of this approach is that it does not distinguish between longitudinal and transverse fragmentation in contrast to independent-jet and string models. It is further noted that the (di)quark-anti(di)quark pairs, produced to split the clusters, are not associated with any dynamical properties, such as energy-momentum or spin, but carry flavour only. This is certainly an idealization; however, it gives definite predictions for the suppression of strange and charm particles and baryons, which in this case is completely determined by the phase space available in cluster decays.

Three exceptions from the above scheme may occur:

1. Clusters containing heavy flavours (b or t) undergo weak $V - A$ decays, giving a lighter quark and a colour singlet fermion-antifermion pair from the decay of a virtual W boson.

2. Low mass clusters, too light to decay into two hadrons, collapse into the lightest hadron of their flavour. Energy-momentum conservation is accomplished by an exchange of energy with a neighbouring cluster.

3. For very massive clusters the two body decay is considered to be too poor an approximation. An iterative fission model is used instead to split those heavy clusters until their mass falls below the fission threshold $M_f = 3.5$ GeV. Only the light $u\bar{u}$, $d\bar{d}$ and $s\bar{s}$ flavours are produced during cluster fission. Energy-momentum is distributed symmetrically among the two decay products: i.e. a cluster of mass M_C formed from a (di)quark of momentum p_1^μ and an anti(di)quark of momentum p_2^μ decays into two clusters X and Y with

$$p_X^\mu = \left(1 - \frac{Q_0}{M_C}\right) p_1^\mu + \frac{Q_0}{M_C} p_2^\mu \,,$$
$$p_Y^\mu = \left(1 - \frac{Q_0}{M_C}\right) p_2^\mu + \frac{Q_0}{M_C} p_1^\mu \,.$$

Thus cluster fission is similar to string fragmentation.

Chapter 3

CELLO experiment

The data studied in this thesis were taken in the year 1986 with the CELLO detector at the e^+e^- storage ring PETRA at DESY in Hamburg. Since 1978 five collaborations conducted experiments with centre of mass energies up to 46.8 GeV in the four interaction regions at PETRA [12] (see figure 3.1). After 1986 data taking was stopped and PETRA was modified for its present role as an injector for the HERA storage ring. In 1986 measurements were performed at a centre of mass energy of 35 GeV. For CELLO this last year yielded data corresponding to a time integrated luminosity of 86 pb^{-1}.
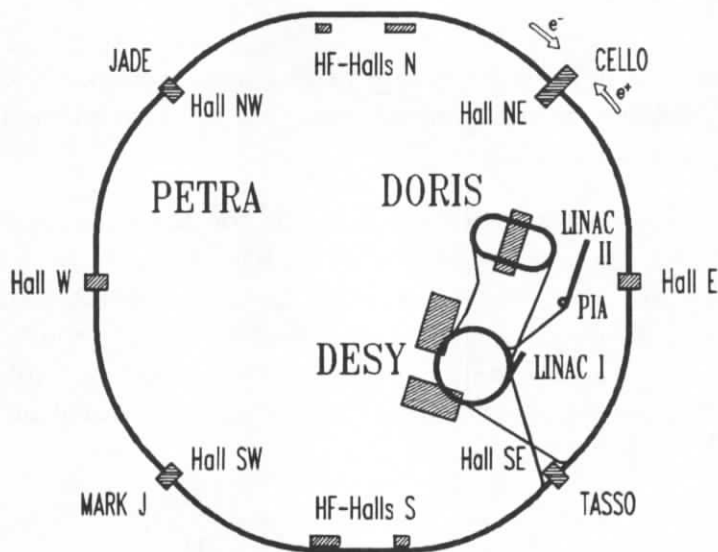
Figure 3.1: Storage ring PETRA with injection scheme.

The first section of this chapter describes the main features of the CELLO detector which are relevant for the analyses presented in this thesis. A description of the storage ring PETRA and the other experiments can for instance be found in [12]. The subsequent sections describe the data flow through the chain trigger – data acquisition – filter – event reconstruction – data reduction.

16

3.1 CELLO detector

Due to the relatively low event rate most detectors at e^+e^- machines are designed as general purpose detectors. In contrast to detectors at fixed target machines, which select one or more particular processes to be studied, these are built to record all types of events of interest.

CELLO was constructed as such a general purpose detector in 1978 by a group of French and German institutes [13]. The main requirements are a full coverage of the solid angle to measure and possibly identify charged and neutral particles. A special technical feature of the CELLO detector is the superconducting coil, of an novel design at that time, with an overall thickness of only 0.5 radiation lengths including the cryostat and insulating material. This design allows an undistorted energy measurement of photons and electrons in the lead liquid argon calorimeter surrounding the coil. Due to the fine segmentation of the calorimeter, shower topologies are easily reconstructed and photons and electrons can be identified and separated from hadrons [14]. The above components surround the cylindrically symmetric central tracking chamber which has a length of 2.2 m and thus allows us to measure charged particles over a large solid angle (97 % of 4π). With good hermeticity of the calorimeters (coverage down to an angle of 45 mrad with respect to the beam axis), CELLO has a large efficiency for reconstructing truly exclusive events, i.e. events where all final state particles are detected.

3.1.1 Survey

Figure 3.2 shows a schematic view of the detector at the time of construction. Various components have later been added or modified. The following list gives a survey of the detector parts at the time of the last run period in 1986. Those parts which are relevant for the analysis will be described below. A detailed description of the other components can be found in [13]. Going from the inner parts to the outer parts of the detector, one finds the following components:

- **Beam pipe:** the aluminium vacuum pipe surrounds the beam axis at a distance $r = 7.8$ cm. The wall thickness is 0.03 radiation lengths (X_0) (before 1982 0.07 X_0).

- **Beam pipe chambers:** since 1982 two staggered layers of drift tubes with a length of 1 m surround the beam pipe. Their thickness amounts to 0.01 X_0. These chambers were added in order to improve the vertex reconstruction and momentum resolution [17].

- **Central detector:** the central detector consists of a system of cylindrical drift and proportional chambers that measure track coordinates of charged particles between $r = 17$ cm and $r = 70$ cm. The amount of matter in these components sums up to 0.02 X_0.

- **Superconducting solenoid:** the aluminium coil with a wall thickness of 0.5 X_0 creates a solenoidal field of 1.32 T.

- **Barrel calorimeter:** the central barrel shaped lead liquid argon calorimeter consists of 16 identical modules with a depth of 20 X_0. Their distance from the beam axis is $r = 106.7$ cm.

CELLO
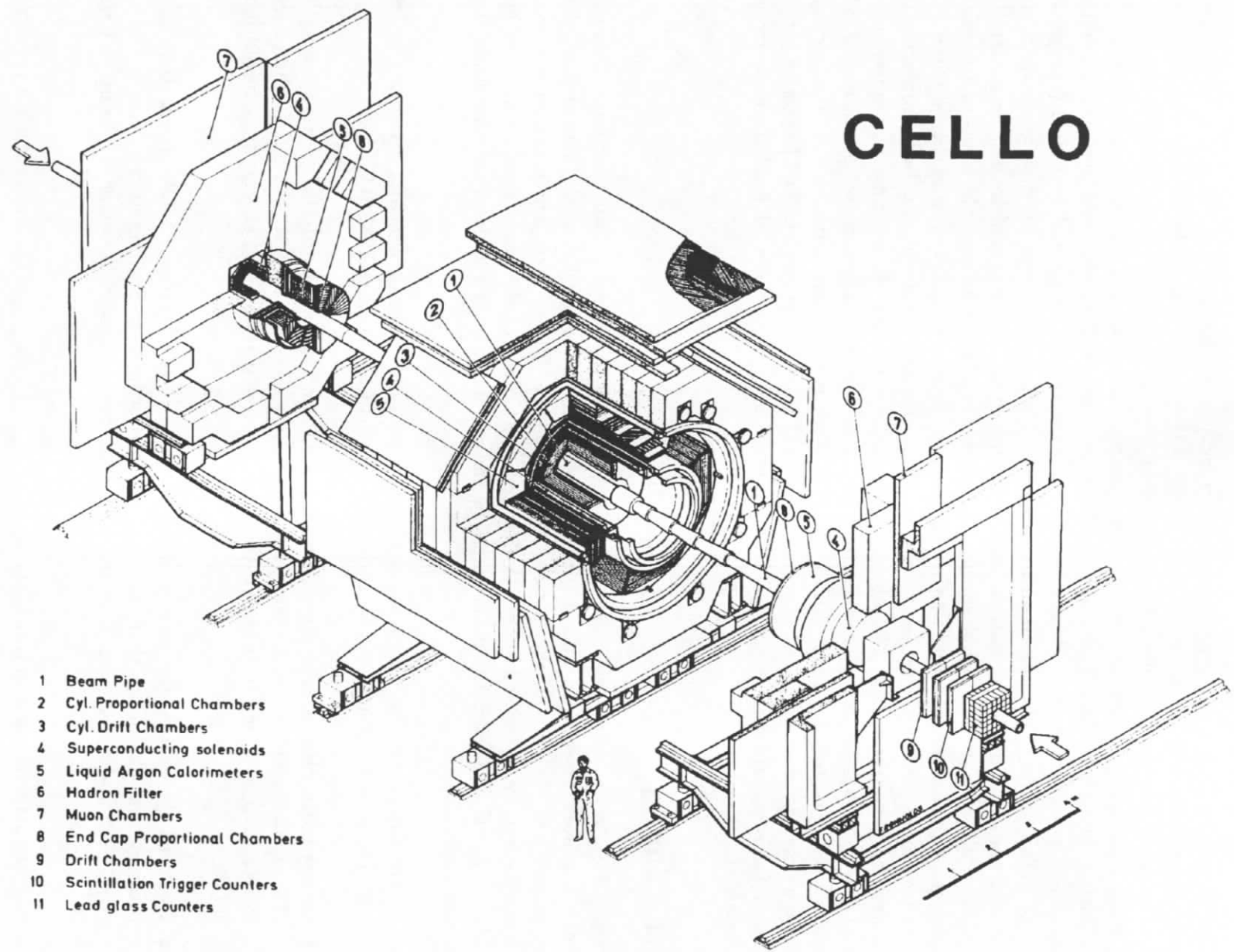
1 Beam Pipe
2 Cyl. Proportional Chambers
3 Cyl. Drift Chambers
4 Superconducting solenoids
5 Liquid Argon Calorimeters
6 Hadron Filter
7 Muon Chambers
8 End Cap Proportional Chambers
9 Drift Chambers
10 Scintillation Trigger Counters
11 Lead glass Counters

Figure 3.2: Sideview of the CELLO detector.

- **Return yoke:** the 80 cm thick iron construction serves not only as a return yoke for the magnetic flux but also as a hadron filter of 5-8 absorption lengths.

- **Muon chambers:** muons with momenta $p > 1.2$ GeV traverse the hadron filter and are subsequently detected in the muon chambers. These large area chambers with a drift cell structure are read out as proportional chambers and cover approximately 90 % of the solid angle.

In the forward region the detector is completed by:

- **End cap calorimeter:** this lead liquid argon calorimeter consists of four modules of 21 X_0 complementing the barrel calorimeter in the forward region.

- **Hole tagger:** a set of scintillation counters with 4 X_0 material in between was added in 1982 to close the acceptance hole for neutral particles between the barrel and end cap calorimeters.

- **End cap proportional chambers:** two crossed layers of proportional chambers in front of the end cap calorimeter improve the reconstruction of forward going tracks.

- **Forward calorimeter:** due to the installation of mini beta quadrupoles in 1982, the forward detector was totally remodeled and now consists of a set of scintillator strips and lead glass blocks to measure the position and energy of scattered electrons and positrons.
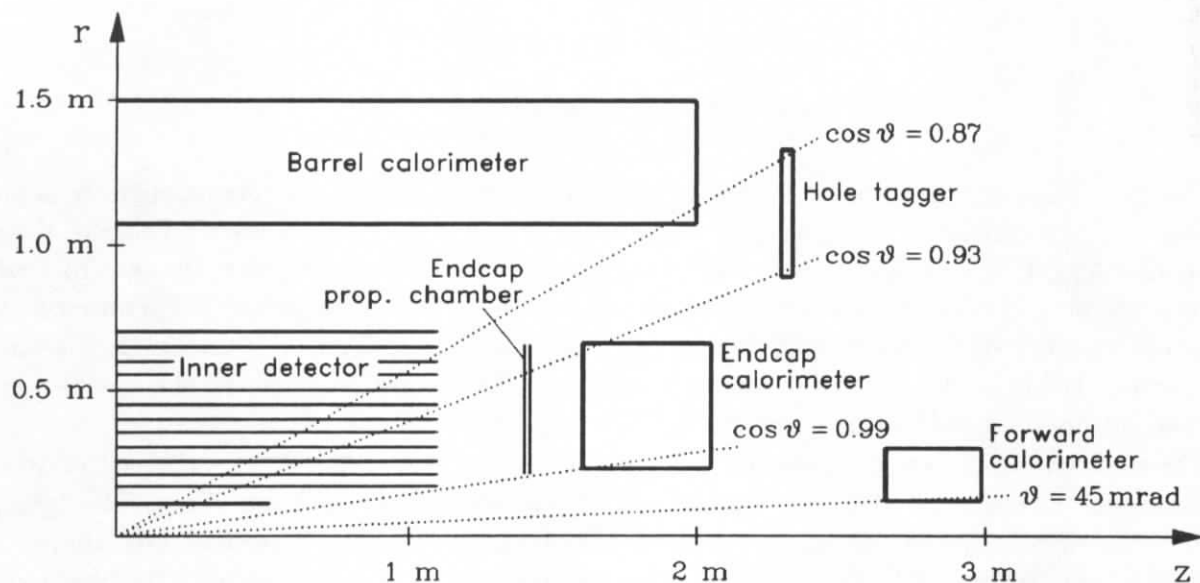
Figure 3.3: Geometrical acceptance of the CELLO detector.

A schematic view of the geometrical acceptance of the detector components is given in figure 3.3. Here, only the innermost components of the detector are shown. The CELLO coordinate system is defined with the z-axis along the flight direction of the incoming electrons. The x-axis lies in the plane of the storage ring pointing outwards, the y-axis is defined by $\vec{y} = \vec{z} \times \vec{x}$. In the plane perpendicular to the beam axis the polar coordinates r and φ are used; the angle ϑ is determined with respect to the z-axis.

3.1.2 Central track detector

The central detector consists of a system of cylindrical drift and proportional chambers, as depicted in figure 3.4. They are mounted concentrically to the beam axis and have an outer radius of 0.7 m and an overall length of 2.2 m. Altogether there are 7 drift and 5 proportional chambers. Their position and other parameters can be taken from table 3.1.
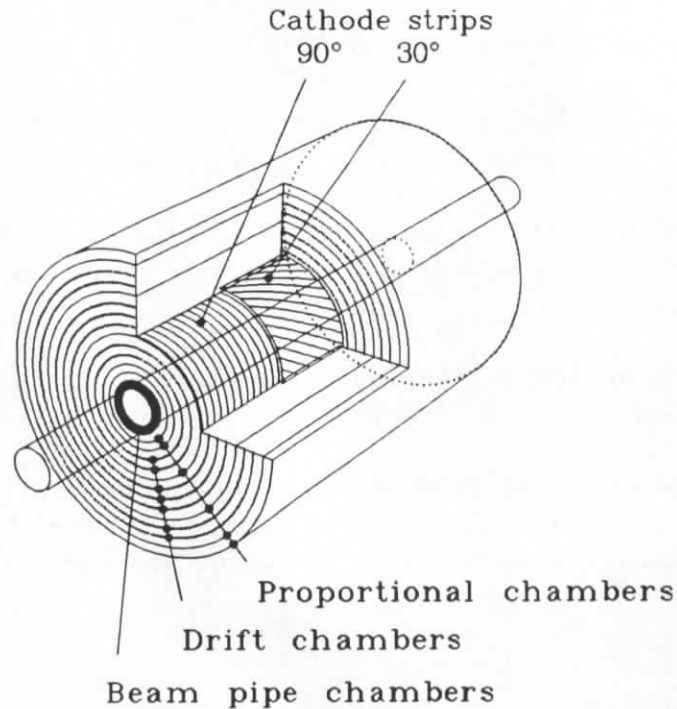
Figure 3.4: Central tracking device.

The two inner chambers were added in 1982 to improve the vertex reconstruction in the $r\varphi$-plane. They consist of two layers of drift tubes which are arranged parallel to the beam axis with a length of 1 m. Each of the drift tubes contains a single anode wire in a gas mixture of 50 % argon and 50 % ethane at atmospheric pressure. The coordinates perpendicular to the beam axis are determined by a measurement of the time difference between the passage of a particle through the drift tube and the arrival of the ionization pulse on the anode wire. The resolution achieved in this chamber is 180 μm [17].

The drift chambers are constructed from entirely open drift cells. Each drift cell consists of one anode wire separated from adjacent ones by a set of three cathode wires. The lateral distance between adjacent anode wires is on the average 15 mm. The drift chambers are grouped in sets of two or three chambers with a common gas volume enclosed by two mylar cylinders. As in the case of the drift tubes a gas mixture of argon and ethane in a ratio of 1:1 at atmospheric pressure is used. The resolution of the $r\varphi$-coordinates reconstructed from the space-drift-time-relation is 170 μm [18].

The proportional chambers are used to determine the z-coordinate of track points. This is accomplished by two cylindrical cathodes finely segmented in strips oriented at 90° and 30° with respect to the cylinder axis. The two cathode cylinders enclose a large number of axial anode wires with mutual spacings of the order of 2.5 mm. The precision of the $r\varphi$-coordinate measurement is given to first order by the geometrical resolution (spacing/$\sqrt{12} \approx 770$ μm).

chamber number	chamber type	radius [cm]	number of signal wires	distance of wires [mm]	# cathode strips 90°	30°
1	drift tube	10.90	128	5.35	—	—
2	drift tube	11.37	128	5.54	—	—
3	prop. ch.	17.0	512	2.09	252	256
4	prop. ch.	21.0	512	2.58	228	256
5	drift ch.	25.5	104	15.41	—	—
6	drift ch.	30.4	128	14.92	—	—
7	prop. ch.	35.7	1024	2.19	366	512
8	drift ch.	40.2	168	15.03	—	—
9	drift ch.	45.1	192	14.76	—	—
10	drift ch.	50.0	208	15.10	—	—
11	prop. ch.	55.3	1536	2.26	420	768
12	drift ch.	59.8	256	14.68	—	—
13	drift ch.	64.7	256	15.88	—	—
14	prop. ch.	70.0	1536	2.86	494	768

Table 3.1: Geometrical and electrical parameters of the central tracking detector.

The charge induced on the cathode strips at the point of incidence next to the anode wire is measured by an analog readout of each strip. The resolution of the z-position achieved this way is $\sigma \approx 440\ \mu$m. The proportional chambers are run with a gas mixture of 80 % argon and 20 % isobutane with an admixture of 0.2 % freon. Besides determining the z-position of track points the proportional chambers are used in the fast track trigger. The information from both projections is already available after 2 μs.

The tracking detector is completed by two crossed layers of proportional chambers which are mounted onto the front end of the end cap calorimeter. The anode wires measure the x- and y-coordinates while the cathode planes are divided into sectors of $\Delta\varphi$ and concentric rings, respectively. The resolution is of the order of 5 mm. The end cap proportional chambers cover the acceptance region of $0.910 < |\cos\vartheta| < 0.988$ [13].

The geometrical acceptance of the central tracking detector is 84 % of 4π if a track is required to hit all 14 chambers. Using in addition the information of the end cap proportional chambers and requiring only five chambers of the inner detector to determine all track parameters, the acceptance is increased to 97 % of the full solid angle.

The deflection of charged particles in the magnetic field of the CELLO superconducting coil forces the particles onto circular tracks in the $r\varphi$-plane with a curvature inversely proportional to their transverse momentum. The precision of momentum reconstruction depends on the number of track points measured, the resolution of the chambers and on multiple scattering in the detector material traversed. The momentum resolution of the CELLO central detector was determined to be [17]:

$$\frac{\sigma_{p_\perp}}{p_\perp} \approx 2\ \% \cdot p_\perp$$

where $p_\perp$ is measured in GeV. The vertex of a track can be determined with a precision of $\approx 330\ \mu$m.

3.1.3   Lead liquid argon calorimeter
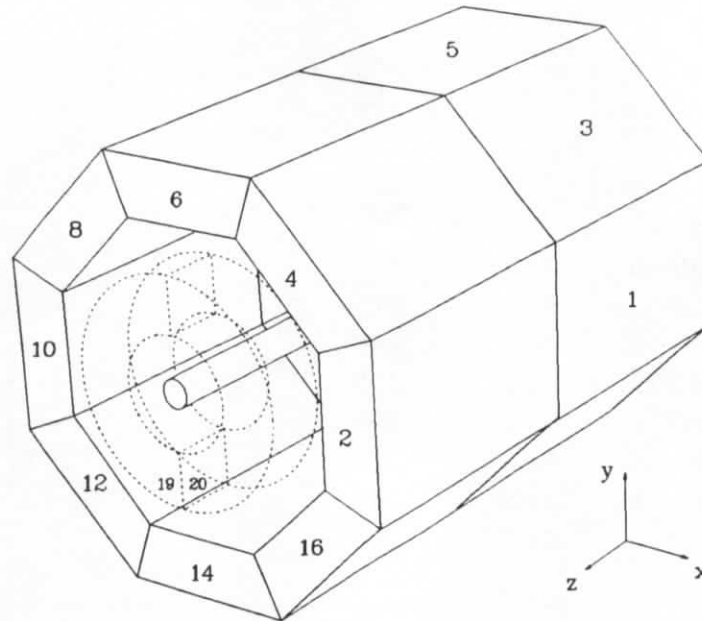
Figure 3.5: Structure of the lead liquid argon calorimeter.

The CELLO calorimeter has a sampling structure of lead layers alternating with layers of the active material argon. Electrons and photons create a secondary particle cascade by means of bremsstrahlung and pair creation. The ionization loss of these secondary particles is recorded in the argon. Electromagnetic showers at the maximum PETRA energies are fully absorbed in the 20 X_0 structure of the calorimeter. A good detection efficiency, energy resolution and spatial resolution of photons is achieved over the entire solid angle. Cascades induced by hadronic particles, however, are not completely contained in the calorimeter due to its depth of only 0.9 absorption lengths. This feature, on the other hand, allows a good electron-hadron separation. This is accomplished by the three-dimensional reconstruction of shower topologies in the highly segmented calorimeter structure [14].

	barrel calorimeter	end cap calorimeter
material in front of calorimeter	1.1 X_0	1.2 X_0
depth of calorimeter	20 X_0	21 X_0
thickness of lead layers	1.2 mm	1.2 mm
distance between lead layers	3.6 mm	3.6 mm
number of layers	41	42
number of electronic channels	9248	1472
angular resolution	4 mrad	6 mrad
acceptance in $|\cos\vartheta|$	< 0.86	$0.92 - 0.99$

Table 3.2: Technical data of the liquid argon calorimeters.

The barrel calorimeter is composed of 16 modules with trapezoidal cross section corresponding to a sector of an octagon. The two octagons are mirror images arranged symmetric

to $z = 0$ inside one large cryostat with an overall length of 4 m. The end cap calorimeter consists of four half-cylindrical stacks: two at each end of the detector enclose the beam pipe (cf. figure 3.5).

The modules in each of the calorimeters are identical. Layers of 1.2 mm lead plates (cathodes) and 1.2 mm lead strips (anodes) alternate (see figure 3.6 a)). The gap width between the lead layers is 3.6 mm (4 mm in the end cap calorimeter) and is filled with liquid argon. The lead strips and plates are at a relative voltage of 2.5-5 kV. The orientation of the strips in the barrel part alternates between an alignment parallel to the beam axis (φ-measuring), with an angle of 90° (ϑ-measuring) and at 45° (to resolve ambiguities). The strips in the end cap calorimeter are alternately vertical, horizontal and circular. The width of the strips is of the order of 2-3 cm. In front of the calorimeter there are two additional copper liquid argon layers (three in the end cap) which serve as dE/dX-gaps.
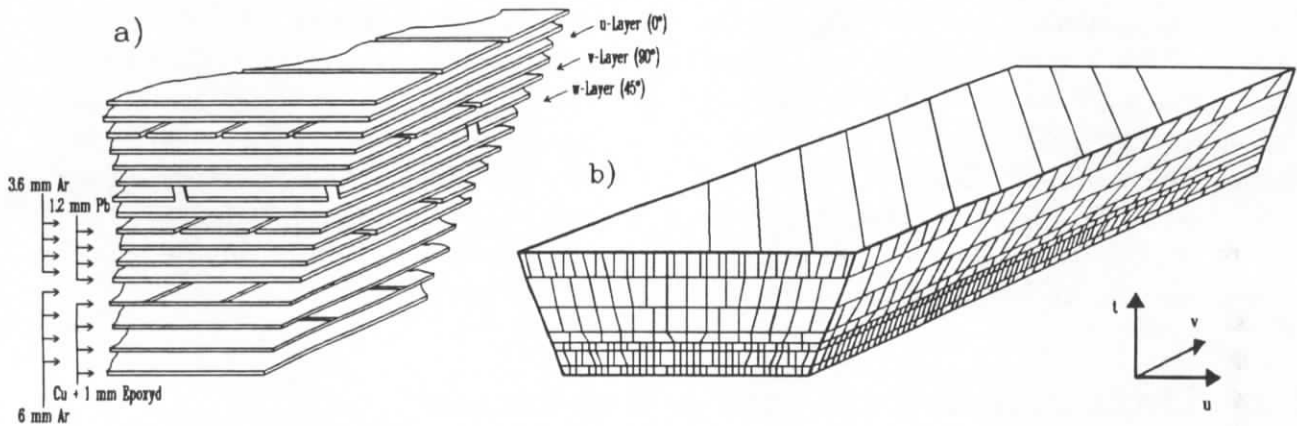
Figure 3.6: Geometric (a) and electronic (b) structure of the lead liquid argon calorimeter

There are more than 3000 strips in each of the modules. In order to decrease the number of electronic channels, neighbouring strips have been grouped to block layers (see figure 3.6 b)) with a scheme that yields a uniform angular resolution. For the azimuthal angle φ this uniform resolution is given by the octagonal structure of the calorimeter, for the polar angle ϑ (measured from the beam axis) it is achieved by a coarser read out structure towards the forward region. A detailed description of this read out block structure is given in [14]. The number of channels to be read out is thus reduced to 576 in a barrel module and 368 in an end cap module. To reduce the amount of data written to tape, channels with a signal below 2 σ above the electronic noise pedestal are suppressed. The electronic noise in a double layer corresponds to $\approx$ 1 fC. This has to be compared with the charge deposit of 5 fC for a minimum ionizing particle [14].

The energy resolution of the calorimeter is given by the sampling fluctuations. A further degradation results from material in front of the calorimeter, miscalibration, dead channels etc. The resolution for electromagnetic showers in the CELLO calorimeter achieved in the running experiment is:

$$\frac{\sigma_E}{E} = 5\,\% \oplus 10\,\%/\sqrt{E}$$

with E being measured in GeV ($\oplus$ = quadratic addition of the terms).

3.1.4   Forward calorimeter

The forward calorimeters measure electrons that are scattered at small angles not accessible to the end cap calorimeter. They serve as a monitor for the luminosity measurement based on Bhabha events and are used to trigger, and to measure the Q^2 of two-photon reactions.

The calorimeters are located at a distance of 2.65 m from the interaction point and cover the acceptance region from 45-110 mrad. Lead glass blocks are used as shower counters; 20 blocks are found on each side of the detector. Each half-circular quarter containing 10 blocks is mounted directly onto the beam pipe. The lead glass blocks have lateral dimensions of typically 5 cm ($= 2\ X_0$) and a length of 13 X_0. The Cherenkov light emitted by the charged particles in the shower cascade is detected by photomultipliers. The positional measurement of the tagged electrons is improved by means of a scintillator hodoscope. Half circular scintillator strips of 1 cm width are read out by photomultipliers at each end. A thin layer of lead (0.5 X_0) gives an early start to the shower cascade and hence an increased signal in the scintillators. Comparing the light output at each end allows a determination of the position along the scintillator (φ-coordinate), the radial position of the scintillator hit determining the angle with respect to the beam axis. This information is combined with the centre of gravity position from the lead glass blocks.

Due to the location of the forward counters a large amount of material is positioned in front of the calorimeter. This fact degrades the energy resolution over a large range; in some angle regions the energy measurement cannot be used at all. On average the material in front of the calorimeter amounts to 2 X_0 up to an angle of 90 mrad; above this the end cap cryostat shields the forward calorimeter with 10 X_0 of material.

3.2   Data acquisition and event reconstruction

Every 3.8 μs the electron and positron bunches cross each other in the interaction region of the CELLO detector. Most of the bunch crossings do not result in any physically interesting interaction. Owing to the small cross section, annihilation events occur at a rate of 1 per 10 minutes at the typical luminosity of $5 \cdot 10^{30}$ cm^{-2}s^{-1}. Background reactions such as interactions of beam particles with the residual gas in the beam pipe (*beam gas events*), interactions with the material of the beam pipe wall (*beam wall events*), cosmic ray events (*cosmics*) and synchrotron radiation are by far more abundant. In order to suppress this background and still accept the majority of physically interesting events a fast trigger logic is essential. The time needed to read out fully all the detector components limits the data acquisition rate to about 5 Hz. In order not to lose too many interesting events the trigger conditions cannot be too strict, and hence a second filter is needed to reduce the amount of background accepted by the loose trigger conditions and to minimize the expenditure of computer time needed for the full reconstruction of the data.

The forthcoming sections describe the sequence of data acquisition and reconstruction through the chain trigger, filter, event reconstruction and data reduction.

3.2.1   Trigger system

The trigger uses information from all components of the detector. A number of basic conditions are combined to give the trigger conditions selected. Basic conditions are for example the energy sums in the calorimeter modules, the energy in the forward calorimeter and the

number of tracks in the central and end cap track detector. Altogether there are 16 trigger conditions defined for the CELLO detector. at least one of which has to be fulfilled for an event to be recorded. The different conditions cover the various signatures of e^+e^- collisions. Here we describe only those conditions that are relevant for triggering annihilation events.

The fundamental ingredient for the charged particle trigger is a software programmable hardware track finding processor [19]. This processor employs the information of the five proportional chambers and of two of the drift chambers for the identification of tracks in the $r\varphi$-projection and of the 90° cathodes for the rz-projection. The chamber signals are divided into 64 azimuthal (as shown in figure 3.7) and 37 polar sectors. Each track creates a certain
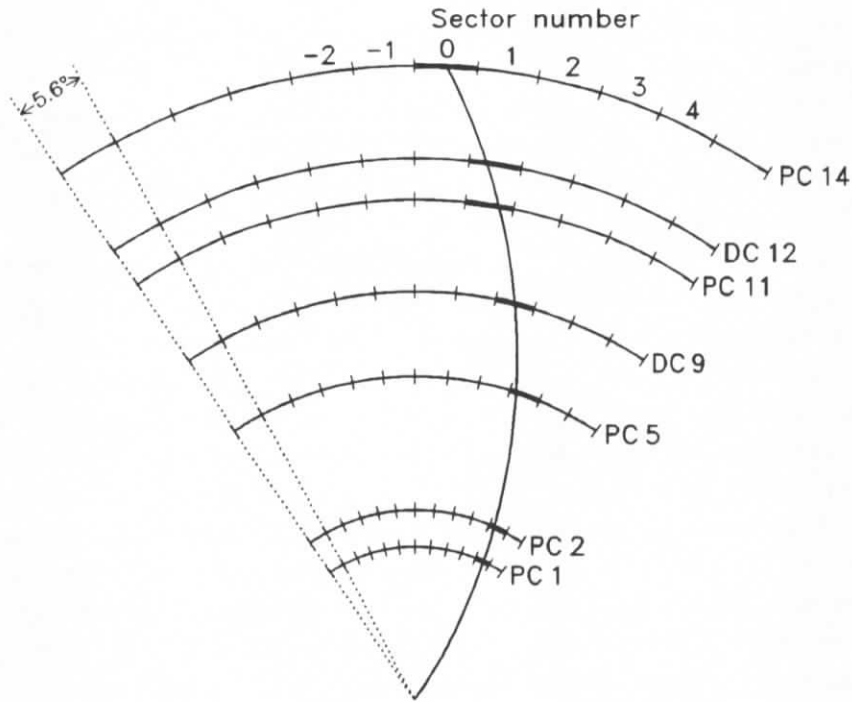
Figure 3.7: $r\varphi$-sectors for the trigger logic: Shown are the seven chambers used in the trigger, their segmentation in the $r\varphi$-projection and a track that ends in sector 0.

signal pattern in the sectors of the seven chambers. All possible patterns of tracks above a certain transverse momentum can be determined. These patterns are then stored in random access memories (RAM) – one set for transverse momenta above 650 MeV ($r\varphi_H$ masks) and one set for $p_\perp > 250$ MeV ($r\varphi_L$ masks). To take into account chamber inefficiencies, additional masks are stored with only 5 or 6 points per track. These precomputed masks are compared with the signals from the central detector. If the pattern coincides with any of the masks the corresponding condition is transfered to the master trigger unit. A similar identification is done in the rz-projection where at least three out of five hits in the proportional chambers are required. The location of masks is done in less than 1 μs.

The neutral particle trigger makes use of the information from the liquid argon calorimeter. Here the energy of a stack is computed by means of a hardware sum of all channels. Using discriminators, several trigger conditions can be defined corresponding to the energy deposited in the calorimeter. This system of discriminator triggers (LA1 to LA4) has been supplemented with and partly replaced by a system of flash ADCs [20]. For every module two trigger sums are formed by summing up all channels or those channels that lie in the region of the maximum of electromagnetic showers (4-7 X_0). The second sum is taken at a different time to exploit

the shape of the FADC signal. Thus showers can be rejected that do not coincide with the beam crossing (e.g. cosmics, electronic noise). All the above information is combined to four trigger conditions LA1FL to LA4FL. Inside the master trigger unit the number of masks $r\varphi(n)$ and $rz(m)$ satisfied is combined with further basic conditions to give the final trigger criteria.

3.2.2 Data acquisition

The CELLO data acquisition system is steered and controlled by an online computer of the type DEC PDP-11. The detector is read out by a CAMAC* system which is organized in a tree like structure: each detector component is assigned to a branch, and the online computer is the root. Each branch is controlled by a minicomputer. These minicomputers are used to calibrate and test the assigned detector components without interfering with the rest of the system. During data acquisition they monitor the performance of their detector component. Zero suppression of channels without information is already accomplished at this level; block addresses are added to the remaining data words for identification.

Once the master trigger unit sends its interrupt signal to the online computer, the PDP-11 stops all other operations, disables further triggers and starts with the data acquisition. The information from all branches is transfered to the main memory where it is formated into a data structure with variable length (typically several hundred to several thousand 16-bit words). During this process the data structure is checked, and in the case of severe readout errors the event is rejected. Already at this stage a fast track reconstruction is done which is used to verify the track triggers, and on the basis of the number of tracks found the event is classified. Candidates for multihadronic and Bhabha events are marked for separate reconstruction. All events are then passed on and the readout system is again enabled for further data acquisition. This whole process takes about 50 ms. The events are stored on a disk file which is organized as a ring buffer. Once the space on this buffer is almost exhausted the data are transmitted via a permanent link to the IBM in the DESY computer centre and are copied to magnetic tape (DUMP tapes).

Events marked by the online computer are immediately reconstructed and then written to a special disk file. These events are scanned by the shift crew using an interactive display program to monitor detector performance and reconstruction chain.

The Bhabha events are furthermore used to determine the position of the interaction point of each filling of the PETRA storage ring. The knowledge of this position is crucial for the further reconstruction of the data, since all track parameters are determined relative to the primary vertex.

3.2.3 Filter

Soft trigger conditions are essential for the data acquisition at general purpose detectors. This, of course, increases the amount of background reactions acquired, and hence a preselection of events is necessary before the time-consuming full reconstruction of the data is done. Such a filter offers the possibility to conduct a more refined analysis of the events than that done at the trigger level.

The CELLO filter program [21] analyses the events without refering to the trigger explicitly. The basic input informations used in this program are:

---

*Computer Automated Measurement And Control

- the inner detector wire chamber coordinates

- the hardware energy sums in the calorimeters

- the energy of single channels in the liquid argon calorimeter

In a first step charged tracks coming from the interaction point (assumed at $r=0$ with an uncertainty of 3 cm) are reconstructed in the $r\varphi$-plane requiring a minimum of 9 points per track. In a second stage the reconstruction of tracks in the rz-projections is performed with no assumptions about the interaction point. Instead, there must be at least one track with a z-vertex not more than 5 cm apart from the z-vertices of 60 % of all other tracks. For those events a common z-vertex is computed that has to be within ± 15 cm around the origin ($z = 0$). Otherwise all reconstructed tracks are ignored.

The energy sums of the calorimeters are classified according to their energy levels. For each stack the signal time relative to the time of the interaction is computed from the FADC sums taken at two different times. Signals in a stack within $\pm$ 300 ns around the expected time are classified as *in time*. In a second stage showers are reconstructed from the signals of the single channels in the liquid argon calorimeters.

Finally, at least one of the fired triggers has to be verified on the basis of the analysis described above. Less than 1 % of all reconstructable events for most of the reactions are affected this way.

During data acquisition the filter program runs on an IBM 370/E emulator. The events are read in from the online disk and marked *accepted* or *rejected* according to the criteria selected. An identical program executes on the central DESY IBM computer. This program reads in all events, analyses all events accepted by the emulator and those not analysed by the emulator due to time limitations, and writes all accepted events onto magnetic tapes (FILTER tapes). As an additional check 5 % of the events marked rejected are reconstructed once more.

In the run period 1986 out of 61.5 million triggered events 7.5 million (12.2 %) were accepted by the filter. The FILTER tapes for that year are used as an input for the full event reconstruction described in the following section.

3.2.4 Event reconstruction

The raw event data are processed by several independent programs, called processors. The main program OFFRAM constitutes a frame around these processors, steers the sequence of reconstruction and delivers the required information about the conditions of the detector components (calibration constants, defect channels, resolutions, etc.) to these processors. The results of the reconstruction, e.g. track and shower parameters, are stored in *banks* and are written together with the raw data onto data summary tapes (DST tapes). Because of the huge amount of computing time needed, the production of the DST tapes is split up between several of the institutes participating in the CELLO collaboration.

The program OFFRAM embodies the following processors:

CELPAT: The program CELPAT reconstructs tracks of charged particles in the inner detector by an iterative procedure described below. First, the signal of the anodes and the $30°$ and $90°$ cathodes of the proportional chambers are correlated to form three dimensional space points; tracks in the rz-plane are formed by a fit to a straight line pointing to the

interaction region. Then, three points in the $r\varphi$-projection are searched for, that can be connected by a segment of a circle passing within 15 cm of the interaction point. The points used have to lie within one of the predefined sectors in the inner detector which corresponds to a cut in the transverse momentum of the particle. In the vicinity of the segment, further points are sought for. A collection of at least 7 points (6 points for low momentum tracks) is called a track candidate. After a successful fit of these track candidates the points used are excluded from the search for further candidates. This procedure is repeated with larger sectors corresponding to smaller transverse momenta until, finally, low energy tracks with transverse momenta down to 100 MeV are reconstructed. At last, complete tracks are formed by combining the $r\varphi$ and rz-parts with the help of the spatial information of the proportional chambers.

CLGEOM: For the tracks found by CELPAT, a further fit is performed including the interaction point and taking into account the inhomogeneities of the magnetic field. The use of the primary vertex position determined from the Bhabha events improves the momentum resolution of tracks coming from the interaction point. For the case of particles created at secondary vertices this result cannot be used.

ECCPAT: Particles traversing the detector in the very forward region ($0.91 < |\cos\vartheta| < 0.99$) hit few chambers of the inner detector. Using in addition the hits in the end cap chambers and including the primary vertex as a measured point, ECCPAT reconstructs these forward going tracks.

LATRAK: The processor LATRAK reconstructs showers in the liquid argon calorimeters. At first, two-dimensional shower energy clusters are formed in each layer of the calorimeter employing the different directional orientation of the lead strips (cf. section 3.1.3). For all tracks in the inner detector pointing to the two-dimensional clusters, three-dimensional clusters are constructed along the flight direction of the particle. A straight line fit is applied including the intersection point of the track with the magnetic coil to determine the orientation of the shower inside the liquid argon. All other three-dimensional showers are constructed under the assumption that they are created by photons coming from the primary vertex.

LNKJOB: This program links showers to tracks in the inner detector. This assignment of showers initiated by charged particles prevents them from being treated as photons later on.

MUCH: This last processor extrapolates tracks through the calorimeter and the hadron filter and combines them with the hits in the muon chambers. The distance between the extrapolated position and the actual hit is a measure for the quality of the identification as a muon.

For the purpose of this and several other analyses substantial improvements have been implemented in the reconstruction chain, e.g. identification of secondary vertices [22,23], particle identification below 1 GeV in the liquid argon calorimeter [14], shower reconstruction in the forward calorimeter and an improvement of photon identification and their discrimination from electronic noise [16,15].

Chapter 4

Multihadronic events

4.1 Multihadronic event selection

Following the data reconstruction there are two more selection steps. The first one consists of soft cuts to obtain all annihilation and two-photon events [24]. This selection is the basis for next to all physical analyses conducted in the CELLO collaboration. The second selection yields events resulting from multihadronic e^+e^- annihilation processes.

On average, multihadronic events produced at **35 GeV** centre of mass energy consist of 14 charged and 16 neutral particles, about 70 % of which are recorded by the CELLO detector. The remainder escape detection due to limited geometrical acceptance and detection thresholds. Owing to the high energy release in the detector, multihadronic events have a distinct signature which allows us to select them very efficiently from the far more abundant background. Nevertheless, several physical processes remain that may fake multihadronic annihilation events:

1. The creation of τ pairs ($e^+e^- \to \tau^+\tau^-$) may result in two-jet like events of low multiplicity. Most of the events contain between two and six charged particles, which carry a large fraction of the total centre of mass energy. Events with more than four charged particles are rare and occur only in about 2 % of all cases.

2. Higher order QED processes with leptons and photons in the final state [25], e.g. radiative Bhabha events $e^+e^- \to e^+e^-\gamma$. Events with more than two charged particles in the final state are suppressed at order α_{em}^4.

3. The two-photon process, as depicted in figure 4.1, generates events with mainly low invariant mass and often with a large boost in direction of the incoming electrons.

4. The interaction of the electron (positron) bunches with the residual gas in the vacuum chamber* creates events with a large boost along the beam pipe. These so-called *beam gas events* are uniformly distributed along the z-axis. It should however be remembered that trigger biases may lead to a non-uniform acceptance. Beam gas events are due to interactions with atomic nuclei and therefore have a positive net charge.

---

*The gas pressure in the PETRA vacuum chamber is about 10^{-9} mbar and is mainly due to Hydrogen, Oxygen and Water.

5. Electrons or positrons leaving their nominal orbit may interact with the beam pipe. The *beam wall events* originating in this way also have a positive net charge, and occasionally cause a high activity in the beam pipe chambers.

e^+

e^-
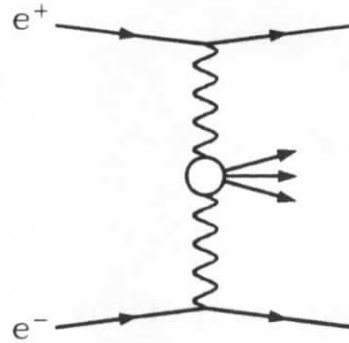
Figure 4.1: Schematic view of the two-photon process.

On the basis of the above listed characteristics it is possible to select multihadronic events with a high efficiency at a very low background rate. This is achieved by the following cuts:

- Charged particles are accepted if:

  1. Their polar angle is in the range from $25°$ to $155°$.

  2. Their momentum component perpendicular to the beam axis is greater than 150 MeV.

  3. Their distance of closest approach to the beam axis is less than 15 mm.

  4. Their z position lies within three standard deviations of the mean event z position, as determined from all charged particles in the event.

  5. They have no sequence of more than three successive missing chambers.

  6. They register in more than 50 % of the chambers available to them.

  7. In addition, for each pair of particle candidates it is checked whether their hit patterns in the central detector are identical within the chamber resolution. From such particle pairs only the track with the better primary vertex compatibility is kept.

- Calorimeter showers are identified as neutral particles if:

  1. They are not linked to extrapolations of charged particle tracks.

  2. Their polar angle is in the range from $32°$ to $148°$.

  3. Their measured energy exceeds 250 MeV.

- Multihadronic events are selected for analysis if:

  1. They contain at least five charged particles.

2. The visible energy in charged particles is at least 22 % of the total centre of mass energy.

3. The total energy recorded in the calorimeters is at least 16 % of the total CM energy.

4. To an alternative to points 2 and 3 it is sufficient that the visible energy in charged and neutral particles is at least 33 % of the total CM energy.

5. The net charge sum is less than six.

6. The magnitude of a longitudinal momentum imbalance in the event is less then 57 % of the beam energy.

7. The event axis, taken to be the sphericity axis as determined from all charged and neutral particles, has $|\cos\theta| \leq 0.865$.

8. The number of hits recorded in the beam pipe chambers is less than 70.

18,543 events passed the above selection and are the basis for the subsequent analysis. The remaining background rate was estimated from visual scanning to be below 3 % and consists mainly of τ pair, two-photon and beam gas events.

The efficiency of the multihadronic event selection (including the complete data acquisition chain) can be computed from the measured luminosity $\mathcal{L} = 86$ pb^{-1} [26] and the total hadronic cross section $\sigma(e^+e^- \rightarrow \text{hadrons}) = 377$ pb and amounts to 57 %. This figure is well reproduced by Monte Carlo simulations.

4.1.1 Two-jet selection

In part II of this thesis two-jet events will be used for analyses of particle correlations. For this purpose two-jet events are defined by the following criteria:

1. The number of clusters, as determined by the LUCLUS algorithm [9] using charged and neutral particles in an event, must be equal to two. The resolution scale d_{join}, above which two clusters may not be joined has been set to 7 % of the total visible mass.

2. The two cluster axes must be parallel within a margin of 25°.

The first requirement selects events that consist entirely of two particle clusters, while the second requirement effectively rejects events with hard initial state radiation. The latter process can occur as a high energy photon escaping detection through the beam pipe, leaving behind a boosted jet system at reduced energy, which appears V-shaped in the laboratory system. In this case the definition of an event axis by the final state particles is meaningless.

The above selection yields 6,831 events, i.e. 36.8 % of the total event sample. This number may be compared to the corresponding Monte Carlo results: from the Jetset 7.2 PS simulation 26,645 out of 76,899 events are classified as two-jet events, i.e. 34.6 %. The Jetset 7.2 PS+BE simulation yields 9,401 out of 25,588 events, i.e. a fraction of 36.7 %.

4.2 Global event shapes

The topic of this section is those *global* properties, related to the shape of the annihilation event, which can be expressed as a single number. Various quantities of this kind have been

constructed that are sensitive measures for certain aspects of e^+e^- annihilation. It is obvious that the information obtainable from these measurements cannot be very detailed . However. it is a minimal requirement that the Monte Carlo must reproduce these global quantities if it is to serve as a reference standard in more detailed analyses. It is the purpose of the following paragraphs to investigate this for the Jetset model.

Thrust observables: Thrust T is defined by the expression:

$$T = \max \left(\frac{\sum_i |\vec{p}_i \cdot \vec{\eta}|}{\sum_i |\vec{p}_i|} \right) , \qquad (4.1)$$

where the sum includes charged and neutral particles. The iterative solution of this equation is done with the routine LUTHRU [9]. The so-called thrust axis $\vec{\eta}_{thrust}$, for which (4.1) is satisfied, is used to define the corresponding $\vec{\eta}_{major}$ axis, which fulfills the relation $\vec{\eta}_{major} \cdot \vec{\eta}_{thrust} = 0$ and obeys (4.1) for $T \to T_{major}$ and $\vec{\eta} \to \vec{\eta}_{major}$. The $\vec{\eta}_{minor}$ axis and the corresponding T_{minor} value simply follow from (4.1), with the direction being defined by orthogonality instead of maximization.

Two-jet events, in the ideal one-dimensional case without any transverse degree of freedom, are characterized by $T = 1$ and $T_{major} = T_{minor} = 0$, while isotropic events have $T = 0.5$. The projected quantities T_{major} and T_{minor} are a measure for the transverse extension of the event with respect to the thrust axis. The imbalance between both transverse directions is called oblateness O; $O = T_{major} - T_{minor}$, thus events which are symmetric around $\vec{\eta}_{thrust}$ have $O = 0$.

Sphericity observables: Sphericity is based on the momentum tensor:

$$S^{\alpha\beta} = \frac{\sum_i p_i^\alpha p_i^\beta}{\sum_i p_i^2} ; \qquad \alpha, \beta = 1, 2, 3 . \qquad (4.2)$$

Due to its symmetry this tensor has only six independent components. Diagonalizing this tensor removes three further components; the remaining three eigenvalues λ_i satisfy the conditions $\lambda_1 \geq \lambda_2 \geq \lambda_3$ and $\sum_i \lambda_i = 1$. Sphericity S and aplanarity A are then expressed in terms of these eigenvalues:

$$S = \frac{3}{2} (\lambda_2 + \lambda_3) , \qquad A = \frac{3}{2} \lambda_3 . \qquad (4.3)$$

Ideal two-jet events have $S = 0$ and $A = 0$, while spherical events are characterized by $S = 1$. Deviations from a planar shape are indicated by $A > 0$.

4.2.1   Unfolded distributions

The measured event shape distributions are influenced by three effects which have to be accounted for in a comparison of the data to the model.

- Limited detector acceptance implies that only a certain fraction of events is accepted for analysis.

- Finite detector resolution and loss of particles cause a smearing of the measured quantities.
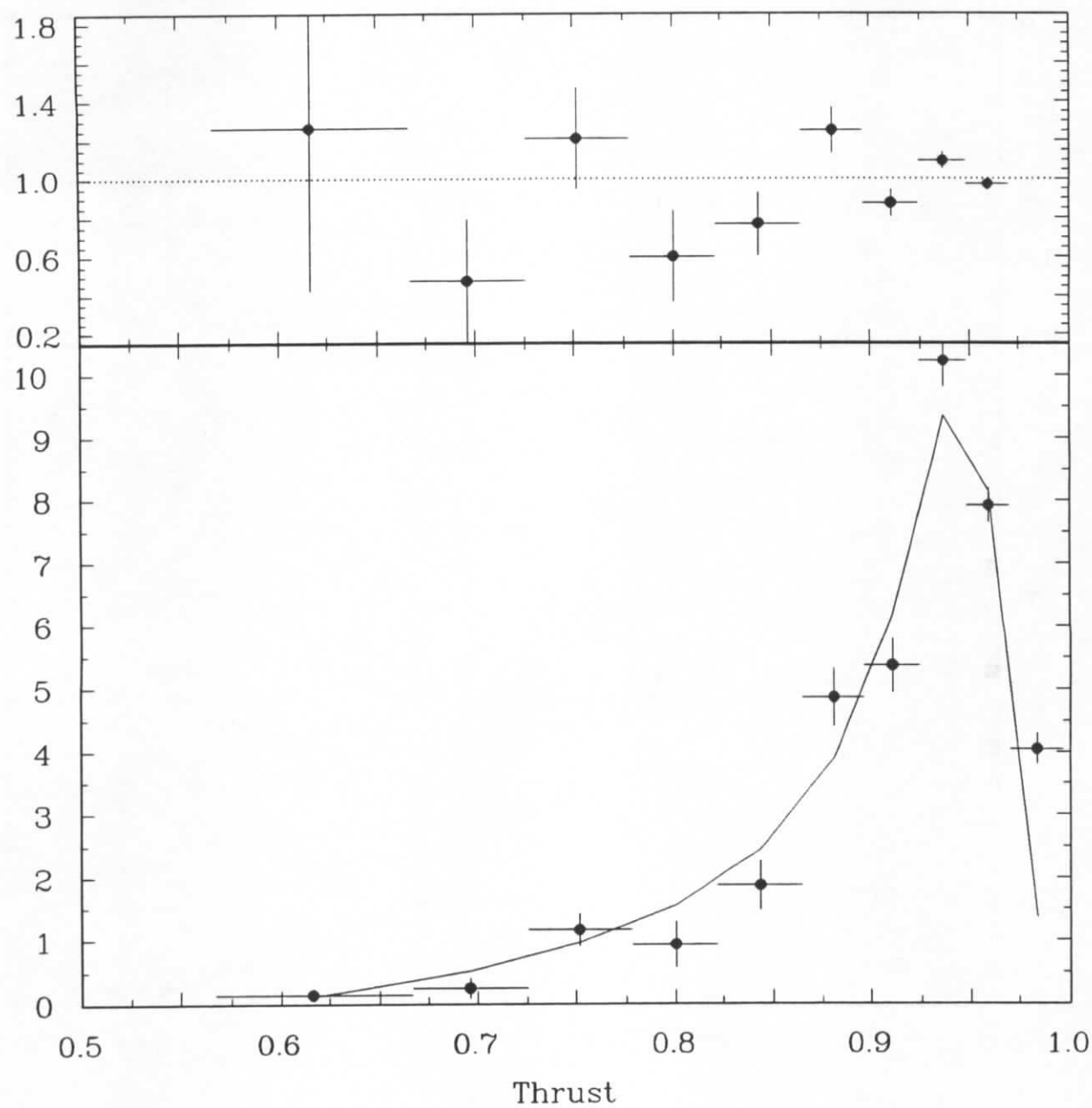
Figure 4.2: Differential thrust cross section in comparison with the Jetset 7.2 PS model. The data are shown with statistical errors and the Monte Carlo result is represented by the solid line; the upper plot shows the data normalized to the Monte Carlo.
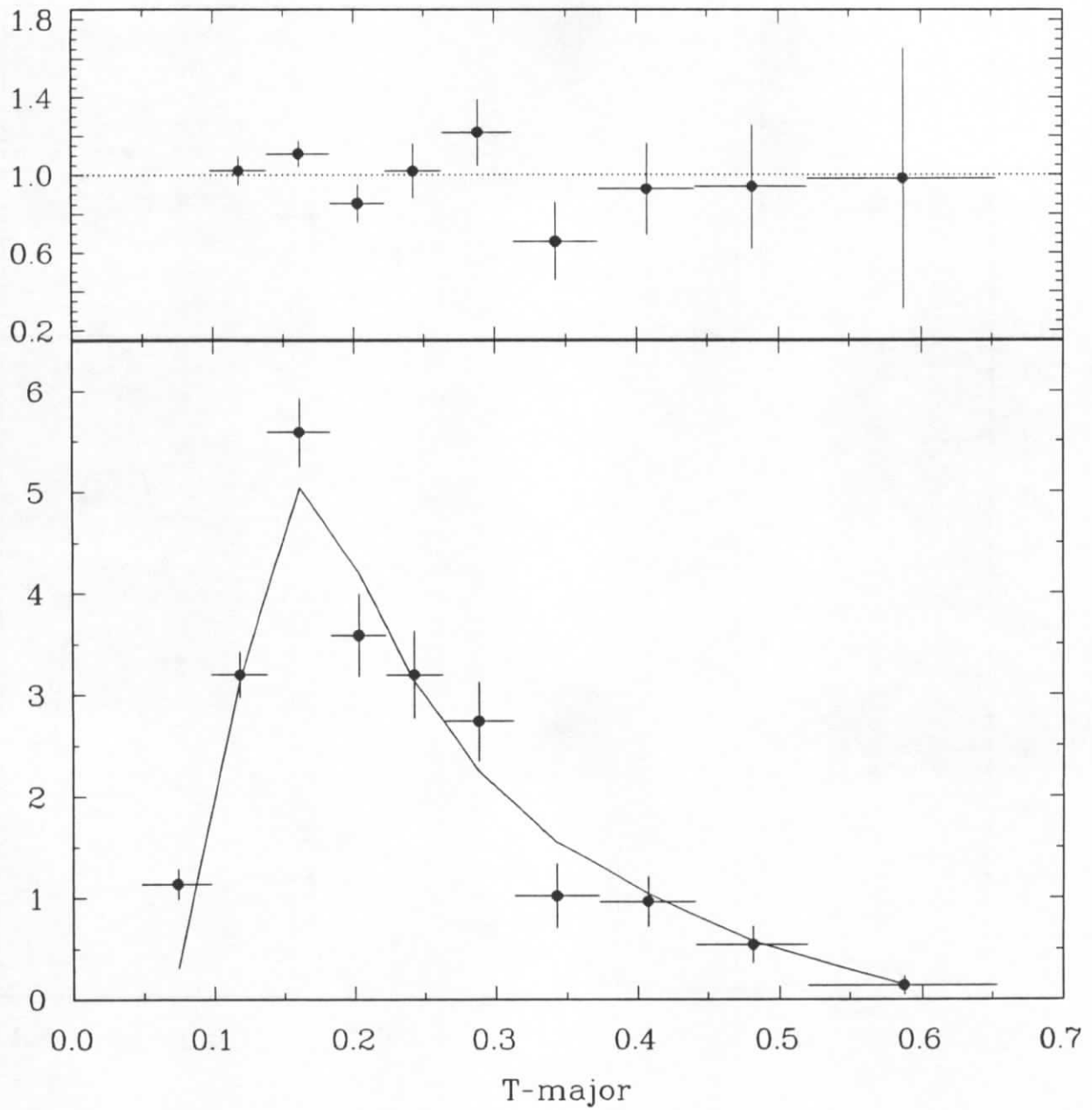
Figure 4.3: Differential T_{major} cross section in comparison with the Jetset 7.2 PS model. The data are shown with statistical errors and the Monte Carlo result is represented by the solid line; the upper plot shows the data normalized to the Monte Carlo.
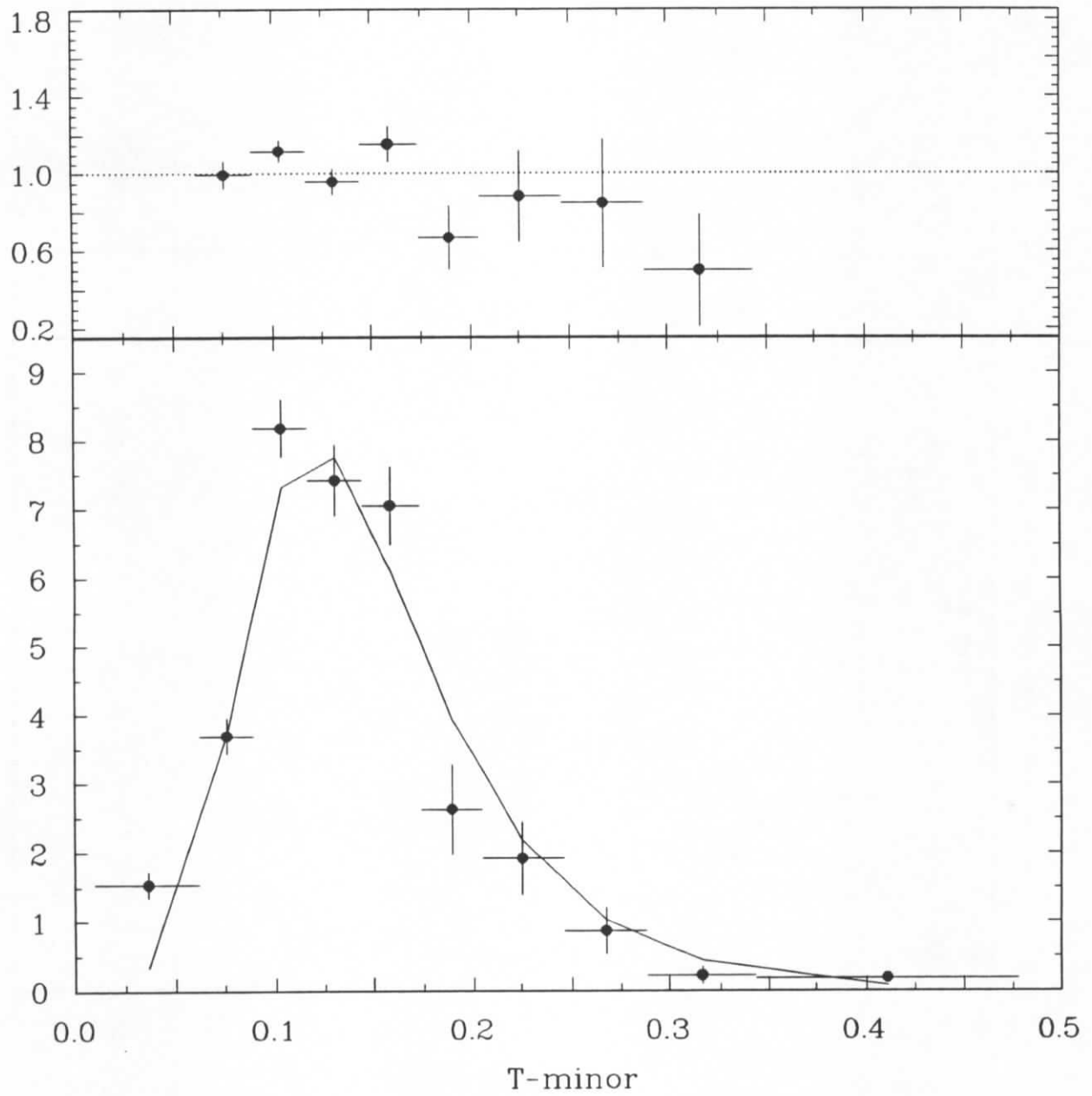
Figure 4.4: Differential T_{minor} cross section in comparison with the Jetset 7.2 PS model. The data are shown with statistical errors and the Monte Carlo result is represented by the solid line; the upper plot shows the data normalized to the Monte Carlo.
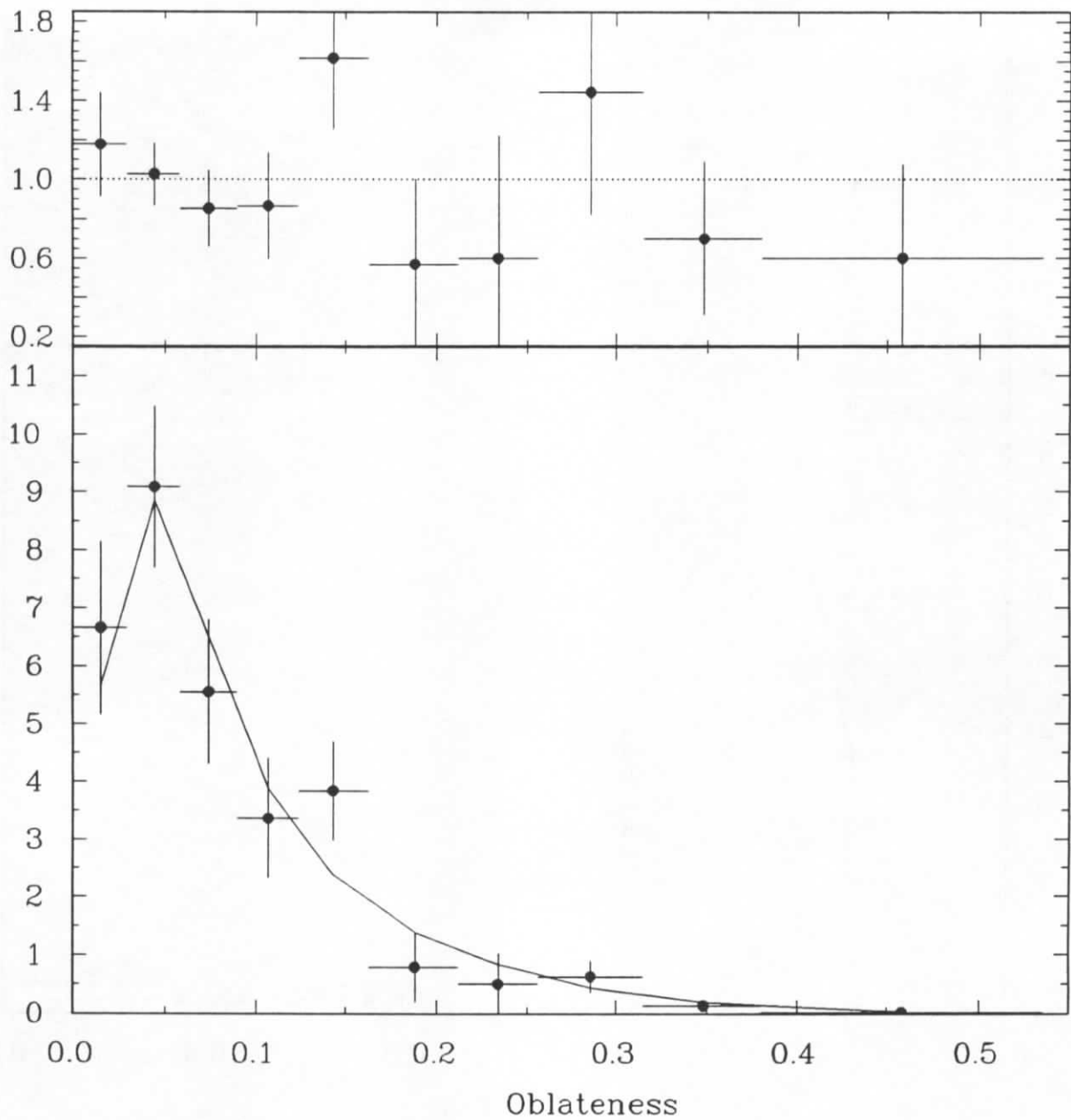
Figure 4.5: Differential oblateness cross section in comparison with the Jetset 7.2 PS model. The data are shown with statistical errors and the Monte Carlo result is represented by the solid line; the upper plot shows the data normalized to the Monte Carlo.
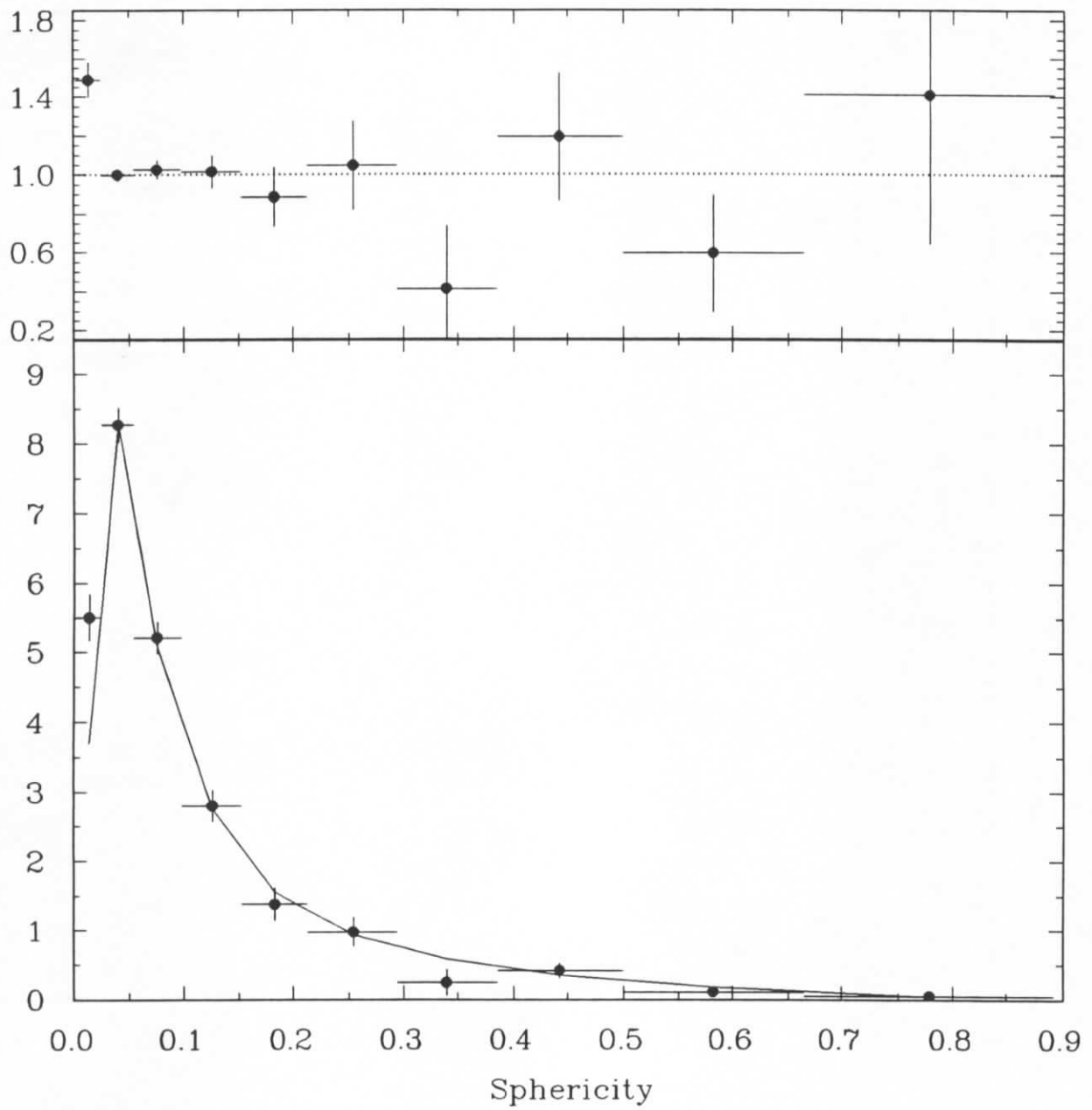
Figure 4.6: Differential sphericity cross section in comparison with the Jetset 7.2 PS model. The data are shown with statistical errors and the Monte Carlo result is represented by the solid line; the upper plot shows the data normalized to the Monte Carlo.
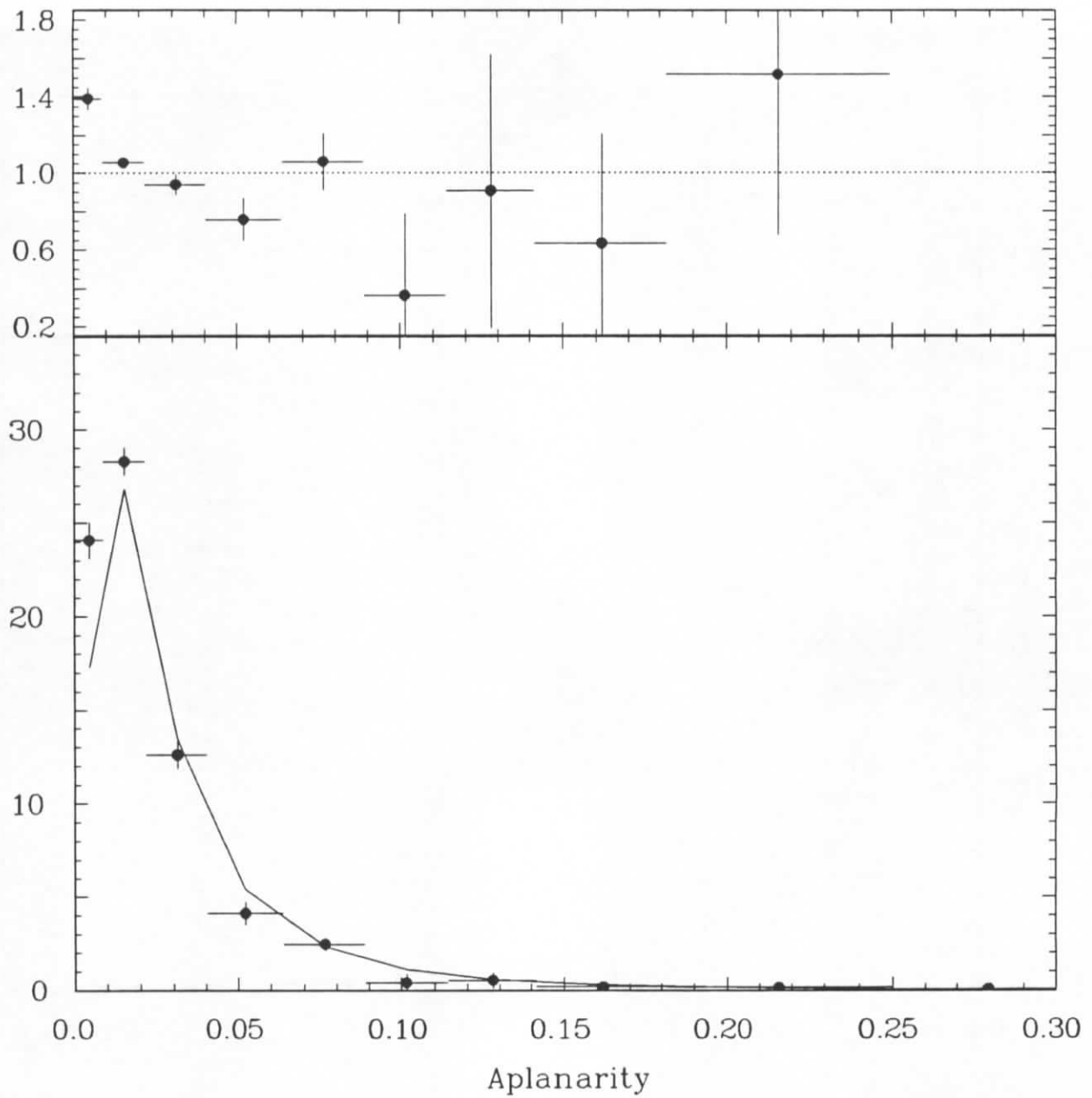
Figure 4.7: Differential aplanarity cross section in comparison with the Jetset 7.2 PS model. The data are shown with statistical errors and the Monte Carlo result is represented by the solid line; the upper plot shows the data normalized to the Monte Carlo.

- Radiative corrections imply a certain transformation of the observed quantities.

A statistically correct way to account for the above effects, i.e. to measure the "true" distributions with correct statistical errors, is provided by the method of regularized unfolding [27]. Of course, the unfolding requires the complete knowledge of the above effects: this information is available through Monte Carlo simulations. For this analysis the program RUN (Regularized UNfolding) [28] is used, which is especially designed for usage in high energy experiments. The program requires as input the correlations of generated and measured quantities from Monte Carlo events and, of course, the experimental distributions. To account for radiative effects the event shape variables of generated Monte Carlo events were computed in the centre of mass system of the virtual photon:

$$p_{cm} = p_{e^+} + p_{e^-} - p_\gamma , \qquad (4.4)$$

where $p_{e^\pm}$ is the 4-vector of the incoming electron (positron) and p_γ is the radiative photon. For non-radiative events the centre of mass system coincides with the laboratory system.

The unfolded thrust-based distributions are presented in figures 4.2 – 4.5, where they are compared to the Jetset 7.2 PS model. The general agreement between data and Monte Carlo is very good: only the tails of the distributions show systematic deviations at the ten per cent level. This is due to a slight mismatch between the longitudinal and transverse extension of the events in the model, since there appear too many events at large thrust values and too few at large T_{major} and T_{minor} values. The transverse properties itself are particularly well reproduced, as can be judged from the oblateness distribution. From this it is concluded that the model behaviour could easily be rectified if simultaneously a harder longitudinal momentum spectrum and less transverse momentum were used in the fragmentation.

In addition an excess of ≈ 130 events is observed at very high thrust, well compatible with the rate expected from residual τ pair events.

The sphericity and aplanarity distributions are displayed in figures 4.6 and 4.7. Of course, these quantities are related to the thrust variables; there is e.g. a 85 % anti-correlation between thrust and sphericity and a 85 % correlation between T_{minor} and aplanarity and, perhaps less obviously, a 85 % correlation between sphericity and T_{major}. However, the tensor (4.2) is quadratic in momentum, while thrust depends only linearly on momentum. Therefore the sphericity-based measures have a larger sensitivity to high momentum particles. This means that sphericity is not infrared stable. Besides giving theoretical problems, this also implies that sphericity-based observables are more sensitive to detector effects. There is only a 70 % correlation between the generated and reconstructed sphericity observables, while the thrust observables show correlations between 75 and 80 %.

Interestingly, the same systematic deviations from the Jetset 7.2 PS model as seen in this experiment are also observed in the OPAL experiment [29].

4.3 Inclusive charged particle cross section

The momentum distribution of charged particles reflects properties of the underlying hadronization process. Therefore it is worthwhile to study, and it furthermore assists tests of the Monte Carlo model.

4.3.1 Unfolding procedure

The measurement of the $x_p = p/E_{beam}$ distribution is complicated by four effects:

- The probability to observe a charged particle is less than one, i.e. a certain fraction of particles escapes detection.

- Initial state radiation implies that not the true x_p is measured, but a related quantity x'_p which is given by some transformation.

- The measured x'_p is smeared out due to the finite detector resolution.

- Spurious tracks may be generated by the track finding algorithm, not corresponding to a real particle. In addition, photon conversion in detector material produces low energetic particle pairs.

The program RUN for regularized unfolding [28] allows a proper treatment of this case. For the unfolding procedure the above effects have to be known precisely. This requires us to identify reconstructed particles (after detector simulation) with the generated particles. For this purpose the following procedure has been adopted: the parameters of all reconstructed particles are compared with the parameters of all generated particles. Using the covariance matrix from the track fit, a χ^2 table is constructed on the basis of which the associations generated $\rightarrow$ measured particle are made. In practice there are almost every time fewer particles reconstructed than generated, and therefore all reconstructed particles can be associated with generated particles. In the few other cases the additional reconstructed tracks are classified as background.

If there were no background in the events, the probability distribution of the associations would be constant between zero and one, otherwise a peak at zero probability is expected. Particles below a certain minimum probability are thus identified as background and it is assumed that they occur at the same rate in the experimental data. The background rate determined in this way corresponds to approximately one particle per event. This background is subtracted from the data before unfolding.

4.3.2 Radiative corrections

The effect of radiative corrections is twofold: firstly initial state radiation reduces the effective centre of mass energy and secondly virtual corrections lead to an increased cross section. If these electro-weak corrections are applied to the cross section, it is possible to compare data at different energies, which eventually reveals the scaling violations caused by the running of the strong coupling constant.

The radiative corrections are calculated within the Jetset 7.3 program [9]. The total cross section in order α_{em}^3 reads [30]:

$$\sigma_{tot}(s) = \sigma_0(s) \left[1 + \delta(k_{min}) + \frac{2\alpha}{\pi} \int_{k_{min}}^{k_{max}} \left(1 - \frac{k}{E} + \frac{k^2}{2E} \right) \frac{\sigma_0(4E(E-k))}{\sigma_0(4E^2)} \frac{dk}{k} \right] , \qquad (4.5)$$

here E is the beam energy and k is the energy of the radiated photon. The upper and lower bounds for k have been set to $k_{min} = 0.01 \cdot E$ and $k_{max} = 0.99 \cdot E$ respectively. At 35 GeV centre of mass energy the total cross section amounts to 377 pb. The cross section σ_0 corresponds to single photon annihilation and is given by the following formula:

$$\sigma_0(s) = \frac{4\pi\alpha^2}{3s} R = 86.8 \frac{R}{s} \, \text{nb} \, \text{GeV}^2 , \qquad (4.6)$$

where R (=3.91 at 35 GeV) is the ratio of the continuum cross section to the lowest order muon pair production cross section. At 35 GeV centre of mass energy σ_0 takes the value 277 pb. The cross section (4.5) consists of two terms: the $1 + \delta$ term is a function of the cutoff k_{min}, such that singular terms cancel between the real and virtual emission probabilities. This term corresponds to events without a detectable photon in the final state, while the integral represents events that did radiate a photon. The corresponding Feynman diagrams are depicted in figure 4.8. For the purpose of unfolding the x_p is calculated after the particles
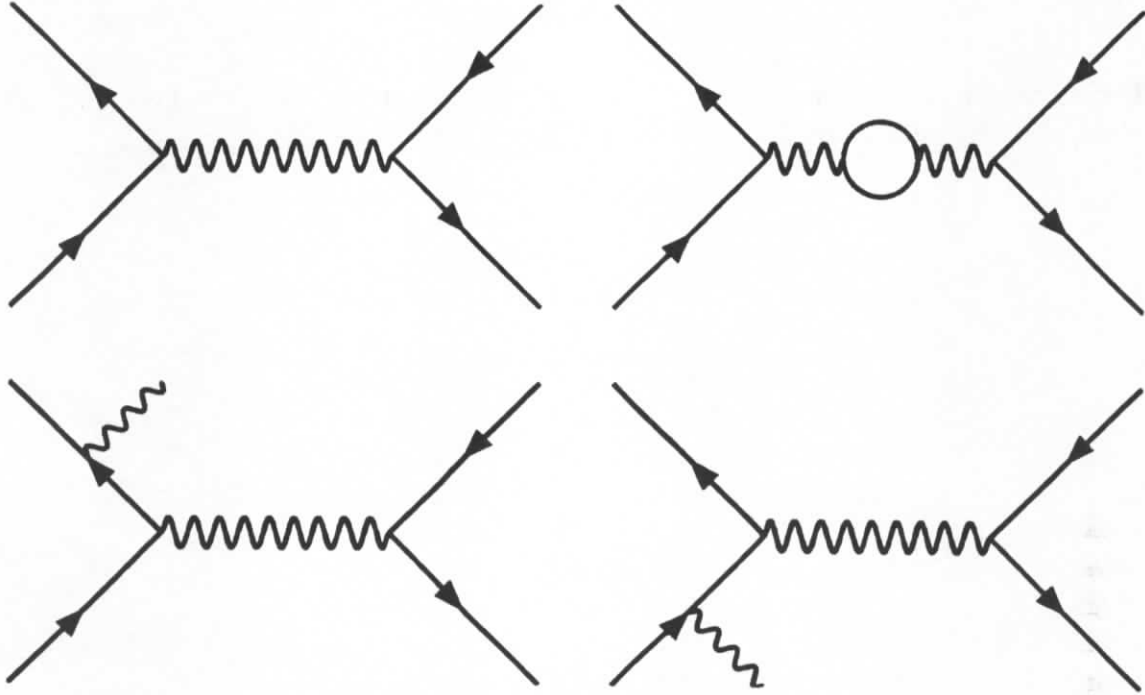
Figure 4.8: Feynman diagrams for e^+e^- annihilation.

are boosted in the centre of mass of the virtual photon (4.4). If no initial state radiation occurs this system coincides with the laboratory frame. This procedure is only applicable for generated particles, since finite detector acceptance and resolution do not allow to determine the 4-vector of a radiated photon with the required precision. With this definition of x_p the unfolding program implicitly determines the transformation caused by initial state photon radiation. The remaining correction ε_{rad} takes care of the increased cross section due to virtual emission and accounts for the lower average multiplicity in radiative events:

$$\varepsilon_{rad} = \frac{\langle n \rangle_{tot}}{\langle n \rangle_0} \frac{\sigma_{tot}}{\sigma_0} \quad : \tag{4.7}$$

this factor is 1.257 at 35 GeV. The differential cross section $1/\sigma_{tot} \, d\sigma/dx_p$ is presented in figure 4.9 and listed in table 4.1. The comparison with data from TASSO [31] and TPC [32] shows consistent agreement among the different experiments. The Jetset 7.2 PS simulation is seen to give too few particles at large x_p and too many at small x_p, although the general agreement is satisfactory. The observed deviations from the Jetset model are largest for the CELLO experiment, however, this is not surprising since Jetset is tuned to TPC and TASSO data. The differences observed among the experiments reveal systematic uncertainties. In this experiment, the systematic uncertainty is estimated to vary between 2 and 10 %, and is largest for very small and very large x_p, where detector effects are more important.

The underestimation of the production rate of high energetic particles in the Jetset model has already been discussed in the analysis of global event shapes in the previous section.

The mean multiplicity $\langle n \rangle$ and the mean fractional momentum $\langle x_p \rangle$ can be obtained from the cross section by integration:

$$\langle n \rangle = \frac{1}{\sigma_{tot}} \int \frac{d\sigma}{dx_p} dx_p \tag{4.8}$$

$$\langle x_p \rangle = \frac{1}{\sigma_{tot} \langle n \rangle} \int x_p \frac{d\sigma}{dx_p} dx_p \,. \tag{4.9}$$

The following values are obtained in the x_p range from 0.019 to 0.955: $\langle n \rangle = 11.4$, $\langle x_p \rangle = 0.11$ for the data and $\langle n \rangle = 11.9$, $\langle x_p \rangle = 0.10$ for the Jetset 7.2 PS simulation.

x_p range	$1/\sigma_{tot} d\sigma/dx_p$ CELLO	$1/\sigma_{tot} d\sigma/dx_p$ Jetset 7.2 PS
$0.02 - 0.03$	143.4 ± 1.1	179.1 ± 0.5
$0.03 - 0.05$	119.4 ± 0.7	137.1 ± 0.3
$0.05 - 0.07$	75.6 ± 0.6	83.3 ± 0.2
$0.07 - 0.10$	50.5 ± 0.5	52.7 ± 0.2
$0.10 - 0.13$	37.4 ± 0.4	36.4 ± 0.1
$0.13 - 0.15$	26.6 ± 0.4	26.1 ± 0.1
$0.15 - 0.18$	20.4 ± 0.4	19.5 ± 0.1
$0.18 - 0.20$	15.5 ± 0.4	14.6 ± 0.1
$0.20 - 0.23$	12.3 ± 0.4	11.2 ± 0.1
$0.23 - 0.26$	9.9 ± 0.3	8.6 ± 0.1
$0.26 - 0.29$	7.5 ± 0.3	6.6 ± 0.05
$0.29 - 0.32$	6.1 ± 0.3	5.2 ± 0.04
$0.32 - 0.36$	5.0 ± 0.3	3.8 ± 0.03
$0.36 - 0.40$	3.3 ± 0.2	2.6 ± 0.03
$0.40 - 0.45$	2.4 ± 0.2	1.7 ± 0.02
$0.45 - 0.52$	1.6 ± 0.2	1.1 ± 0.01
$0.52 - 0.59$	0.8 ± 0.1	0.55 ± 0.01
$0.59 - 0.70$	0.46 ± 0.07	0.24 ± 0.005
$0.70 - 0.95$	0.16 ± 0.02	0.04 ± 0.001

Table 4.1: Inclusive charged particle x_p cross section.

4.4   Cross sections for various particle species

In this section we present the cross sections of identified particles measured by CELLO and compare them to the predictions from Monte Carlo models.

In the scope of this thesis a method has been developed which allows a measurement of the differential $x_E = E_{D^*}/E_{beam}$ cross section for charged D^* meson production from the so-called slow pion (π_S). Compared to the usual method of explicit D^* reconstruction
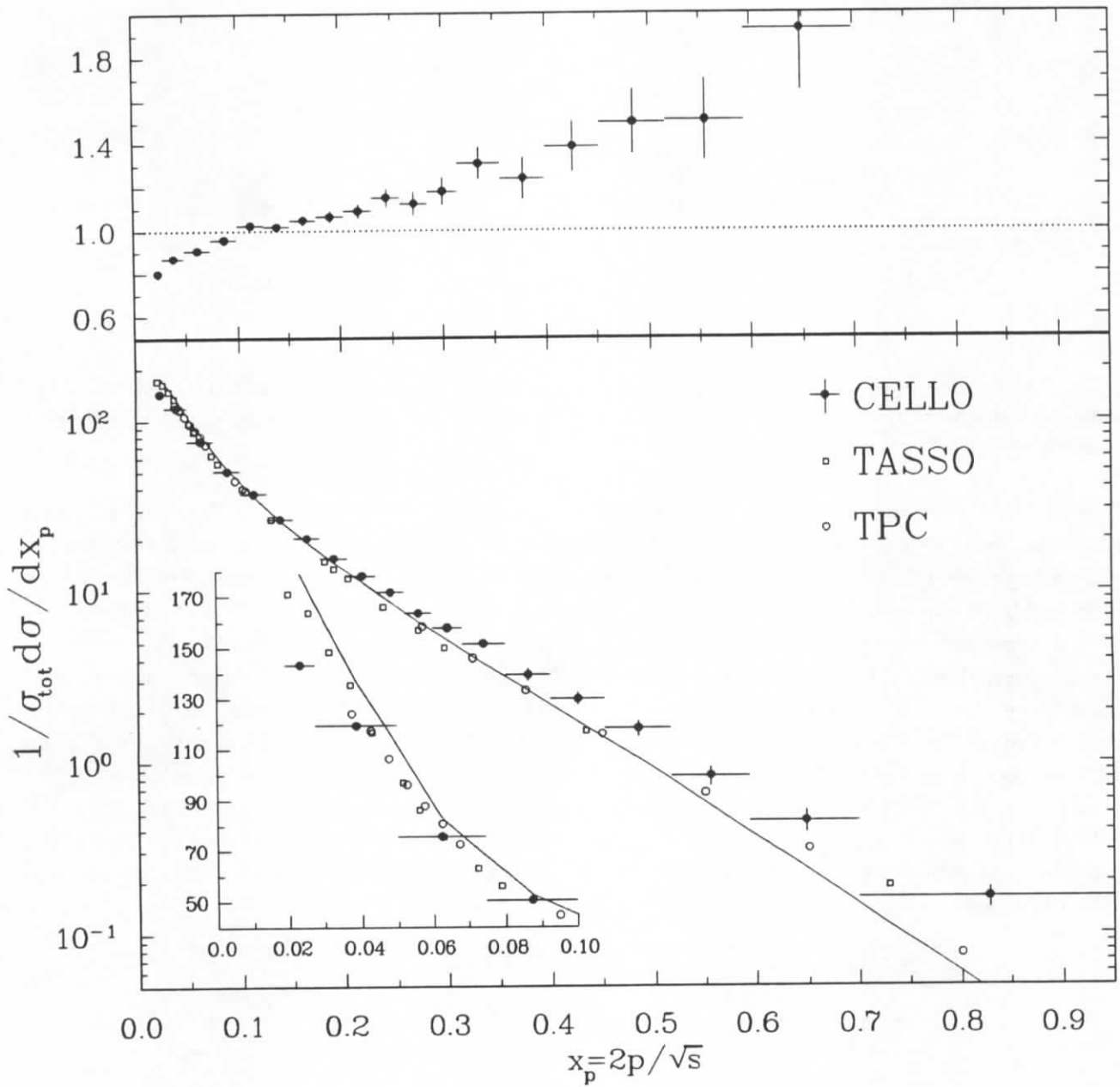
Figure 4.9: Differential charged particle cross section: CELLO data are shown with statistical errors, the horizontal bars indicate the range over which the measured values are supposed to represent the average. The data are compared to the Jetset 7.2 PS model and to the TASSO (open squares) and TPC (open dots) results (errors omitted for clarity). The inset shows the cross section at small x_p on a linear scale. The upper plot shows the data normalized to the Monte Carlo.
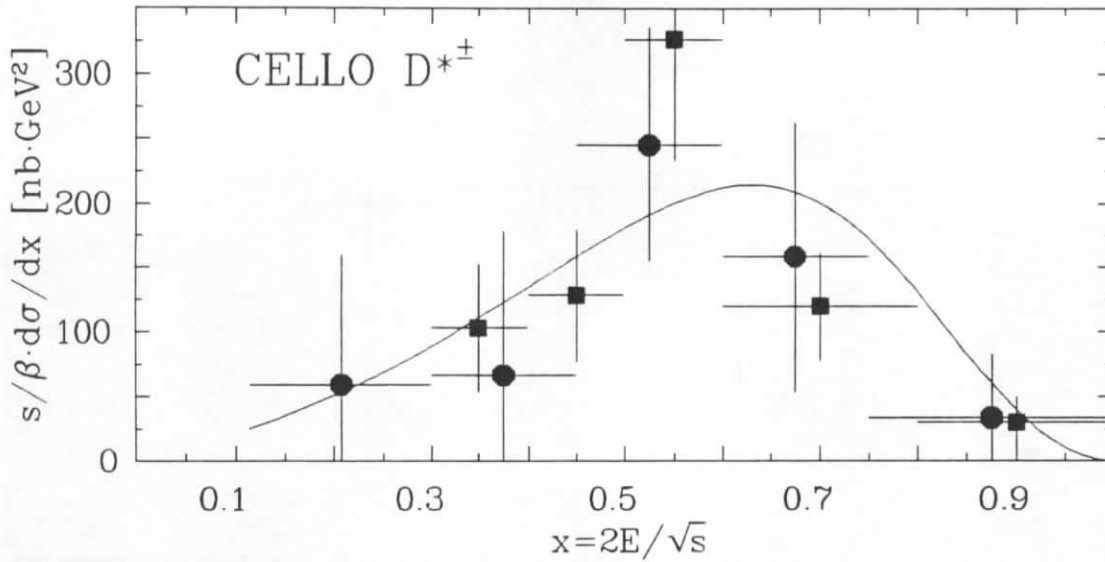
Figure 4.10: $D^{*\pm}$ cross section: the squares are from reconstructed $D^{*\pm}$ mesons and the circles show the unfolded result from the $p_{\parallel}$ distribution of slow pions. The solid line shows the fit result for the Peterson fragmentation function.

this method has the advantage to use the full statistics of the decay $D^{*+} \rightarrow D^0 \pi_S^+$, and furthermore it is independent of any D^0 branching ratios. The advantage of high statistics is partially compensated by a larger background rate such that the overall statistical accuracy is about the same in the two methods. The analysis has been described in detail in [35] and is repeated here only briefly: due to the low energy release in the decay $D^{*+} \rightarrow D^0 \pi_S^+$, the π_S^+ is restricted to very low $p_\perp$ relative to the D^* flight direction. The latter is almost parallel to the event axis (determined e.g. by the linearized sphericity tensor (5.3)) since the inertia carried by the charm quark is retained in the $D^{*\pm}$ meson. Therefore, slow pions from $D^{*\pm}$ decays show up as an enhanced production of particles with very low $p_\perp$ relative to the event axis. Finally, the longitudinal momentum of the slow pion is highly correlated with the $D^{*\pm}$ energy, which makes it possible to unfold the $D^{*\pm}$ energy spectrum from the measured longitudinal momentum spectrum of slow pions. In figure 4.10 the two methods are seen to give consistent results of the charged D^* meson cross section.

Particle	CELLO	Jetset	Ariadne	Herwig
γ	$13.6 \pm 0.3 \pm 0.8$ [34]	14.54	14.56	14.63
π^0	$6.4 \pm 0.6 \pm 0.9$ [34]	6.64	6.64	6.84
η	$0.63 \pm 0.12 \pm 0.15$ [34]	0.79	0.80	0.79
$K^0 + \overline{K}^0$	$1.42 \pm 0.09 \pm 0.18$ [33]	1.38	1.38	1.40
$K^{*+} + K^{*-}$	$0.77 \pm 0.17 \pm 0.14$ [33]	0.74	0.74	0.59
$D^{*+} + D^{*-}$	0.27 ± 0.03 [35]	0.273	0.279	0.248
$\Lambda + \overline{\Lambda}$	$0.21 \pm 0.03 \pm 0.03$ [33]	0.225	0.224	0.271

Table 4.2: Cross sections of identified particles: the results from Jetset 7.3 PS, Ariadne 3.1 CD and Herwig 5.0 PS are based on 70,000 events for each model. All programs are run with the default parameter values provided by the authors [9,4,5]. Herwig has been modified to call the Jetset routines for particle decays.

In table 4.2 the measured cross sections of various particle species can be seen to be in good agreement with the results from different Monte Carlo simulations.

Part II

Multiparticle Production

Chapter 5

Preliminaries

5.1 Introduction

In this section of the thesis a comprehensive analysis of multiparticle production is presented. The analysis is based on data taken with the CELLO detector at the PETRA e^+e^- collider. The general framework of e^+e^- annihilation is discussed in the previous section.

The present study consists of an analysis of particle fluctuations and correlations up to the finest resolution scales accessible by the experiment. Owing to the clean initial state, e^+e^- experiments are very well suited for this type of analysis.

The main interest in these studies is focussed on the experimentally observable properties of hadron distributions and their relation to QCD, the gauge theory of the strong interactions. This relation is not straightforward since the theory is solved only perturbatively, restricting its application to high Q^2 processes and thus leaving the description of hadron formation to phenomenological Monte Carlo models. These models are therefore of vital importance to relate the experimentally accessible information to the fundamental theory.

Various methods, of a similar kind and complementing each other, are applied to unravel the complex structure of the hadronization process. In the present chapter general aspects, relevant to all subsequent analyses, are described. Chapter 6 presents an analysis of multiplicity distributions in rapidity space via a novel method. This procedure gives access to the different patterns of particle production in cluster and string models, which are compared and discussed in detail. Chapters 7 and 8 are dedicated to intermittency analyses, i.e. to analyses of multiplicity fluctuations in phase space domains of variable size and dimension. Several aspects of multiparticle production are isolated in this complex analysis and studied in some detail; this comprises an interpretation of the results in terms of fractal dimensions. Some of the applied methods and techniques have been developed in the course of this thesis. Chapter 9 contains an analysis of two-particle correlations, including the analysis of Bose-Einstein correlations. Finally the summary and conclusions are presented in chapter 10. Part of the work presented here is already published [53–55,60–63], and these references should be consulted for further details.

5.2 Variable definition

It is the aim of this study to investigate the correlation structure of particle production in three-dimensional phase space and in its lower-dimensional projections. For this purpose the

47

Lorentz invariant phase space element *dLips* of a single particle is decomposed as follows:

$$dLips = \frac{1}{2(2\pi)^3} \frac{dp_x dp_y dp_z}{E} , \tag{5.1}$$

$$dLips = \frac{1}{4(2\pi)^3} dy\, d\phi\, dp_\perp^2 . \tag{5.2}$$

The symmetric decomposition (5.1) has the advantage of being independent of the choice of a reference axis. This parameterization of *dLips* will be used in chapter 8 for a three-dimensional intermittency analysis. In contrast, the decomposition (5.2) breaks rotational invariance. In this case the three variables rapidity ($y = 0.5\ln[(E + p_\parallel)/(E - p_\parallel)]$), azimuth ($\phi$) and transverse momentum squared ($p_\perp^2$) must be evaluated with respect to a suitably chosen reference axis. A graphical representation of the used variables is given in figure 5.1 with a three-jet event as example.
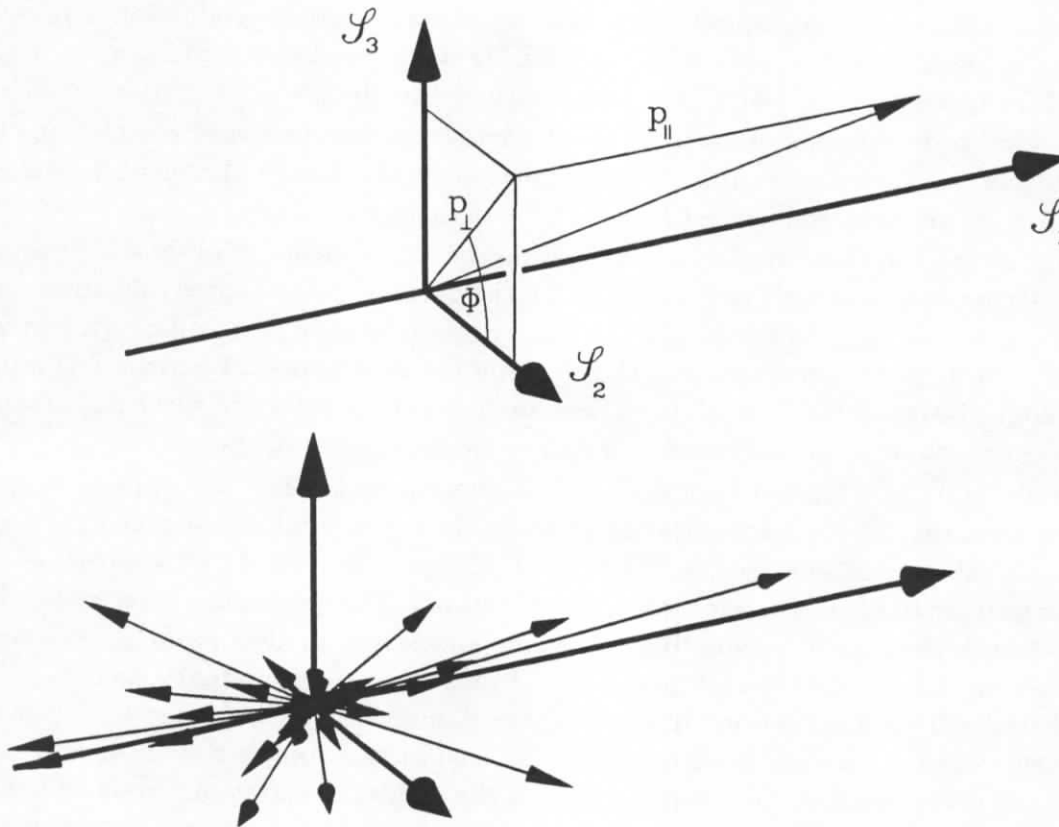
Figure 5.1: Definition of variables and event axes; the depicted three-jet event is generated by Jetset 7.3 PS. The coordinate system is defined by the eigenvectors S_i of the linearized sphericity tensor.

Since the main concern in the study of multiparticle production is the soft hadronization process, it is natural to take the event axis as reference axis, and thereby eliminate distortions due to the $1 + \cos^2 \vartheta$ angular distribution of the hard scattering process $e^+ e^- \rightarrow q\bar{q}$. This axis is obtained as the first eigenvector S_1 of the *linearized* sphericity tensor (5.3), which is determined by the three-momenta of charged and neutral particles in an event. Note that throughout this analysis charged particles are identified as pions and neutral particles as

photons, if not explicitly stated otherwise.

$$S_{lin}^{ab} = \frac{\sum_i p_i^a p_i^b / |\vec{p_i}|}{\sum_i |\vec{p_i}|} \qquad (5.3)$$

In the above definition of S_{lin} one power of p has been removed compared to the usual definition of sphericity ((4.2) on page 32). Therefore S_{lin} is much closer to thrust, which is also linear in momenta.

In general the orientation of the sphericity axis is arbitrary, implying that there is no principal difference between positive and negative rapidity values. However, individual e^+e^- annihilation events are not symmetric in rapidity since density fluctuations due to limited statistics, finite detector resolution and acceptance or gluon radiation occur. To account for these effects the sphericity axis is oriented in direction of the most energetic jet. For this purpose the jet configuration and jet energies are determined by the LUCLUS clustering algorithm [9]. By means of the above definition positive rapidity values indicate particles belonging to the most energetic jet (which is likely to be a quark jet that did not radiate hard gluons) and negative values signify particles from the less energetic jets (preferentially quark jets and their radiated gluon jets). In an analogous way the origin of the azimuthal coordinate, i.e. $\phi \equiv 0$, is taken to be the second eigenvector S_2 of the linearized sphericity tensor. With these definitions the corresponding inclusive (averaged over many events) distributions contain information about "trivial" fluctuations, which are present in every event.

In figures 5.2 – 5.4 the inclusive distributions corresponding to the decompositions (5.1) and (5.2) are shown and compared to the Jetset 7.2 PS+BE Monte Carlo simulation. The perfect reproduction of these distributions by the Monte Carlo is a necessary precondition for the subsequent analyses. In this context it is noteworthy that the Jetset 7.2 Monte Carlo is run with default parameters [9], except for the inclusion of Bose-Einstein correlations as will be discussed in section 9.1.

5.3   Detector resolution

Detector resolution	
$\sigma(\delta y) = 0.10$ $\sigma(\delta\phi) = 10°$ $\sigma(\delta p_\perp^2) = 0.025$ GeV^2	$\sigma(\delta p_x / E^{\frac{1}{3}}) = 0.054$ GeV$^{\frac{2}{3}}$ $\sigma(\delta p_y / E^{\frac{1}{3}}) = 0.060$ GeV$^{\frac{2}{3}}$ $\sigma(\delta p_z / E^{\frac{1}{3}}) = 0.050$ GeV$^{\frac{2}{3}}$

Table 5.1: Average two-particle resolution from the Monte Carlo simulation.

In an analysis of particle correlations the detector resolution must be known to allow an interpretation of the data. The two-particle resolution has been estimated by comparing the differences (δ) in the studied variables of particle pairs prior to the detector simulation with the corresponding values after detector simulation. In doing this, effects due to particle misidentification and uncertainties in determining the event axis are taken into account.
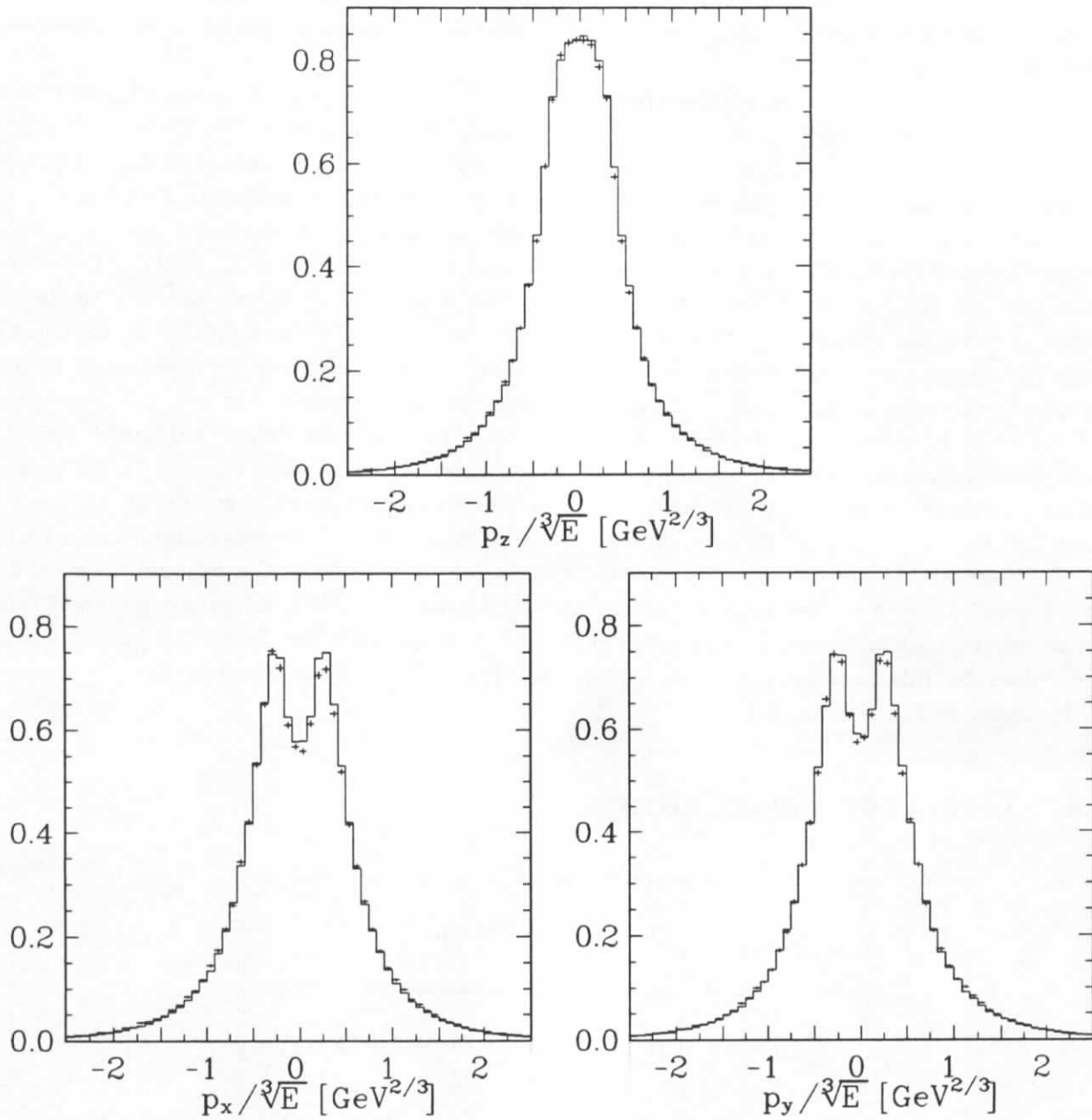
Figure 5.2: Inclusive $p_x/E^{\frac{1}{3}}$, $p_y/E^{\frac{1}{3}}$ and $p_z/E^{\frac{1}{3}}$ distributions: CELLO data (statistical errors indicated) are compared to the Jetset 7.2 PS+BE simulation (histograms). The dips at $p_x = 0$ and $p_y = 0$ are caused by the acceptance threshold at $p_\perp \simeq 150$ MeV.
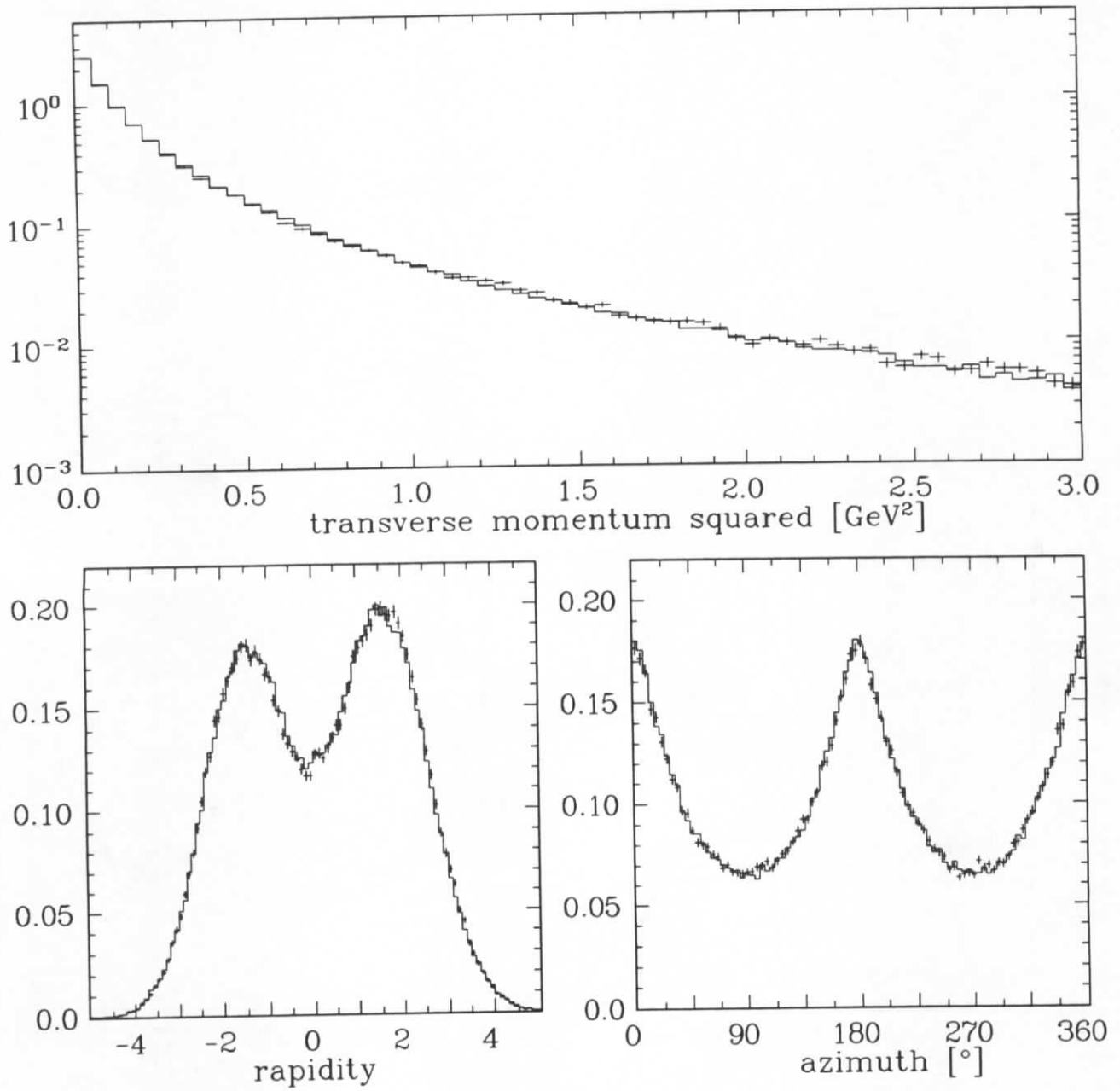
Figure 5.3: Inclusive y, ϕ and $p_\perp^2$ distributions: CELLO data (statistical errors indicated) are compared to the Jetset 7.2 PS+BE simulation (histograms).
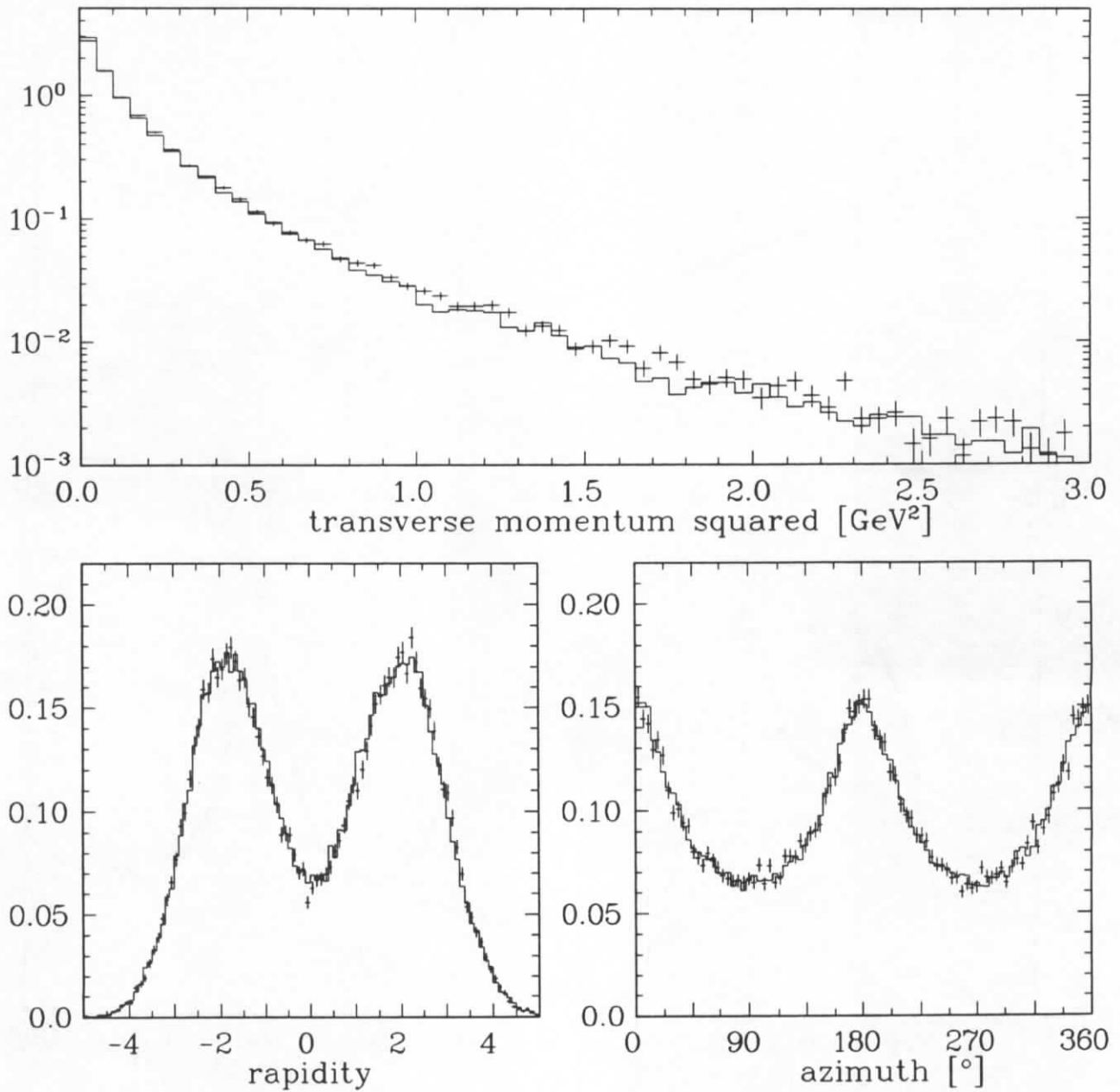
Figure 5.4: Inclusive y, ϕ and $p_\perp^2$ distributions for two-jet events: CELLO data (statistical errors indicated) are compared to the Jetset 7.2 PS+BE simulation (histograms).

The average two-particle resolution for the decompositions (5.1) and (5.2) can be found in table 5.1. It should be noted that the detector resolution function is truely three-dimensional and therefore the quoted values can be considered as upper limits: that is to say the detector can easily resolve two particles with e.g. a δy of 0.01 provided their azimuthal coordinates differ sufficiently.

It is obvious that a very accurate simulation of the detector performance is required to allow the analysis of particle production in small regions of phase space. In this context the experience CELLO has gained through many two-photon analyses (see e.g. [14,15,51]) turned out to be very helpful. These analyses typically deal with detection efficiencies of a few per mill, which assisted tests and improvements of the detector simulation.

5.4 CELLO "toy" model

Complementary to the standard e^+e^- annihilation Monte Carlo models such as Jetset, Herwig, and Ariadne, which are described in chapter 2, a CELLO "toy" model is used for reference. This model serves as a null model for correlation studies, insofar as it does not contain any genuine particle correlations but reproduces the inclusive distributions. The model has been designed as follows:

- The same number of events as in the CELLO data are generated.

- The charged particle multiplicity distribution is exactly reproduced.

- Particles are randomly distributed in individual events.

- No correlations between y, ϕ and $p_\perp^2$ exist.

- The inclusive y, ϕ and $p_\perp^2$ distributions are reproduced on average, but not event by event.

This is realized as follows: in a first step the charged particle multiplicity, rapidity, azimuth and transverse momentum squared distributions of the CELLO data are recorded and stored. In the second step events with particle multiplicities according to the stored values are generated. A random number generator assigns y, ϕ and $p_\perp^2$ values independently to the particles, such that the inclusive distributions are reproduced. This is achieved with the routine HISRAN [72], which makes use of the cumulative distribution, obtained from CELLO data, to transform a uniform random number distribution into the desired inclusive distribution.

The same procedure can, of course, be used for the variable decomposition (5.1).

Chapter 6

Multiplicity distributions

In this chapter multiparticle production in e^+e^- annihilation processes is studied via the multiplicity distribution of charged particles. This study reveals properties of both the perturbative and the non-perturbative hadronization phase, thus providing access to the fundamental structure of the strong interactions.

In the following section the general features of multiplicity distributions are discussed. This is followed in section 6.2 by the standard analysis of multiplicity distributions in central rapidity intervals of different width. In this context Monte Carlo simulations are used to relate the experimental findings to physical processes.

In section 6.3 multiplicity distributions are analysed in rapidity intervals of constant width but different central values. This scan covers the entire rapidity range, a procedure which shows the underlying physical processes in a very transparent way. The observed features motivate a discussion of particle production in string and cluster models, which is presented in section 6.4. An outlook for LEP is given in section 6.5 and finally the results are summarized in section 6.6.

6.1   General features

The basis for the present investigation is a sample of 18,543 multihadronic events which passed the selection described in section 4.1. The measured charged particle multiplicity distribution is presented in figure 6.1, where it is seen to be accurately reproduced by the Jetset 7.2 PS model including a detailed detector simulation. Two-jet events, selected according to the prescription given in section 4.1, are compared in figure 6.1 to the total event sample. An astounding similarity of both distributions is observed, evidently reproduced by the Jetset parton shower Monte Carlo. This reveals an adequate treatment of gluon radiation in the model.

The invariance of the Ψ function (6.1) under a two-jet selection suggests that it is of fundamental meaning. In this context the so-called KNO scaling [42] is of some interest. For asymptotically high energies it means that the multiplicity distribution P_n can be expressed in the universal form:

$$P_n = \frac{1}{\langle n \rangle} \Psi(z) , \qquad z = \frac{n}{\langle n \rangle} , \qquad (6.1)$$

where $\langle n \rangle = \sum_{n=0}^{\infty} n P_n$ and $\Psi(z)$ is an energy independent scaling function. Already at lower energies KNO scaling seems to be approximately fulfilled [45,46], although this is only a transient phenomenon unrelated to the exact KNO scaling predicted by QCD [6].
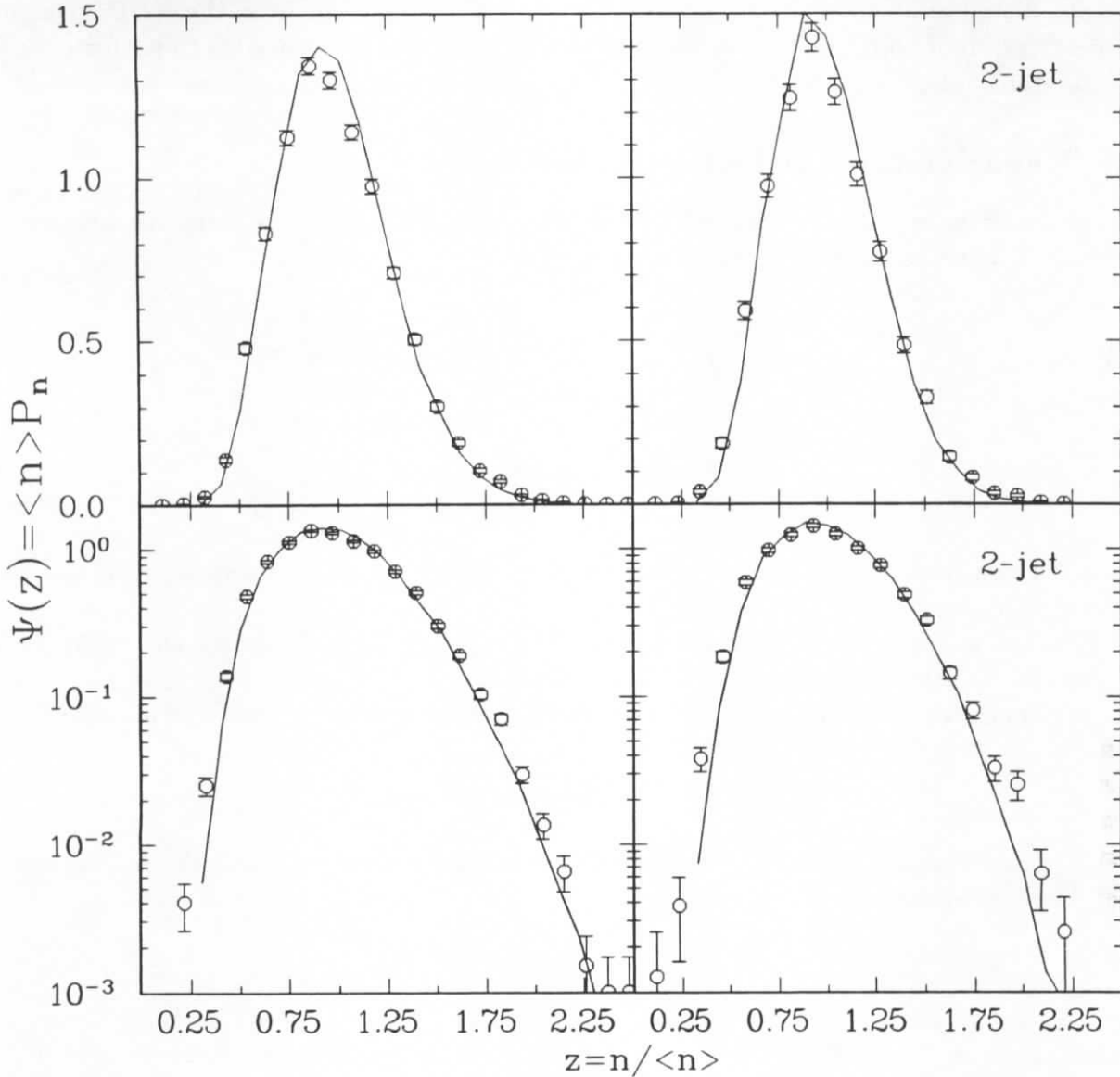
Figure 6.1: Multiplicity distributions of charged particles of the total event sample (left) and of two-jet events (right) compared to the Jetset 7.2 PS simulation (solid lines).

In this connection the asymptotic QCD prediction of a 9/4 times larger multiplicity in gluon jets compared to quark jets should be mentioned [74]. This is due to the greater colour charge of the gluon, which leads to increased gluon bremsstrahlung. However, the observable differences expected at present energies are small [48,6].

It had been realized at an early stage that multiplicity distributions reflect the underlying dynamical and kinematical structure of multiparticle production processes and therefore provide information on the production mechanism (see [64] for a recent review). Subsequently, various statistical distributions were proposed to describe the data; e.g. negative binomial, gamma and log normal distributions.

The analysis presented here is not aimed at determining which specific distribution provides the best description of the data. We shall restrict ourselves to the Negative Binomial Distribution (NBD), which is known to describe multiplicity distributions from a variety of high energy processes reasonably well, and condenses the entire information contained in the

multiplicity distribution into two numbers. This is feasible inasmuch as the NBD gives a precise description of multiplicity spectra. Under this condition it is possible to perform and present differential analyses of the data.

6.1.1   Negative binomial distribution

To obtain an effective parameterization of the observed behaviour, the negative binomial distribution is fitted to the multiplicity distributions:

$$P_n(\langle n \rangle, k) = \left(\begin{array}{c} n + k - 1 \\ k - 1 \end{array} \right) \frac{\langle n \rangle^n k^k}{(\langle n \rangle + k)^{n+k}} , \tag{6.2}$$

$$= \frac{\Gamma(n + k)}{\Gamma(k)\Gamma(n + 1)} \frac{\langle n \rangle^n k^k}{(\langle n \rangle + k)^{n+k}} , \tag{6.3}$$

$$= \frac{(n + k - 1)(n + k - 2)\cdots(k)}{n!} \frac{\langle n \rangle^n k^k}{(\langle n \rangle + k)^{n+k}} . \tag{6.4}$$

Equation 6.4 can be transformed into a very efficient algorithm, facilitating the application of a fitting procedure.

For illustration the negative binomial distribution is presented in figure 6.2 and compared to the Poisson distribution.

The variance $Var(n)$ of the negative binomial distribution is given by the expression:

$$Var(n) \equiv \langle n^2 \rangle - \langle n \rangle^2 = \langle n \rangle + \frac{\langle n \rangle^2}{k} . \tag{6.5}$$

From this it immediately follows for the second normalized moment C^2 and the second normalized *factorial* moment F^2:

$$C^2 \equiv \frac{\langle n^2 \rangle}{\langle n \rangle^2} = 1 + \frac{1}{\langle n \rangle} + k^{-1} , \qquad F^2 \equiv \frac{\langle n(n - 1) \rangle}{\langle n \rangle^2} = 1 + k^{-1} . \tag{6.6}$$

In the limit $k \to \infty$ the NBD goes over in a Poisson distribution. It is therefore evident that the Poisson distribution has constant factorial moments, the direct measurement of which is presented in detail in chapters 7 and 8.

Different mechanisms have been suggested which give rise to negative binomial or similar distributions: stimulated emission [39,40], cluster or clan production [40] and parton branching [43,44]. Depending on the assumed mechanism the parameter k acquires different meaning, as will be discussed further below.

Negative values of the parameter k correspond to a positive binomial distribution, i.e.:

$$P_i(n, p) = \left(\begin{array}{c} n \\ i \end{array} \right) p^i q^{n-i}, \qquad i = 0, 1, 2, \ldots n . \tag{6.7}$$

The generalization to non-integer n is conveniently done in terms of Γ functions, yielding:

$$P_i(n, p) = \frac{\Gamma(n + 1)}{\Gamma(i + 1)\Gamma(n - i + 1)} p^i q^{n-i}, \qquad i < n + 1 . \tag{6.8}$$

The binomial distribution has mean $\langle i \rangle = np$ and variance $Var(i) = npq$. This allows us to express the parameters of the binomial distribution (n, p) in terms of parameters of the negative binomial distribution $(\langle n \rangle, k)$: i.e. $n = -k$ and $p = -\langle n \rangle / k$.
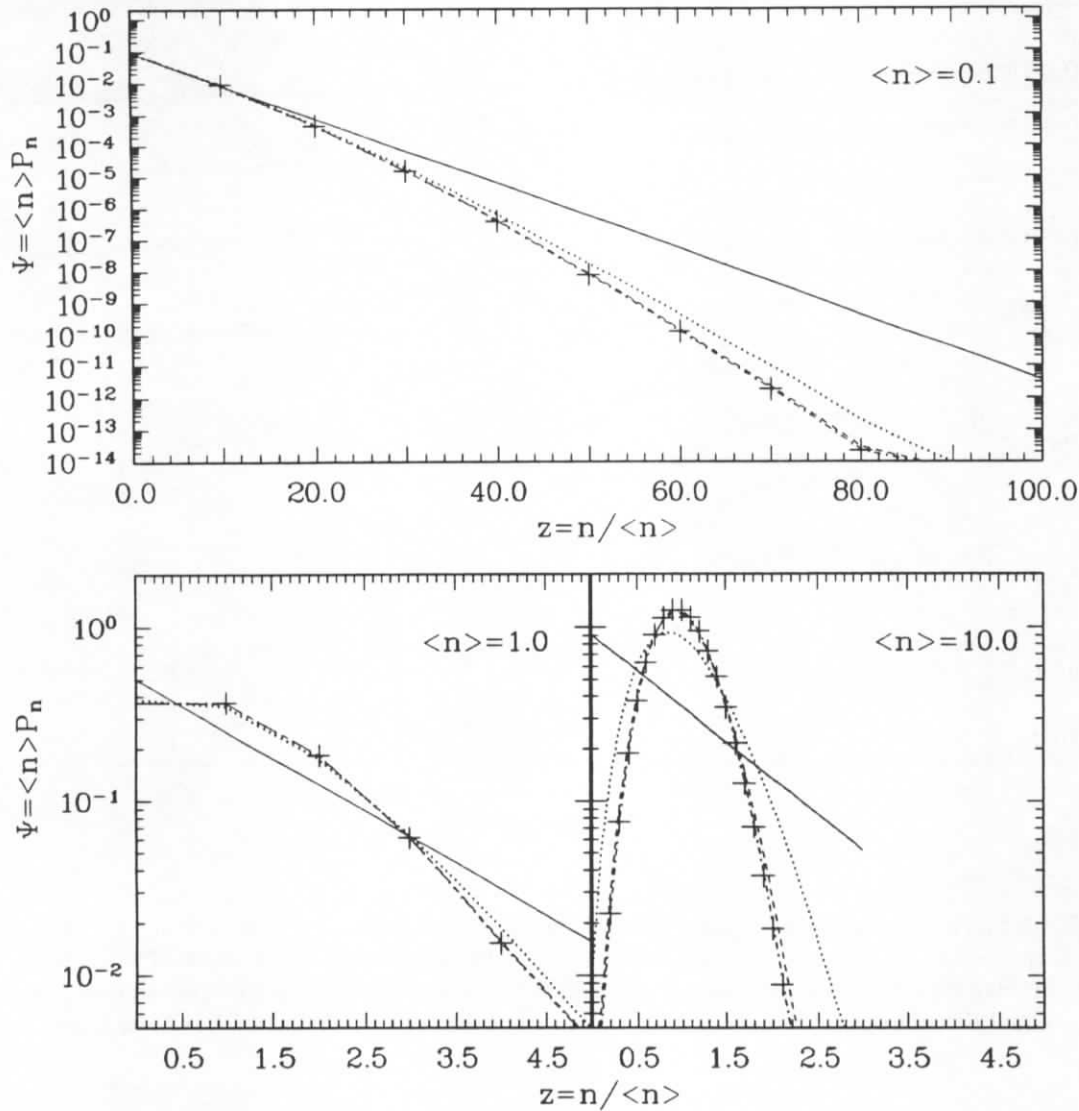
Figure 6.2: Negative binomial distributions for different k^{-1} and $\langle n \rangle$ values compared to the Poisson distribution (crosses): $k^{-1} = 1 \mapsto$ solid line, $k^{-1} = 10^{-1} \mapsto$ dotted line, $k^{-1} = 10^{-2} \mapsto$ dashed line and $k^{-1} = 10^{-3} \mapsto$ dash-dotted line.

6.2 Central rapidity intervals

In this section the charged particle multiplicity in central symmetric rapidity bins of variable size is studied. For the particular definition of rapidity used in this analysis the reader should consult section 5.2.

The resulting multiplicity distributions are presented in figure 6.3 as a function of the scaling variable z: starting at the smallest value of $|y| \leq 0.05$ the rapidity window is successively enlarged until finally the full rapidity range is covered. In doing this the average multiplicity $\langle n \rangle$ increases from 0.12 to 9.3 (cf. table 6.1). This implies, by virtue of the definition of z (6.1), a rapidly changing distribution $\Psi(z)$ if $\langle n \rangle$ is large (see also figure 6.2 for illustration). The details of this general behaviour, however, will depend on the dynamics of the production process – and via this relation information on the physics of that process is extracted.

The solid curves in figure 6.3 show the corresponding results from the Jetset 7.2 PS+BE simulation including detector simulation. Notable agreement is observed between data and
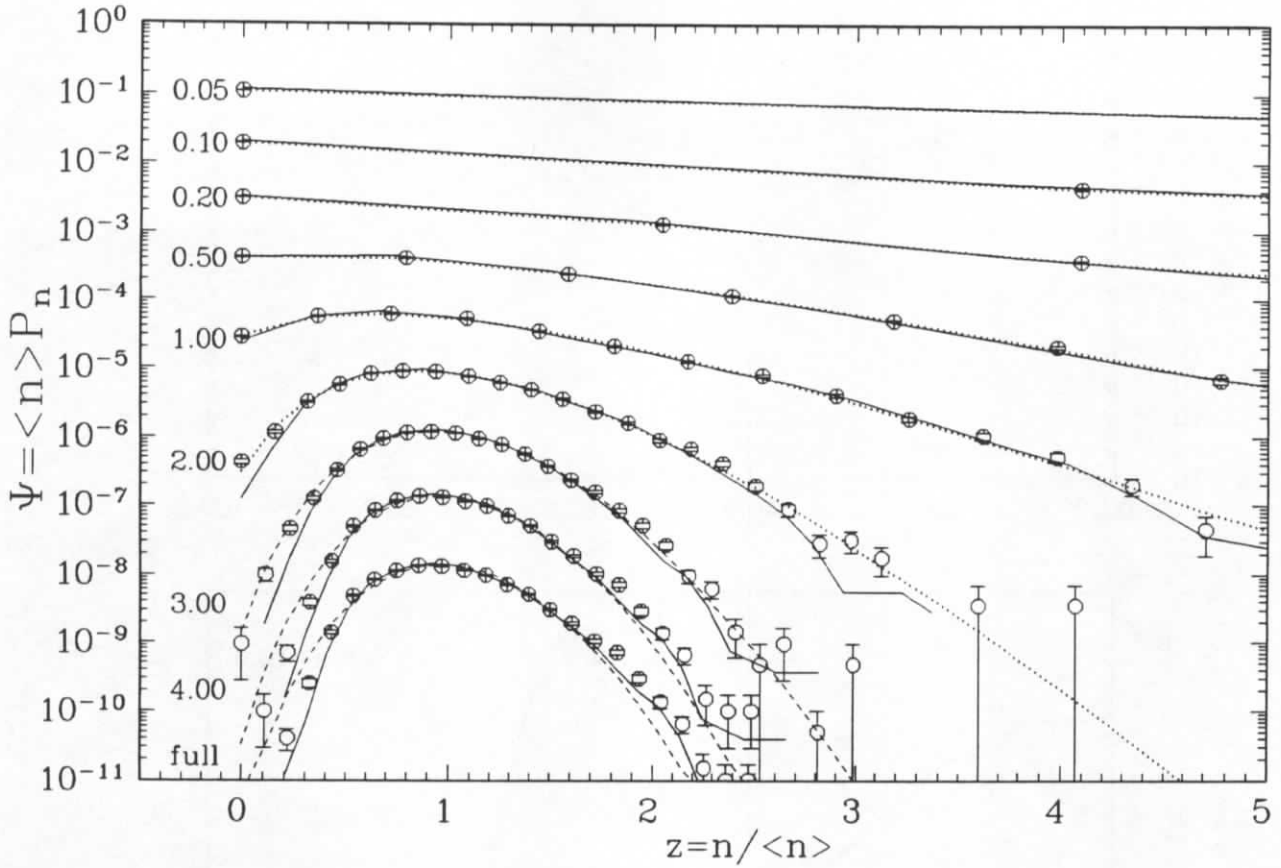
Figure 6.3: Multiplicity distribution of charged particles in central symmetric rapidity bins: CELLO data (statistical errors indicated) are compared to the Jetset 7.2 PS+BE simulation (solid lines). The dotted lines represent fits to the negative binomial distribution. The dashed lines indicate negative k parameters, i.e. the occurrence of binomial distributions. Starting at $|y| \leq 0.05$ each subsequent distribution has been scaled down by one decade.

Monte Carlo.

The (negative) binomial analysis has been performed on the total event sample and on selected two-jet events using the routine VALLEY [50]. In table 6.1 the fit results and statistical errors are presented; a graphical impression of the dependence of k^{-1} on the rapidity bin width is given in figure 6.4 for the total event sample and the two-jet selection respectively.

6.2.1   Total event sample

From figure 6.4 it is seen that the multiplicity in central rapidity bins $|y| \geq 2$ is distributed binomial, indicated by $k^{-1} < 0$. In smaller rapidity bins negative binomial distributions occur signified by non-zero values of k^{-1}. For bin sizes smaller than 0.5 units the k^{-1} parameter appears to be approximately constant within the experimental accuracy, despite the fact that the mean multiplicity $\langle n \rangle$ decreases rapidly (cf. table 6.1).

The description provided by Jetset 7.2 PS is unsatisfactory in that the model underestimates the size of the k^{-1} parameter. The situation is considerably improved if Bose-Einstein correlations are included in the simulation. In this way an adequate description of the data is obtained. Firstly this shows the significance of Bose-Einstein correlations and second it reveals the meaning of the k^{-1} parameter. Since Bose-Einstein correlations effectively pro-

$|y|$ range	Total sample		Two-jet sample	
	$\langle n \rangle$	k^{-1}	$\langle n \rangle$	k^{-1}
full	9.33 ± 0.020	-0.02 ± 0.001	8.63 ± 0.030	-0.04 ± 0.001
	9.87 ± 0.018	-0.03 ± 0.001	9.04 ± 0.027	-0.05 ± 0.001
	9.93 ± 0.010	-0.03 ± 0.001	9.05 ± 0.010	-0.05 ± 0.001
4	9.27 ± 0.020	-0.02 ± 0.001	8.52 ± 0.030	-0.03 ± 0.001
	9.82 ± 0.017	-0.03 ± 0.001	8.95 ± 0.025	-0.05 ± 0.001
	9.87 ± 0.010	-0.03 ± 0.001	8.94 ± 0.015	-0.04 ± 0.001
3	8.71 ± 0.021	0.00 ± 0.001	7.60 ± 0.030	-0.01 ± 0.002
	9.24 ± 0.018	-0.01 ± 0.001	8.02 ± 0.025	-0.03 ± 0.001
	9.33 ± 0.011	-0.01 ± 0.001	8.01 ± 0.015	-0.03 ± 0.001
2	6.38 ± 0.020	0.06 ± 0.002	4.75 ± 0.025	0.02 ± 0.004
	6.81 ± 0.018	0.05 ± 0.002	5.06 ± 0.021	-0.01 ± 0.003
	6.97 ± 0.010	0.05 ± 0.001	5.09 ± 0.012	-0.01 ± 0.002
1	2.75 ± 0.012	0.17 ± 0.006	1.69 ± 0.013	0.04 ± 0.010
	2.97 ± 0.011	0.17 ± 0.005	1.81 ± 0.011	-0.03 ± 0.008
	3.12 ± 0.007	0.16 ± 0.003	1.87 ± 0.007	-0.03 ± 0.004
0.5	1.26 ± 0.007	0.27 ± 0.012	0.70 ± 0.007	0.06 ± 0.024
	1.35 ± 0.006	0.26 ± 0.010	0.75 ± 0.006	-0.04 ± 0.017
	1.44 ± 0.004	0.23 ± 0.005	0.79 ± 0.004	-0.04 ± 0.010
0.2	0.49 ± 0.003	0.37 ± 0.030	0.26 ± 0.003	0.08 ± 0.068
	0.53 ± 0.003	0.28 ± 0.022	0.29 ± 0.003	-0.05 ± 0.051
	0.57 ± 0.002	0.27 ± 0.012	0.30 ± 0.002	-0.02 ± 0.029
0.1	0.24 ± 0.002	0.40 ± 0.055	0.12 ± 0.001	-0.04 ± 0.133
	0.27 ± 0.002	0.31 ± 0.045	0.14 ± 0.001	-0.13 ± 0.078
	0.28 ± 0.001	0.27 ± 0.021	0.15 ± 0.001	0.03 ± 0.064
0.05	0.12 ± 0.001	0.37 ± 0.101	0.06 ± 0.001	0.01 ± 0.322
	0.13 ± 0.001	0.36 ± 0.081	0.07 ± 0.001	-0.01 ± 0.236
	0.14 ± 0.001	0.30 ± 0.041	0.07 ± 0.001	0.03 ± 0.131

Table 6.1: Negative binomial parameter for central rapidity bins. The first entry in a block corresponds to the CELLO data, the second and third entry show the Jetset 7.2 PS+BE and the Jetset 7.2 PS results respectively.
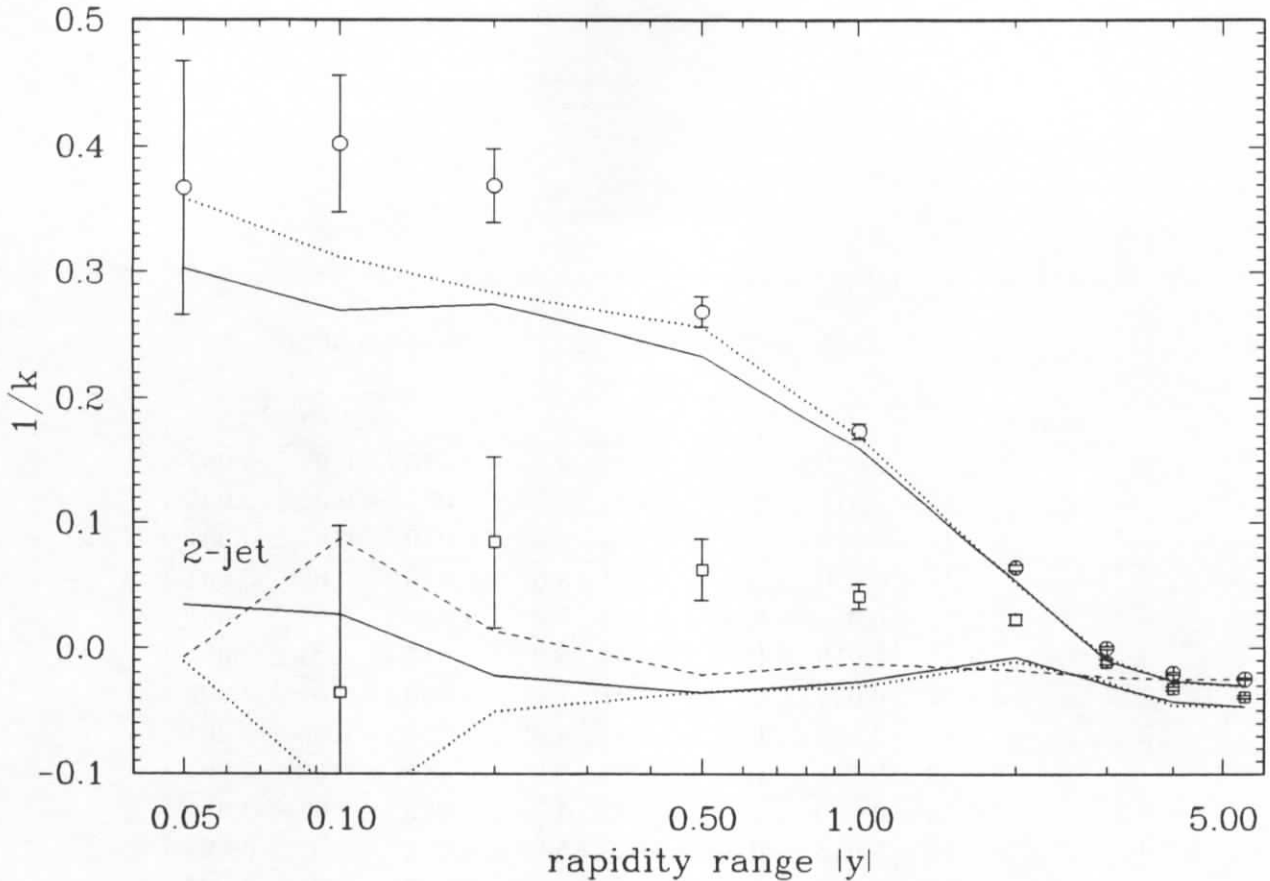
Figure 6.4: k^{-1} for central rapidity bins: The open symbols show the CELLO data (total event sample $\mapsto$ open dots, two-jet sample $\mapsto$ open squares). The solid and dotted curves show the corresponding results from Jetset 7.2 PS and Jetset 7.2 PS+BE respectively. The dashed curve is the result from the CELLO "toy" model.

duce more particles close by in phase space, it can be concluded that the k^{-1} parameter is a measure of *aggregation*. This is also the meaning assigned to k^{-1} by Giovannini and Van Hove [40]. In this context it is noteworthy that nothing of the kind is observed in the CELLO "toy" model (cf. section 5.4 for a description of the model), which makes it amply clear that *dynamical* and *kinematical* particle correlations and fluctuations inside individual events are at the basis of the observed behaviour.

6.2.2　Two-jet event sample

From the above discussion it can be conjectured that hard gluon radiation modifies the multiplicity distribution. In particular it can be expected that gluon fragments, if projected onto the event axis, will populate certain rapidity regions. And, since hard gluons occur only in a fraction of the total event sample, strong fluctuations in the multiplicity distribution of all events will occur as a consequence. For this reason the analysis of the total event sample mainly tests the perturbative phase of QCD; i.e. properties related to hard gluon radiation. This is complemented by the analysis of two-jet events, which is mainly sensitive to the non-perturbative phase of QCD.

From figure 6.4 it is apparent that particle production in two-jet events is less influenced by correlations and fluctuations than is the total event sample, justifying the above conjecture. This subject is also discussed by Andersson et al. in [67].

An observation of great importance is the significant failure of both the Jetset 7.2 PS and the Jetset 7.2 PS+BE simulations in describing the two-jet data: while the data show clear evidence for negative binomial distributions for $|y| \leq 2$, the Monte Carlo still predicts binomial multiplicity fluctuations. This is a very interesting observation, in line with the conjecture of Ochs [68,70] that the notion of local parton hadron duality, which means a duality between parton and hadron distributions [71], requires a local hadronization process, in possible contradiction to the energy dissipating string mechanism.

The explanation for the observed behaviour of the k^{-1} parameter and the failure of the Lund string model to reproduce the effect is subject of the following sections.

6.3 Rapidity scan

In this section a detailed analysis of the origin of the observed (negative) binomial regularities is presented. In the previous section an increase of the k^{-1} coefficient with decreasing rapidity bin size has been observed. Here it will be demonstrated that this behaviour is not originally related to the decreasing bin size, but is actually due to the absolute position of the rapidity bin.

For this purpose the rapidity range extending from -4 to $+4$ is divided into overlapping bins of 0.5 units each, yielding 31 individual multiplicity distributions. In a second step the (negative) binomial distribution (6.4, 6.8) is fitted to these multiplicity distributions. In figures 6.5 and 6.6 the fitted k^{-1} parameter from the rapidity scan is displayed for the total event sample and for two-jet events separately.

Before discussing the figures let me recall the definition of rapidity used here, since this is necessary for a thorough understanding of the results. In this study rapidity is defined with respect to the linearized sphericity axis (5.3). Furthermore the sphericity axis has been oriented in direction of the most energetic jet. Due to this definition negative rapidity values signify phase space regions where gluon radiation preferentially occurs, positive rapidity values, on the other hand, indicate phase space regions dominated by pure quark fragmentation. It should however be remembered that this ideal separation is diluted by detector resolution and acceptance effects.

6.3.1 Total event sample

In figure 6.5 the fitted k^{-1} parameter is displayed for the total data sample and compared to the Jetset 7.2 PS and Jetset 7.2 PS+BE simulations. A strong variation with rapidity is observed. For large values of $|y|$ binomial multiplicity distributions are indicated by negative k^{-1} values. In the other parts of phase space negative binomial distributions occur, expressed by positive k^{-1} values. The observed functional dependence is not symmetric in rapidity, as is expected for the rapidity definition used here. And, as outlined above, the correlations for negative rapidity are indeed larger than for positive rapidity. Given this behaviour it is readily understood that the k^{-1} parameter will also depend on the size of the rapidity bin, although this is not the genuine cause.

The comparison with model simulations in figure 6.5 demonstrates that Jetset 7.2 PS gives an adequate description of the data, provided Bose-Einstein correlations are included. In fact, the difference in the k^{-1} distribution due to Bose-Einstein correlations is remarkably large and again shows their significance to the overall fluctuations and correlations. It is worthwhile to note that the corresponding k^{-1} values from the CELLO "toy" model are independent of
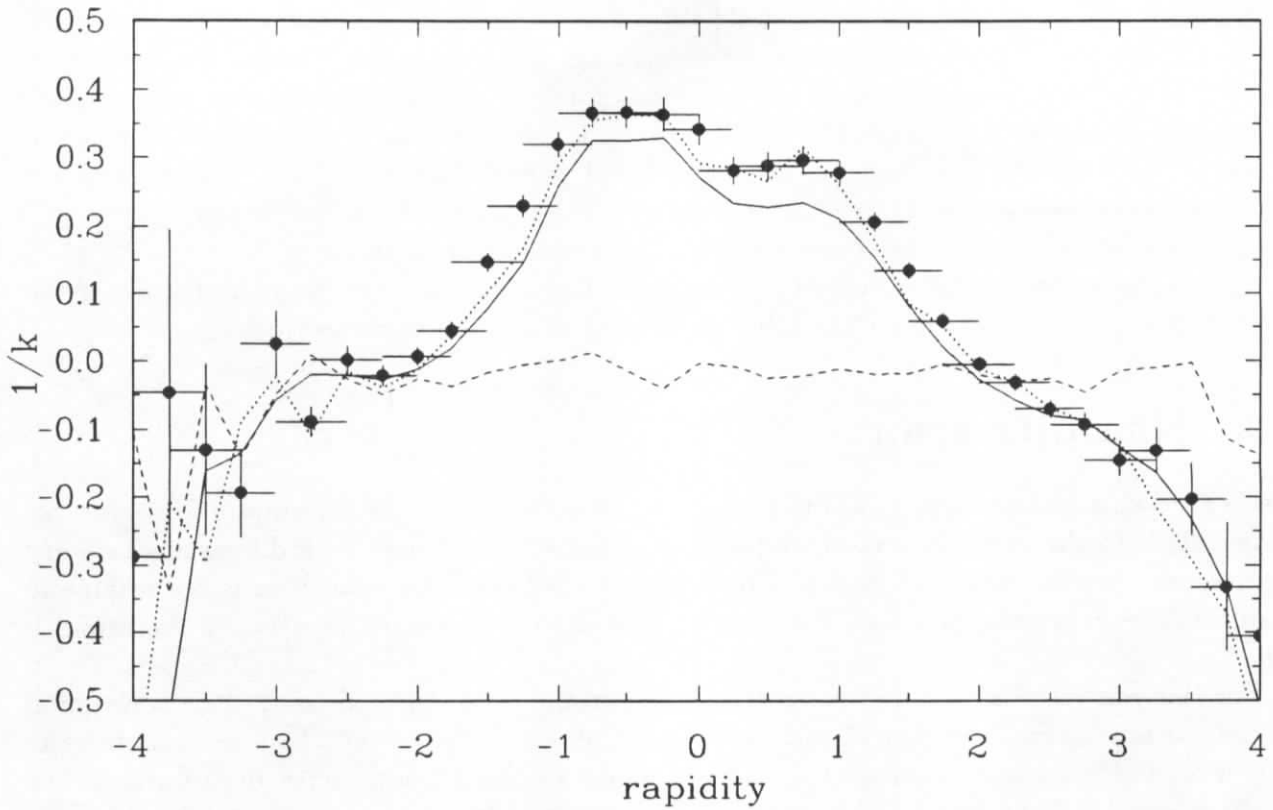
Figure 6.5: k^{-1} as a function of rapidity: CELLO data (total event sample) are shown with error bars. The solid and dotted curves show the corresponding results from Jetset 7.2 PS and Jetset 7.2 PS+BE respectively. The dashed curve is the result from the CELLO "toy" model.
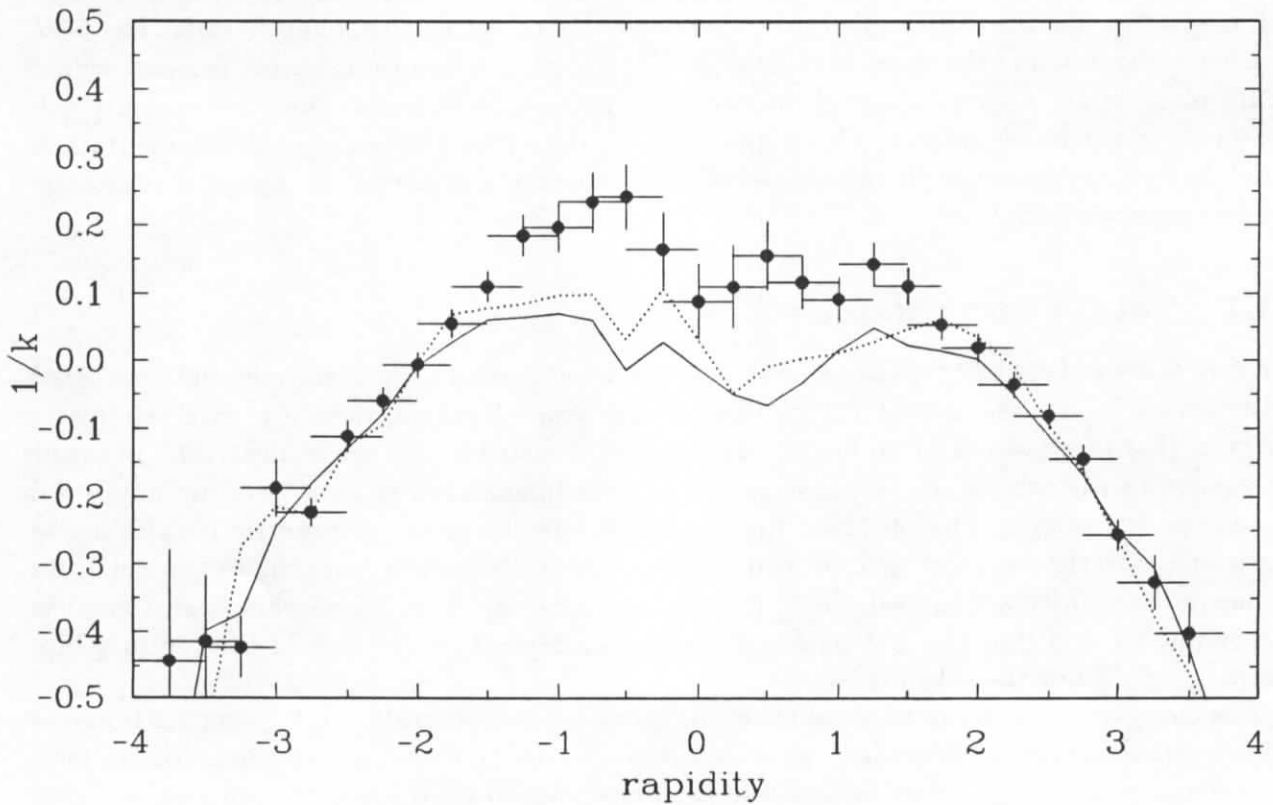
Figure 6.6: k^{-1} as a function of rapidity: CELLO data (two-jet event sample) are shown with error bars. The solid and dotted curves show the corresponding results from Jetset 7.2 PS and Jetset 7.2 PS+BE respectively.

rapidity and moreover always close to zero, revealing only Poissonian fluctuations. From this it is concluded that the occurrence of negative binomial distributions in parts of phase space, as observed in the data (and also in Jetset) is due to dynamical and kinematical properties of the particle production process. This point is further elaborated in section 6.4.

6.3.2 Two-jet event sample

The most spectacular observation in the two-jet study is the failure of the Jetset Monte Carlo in reproducing the rapidity dependence of the k^{-1} parameter. The observed discrepancy is statistically significant. To consolidate this further, systematic studies have been performed to make sure the effect is not artificial. This has been done by varying the two-jet selection criteria as well as the acceptance criteria for charged particles. The discrepancy between Jetset and CELLO data always remained.
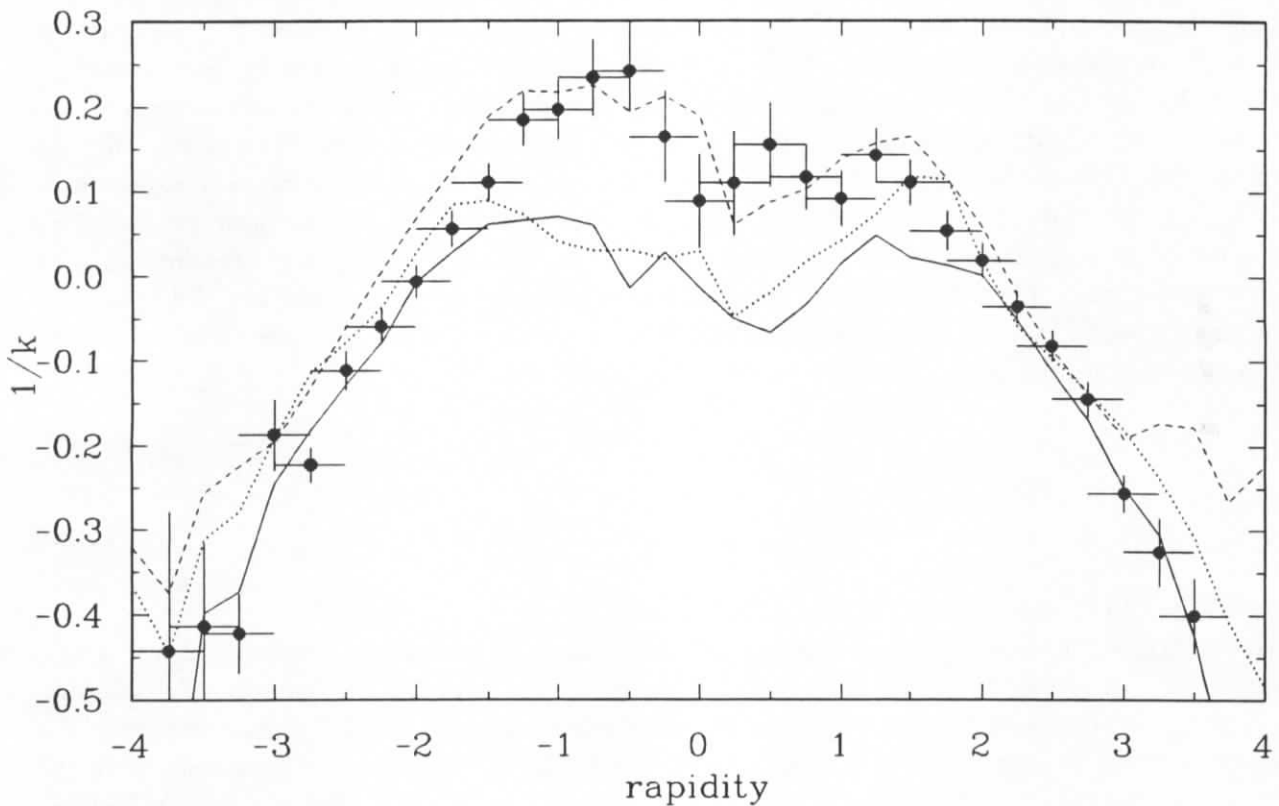
Figure 6.7: CELLO two-jet data on k^{-1} are compared to Jetset 7.2 PS after detector simulation (solid line) and before detector simulation (dotted line). The dashed line shows the Herwig 5.0 PS result.

Besides this observation it is also evident when comparing figures 6.5 and 6.6 that the strength of correlations is reduced in two-jet events. This is easily understood from what has been said before, namely that hard gluon radiation (which is absent in the two-jet selection) contributes significantly to fluctuations and correlations in multihadron production.

Already at this stage it can be assumed that the failure of the Jetset Monte Carlo has its origin in the treatment of the *non-perturbative* phase. This conjecture is based on the fact that the discrepancy appears only in two-jet events where the non-perturbative hadronization phase dominates the particle production process. In contrast to that hard bremsstrahlungs gluons characterize the total event sample and thereby conceal details of the soft hadroniza-

tion process. A detailed study of fluctuations and correlations in the Jetset and Herwig Monte Carlo programs is presented in section 6.4, concentrating on these aspects.

An intriguing result is presented in figure 6.7, where it is immediately seen that the Herwig 5.0 PS simulation provides a very good description of the data, concerning both the shape and the magnitude of the k^{-1} distribution. And, since Herwig involves *cluster* and Jetset *string* fragmentation i.e. completely different schemes for the non-perturbative regime, this comparison also provides the key to understand the difference of the two models. It should be emphasized that there is, as far as is known, no other distribution revealing such strong differences between cluster and string-based models. It is further seen from this picture that detector effects only cause a minor distortion of the k^{-1} distribution. This is important insofar as the following model studies are done without detector simulation.

6.3.3 Clan production

According to Giovannini and Van Hove the negative binomial distribution is generated by independent emission of entities, which they call *clans*, which subsequently decay. At the basis of this process they see the QCD parton shower with the gluon self-interaction as the dominant multiplication mechanism [40,41]. It is assumed that the number of clans follows a Poisson distribution. In addition, the decay of these clans is assumed to cause a logarithmic distribution for the number of particles per clan. In this context the parameter k^{-1} gives the ratio of probabilities for the two cases that two particles belong to the same clan or to different clans. Therefore the k^{-1} parameter is a measure of *aggregation*. The average number of clans $\langle N_c \rangle$ and the average number of particles per clan $\langle n_c \rangle$ are then related to the negative binomial parameters as follows:

$$\langle N_c \rangle = k \ln \left(1 + \frac{\langle n \rangle}{k} \right), \qquad\qquad \langle n_c \rangle = \frac{\langle n \rangle}{\langle N_c \rangle}, \qquad\qquad (6.9)$$

$$\lim_{k \to \infty} \langle N_c \rangle = \langle n \rangle, \qquad\qquad \lim_{k \to \infty} \langle n_c \rangle = 1 . \qquad\qquad (6.10)$$

Equation 6.10 corresponds to the Poissonian limit.

To a large extent the above ideas are actually incorporated in the Herwig Monte Carlo program [5] (cf. also chapter 2). It is therefore tempting to compare the rapidity distribution of clusters, produced in the preconfinement phase of the Herwig 5.0 PS simulation with the number of clans as derived from negative binomial fits to the multiplicity distribution in the corresponding rapidity bins. This comparison, presented in figure 6.8, shows that the shape of both distributions is in fact similar, however, the normalization differs by a factor of two.

In figures 6.9 and 6.10 the number of clans $\langle N_c \rangle$ and the average multiplicity per clan $\langle n_c \rangle$ are shown for the total data sample and are compared to the two-jet selection.

It is to note that $\langle N_c \rangle$ is mainly sensitive to the average multiplicity $\langle n \rangle$, while $\langle n_c \rangle$ has a larger sensitivity to the k^{-1} parameter. This is easily seen if $\langle N_c \rangle$ is expanded in a power series:

$$\langle N_c \rangle \simeq \langle n \rangle \left[1 - \frac{1}{2} \frac{\langle n \rangle}{k} + \frac{1}{3} \left(\frac{\langle n \rangle}{k} \right)^2 - \cdots \right] . \qquad\qquad (6.11)$$

The comparison with the Jetset simulation shows reasonable agreement in case of the $\langle N_c \rangle$ distribution both for the total event sample and the two-jet selection, this is because the mean multiplicity is slightly too large in the Monte Carlo. In the total event sample the multiplicity per clan is reproduced only if Bose-Einstein correlations are included in the
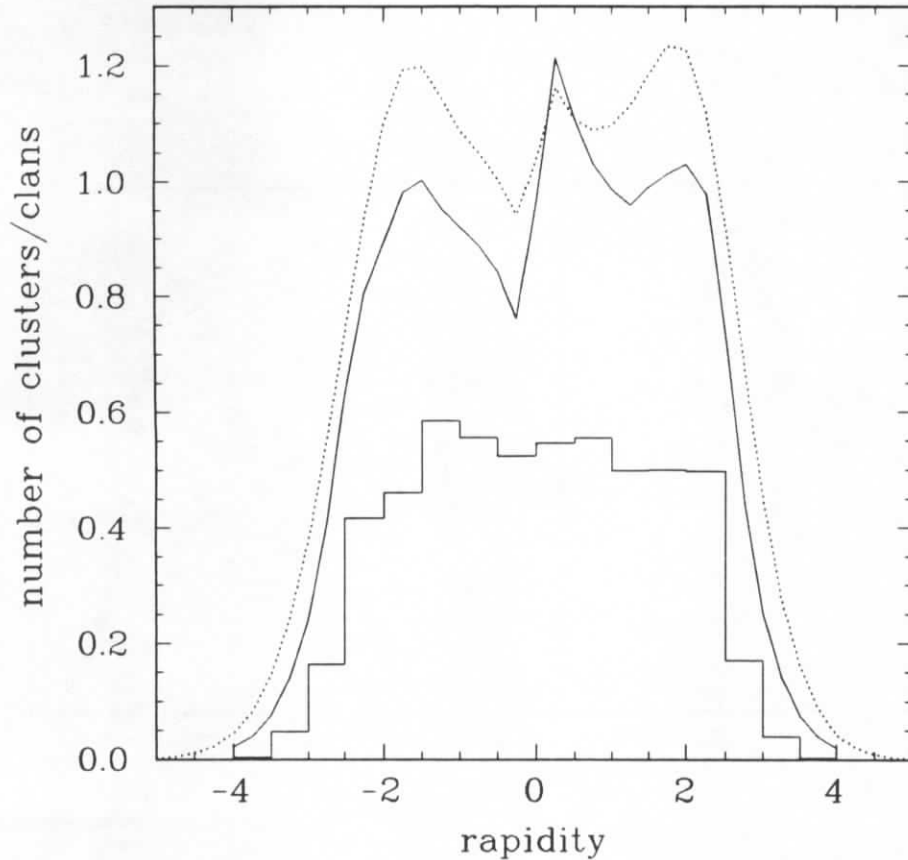
Figure 6.8: Rapidity distribution of clusters in the Herwig 5.0 PS model compared to the distribution of clans obtained from negative binomial fits to the multiplicity distribution (solid line $\mapsto$ primary particles; dotted line $\mapsto$ final state charged particles).

simulation; otherwise the particle density provided by the Monte Carlo is significantly too low for positive rapidity values. This shows again that the "negative" rapidity region is dominated by gluon bremsstrahlung, concealing other effects.

Both Monte Carlo versions fail to describe the average multiplicity per clan in two-jet events. Of course, this reflects the discrepancy already noted in the k^{-1} parameter. It is further observed that negative binomial distributions occur if the average multiplicity per clan $\langle n_c \rangle$ is larger than one, as it is expected from (6.10).

6.3.4   Interpretation

The interpretation of the results obtained so far is as follows: the perturbative QCD phase generates primary massive colour singlet states. Their fluctuations in rapidity space are Poissonian to a good approximation. In the case where additional gluon fragments are projected onto the event axis negative binomial distribution occur already at this level. The subsequent decay* generates negative binomial distributions for the final state particles, provided there is a sufficient overlap among the decay products from different primary sources. This is observed in the rapidity region $|y| \leq 2$ (see figures 6.5 and 6.6). The probability to have more than one primary particle in a given rapidity interval is essentially zero for absolute rapidity

---

*N.B. that decay products are approximately Gaussian distributed with $\sigma(y) \approx 0.5$ around the rapidity of the decaying particle.
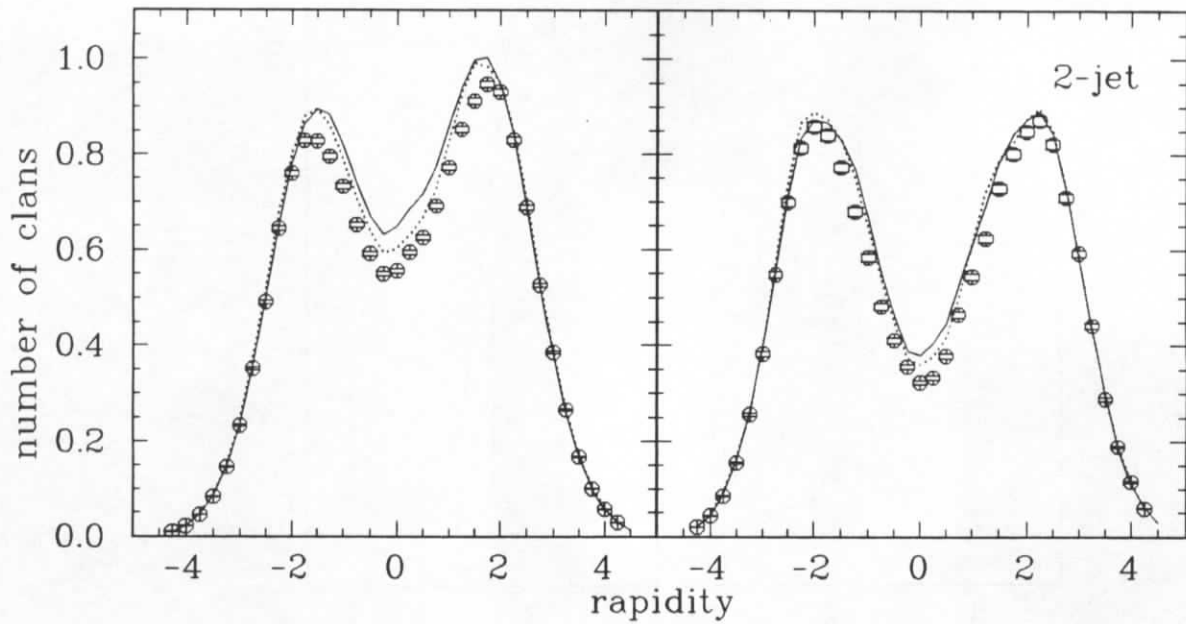
Figure 6.9: Distribution of clans for the total event sample (left) and for two-jet events (right) compared to the Jetset 7.2 PS and Jetset 7.2 PS+BE model (solid respectively dotted lines).
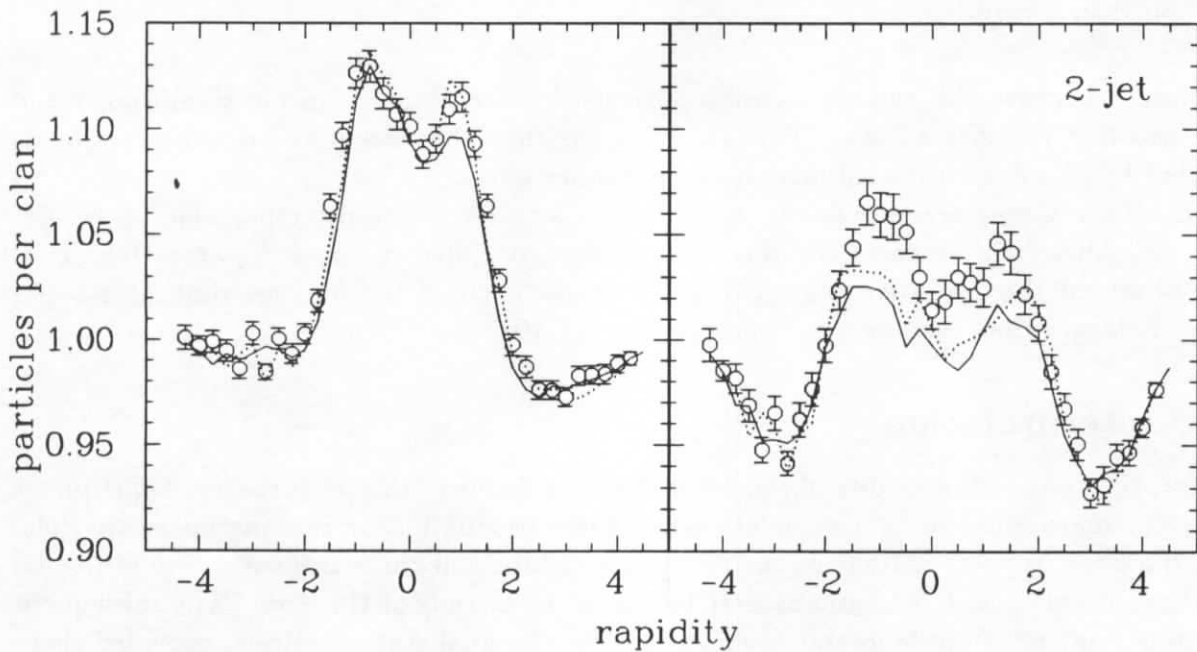
Figure 6.10: Multiplicity per clan for the total event sample (left) and for two-jet events (right) compared to the Jetset 7.2 PS and Jetset 7.2 PS+BE model (solid respectively dotted lines).

values larger than two. This fact is, of course, related to the fragmentation process. In the Jetset 7.3 PS simulation at 35 GeV centre of mass energy, for instance, the average momentum of primarily produced particles is $\langle p \rangle = 3.29$ GeV and the average mass of these objects is $\langle m \rangle = 0.82$ GeV: this implies average rapidity values of $\langle y \rangle = 2.1$ (if transverse momentum is neglected). This is exactly the rapidity value where the k^{-1} distribution approaches zero (see figure 6.12), indicating the transition from the rapidity region where primary particles are close enough to give an effective overlap of their decay products, to the region where primary particles occur only isolated and hence an overlap is impossible.

6.4 Discussion of models

It is the purpose of this section to demonstrate how the observed properties of multiplicity distributions are accomplished in e^+e^- Monte Carlo simulations and thereby justify the conjectures and conclusions drawn in the preceding sections.

The striking difference between Herwig and Jetset concerning the rapidity dependence of the k^{-1} parameter in two-jet events is examined in detail and traced to its origin.

6.4.1 Correlations and fluctuations

According to the procedure presented in section 6.3 the multiplicity distributions generated by various Monte Carlo models are studied. The following models, discussed in detail in chapter 2, are considered for analysis. A short list of their basic properties is given here:

- **Jetset 7.3 $q\bar{q}$**: a pure Lund string model without gluon radiation. In this case (di)-quark pair creation in a string-like force field is the only source for particle production. This model is available as an option in Jetset 7.3.

- **Jetset 7.3 ME**: an $\mathcal{O}(\alpha_S^2)$ matrix element QCD approximation followed by Lund string fragmentation. Here it should be noted that compared to the "standard" parton shower model the matrix element model requires a change of the longitudinal and transverse fragmentation parameters: i.e. from $a = 0.5 \rightarrow 1$ and from $b = 0.9 \rightarrow 0.7$ GeV^{-2} for the Lund symmetric function (2.13) and from $\sigma_{p_\perp} = 0.35 \rightarrow 0.4$ GeV for the width of the Gaussian $p_\perp$ distribution. In addition, the joining parameter should be increased from 0.8 to 1.1 GeV [9].

- **Jetset 7.3 PS**: the Lund parton shower model followed by string fragmentation.

- **Herwig 5.0 PS**: the Herwig parton shower model followed by cluster fragmentation.

- **Ariadne 3.1 CD**: the Lund colour dipole parton shower model followed by string fragmentation.

6.4.1.1 Primary and final state particles

In figure 6.11 the fitted k^{-1} values are displayed for the Jetset 7.3 $q\bar{q}$ model for primary[†] and final state particles. A marked difference between the two distributions is observed: while the

---

[†]The term *primary* refers to *charged* and *neutral* particles, which in the case of string fragmentation come directly from the string, or to cluster decay products in the case of cluster fragmentation.
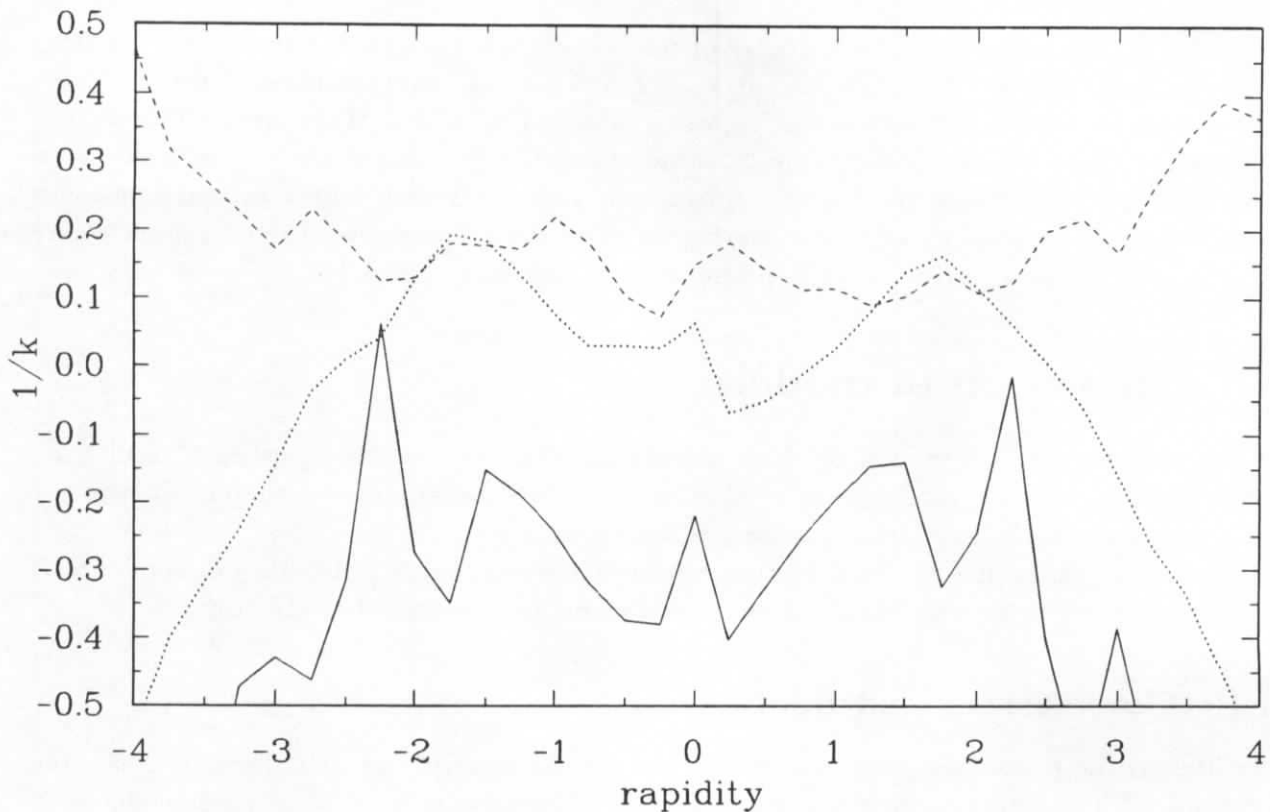
Figure 6.11: Rapidity dependence of k^{-1} in the Jetset 7.3 $q\bar{q}$ model (dotted line) compared to a "toy" model (dashed line). The solid line indicates the results obtained for primary particles.

k^{-1} values for primary particles are always negative, thereby signifying binomial multiplicity distributions, the analogous curve for final state particles indicates the occurrence of negative binomial distributions in parts of phase space.

To illustrate this further a simple "toy" model is designed in analogy to the CELLO "toy" model as described in section 5.4 on page 53. This model generates the *inclusive* rapidity distribution as obtained from the Jetset 7.3 $q\bar{q}$ simulation: that is to say it reproduces the rapidity distribution on average, without generating genuine particle correlations in *individual* events. In this model each primary particle is split in two according to a Gaussian distribution with a width of 0.5 units in rapidity.

In figure 6.11 the rapidity dependence of the k^{-1} parameter is displayed both for the primary particles and the decay products. As expected the primary multiplicity distribution is characterized by $k^{-1} < 0$; i.e. it is binomial. In contrast to that the final multiplicity distribution has negative binomial form, indicated by positive k^{-1} values. Comparing the "toy" model with the Jetset 7.3 $q\bar{q}$ simulation in figure 6.11 similar features are observed, but also apparent differences occur. While the "toy" model gives rise to negative binomial distributions in the total rapidity range, these are only observed in restricted intervals in the $q\bar{q}$ simulation. This difference is partly due to kinematical constraints, which are not fulfilled in the "toy" model: e.g. nothing prevents two primary particles from being produced at rapidity values of e.g. $y = +3.5$ in the "toy" model, which will be clearly impossible if four-momentum is conserved. A further property of the Lund string model is revealed by this study – namely that fluctuations of the primary particle multiplicity are less than Poissonian [8] (cf. also chapters 7 and 8).
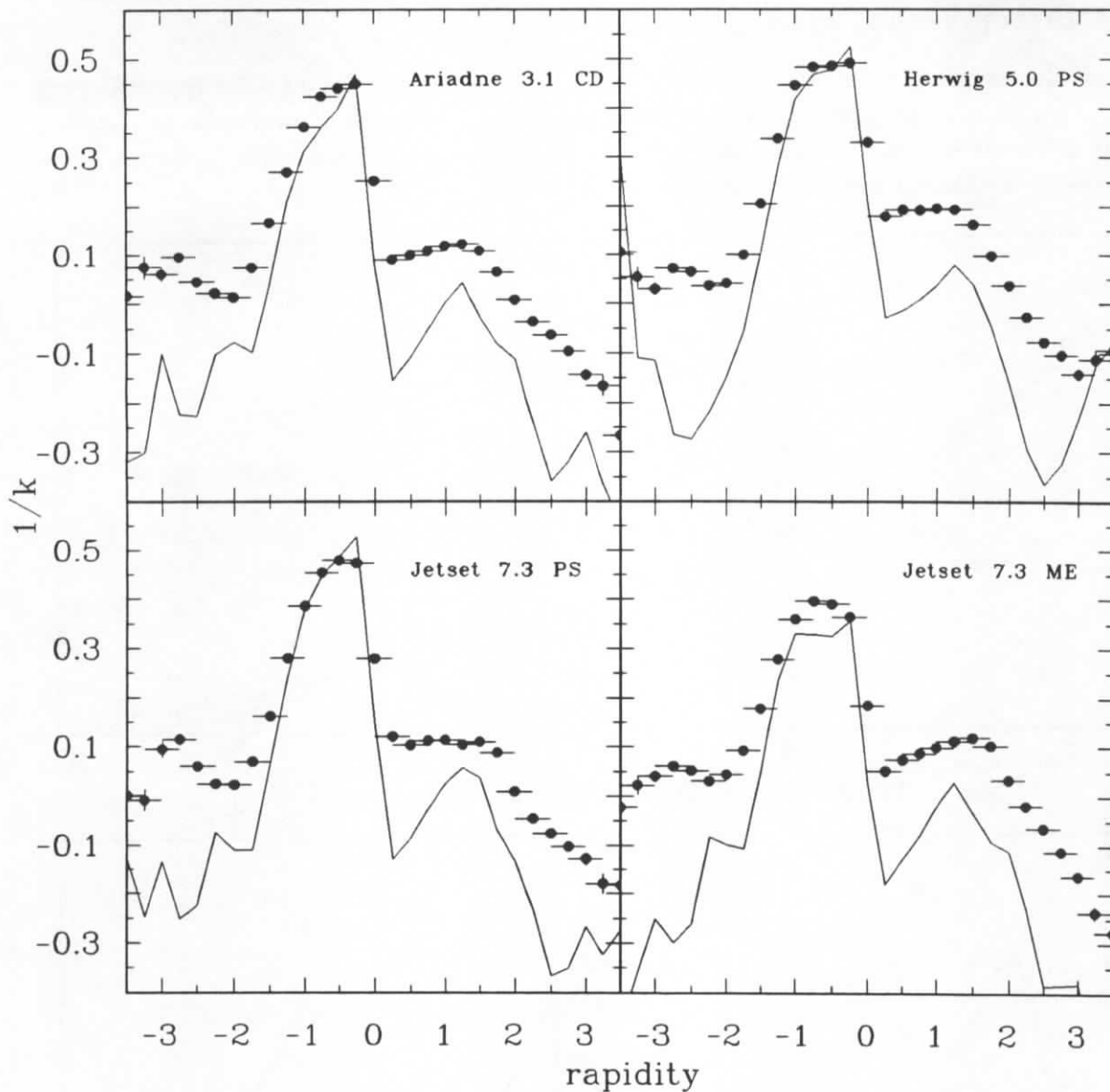
Figure 6.12: Rapidity dependence of k^{-1} for various models (solid line $\mapsto$ primary particles, dots $\mapsto$ final state charged particles).

6.4.1.2 Gluon radiation

The significance of hard gluon radiation is demonstrated in figure 6.12, where large k^{-1} parameters are observed in the rapidity range from -1.5 to 0. This effect is already observed at the level of primary particles, making it clear that gluon fragments induce negative binomial distributions in those parts of phase space where an overlap with the pure quark fragments occurs.

At this level the four studied models do not differ significantly enough to be distinguished by experiment. This is due to the fact that perturbative gluon radiation dominates the observed fluctuations and correlations, thus masking the non-perturbative hadronization process. In the following section only those events that pass a two-jet selection will be considered for analysis, tacitly focussing on the non-perturbative phase.

6.4.2   Cluster versus string models

The topic of this section is the dramatic difference observed as the Jetset 7.3 PS and Herwig 5.0 PS simulations are compared regarding the rapidity dependence of multiplicity distributions. This difference is only revealed in fluctuations of the particle multiplicity, the inclusive distributions being almost identical (see figure 6.13).
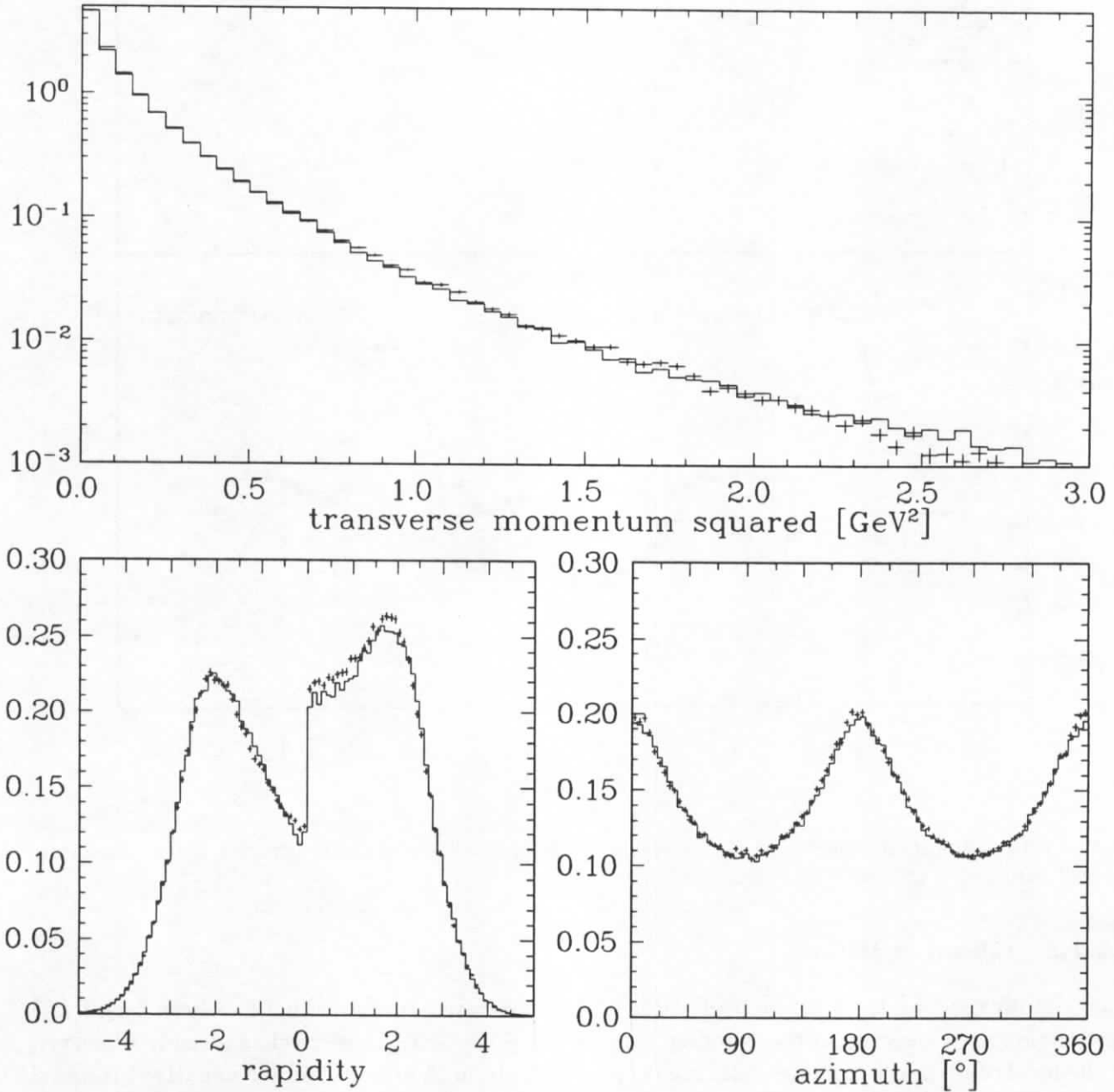
Figure 6.13: Inclusive y, ϕ and $p_\perp^2$ distributions for two-jet events: Herwig 5.0 PS (statistical errors indicated) is compared to the Jetset 7.2 PS simulation (histograms).

First of all it will be demonstrated that this difference has its origin in the treatment of the non-perturbative hadronization phase and is not due to different parton shower approximations. Throughout this section solely two-jet events will be considered for analysis.

For this purpose parton showers generated with the Herwig 5.0 PS program are transferred
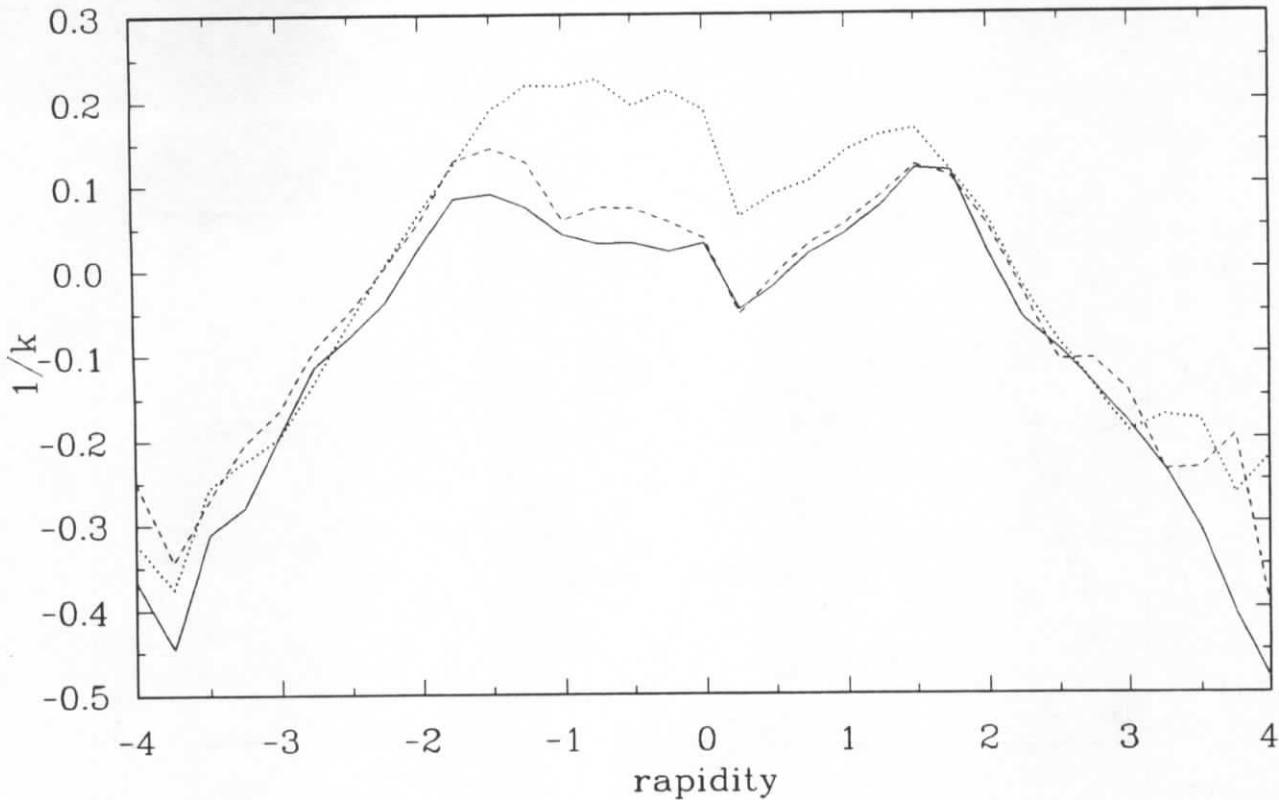
Figure 6.14: Rapidity dependence of k^{-1} in two-jet events: Jetset 7.3 PS (solid line), Herwig 5.0 PS (dotted line) and the Herwig parton shower with Lund string fragmentation (dashed line).

to the Jetset 7.3 program. Partons are then connected to Lund strings, keeping trace of the colour flow: from this point on fragmentation commences as usual.

In figure 6.14 the resulting k^{-1} distributions from the pure Herwig 5.0 PS and Jetset 7.3 PS simulations are compared to the hybrid scheme. Obviously, the hybrid scheme is very close to the Jetset 7.3 PS simulation, thus identifying differences in string and cluster fragmentation as the reason for the apparent difference between Herwig and Jetset. In addition, a slight difference between the two parton showers, when connected to strings, is observed. And, since hard gluon radiation is excluded by means of the two-jet selection, this effect has its explanation in terms of different approximations in the treatment of soft gluons during parton shower evolution.

6.4.2.1 Lund string model

In the following paragraphs the occurrence of correlations and fluctuations in the Lund string model is investigated. An attempt is made to "retune" the string model in order to reproduce the measured k^{-1} distribution. The following aspects come to mind which might have an impact on correlations and fluctuations in two-jet events:

Longitudinal fragmentation

Lund symmetric fragmentation: The Jetset 7.3 PS model uses the Lund symmetric function ((2.13) on page 12) to generate the longitudinal splitting variable z; i.e. to determine
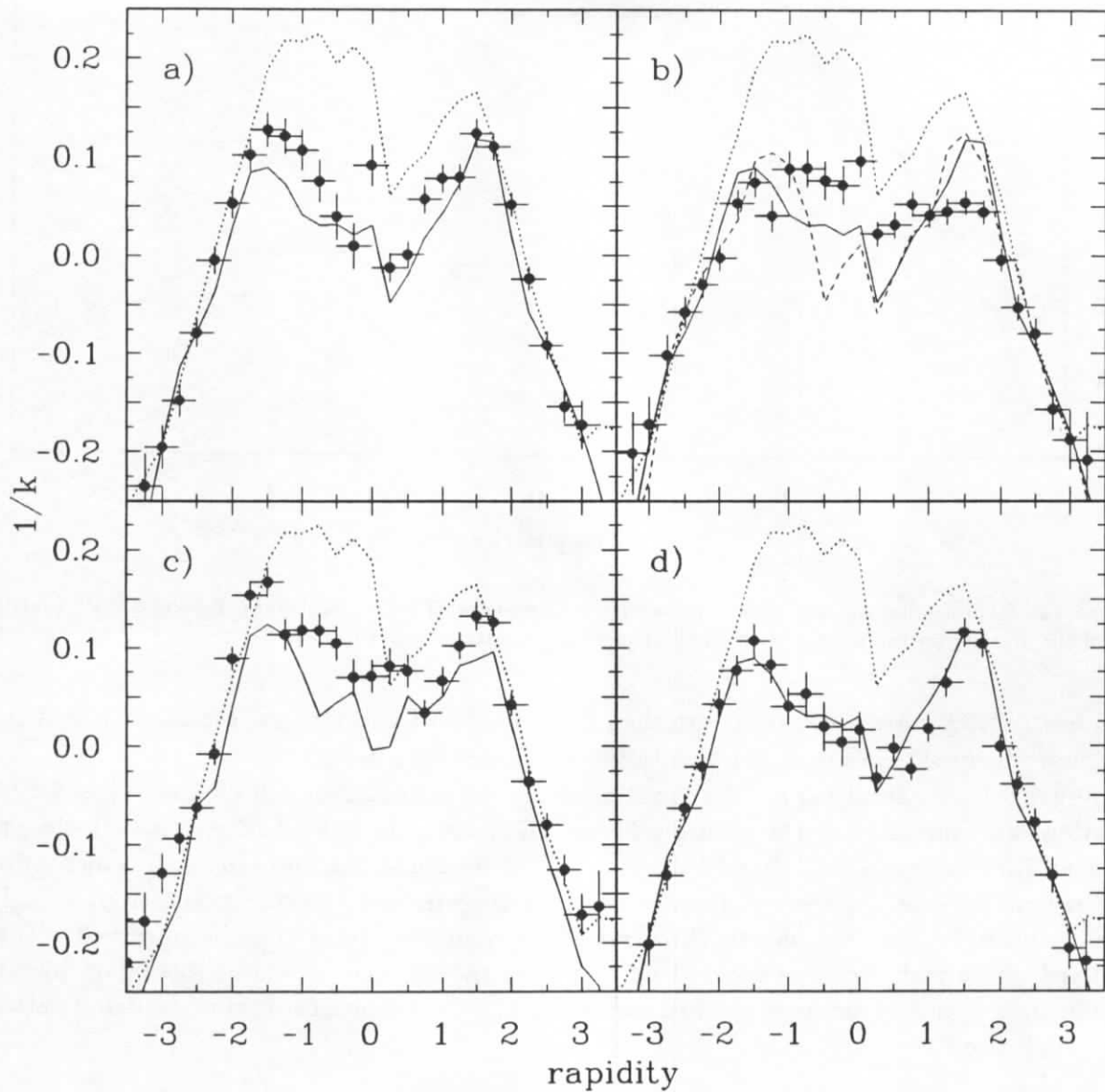
Figure 6.15: Studies of the k^{-1} rapidity dependence on two-jet events in the Lund string model: the solid line shows the result obtained from the default Jetset 7.3/6.3 PS simulation and the dotted line is the Herwig 5.0 PS result for comparison. The modified Jetset 7.3/6.3 PS results are displayed with error bars: **a:** Lund symmetric fragmentation function with $a = 0.0$ and $b = 0.4$ GeV^{-2}; **b:** Field-Feynman, Peterson scenario, the dashed line corresponds to string fragmentation according to Bowler; **c:** Jetset 6.3 PS with $P/(V+P) = \sqrt{2} \cdot 0.5$ and $\langle p_\perp^2 \rangle = (50$ MeV$)^2$ for π mesons and $(450$ MeV$)^2$ for ρ mesons; **d:** Jetset 7.3 PS including higher meson multiplets.

the energy-momentum fraction taken by a hadron. This function is controlled by two parameters a and b which are highly correlated. The average multiplicity is essentially determined by the ratio a/b while multiplicity fluctuations are related to the expression $(ab)^{-1}$ [67]. The correlation of the two parameters is shown in figure 6.16. The line is a fit to those a and b values which reproduce the default average fractional energy $\langle x_E \rangle = 0.22$ and the corresponding average multiplicity $\langle N \rangle = 9.0$ of primary particles in the simple $q\bar{q}$ model. The relation is almost linear with $b \simeq 0.4 + a$. Evidently a wide range of a and b values gives essentially the same results with respect to inclusive distributions, but correlations and fluctuations are expected to increase as a and b are decreased.
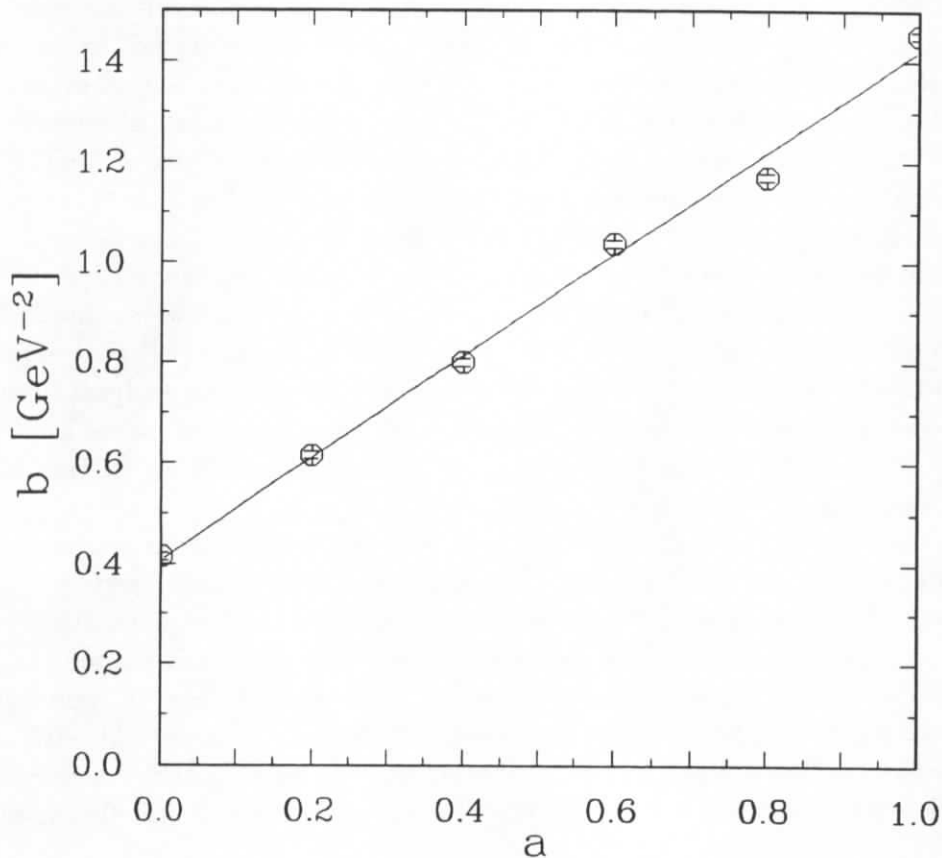
Figure 6.16: Correlation of parameters for the Lund symmetric function in a pure $q\bar{q}$ model.

In the case of large a and b parameters the *ordering* of particles, i.e. the coincidence between rapidity and rank is strict, corresponding to a coherent string state. If both a and b are decreased the ordering is diminished and consequently fluctuations are enhanced [8,47]. This is proven in figure 6.15a, where the k^{-1} distributions from the rapidity scan are shown for the two parameter sets $a = 0.5, b = 0.9$ GeV^{-2} (default values) and $a = 0.0, b = 0.4$ GeV^{-2}. However, the effect is not large enough to explain the difference between Jetset 7.3 PS and Herwig 5.0 PS.

Field-Feynman & Peterson and Bowler fragmentation: The Peterson function ((2.14) on page 12) offers an alternative parameterization for the energy-momentum splitting in the longitudinal fragmentation process of heavy charm and bottom quarks. In this case the average energy-momentum fraction taken by the heavy hadron is in accord with the Bjorken

formula [73]:

$$\langle z \rangle \simeq 1 - \frac{1\ \mathrm{GeV}}{m_Q} \ , \tag{6.12}$$

where m_Q is the mass of the heavy quark. In contrast to that the Lund symmetric function leads to the relation [48]:

$$\langle z \rangle \simeq 1 - \frac{1+a}{bm_H^2} \ , \tag{6.13}$$

where m_H is the mass of the heavy hadron.

The underlying space-time structure of the Lund string model, which implies that on average all string breakups take place along a hyperbola of constant invariant time [8,47], implies a different average rapidity separation for heavy and light hadrons. In case of the Peterson function the heavy hadron is on average 0.7 units in rapidity ahead of any other hadron, which is the same rapidity separation as between neighbouring ordinary hadrons. The requirement of left-right symmetry in the Lund function implies a larger rapidity separation for heavy particles; i.e. heavy particles appear to be more isolated in this approach, as a consequence of the larger amount of energy taken from the string by a heavy hadron[‡]. Hitherto the experimental and theoretical situation is ambitious, although there is experimental evidence against the Lund symmetric function, which predicts a too hard bottom quark fragmentation at LEP energies [49]. It has been shown by Bowler [84] that also in the string model it is possible to retain a $1/m$ dependence (6.12) for massive endpoint quarks.

This issue is very important for the determination of the top quark mass at a future e^+e^- linear collider [89]. In this context the study of particle correlations in the different fragmentation approaches is certainly worthy.

In figure 6.15b the resulting k^{-1} distribution is shown for a simulation where the light up, down and strange quarks are treated according to the Field-Feynman function ((2.7) on page 10) with $a = 0.77$ and charm and bottom quarks are fragmented with the Peterson function with $\varepsilon_c = 0.1$ and $\varepsilon_b = 0.01$. The comparison with the standard simulation shows that particle correlations are different in this approach. Similarly the Bowler type fragmentation (dashed line in figure 6.15b) does not provide a significant improvement with respect to Herwig. None of the studied string fragmentation schemes is particularly favoured by the data, and there still remains a general discrepancy between string and cluster fragmentation.

Transverse fragmentation: The tunneling mechanism implies a Gaussian $p_\perp$ distribution for the emerging quarks (cf. the discussion in section 2.2.2 on page 11). Furthermore, since the string is assumed to be one-dimensional the $p_\perp$ must be compensated locally: i.e. $\vec{p}_\perp(q) + \vec{p}_\perp(\bar{q}) = \vec{0}$. As a consequence half of a hadron's $p_\perp$ will be compensated in each of its neighbours. For this reason two neighbouring hadrons, sharing a $q\bar{q}$ pair have a tendency to appear at opposite azimuthal angles. These *anti-correlations* are not accessible through the sole analysis of the rapidity distribution. The two- and three-dimensional intermittency analyses presented in chapter 8 are sensitive to this aspect of multiparticle production.

In the standard Lund string model the average $p_\perp^2$ a quark acquires due to the tunneling process is assumed to be $\langle p_\perp^2 \rangle = (350\ \mathrm{MeV})^2$ independent of its mass. If this is interpreted as being due to a *transverse* extension of the string a mean square radius of $\langle r^2 \rangle = (0.56\ \mathrm{fm})^2$ is obtained. This result is in striking agreement with the radius of the "pion source", as obtained from the analysis of Bose-Einstein correlations in section 9.1.

[‡]The rapidity separation between first and second rank hadrons is 0.55 for light hadrons, 0.94 for charmed hadrons and 1.5 for bottom hadrons [8].

According to an argument of Gustafson and Sjögren [65] the $\langle p_\perp^2 \rangle$ of a hadron species should be smaller the lighter the produced hadron is. In addition lighter hadrons have a tendency to appear in "bunches". The argument is repeated here briefly: the probability for a quark to fit into a bound state meson is proportional to $m_\perp^{-1}$ [8], i.e. it depends on $p_\perp$. For heavy particles the $p_\perp$ dependence is only weak, but pions have a mass much smaller than the average $p_\perp$. For this reason primary pions should have smaller transverse momenta than other mesons. And since a $q\bar{q}$ pair with small $p_\perp$ produces two mesons, these have an increased probability to end up as two pions. Primary pions thus have a tendency to come in bunches, an effect not included in the standard Jetset model.

A modified version of the Jetset 6.3 PS program [66] has been used to study this effect. This version allows us to chose the width of the Gaussian $p_\perp$ distribution separately for e.g. π and ρ mesons. This simplified treatment does not include the "bunching" of pions. The latter effect certainly would increase the k^{-1} values due to a stronger aggregation of particles. To simulate this behaviour the $P/(V + P)$§ ratio has been changed from its default value 0.5 to $\sqrt{2} \cdot 0.5$. This doubles the probability to produce two neighbouring pions, because this probability is proportional to $[P/(V + P)]^2$. In addition, the $\langle p_\perp^2 \rangle$ has been chosen to be $(50 \text{ MeV})^2$ for π mesons, $(450 \text{ MeV})^2$ for ρ mesons and $(350 \text{ MeV})^2$ for all other primary particles. The corresponding result is presented in figure 6.15c. Although the k^{-1} distribution has changed in the right direction, the effect is still too small to account for the difference between CELLO and Jetset.

Higher multiplets: Other differences between Jetset 7.3 PS and Herwig 5.0 PS concern the primary particle composition and the treatment of particle decays. Herwig generates the meson multiplets listed in table 6.2, where the corresponding Jetset parameterization of production probabilities is also given. The parameters $\alpha, \beta, \gamma, \delta$ and $\left(\frac{V}{V+P}\right)_f$ refer to particles

Multiplet	Quark spin S	Orbital angular momentum L	Meson spin J^P	Jetset 7.3 parameterization
Pseudoscalar	0	0	0^-	$\left(\frac{P}{V+P}\right)_f (1 - \alpha)$
Axialvector	0	1	1^+	$\left(\frac{P}{V+P}\right)_f \alpha$
Vector	1	0	1^-	$\left(\frac{V}{V+P}\right)_f (1 - \beta - \gamma - \delta)$
Scalar[a]	1	1	0^+	$\left(\frac{V}{V+P}\right)_f \beta$
Axialvector	1	1	1^+	$\left(\frac{V}{V+P}\right)_f \gamma$
Tensor	1	1	2^+	$\left(\frac{V}{V+P}\right)_f \delta$

a) Scalars are not included in Herwig

Table 6.2: Meson multiplets.

produced directly from the string and have the following meaning:

§P and V are used to abbreviate the production probability for pseudoscalar and vector mesons respectively.

- α is the probability that a spin one meson ($J^P = 1^+$) is produced with a total quark spin $S = 0$ and orbital angular momentum $L = 1$.

- β is the probability that a spin zero meson ($J^P = 0^+$) is produced with a total quark spin $S = 1$ and orbital angular momentum $L = 1$.

- γ is the probability that a spin one meson ($J^P = 1^+$) is produced with a total quark spin $S = 1$ and orbital angular momentum $L = 1$.

- δ is the probability that a spin two meson ($J^P = 2^+$) is produced with a total quark spin $S = 1$ and orbital angular momentum $L = 1$.

- $\left(\frac{V}{V+P}\right)_{ud} = 0.5$ is the probability that a meson, containing u and d quarks only, has spin one.

- $\left(\frac{V}{V+P}\right)_{s} = 0.6$ is the probability that a strange meson has spin one.

- $\left(\frac{V}{V+P}\right)_{cb} = 0.75$ is the probability that a charm or bottom meson has spin one.

The standard Jetset 7.3 simulation includes only pseudoscalar and vector mesons, i.e. the parameters α, β, γ and δ are equal to zero, although these multiplets are implemented. It can be expected that the absence of higher multiplets, which implies a suppression of higher mass states, has an influence on particle correlations. To study this the parameters α, β, γ and δ in the Jetset 7.3 PS model have been chosen to reproduce the primary meson multiplicities of the Herwig 5.0 PS model. This four parameter fit has been performed with the routine VALLEY [50], where each function call generated 5000 Jetset 7.3 PS events according to the actual values of α, β, γ and δ. The χ^2 has been determined from the difference of meson rates in Herwig 5.0 PS and Jetset 7.3 PS. The fit results are: $\alpha = 0.026, \beta = 0.056, \gamma = 0.042$ and $\delta = 0.026$.

Figure 6.15d compares the modified Jetset 7.3 PS simulation to the Herwig 5.0 PS simulation and to the standard Jetset 7.3 PS simulation. Only a minor increase of the k^{-1} values is observed.

A further area of difference between Jetset 7.3 PS and Herwig 5.0 PS concerns the treatment of particle production and decay. Firstly, the masses of several resonances such as ρ, K^* etc. are generated in Jetset according to truncated Breit-Wigner distributions, while in Herwig these particles always acquire the same mass. Secondly, the decay tables and matrix elements used in Jetset are much more detailed compared to the Herwig realization. This case has been analysed by first switching the decay width off in Jetset and then by invoking the Jetset routines for particle decays in Herwig. No significant impact on the k^{-1} distribution was found.

6.4.2.2   Herwig cluster model

Two major reasons are responsible for the apparently different particle correlations in cluster and string models:

1. The *local* formation of clusters from neighbouring quarks and antiquarks preserves fluctuations occuring during parton shower evolution. The string model, by virtue of its underlying space-time structure smoothes these fluctuations.

2. The cluster mass spectrum resembles that of primordial resonances. In contrast to that only relatively light particles are produced in the string model[¶].

To illuminate this situation figure 6.17 shows the cluster mass spectrum obtained from Herwig 5.0 PS in comparison with the primary particle mass spectrum generated by Jetset 7.3 PS. The
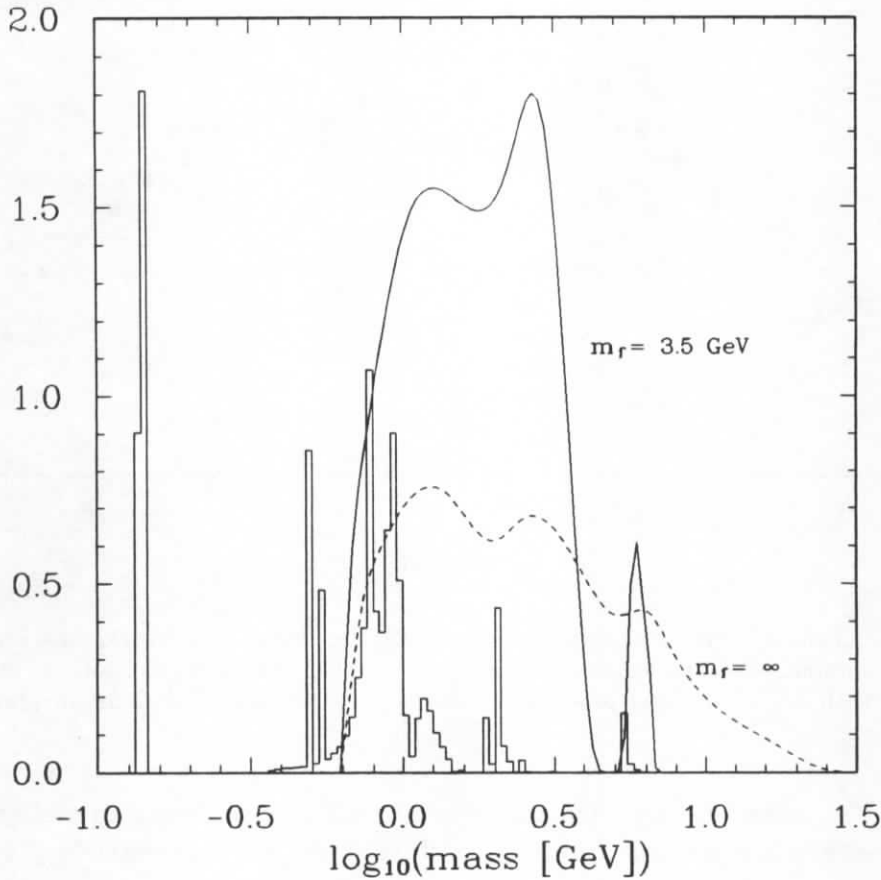
Figure 6.17: Cluster mass spectra from Herwig 5.0 PS (solid line $\mapsto M_f = 3.5$ GeV, dashed line $\mapsto M_f = \infty$ [scaled up by a factor of ten]) and primary particle mass spectrum from Jetset 7.3 PS (open histogram). The bumps in the cluster mass distribution are due to clusters containing charm or bottom quarks.

primary particle mass spectrum is shifted to lower values and moreover has a less developed tail to larger masses. The significance of heavy clusters to the overall particle correlations and fluctuations is revealed in the following study.

Cluster fission: The Herwig model invokes a "symmetrical string breaking" scheme to split a cluster C of mass M_C above the fission threshold $M_f = 3.5$ GeV into two clusters X and Y with masses $M_X^2 \approx M_Y^2 \approx Q_0 M_C$, where Q_0 is the string energy density (cf. section 2.2.3 on page 14 for a detailed description of the cluster model). At most a small fraction of clusters is involved (see figure 6.17) and therefore most event properties are not sensitive to details of the cluster fission model, the particle correlations being one exception.

If cluster fission is completely abandoned ($M_f = \infty$) the particle correlations are strongly enhanced and in fact much too large compared to the data. This effect is revealed in figure 6.18 and is clear evidence for a string-like nature of particle production in the colour field of $q\bar{q}$

[¶] This is not really a property of the model, rather it is due to our limited knowledge of higher resonances.
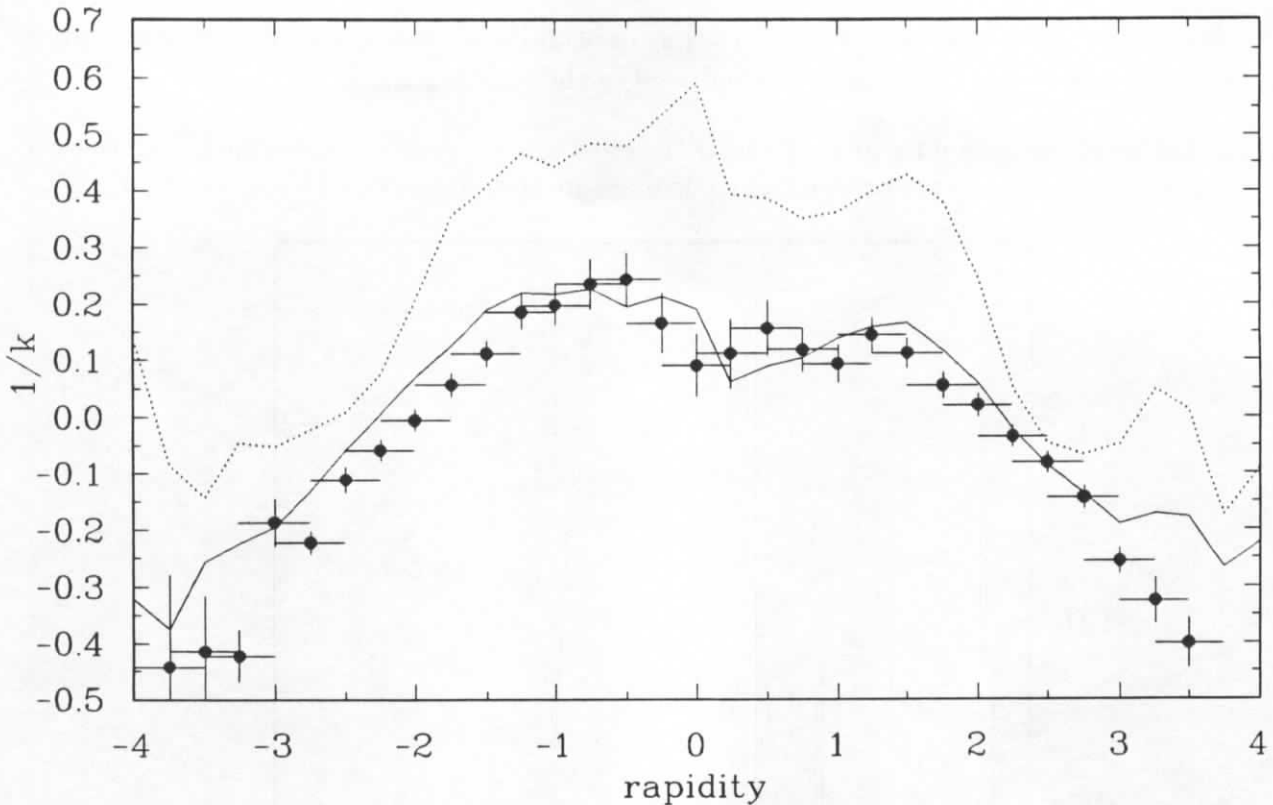
Figure 6.18: Studies of the k^{-1} rapidity dependence in the Herwig cluster model on two-jet events: the solid line shows the result obtained from the default Herwig 5.0 PS simulation with $M_f = 3.5$ GeV, the results from the modified version with $M_f = \infty$ are shown as the dotted line. The CELLO data are displayed with error bars for reference.

pairs created in e^+e^- annihilation. On the other hand a pure string model, as discussed on pages 71ff smoothes fluctuations from the perturbative phase of particle production too rigorously and thereby underestimates the correlations.

6.5   Outlook – e^+e^- annihilation at LEP

The storage ring LEP delivers a high rate of e^+e^- annihilation events at the Z^0 pole at 91 GeV centre of mass energy. The abundant pair production of colour triplet quarks (3) and antiquarks ($\bar{3}$) allows detailed analyses of the strong interactions.

It is generally believed that the perturbative QCD phase is more developed at LEP energies compared to the lower PETRA energies and therefore marked differences for multiplicity fluctuations can be expected. It is not clear a priori whether the differences between cluster and string fragmentation remain observable under these conditions. This question is answered in figure 6.19, where the rapidity dependence of the k^{-1} parameter in the models Jetset and Herwig is compared. If the total event sample is analysed, the two models give almost identical results. This is because gluon radiation is the main cause of fluctuations. Compared to the 35 GeV data in figure 6.12 the fluctuations appear stronger, indicated by larger k^{-1} values. And further, the rapidity range dominated by gluon radiation is enlarged, revealing the larger phase space available at higher energies. The analysis of two-jet events (selected according to the prescription in section 4.1.1 with $d_{join} = 5$ GeV) shows the same difference between cluster and string fragmentation that has been the topic of the preceding
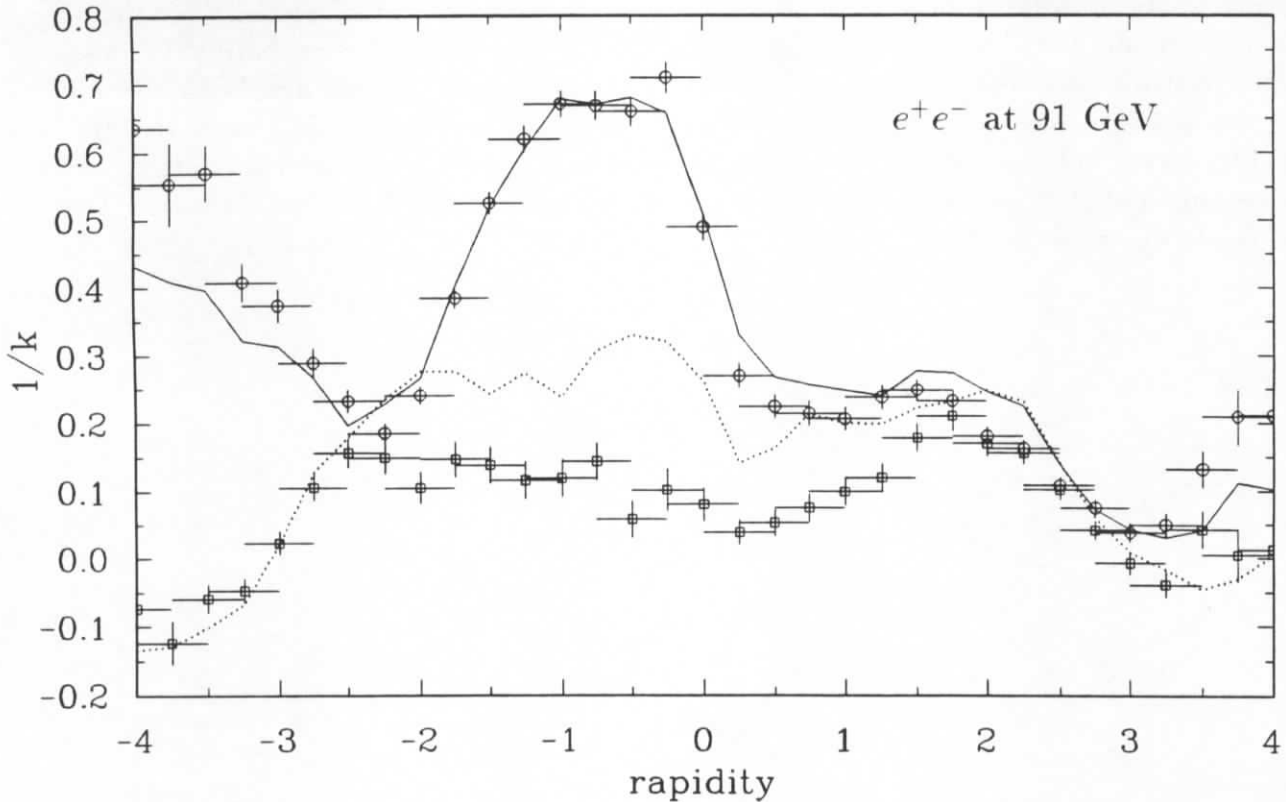
Figure 6.19: Rapidity scan at LEP energies: the total event sample is indicated by the open dots (Jetset) and the solid line (Herwig); the two-jet selection is represented by the open squares (Jetset) and the dotted line (Herwig).

sections. This opens the possibility to continue the study of this effect at LEP.

6.6 Summary on multiplicity distributions

The topic of the present chapter has been the occurrence and interpretation of particle correlations and fluctuations observed in longitudinal phase space. To study this case the multiplicity distributions in central rapidity bins of varying size have been analysed and compared to Monte Carlo simulations. To facilitate these differential analyses the (negative) binomial distribution has been used to condense the information contained in the multiplicity distribution into two numbers: in particular the k^{-1} parameter turned out to be a sensitive measure of correlations and fluctuations. The observed dependence of the correlation strength on the rapidity bin size was found to be genuinely due to a dependence on the rapidity position, as has been made clear by the rapidity scan.

An important result has been that correlations observed in the total event sample are to a large extent caused by the occasional appearance of hard gluons.

The analysis of two-jet events revealed a significant difference between cluster and string models, where the former are favoured by the experimental data. In particular properties of longitudinal and transverse fragmentation have been analysed and modified to improve the performance of the string model. Although an improvement has been obtained it is not sufficient to remove the discrepancy between experimental data and model. From this study it is concluded that pure string fragmentation smoothes the effect of soft gluon radiation

too much. In addition it has been noted that the mass spectrum of primary particles in the string model is too soft and should be modified to reproduce the primordial resonance mass spectrum, as is the case in the cluster model. A problem occurs here with the Lund symmetric fragmentation function, which tends to order heavy particles more strictly in rapidity. Nevertheless, evidence for a string-like nature of particle production is provided by the requirement of string-like fission of heavy clusters, without which the cluster model would also fail to describe the data.

Chapter 7

Intermittency – theory and experiment

In this chapter theoretical and experimental aspects of intermittency analyses are discussed. The term *intermittency* originally names the temporal and spatial fluctuations in turbulent fluids [82] and has been introduced into high energy physics by Białas and Peschanski [75]. The intermittent behaviour of a system reveals itself as factorial moments growing as a power with the decreasing size of the analysed phase space domain δ:

$$\langle F \rangle \propto \left(\frac{1}{\delta} \right)^{\varphi_q} .$$

(7.1)

The existence of such a power law could eventually be interpreted as the manifestation of a self-similar and fractal process. It will become clear in the course of this investigation that this relation is not always straightforward, and therefore the term intermittency is solely used to name the factorial moment analysis and not to express a particular interpretation.

The present study of factorial moments of multiplicity distributions has the analysis of particle correlations and fluctuations in common with the investigations presented in chapters 6 and 9. In addition, factorial moments facilitate the analysis of *higher order* correlations and allow an analysis even in three-dimensional phase space. Moreover the observed behaviour can be attributed to a *fractal dimension* of the multihadronic final state – an intuitive description which eases the understanding of the results.

In the following sections an introduction to the factorial moment method is given. The corresponding analyses are presented in chapter 8. Part of this work is already published [53–55] and was presented at conferences [60–63].

7.1 Factorial moments

The topic of the present chapter is intermittency in one- and two-dimensional projections of phase space and in the three-dimensional phase space itself. The *topological dimension* of the phase space projection under consideration is denoted by D_T. This study consists of an investigation of the resolution dependence of factorial moments and its origin. For this the original phase space is successively, and simultaneously in each dimension, divided into halves, yielding one-dimensional bins for $D_T = 1$, two-dimensional planes for $D_T = 2$ and three-dimensional boxes for $D_T = 3$. The resulting total number of D_T-dimensional phase

space cells m obtained after B bisections in each dimension is given by the following relation:

$$\text{Total number of phase space cells:} \quad m = 2^{D_T \cdot B} \, . \tag{7.2}$$

The normalized factorial moments of rank q are then defined by the following formulae [76]:

$$\langle F_m^q \rangle^h = \frac{1}{m} \sum_{k=1}^{m} \frac{\langle n_k(n_k - 1) \cdots (n_k - q + 1) \rangle}{\langle n \rangle^q} \, , \tag{7.3}$$

$$\langle F_m^q \rangle^v = \frac{1}{m} \sum_{k=1}^{m} \frac{\langle n_k(n_k - 1) \cdots (n_k - q + 1) \rangle}{\langle n_k \rangle^q} \, . \tag{7.4}$$

Two averages are implied in the above definitions: the average over m phase space cells (these might be one-, two- or three-dimensional, depending on D_T) and the average over all events, as indicated by the square brackets. The two above definitions differ in the normalization:

- Equation 7.3 defines the so-called *horizontal* average, where the normalization is done according to the overall average number per bin $\langle n \rangle = \sum_{k=1}^{m} \langle n_k \rangle / m$. Due to this *global* normalization horizontal moments are sensitive to the shape of the inclusive distribution. This implies a rise of the factorial moments up to the scale where the particle density is almost constant over one bin, after that genuine particle correlations become visible.

- Equation 7.4 defines the *vertical* average, where the normalization is done according to the *local* average $\langle n_k \rangle$. Owing to this definition vertical moments are sensitive only to fluctuations within each bin, but not to the overall shape of the inclusive distribution.

The original meaning of intermittency in the sense of Białas and Peschanski as a power law growth (7.1) is only revealed in case of constant inclusive distributions [75]. This reflects a basic intention behind intermittency analyses, namely the main emphasis to particle fluctuations inside *individual* events in contrast to fluctuations of the event *ensemble*. Since a constant inclusive distribution is hardly ever found in nature and in particular $e^+ e^-$ annihilation is characterized by *jet* production, which signals a strong reduction of the transverse phase space, several procedures have been proposed to unfold variations of the event ensemble from the factorial moment analysis. The local normalization implied by (7.4) is a first example; here the weighting according to the average bin population compensates the variation of the inclusive distribution. More sophisticated methods are presented in the following section.

7.2 Variable transformations

It is clearly visible in figures 5.3 and 5.2 that the inclusive distributions observed experimentally are not constant. Their variations would modify the factorial moments at the corresponding resolution scales and therefore fake intermittent behaviour, even in case of complete absence of genuine particle correlations. However, it is possible to unfold these variations from the factorial moments by appropriate variable transformations, as will be explained in the following.

7.2.1   Ochs method

The method proposed by Ochs is intended for use in three-dimensional intermittency analyses [77], where in particular the $p_\perp^2$ distribution shows strong variations. The procedure consists of a variable transformation $x \to \tilde{x}$, such that the distribution $\rho(\tilde{x})$ is constant. This is achieved by the transformation:

$$\tilde{x}(x) = \frac{\int_{x_{min}}^{x} \rho(x')dx'}{\int_{x_{min}}^{x^{max}} \rho(x')dx'} \; , \tag{7.5}$$

where $\rho(x)$ are the inclusive density functions and x is any phase space variable, like y, ϕ or $p_\perp^2$. x_{min} and x_{max} are the lower and upper phase space limits of the variable x. The transformed distribution $\rho(\tilde{x})$ is uniform in the range from zero to one. This transformation is intended to adjust the binsize in such a way that, on average, each bin contains the same number of particles. In figure 7.1 the transformation functions for $y \to \tilde{y}$, $\phi \to \tilde{\phi}$ and $l \to \tilde{l}$
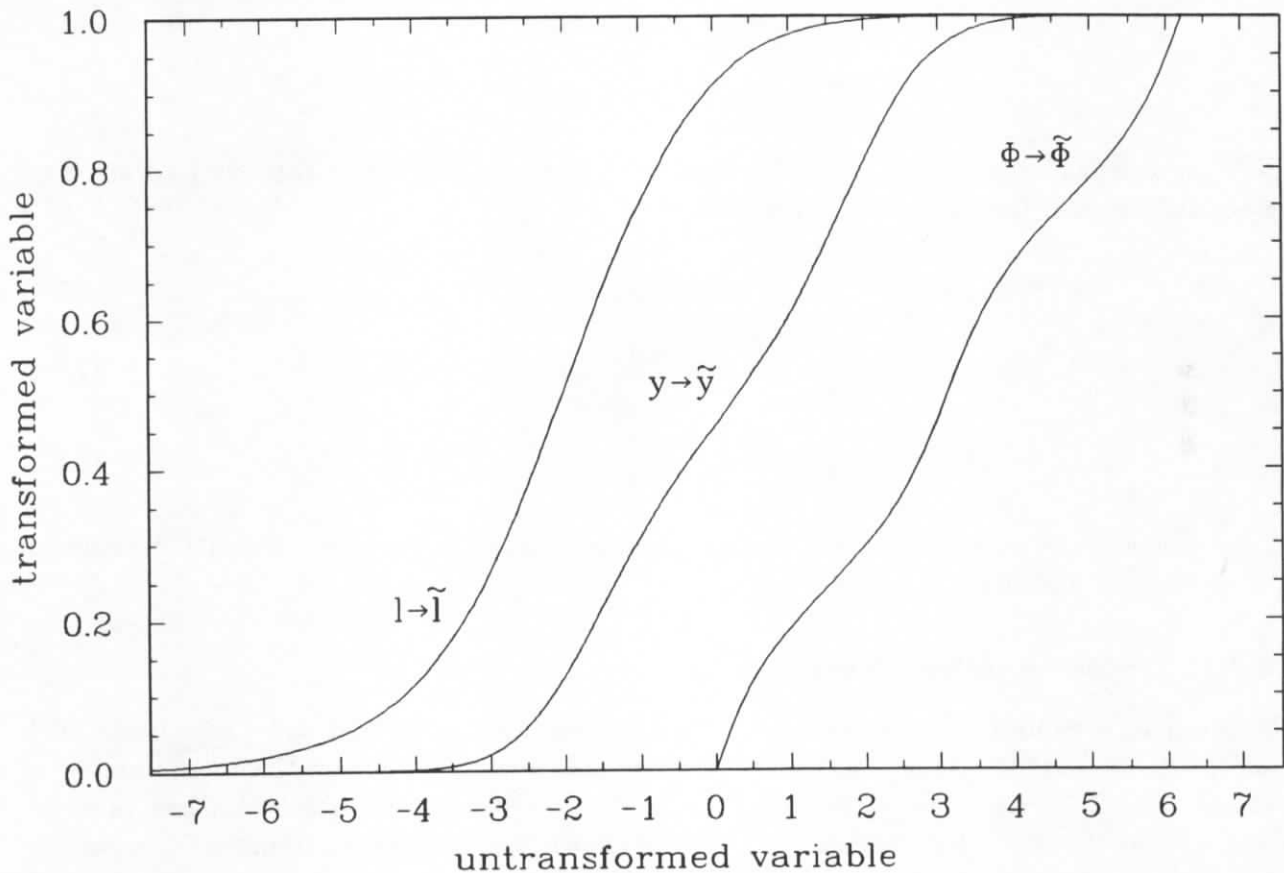
Figure 7.1: Cumulative distributions (CELLO data) of y, ϕ and $\log(p_\perp^2)$ for the variable transformation according to Ochs.

are shown; $l \stackrel{\text{def}}{=} \log(p_\perp^2)$ has been used to reduce the rapid variation of the $p_\perp^2$ distribution and hence to facilitate the numerical treatment. In case of constant inclusive distributions the transformation functions would be straight lines.

The Ochs method is applicable in any dimension, but it has the disadvantage that each linear phase space projection is treated independently and therefore correlations between different variables are neglected – an approximation which is not always sufficient as is demonstrated in figure 7.2. In the ideal case of uncorrelated variables the particle density in the

transformed space would be constant, i.e. every box would contain the same number of particles. This is apparently not the case, since a clearly non-constant particle density is observed after the transformation. The high quality of the Monte Carlo simulation is also visible in figure 7.2, which is seen to reproduce the phase space population extremely well, implying a correct simulation of correlations between the phase space variables.

7.2.2 Białas & Gazdzicki method

A generalization of the previous transformation has been proposed by Białas and Gazdzicki [79]. Their treatment takes the correlations between different variables into account. In the three-dimensional case the method is based on the following integral equations:

$$P(x,y,z) = \frac{\rho(x,y,z)}{\int \rho(x',y',z')dx'dy'dz'} , \qquad (7.6)$$

$$P(x,y) = \int P(x,y,z')dz' , \qquad (7.7)$$

$$P(x) = \int P(x,y')dy' , \qquad (7.8)$$

where the integrals run over the full phase space. The transformed variables $\tilde{x}$, $\tilde{y}$, $\tilde{z}$ are then defined in terms of the probability densities P (7.6−7.8):

$$\tilde{x}(x,y,z) = \int_{x_{min}}^{x} P(x')dx' , \qquad (7.9)$$

$$\tilde{y}(x,y,z) = \int_{y_{min}}^{y} \frac{P(x,y')dy'}{P(x)} = \int_{y_{min}}^{y} P(\tilde{x},y')dy' , \qquad (7.10)$$

$$\tilde{z}(x,y,z) = \int_{z_{min}}^{z} \frac{P(x,y,z')dz'}{P(x,y)} = \int_{z_{min}}^{z} P(\tilde{x},\tilde{y},z')dz' . \qquad (7.11)$$

Since the computational realization of this transformation is non-trivial a short description of the invented algorithm is given here.

7.2.2.1 Transformation algorithm

The problem is to find a decomposition of the three-dimensional phase space into boxes with equal particle content. After e.g. $B = 6$ bisections in every dimension the total number of boxes is $m = 2^{18} = 262,144$. Given six coordinates to define the position of a box in phase space, a total of $\approx 1.57 \cdot 10^6$ coordinates must be known to enable the assignment of a particle to its box. Once these coordinates are defined, the actual assignment requires us to compare three particle coordinates with six coordinates of 262,144 boxes!

The idea to solve this problem is as follows: the information needed to perform a three-dimensional intermittency analysis consists of three phase space variables, e.g. $y, \phi, p_\perp^2$ and the event number for all particles. This data is stored in arrays and is kept in the main memory of the computer. In the first step the y array is ranked in ascending order, providing an index array which is used to trace the remaining variables ($\phi, p_\perp^2$ and the event number) to the elements in the ranked y sequence. Then the y array is divided into the desired number of sub-arrays containing equal numbers of particles. Since particle numbers are integer valued this division is not always possible. Actually N particles are distributed over m boxes as $N = m_1 n + m_2(n-1)$, with $m = m_1 + m_2$. Particles belonging to the same y sub-array
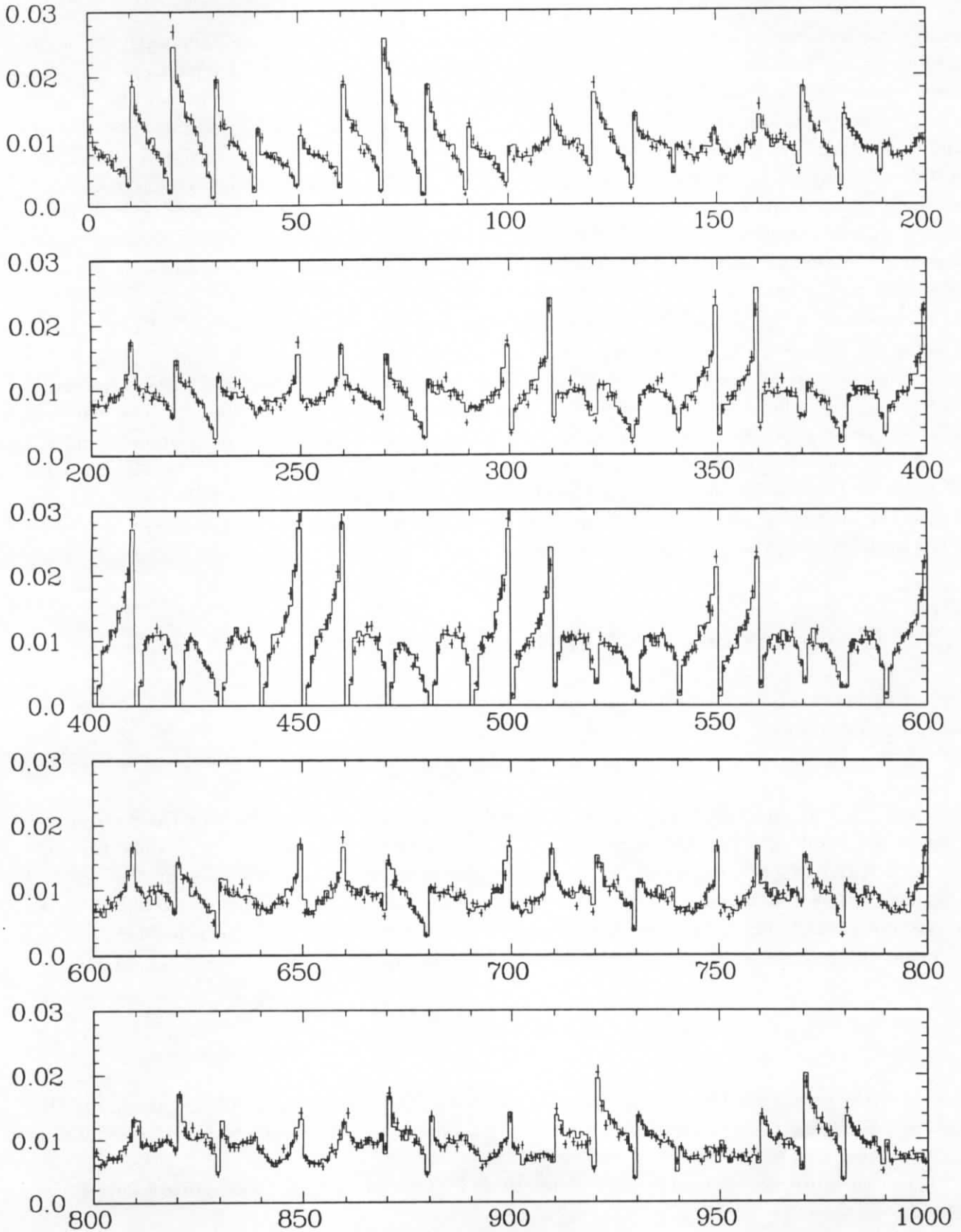
Figure 7.2: Particle density after the Ochs transformation for ten bins in each dimension. The resulting thousand boxes are labeled $100 \times I(\bar{y}) + 10 \times I(\bar{\phi}) + I(\bar{l})$: $I = 0, \ldots, 9$. CELLO data (statistical errors indicated) are compared to the Jetset 7.2 PS simulation (histogram).

are given a common index, replacing the old y values. This index, together with the event number, is later on used to determine the phase space boxes occupied by particles from the same event. In the second step, *for every y sub-array separately*, the corresponding ϕ array is ranked in ascending order, again using an index array to trace the remaining variables ($p_\perp^2$ and event number) to the ranked ϕ sequence. As before the desired division is made and particles belonging to the same ϕ sub-array are assigned a common index, replacing the old ϕ values. In the third step, *for every ϕ sub-array separately*, the corresponding $p_\perp^2$ array is ranked in ascending order. The index array is now used to trace the event number to the ranked $p_\perp^2$ sequence and the desired division is made, replacing the $p_\perp^2$ values of particles belonging to the same $p_\perp^2$ sub-array by a common index.

At the end of the procedure the position of each particle in the transformed phase space is defined by three indices, labeling the phase space box and by its event number. In the final step the entries are sorted according to the event number. This information is readily transformed into factorial moments. The complete procedure for 500,000 particles with six different phase space decompositions, including the calculation of factorial moments and the covariance matrix requires one minute of computer time (including I/O) on the DESY IBM ES 9000/720 vector facility. This fast performance made possible the detailed analyses and Monte Carlo studies presented in chapter 8. For illustration figure 7.3 visualizes a few steps of the algorithm in the two-dimensional case.

7.3   Covariances and statistical errors

The covariances V_{lm}^q between factorial moments F_m^q and F_l^q of the same rank q are defined by the following matrix:

$$V_{lm}^q = \langle F_l^q F_m^q \rangle - \langle F_l^q \rangle \langle F_m^q \rangle \, , \tag{7.12}$$

and the F_m^q are given by (7.3) and (7.4). In case of the horizontal normalization the covariances must be determined after the average over bins has been carried out, since only the bin-averaged moments are expected to have a common mean value. In case of the vertical normalization a mathematical equivalent procedure would be to consider each bin as an individual measurement, but also here the bin-averaged moments have been used.

From the covariance matrix (7.12) the error on the mean value $\langle F_m^q \rangle$ is obtained as:

$$\text{Error on mean value:} \qquad \frac{1}{\sqrt{N_{event}}} \sqrt{V_{mm}^q} \, . \tag{7.13}$$

These are the errors used in the forthcoming analyses. The complete covariance matrix is also used to propagate the errors from the factorial moment measurement to the corresponding fractal dimension, as discussed in section 7.4.

The covariance matrix is of interest in itself: at first it can be transformed into a correlation matrix:

$$C_{lm}^q = \frac{V_{lm}^q}{\sqrt{V_{ll}^q V_{mm}^q}} \, , \tag{7.14}$$

which reveals the *information* inherent in the factorial moments. And second its inverse $(V_{lm}^q)^{-1}$ is predicted to be tridiagonal in the α-model [80].
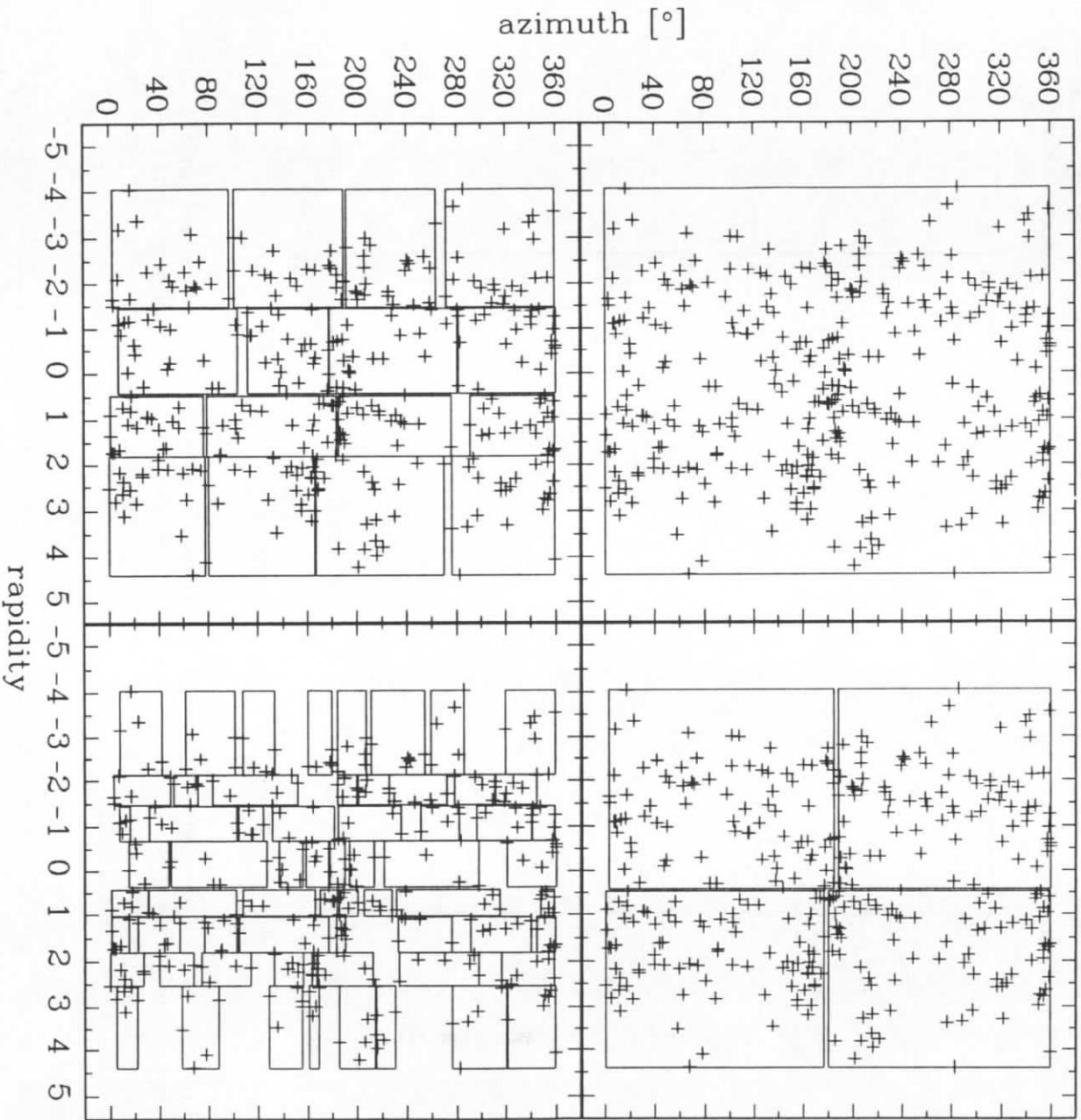
Figure 7.3: Graphical representation of the Bialas and Gazdzicki transformation algorithm in the two-dimensional case: y, ϕ coordinates from 331 particles of forty events are indicated by the crosses. The subdivision into boxes of equal particle content is shown for $B = 0, \ldots, 3$.

7.3.1   Test of statistical errors

To test the validity of (7.13) fifty CELLO type experiments (20,000 events each) have been simulated with Jetset 7.2 PS. The factorial moments $\langle F_m^q \rangle$ from a one-dimensional rapidity analysis in the range $-2 \leq y \leq +2$ have been calculated for each individual experiment. This yields, for every rank q and every bin division m a distribution with fifty entries. The r.m.s. width of these distributions gives an estimate for the "true" standard deviation. In
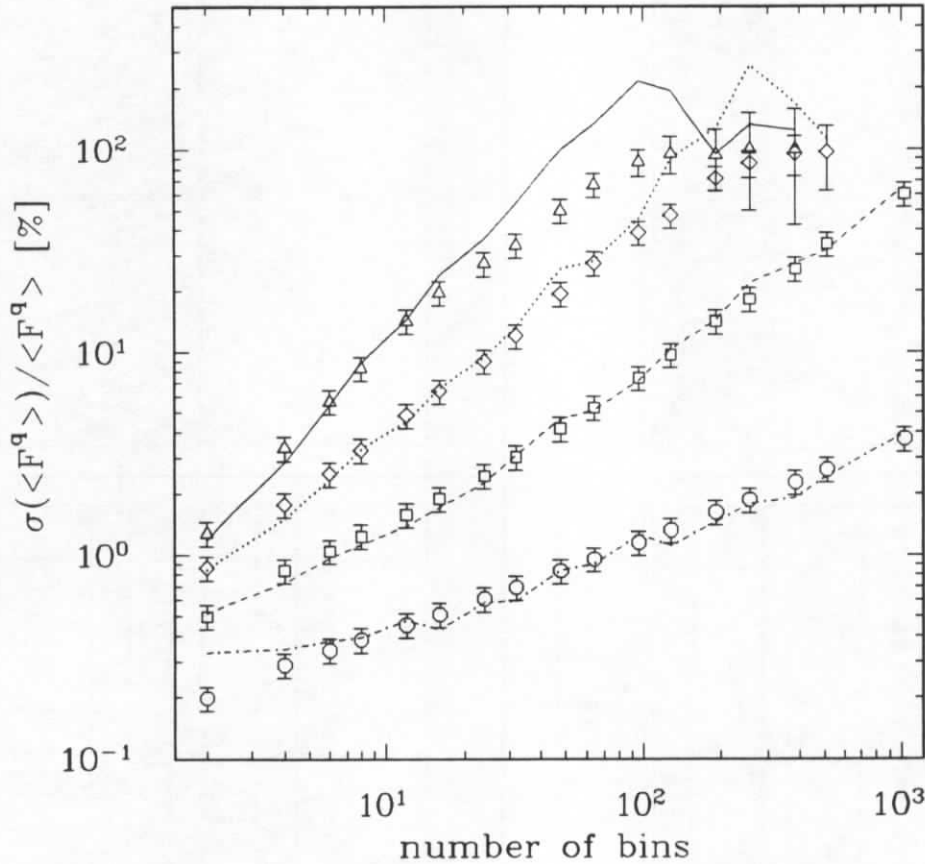
Figure 7.4: Test of error estimate: the per cent errors from the covariance matrix, averaged over fifty experiments, are shown as the open symbols. The "true" errors, obtained as the r.m.s. width from fifty experiments, are shown as the lines ($F^2 \mapsto$ circles and dash-dotted line, $F^3 \mapsto$ squares and dashed line, $F^4 \mapsto$ diamonds and dotted line, $F^5 \mapsto$ triangles and solid line).

figure 7.4 the "true" per cent error on $\langle F_m^q \rangle$ is presented as a function of the number of bins m and compared to the average per cent error derived from the covariance matrix. It is found that the factorial moments from different experiments follow a Gaussian distribution with a standard deviation given by (7.13) for $q = 2, 3$ and for modest values of m in the case of higher ranks. For very large m values and high ranks q the factorial moments show an exponential distribution due to many experiments with zero contribution to the mean value. In this case (7.12) is no longer a robust error estimate; i.e. it underestimates the errors. It is found that the error estimate given by (7.12) is reliable, provided at least ten events from a single experiment contribute to the mean value $\langle F_m^q \rangle$. This criterion applies to all results presented in chapter 8.

7.4 Fractal dimensions

The *local* intermittency exponents φ^q are related to the factorial moments by the following derivative:

$$\varphi^q = \frac{\partial \ln \langle F_m^q \rangle}{\partial \ln m} \,, \tag{7.15}$$

i.e. they correspond to the slopes in a double logarithmic plot of $\ln \langle F_m^q \rangle$ versus $\ln m$. In this context the term local is used to express the m dependence of φ^q.

The theory of fractals [81,82] allows these local intermittency exponents to be interpreted as a *fractal dimension* of the object under study via the linear relation:

$$D_F^q = D_T \left(1 - \frac{\varphi^q}{q-1} \right) \,. \tag{7.16}$$

In general D_F^q may depend on the rank q, in this case the object under study is a multifractal.

A simple example may explain the relation between factorial moments and fractal dimensions: Assume that N particles are randomly distributed in a D_T-dimensional phase space consisting of m cells. Then the particle content of every phase space cell k follows a Poissonian distribution with $\langle n_k \rangle = N/m$, and the $\langle F_m^q \rangle$ calculated according to (7.3) and (7.4) are observed to be independent of m. Consequently the derivatives (7.15) vanish and $D_F^q = D_T$ for all ranks q. Now consider the other extreme case, that all N particles of an event are placed in one singular point, then the sum in (7.4) and (7.3) is constant for any given m and $\langle F_m^q \rangle$ is given by the factor $m^{(q-1)}$, consequently $\varphi^q = q - 1$. Inspecting (7.16) gives $D_F^q = 0$ for all ranks q, which coincides with the intuitive expectation for a point-like object. This example can be generalized to distributions which are phase space like in D_F^q dimensions and singular in $D_T - D_F^q$ dimensions. The factorial moments $\langle F_m^q \rangle$ of such distributions can be shown to exhibit a power law behaviour with slope:

$$\varphi^q = \left(1 - \frac{D_F^q}{D_T} \right) (q - 1) \,. \tag{7.17}$$

Solving this equation for D_F^q leads to the definition of fractal dimensions (7.16).

Chapter 8

Intermittency analyses

The topic of this chapter is intermittency analyses according to various methods which are summarized in table 8.1. These analyses cover different aspects of multiparticle production, depending on the studied variables and their dimensionality. The numerical results are presented in tabular form in the appendices A–C.

Transformation:		None		Ochs		Białas
Normalization:		vertical	horizontal	vertical	horizontal	horizontal
$D_T = 1$	y	+	+	+	+	+
$D_T = 2$	y, ϕ	+	+	+	+	+
$D_T = 3$	$y, \phi, p_\perp^2$	−	−	−	+	+
$D_T = 3$	$p_x/E^{\frac{1}{3}}, p_y/E^{\frac{1}{3}}, p_z/E^{\frac{1}{3}}$	−	+	−	−	+

Table 8.1: Survey of intermittency analyses.

The factorial moments in high energy multiparticle production have a complex structure. This means on the one hand that the interpretation is not straightforward; on the other hand, it opens the possibility to study subtle details of the hadronization process. The strategy of this analysis is to isolate individual effects, if possible directly from the data, or by means of Monte Carlo simulations. This procedure proved very powerful in relating the experimental observations to known physical processes.

In this thesis I will not follow the cumbersome historical evolution of intermittency analyses but rather present the current state of the art. The comparison with results from processes, other than e^+e^- annihilation, is beyond the scope of this work; the interested reader may consult review articles [52]. Intermittency studies from TASSO at PETRA and experiments at LEP can be found in [56,57–59].

This chapter is divided into five sections; the following sections 8.1 and 8.2 are dedicated to one- and higher-dimensional analyses, using cylindrical coordinates defined by the annihilation event. Section 8.3 presents further aspects of intermittency analyses. In section 8.4 a three-dimensional analysis in cartesian coordinates is presented. Finally the results are summarized in section 8.5.

8.1 One-dimensional analysis

The first intermittency analyses were in every case one-dimensional, until the importance of the phase space dimension was noted [78].

8.1.1 Full rapidity range

At first the full rapidity interval from -5 to $+5$ is considered for analysis, over which the inclusive distribution varies strongly (figure 5.3). This situation is ideal to study the effect of a varying inclusive distribution on the factorial moments, and it further emphasizes the effect of the different normalizations implied by (7.3) and (7.4), as well as demonstrating the effect caused by a variable transformation.

8.1.1.1 Horizontal normalization
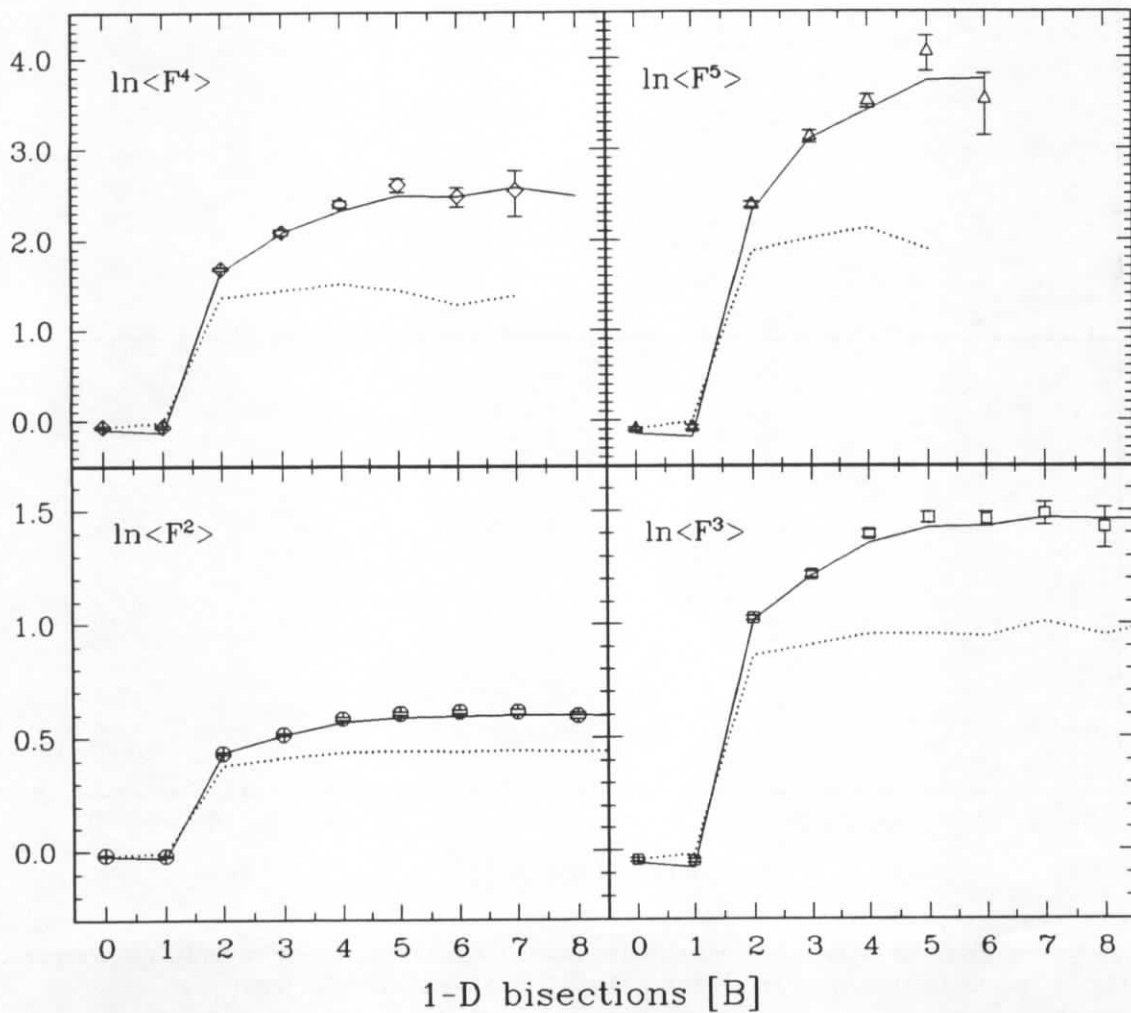
Figure 8.1: Horizontal factorial moments in full rapidity space: CELLO data (open symbols) are compared to the CELLO "toy" model (dotted lines) and to the Jetset 7.2 PS simulation (solid lines).

Figure 8.1 compares the horizontal moments $\langle F^q \rangle^h$ calculated from CELLO data to the corresponding results from the CELLO "toy" model (see section 5.4 on page 53 for a description

of the model). This comparison makes it apparent that the fast initial rise of the factorial moments is entirely due to the variation of the inclusive distribution.

At $B \geq 2$ ($\delta y \leq 2.5$) the onset of genuine particle correlations is signified by almost constant moments in the "toy" model, in contrast to the rising moments observed in real experiment. This extends up to $B = 4$ ($\delta y \approx 0.5$), after which a saturation of the moments is observed both in the data and in the "toy" model.

Figure 8.1 displays also the results obtained from the Jetset 7.2 PS simulation, which are seen to be in good agreement with the data.

8.1.1.2   Vertical normalization
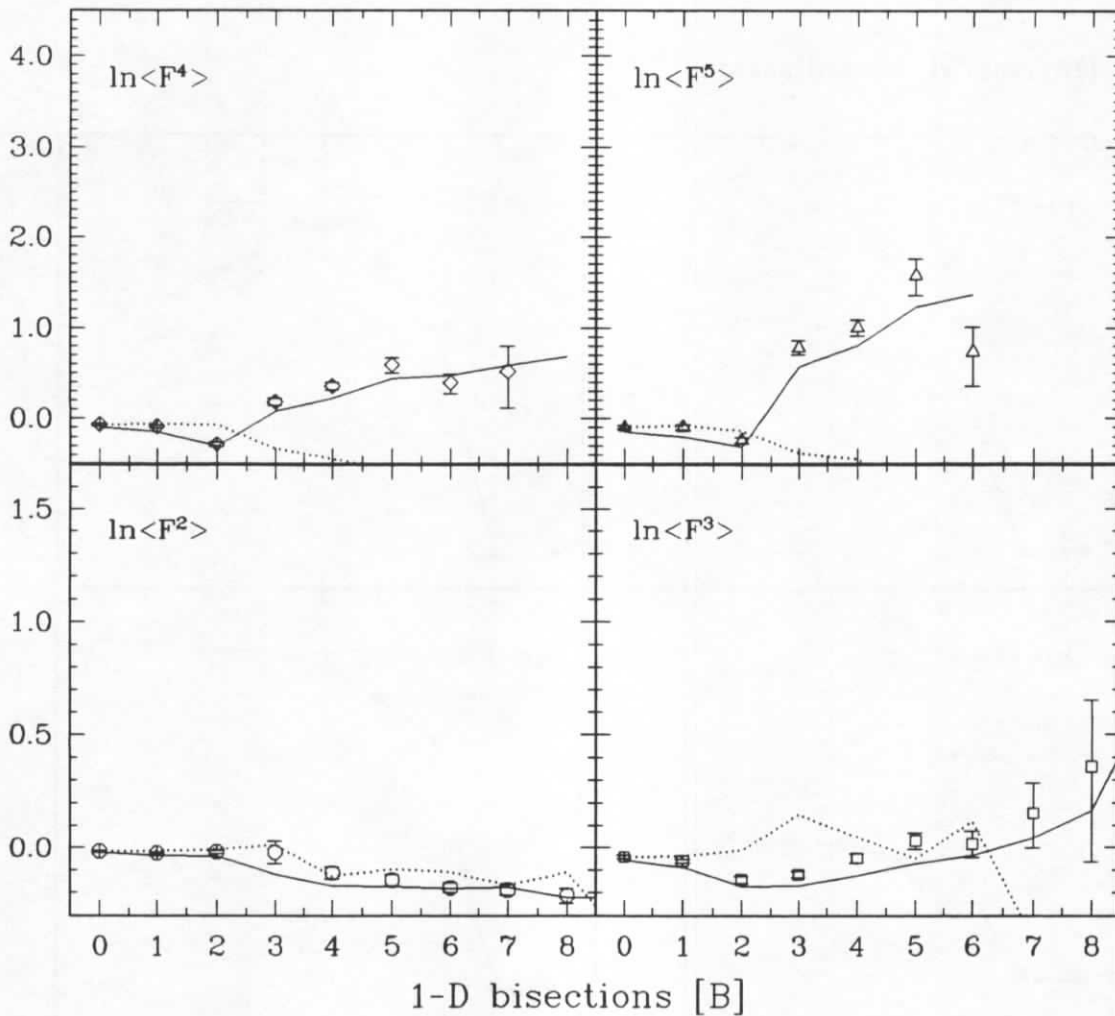
Figure 8.2: Vertical factorial moments in full rapidity space: CELLO data (open symbols) are compared to the CELLO "toy" model (dotted lines) and to the Jetset 7.2 PS simulation (solid lines).

The vertical moments $\langle F^q \rangle^v$ are seen to behave completely differently in figure 8.2. In this case the local normalization (7.4) gives large weights to phase space regions of low particle density, and thereby amplifies this contribution to the bin-averaged moments.

From the analysis of multiplicity distributions in chapter 6 it has become clear that fluctuations in the low density region $|y| \geq 2$ are binomial. This translates, by virtue of

the local normalization, into almost constant factorial moments $\langle F^2 \rangle$ and $\langle F^3 \rangle$. In fact, from the slight decrease of $\langle F^2 \rangle$ it is seen that fluctuations are really smaller than Poissonian.

For higher ranks ($q = 4, 5$) the contribution from the rapidity region $|y| \geq 2$ is drastically reduced, at least in real data, leading to rising factorial moments. This is because factorial moments of rank q receive contributions from those bins only, which contain at least q particles. It is simply energy-momentum conservation whichs makes it impossible to find four or five particles in the rapidity region $|y| > 2$. Fluctuations in the "toy" model are Poissonian by construction, with additional constraints imposed to reproduce the total multiplicity and the inclusive distribution. This leads to the observed constancy or even decrease of the factorial moments.

8.1.1.3 Variable transformation
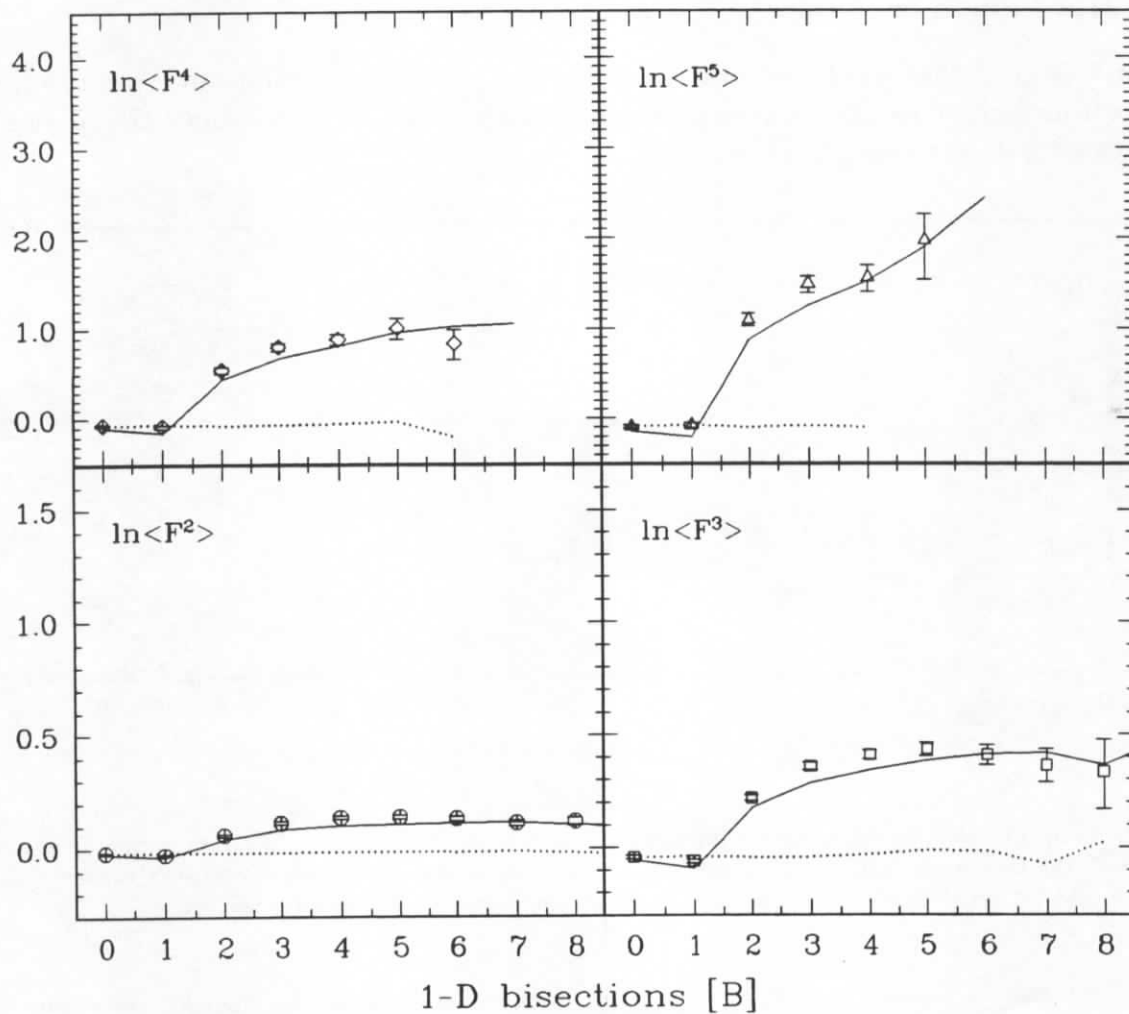
Figure 8.3: Transformed factorial moments in full rapidity space: CELLO data (open symbols) are compared to the CELLO "toy" model (dotted lines) and to the Jetset 7.2 PS simulation (solid lines).

In the case of a one-dimensional analysis the transformation procedures of Ochs and Białas & Gazdzicki, discussed in section 7.2 are identical. Since their computational realization is completely different the one-dimensional analysis serves as a consistency check. Inspecting the tables in appendix A it is seen that both procedures give in fact the same results. Furthermore,

it is noted that the horizontal and vertical normalization in case of the Ochs method yield identical results. This is, of course, as expected since the inclusive distribution is constant after the variable transformation.

In figure 8.3 CELLO data are once more compared to the "toy" model, which shows only Poissonian density fluctuations, indicated by constant factorial moments after the variable transformation. The description provided by the Jetset 7.2 PS simulation is satisfactory, although the model slightly underestimates the data. It is demonstrated in the following section that the description can be considerably improved if Bose-Einstein correlations are included in the Monte Carlo simulation. The significance of the Bose-Einstein effect for fluctuations in the Jetset model has already been noted in the analysis of multiplicity distributions in chapter 6.

8.1.1.4 Hard gluon radiation

It is intuitively clear that hard gluon radiation induces strong fluctuations in rapidity space. Fragments from a gluon radiated under an angle ϑ off a primary quark populate the (pseudo)-rapidity region $\eta = -\ln[\tan(\vartheta/2)]$.
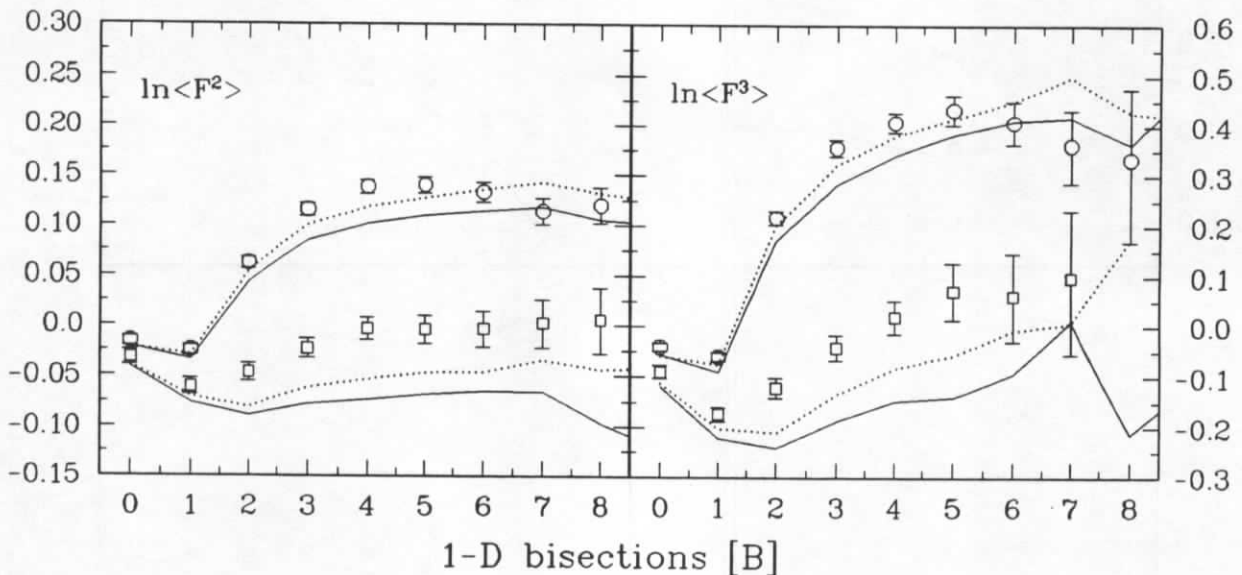
Figure 8.4: Transformed factorial moments for two-jet events compared to the entire data sample in the full rapidity range: the total event sample (open circles) is compared to the two-jet selection (open squares). The Jetset 7.2 PS and 7.2 PS+BE simulations are indicated by the solid and dotted lines respectively.

This effect can be isolated directly from the data by means of the two-jet selection described in section 4.1.1 on page 31. A marked difference is observed in figure 8.4, where the transformed factorial moments from two-jet events are compared to the entire data sample. The initial rise of the factorial moments up to resolution scales of $\delta y \approx 0.5$, exhibited by the total event sample, is considerably reduced in two-jet events.

Another important observation is the apparent failure of the Jetset model in describing the two-jet data. Since this discrepancy becomes visible after effects from hard gluon radiation have been removed, it reveals its non-perturbative origin. This effect has been studied in detail in chapter 6 and is further examined in the following section.

8.1.1.5 Multiplicity dependence

Following a suggestion of Ochs the multiplicity dependence of factorial moments has been studied [68,70]. The idea is that an inadequate treatment of the hadronization process should be emphasized in events of low multiplicity. In particular, it is conjectured under the assumption of local parton hadron duality, that string models should underestimate particle correlations due to their energy dissipating mechanism.
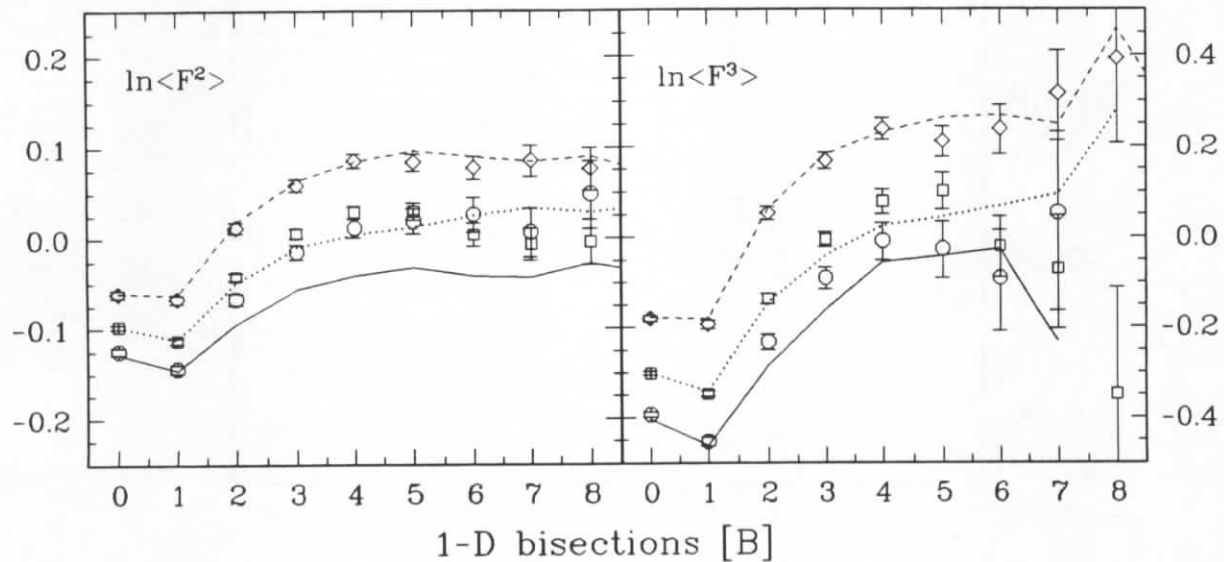
Figure 8.5: Multiplicity dependence of factorial moments in the full rapidity range. The open symbols represent the CELLO data, while the curves show the Jetset 7.2 PS+BE simulation: $\langle N \rangle = 6.8 \mapsto$ open circles and solid lines: $\langle N \rangle = 9.9 \mapsto$ open squares and dotted lines: $\langle N \rangle = 13.5 \mapsto$ open diamonds and dashed lines.

To test this idea the total event sample is split in three sub-samples of mean multiplicities $\langle N \rangle = 6.8$, 9.9 and 13.5, containing approximately the same number of events. The transformed factorial moments from a one-dimensional analysis in the full rapidity range are presented in figure 8.5 and compared to the Jetset 7.2 PS+BE simulation. Apparently the higher multiplicity events are very well described, while a significant failure is observed for very low multiplicity events. This observation supports the results from the factorial moment analysis of two-jet events and is in full agreement with the study of multiplicity distributions in chapter 6.

It is expected that residual τ pair events preferentially appear in the lowest multiplicity sub-sample ($\langle N \rangle = 6.8$). Since these events are not included in the Monte Carlo simulation, it might be asked what their contribution to the factorial moments is. To reject any such events it is required that at least one event hemisphere (defined by the sphericity tensor) must contain a minimum of five charged particles. It is virtually impossible that a τ pair event passes this condition. The factorial moment analysis is then repeated, and it is found that the discrepancy between the CELLO data and the Jetset model remains, although at a reduced level, which can be attributed to the increased mean multiplicity implied by the additional selection criterion. From this it is concluded that the observed discrepancy is a real effect. This observation is further supported by DELPHI and OPAL at LEP [57,58].

The comparison of cluster and string-based fragmentation models in figure 8.6 reveals a marked difference between the two approaches. The general trend is that cluster models show larger correlations than string models due to the local hadronization mechanism in the
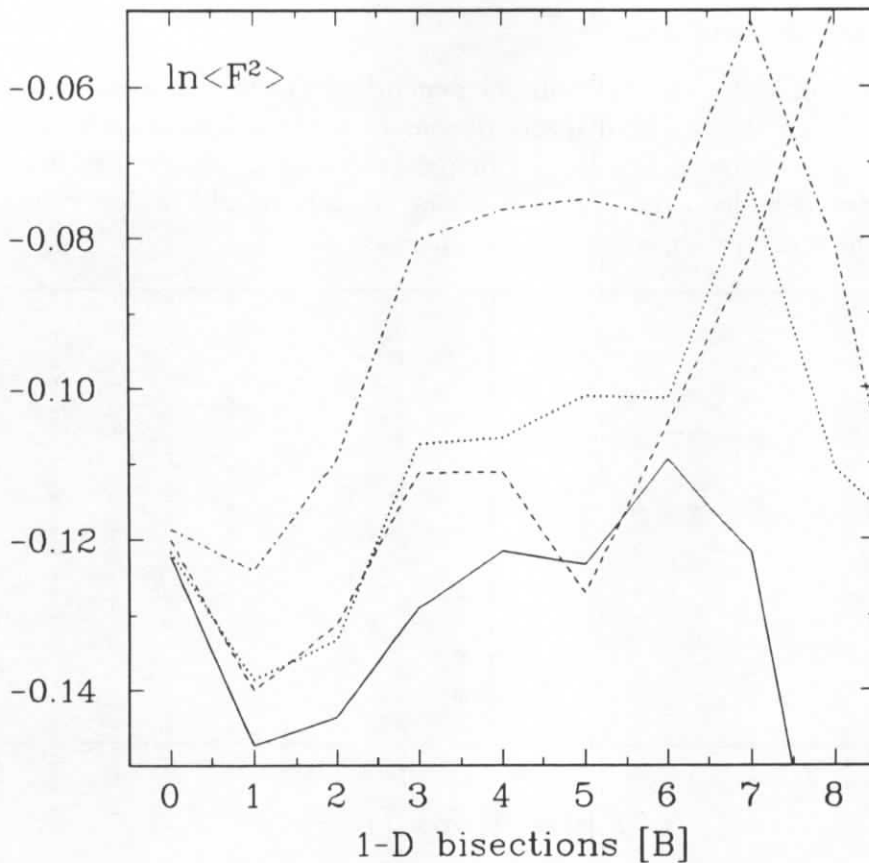
Figure 8.6: Comparison of low multiplicity events ($N = 2-8$) in cluster and string models in a one-dimensional y analysis of $\langle F^2 \rangle$: Jetset 7.3 PS (solid line), Jetset 7.3 ME (dotted line), Ariadne 3.1 CD (dashed line) and Herwig 5.0 PS (dash-dotted line).

former. If this figure is compared to the experimental data (figure 8.5) it can be concluded that the cluster model provides an adequate description of particle correlations in rapidity space, in line with the results obtained in section 6.4. The strong ordering in rapidity space occurring in the Lund string model smoothes particle fluctuations, which is apparently not supported by the data. The Bose-Einstein effect partly removes this ordering and thereby increases the fluctuations, as is visible in figure 8.4.

8.1.2 Central rapidity range

It was pointed out in chapter 6 that particle production in the rapidity region $|y| > 2$ is strongly affected by conservation laws. This rapidity region is excluded from the analyses presented in this section. The difference between horizontal and vertical normalization is small in this case because the rapidity distribution varies only slowly over the range considered here. Therefore figure 8.7 shows only the horizontal factorial moments; for completeness appendix A contains all other results.

The comparison with the "toy" model reveals the full strength of correlations present in the data and makes it clear that the factorial moment method is adequate to extract these.

From figure 8.7 it is immediately seen that the factorial moments of rank $q = 2, \ldots, 5$ rise linearly up to $\delta y \approx 0.5$; after that, the moments bend over and approach a constant value. In this context an important observation has been made by Ochs; namely that the
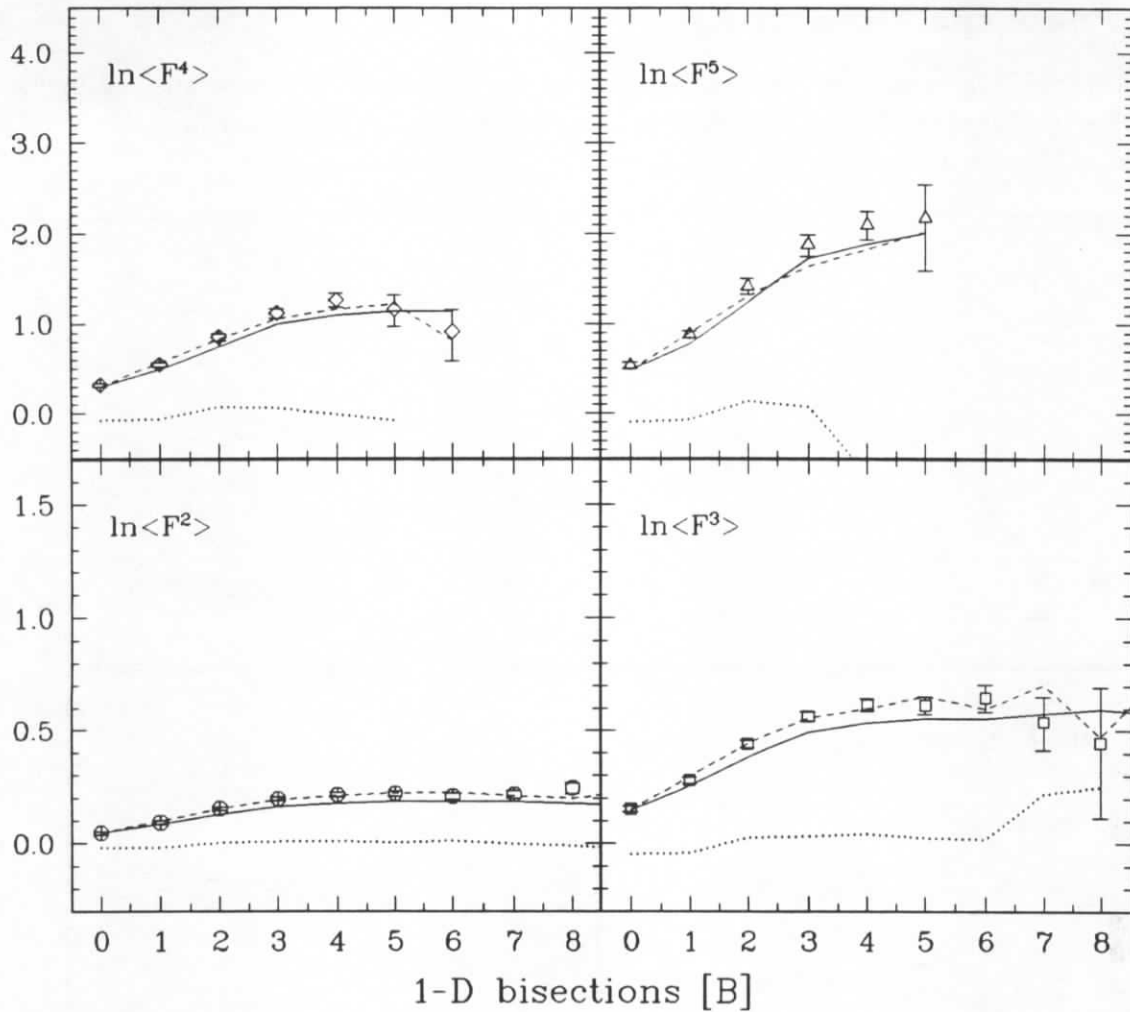
Figure 8.7: Horizontal factorial moments for central rapidity: CELLO data (open symbols) are compared to the CELLO "toy" model (dotted lines), to the Jetset 7.2 PS simulation (solid lines) and to the Jetset 7.2 PS+BE simulation (dashed lines).

intermittent behaviour of a three-dimensional system remains eventually unresolved in one- or two-dimensional analyses [78]. Therefore any conclusion about the existence of intermittent fluctuations in e^+e^- annihilation must be the subject of higher-dimensional analyses, which are presented further below.

The resolution dependence of factorial moments can be compared to the observation made in section 6.2, where the k^{-1} parameter for multiplicity distributions in central rapidity bins was found to approach a constant value for $\delta y < 0.5$, implying constant factorial moments of all ranks. This result has been obtained under the implicit assumption that the multiplicity distributions are of negative binomial type. This assumption is now supported by the direct measurement of factorial moments, which indeed show the expected constancy.

8.2 Higher dimensions

The results presented in this section are based on the variable transformation due to Białas and Gazdzicki described in section 7.2. Results from other methods are available in tabular form and can be consulted in the appendices B and C for reference.

8.2.1   Phase space dimension

An important finding in intermittency studies is the significance of the phase space dimension. It was shown by Ochs [78] that a three-dimensional intermittent system may hide this property if analysed in one- or two-dimensional projections of phase space.
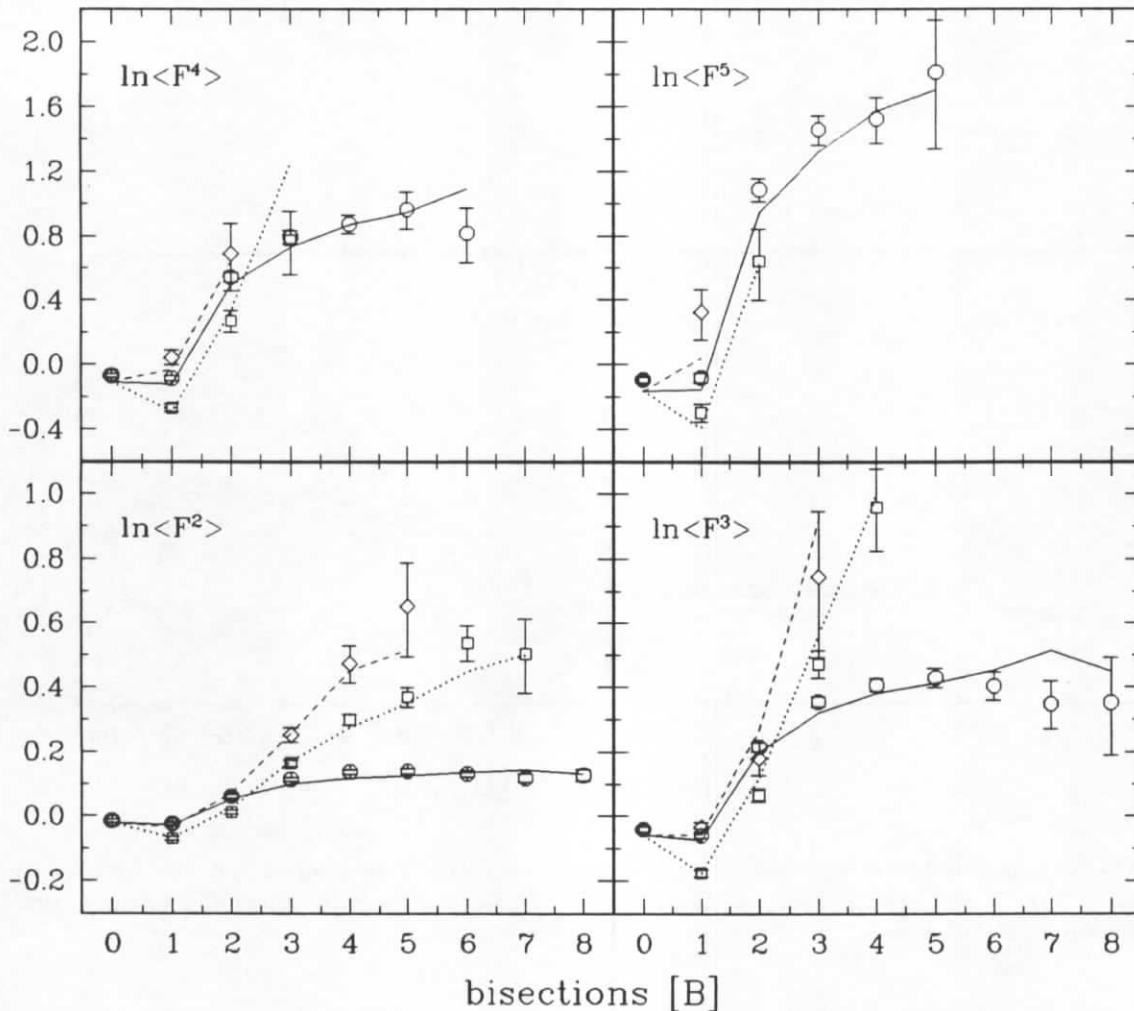
Figure 8.8: Transformed factorial moments $\langle F^2 \rangle - \langle F^5 \rangle$ for increasing number of bins $m = 2^{D_T \cdot B}$. The open symbols represent the CELLO data, while the curves show the Jetset 7.2 PS+BE model. $D_T = 1$; y analysis $\mapsto$ open circles and solid lines: $D_T = 2$; y, ϕ analysis $\mapsto$ open squares and dotted lines: $D_T = 3$; $y, \phi, p_\perp^2$ analysis $\mapsto$ open diamonds and dashed lines.

In the preceding section the one-dimensional factorial moments have been seen to saturate after a strong initial rise. From the analysis of two-jet events it has been concluded that this initial rise of the moments is related to hard gluon bremsstrahlung, which causes strong multiplicity fluctuations in certain rapidity regions. What happens now in higher dimensions?

To answer this question, figure 8.8 compares the factorial moments from the one-dimensional y, the two-dimensional y, ϕ and the three-dimensional y, ϕ, $p_\perp^2$ analyses. Indeed, the higher dimensional factorial moments of rank two and three apparently show a continual rise up to the highest resolution scales, accessible with the given detector resolution. This behaviour can alternatively be expressed as a fractal dimension of the analysed system, as has been discussed in section 7.4 on page 89. Figure 8.9 presents these fractal dimensions,
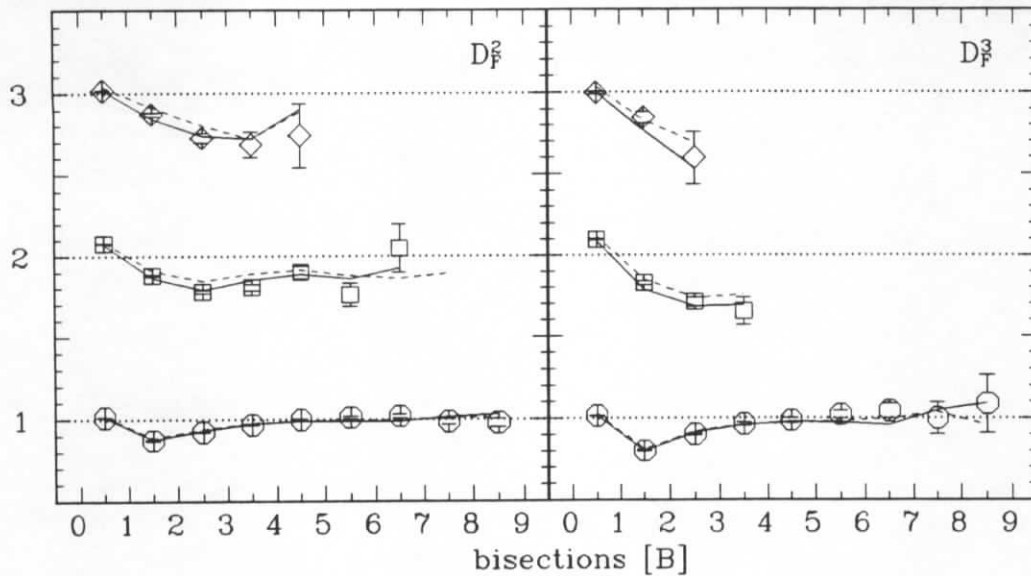
Figure 8.9: Fractal dimensions D_F^2 and D_F^3 for increasing number of bins $m = 2^{D_T \cdot B}$. The open symbols represent the CELLO data, while the solid and dashed lines show the Jetset 7.2 PS model with and without Bose-Einstein correlations.

and it is clearly seen that the dimension of the multihadronic final state is smaller than the topological phase space dimension. It is further noted that this property is observed only in the higher dimensional analyses, revealing the importance of the phase space dimension.

The higher ranks $q = 4, 5$ show a very different pattern: firstly they are very similar in all dimensions and secondly they bend over and approach a constant value. This implies that there are no four- and five-particle correlations. A not very surprising result, since at 35 GeV particle systems of that size correspond to entire jets, of which at most three appear in one event, leaving not much freedom for the development of a cascade with a fractal structure.

The complex behaviour of the factorial moments is further discussed in the following sections. It is certainly due to conventional physics, since it is apparent that the Jetset 7.2 PS+BE simulation provides an excellent description in all dimensions.

8.2.2 π^0 Dalitz decays and resonance decays

The contribution of resonance decays to the complex resolution dependence of factorial moments is best analysed by means of Monte Carlo studies. Their importance is demonstrated in figure 8.10, where the dramatic change in the fractal dimension (see section 7.4 on page 89 for the definition) due to π^0 Dalitz decays is shown. It should be noted that the Dalitz decays are only visible in higher dimensional analyses and moreover they occur at scales where the finite detector resolution becomes important, making it impossible to see the full strength of the effect. However, as shown in figure 9.2, there are many other resonance decays at larger correlation scales, which are easily accessible by the experiment and modify the factorial moments as well. Under these circumstances it is noteworthy that CELLO has measured a variety of inclusive particle cross sections (see section 4.4) to be in good agreement with standard Monte Carlo models.
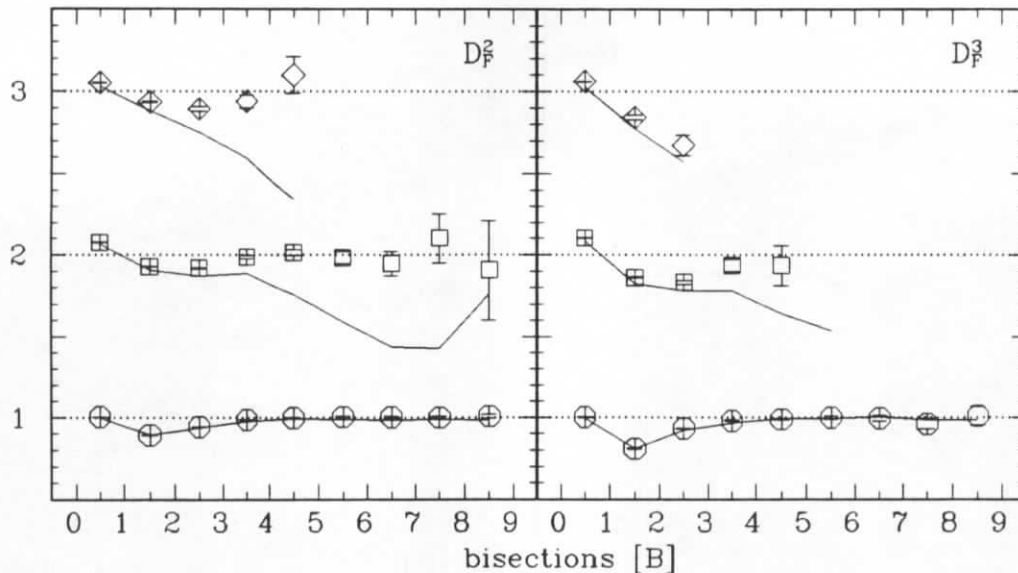
Figure 8.10: Fractal dimensions D_F^2 and D_F^3. The solid lines correspond to the default Jetset 7.3 PS simulation. The open symbols show the same model, neglecting e^+e^- pairs from π^0 Dalitz decays and $\pi^+\pi^-$ pairs from $\eta \to \pi^+\pi^-\pi^0$ and $\eta' \to \pi^+\pi^-\eta$ decays.

8.2.3 Bose-Einstein correlations

In section 9.1 a direct measurement of Bose-Einstein correlations is presented. It is found that the correlation length is $\zeta \simeq 0.1$ GeV^2, from this an effect is expected at intermediate and high resolution scales.

The analysis of like-sign charged particles provides more information on the significance of Bose-Einstein correlations, since the effect of resonance decays is strongly reduced. For this analysis positive and negative particles from one event are considered as two separate events. The corresponding results are shown in figure 8.11. Obviously, the Monte Carlo including Bose-Einstein correlations provides a very good description of the data. And furthermore, the difference between the two Monte Carlo versions is much more pronounced than in the analysis of all charged particles (figures 8.8, 8.9). This makes it clear that Bose-Einstein correlations have to be included in the Jetset model to describe the factorial moments.

Bose-Einstein correlations are one reason for the discrepancy between TASSO data and Jetset version 6 [56], since this model does not include Bose-Einstein effects and further does not include a proper treatment of π^0 Dalitz decays [62].

8.2.4 Azimuthal anti-correlations

In section 6.4.2.1 particle production in the string model was discussed. There it was stated that the one-dimensional nature of the string leads to azimuthal anti-correlations. These correlations are expected to become visible in an analysis including the azimuthal angle around the jet axis, as shown by Sjöstrand [69].

Here we present a one-dimensional analysis of the azimuthal distribution of particles around the jet axis (see section 5.2). Only two-jet events are considered for analysis, since hard gluon radiation would obscure the effect.

The results are presented in figure 8.12: anti-correlations, indicated by decreasing factorial moments, are seen only at very coarse resolution in the data. Contrary to this, the factorial
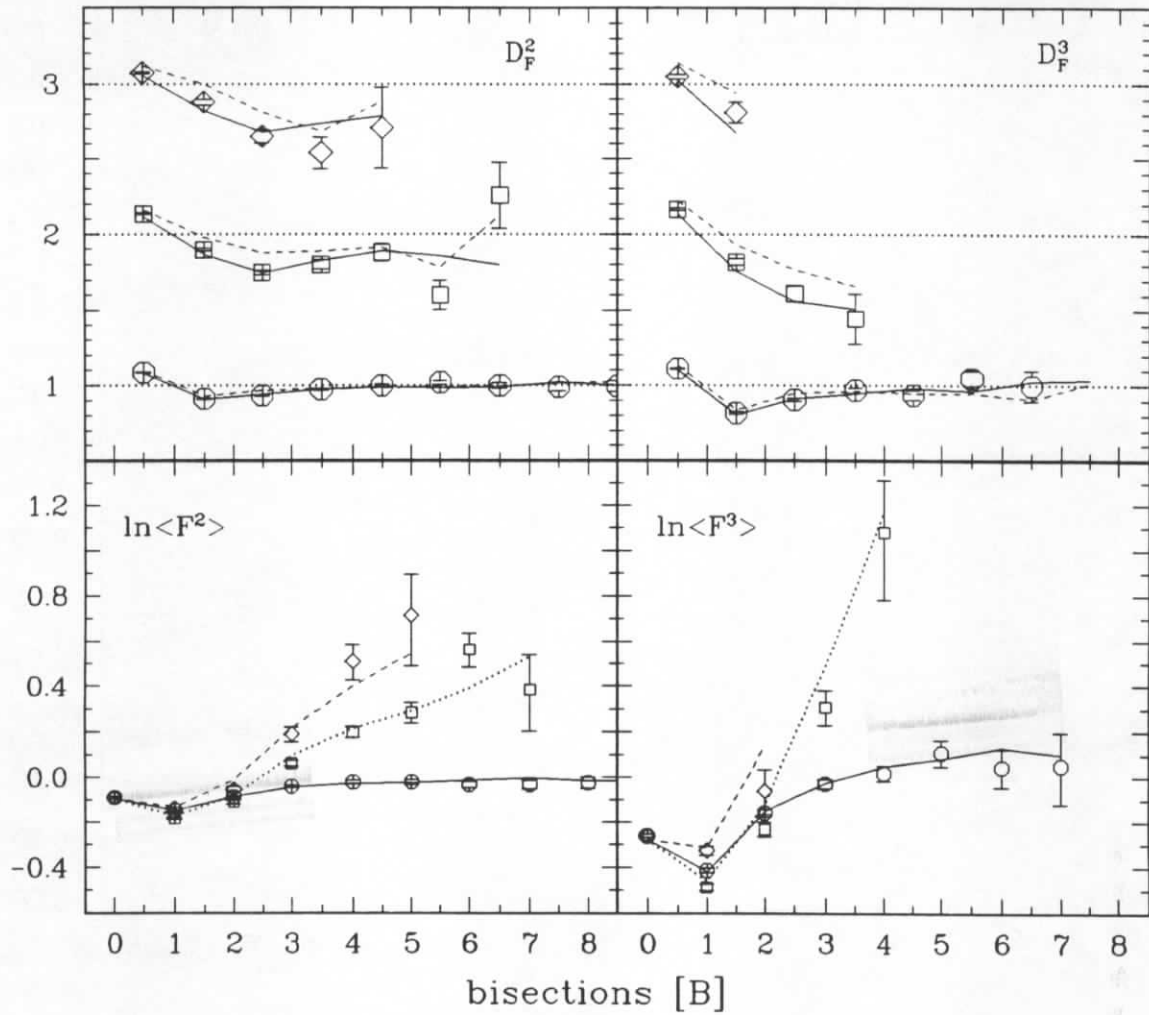
Figure 8.11: Factorial moments and fractal dimensions for like-sign charged particles. Lower plots: $\langle F^2 \rangle$ and $\langle F^3 \rangle$; the data are represented by the open symbols and the Jetset 7.2 PS+BE simulation is indicated by the curves. $D_T = 1$; y analysis $\mapsto$ open circles and solid lines: $D_T = 2$; y, ϕ analysis $\mapsto$ open squares and dotted lines: $D_T = 3$; $y, \phi, p_\perp^2$ analysis $\mapsto$ open diamonds and dashed lines. Upper plots: D_F^2 and D_F^3. The open symbols show the CELLO data while the solid and dashed lines correspond to the Jetset 7.2 PS model with and without Bose-Einstein correlations.

moments from the Jetset 7.2 PS model decrease also at higher resolution and fail to describe the data.

The initial decrease of the moments, at coarse resolution, can be attributed to global $p_\perp$ conservation in the entire event, while the decrease observed at higher resolution scales in the Jetset model is due to the local $p_\perp$ conservation of quark-antiquark pairs produced off a one-dimensional string.

An interesting observation is made when Bose-Einstein correlations are included in the Jetset model: the azimuthal anti-correlations disappear and the model provides a very good description of the data. This is understandable, since the strong anti-correlations induced by local $p_\perp$ compensation are destroyed by the Bose-Einstein effect. Whether the parameterization of the Bose-Einstein effect in the model of Sjöstrand [9] is correct remains an open question. However, this model provides an improved description of particle correlations and fluctuations in the string model and therefore has physical significance at least in this context (cf. section 9.1).
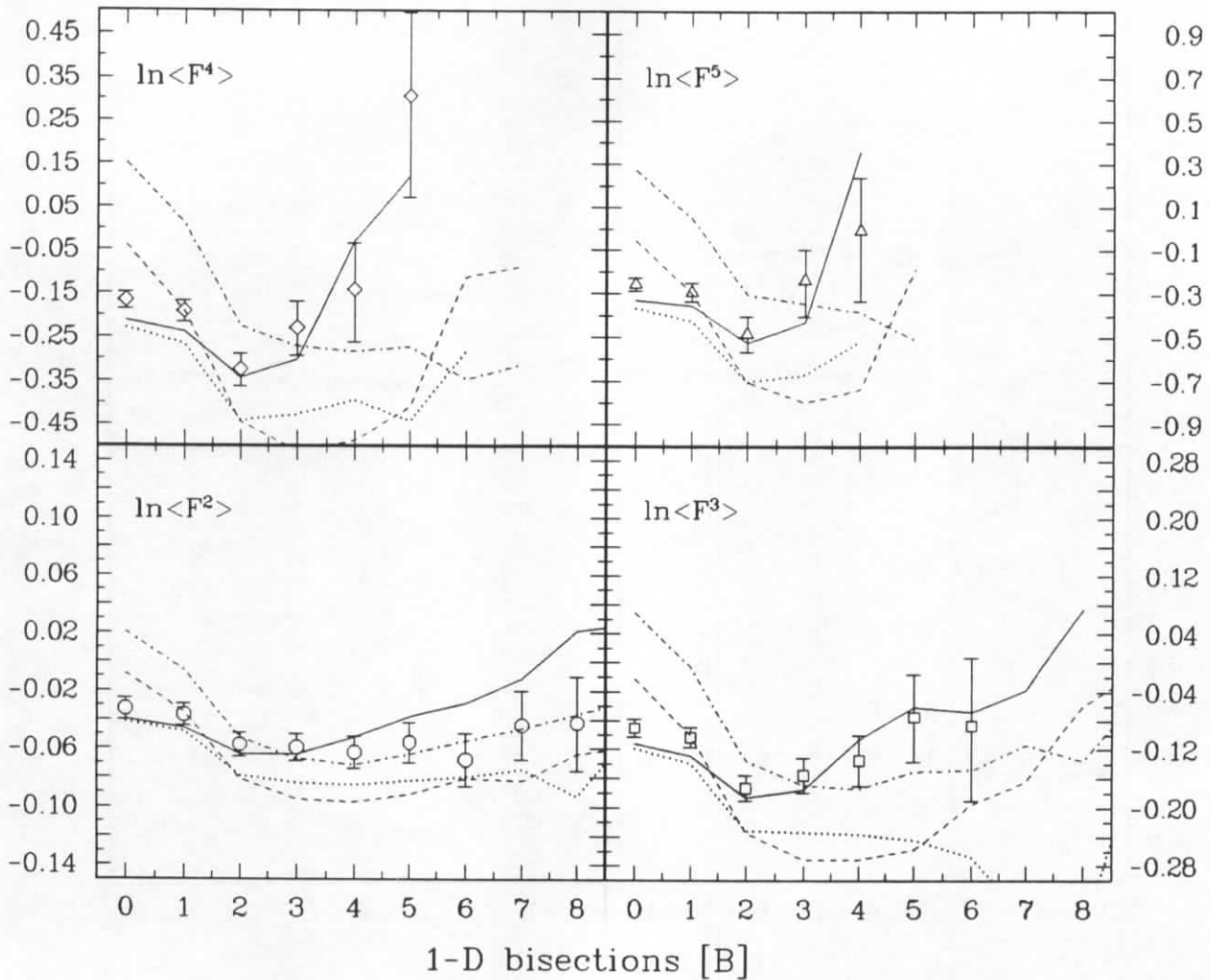
Figure 8.12: Transformed factorial moments for two-jet events in ϕ space. CELLO data (open symbols) are compared to the Jetset 7.2 PS simulation with and without Bose-Einstein correlations after detector simulation, shown by the solid and dotted lines respectively. The Lund string model (dashed line) is compared to the Herwig cluster model (dash-dotted line) on the generator level.

Finally it should be pointed out that the Herwig model fails significantly to describe azimuthal correlations in the data (figure 8.12). It might be objected that the Herwig simulation does not include the Bose-Einstein effect. However, this objection does not apply here – particle correlations in the Herwig model remain almost unchanged when Bose-Einstein correlations are introduced according to the recipe of Sjöstrand. This holds for both azimuthal and rapidity correlations, although the expected effect is visible in the Q^2 distribution. The reason for this is twofold: firstly, Herwig contains fewer like-sign charged particle pairs than Jetset, such that the generated correlation strength is weaker (see section 9.1). Secondly, the disorder of the final state particles already before Bose-Einstein correlations are turned on is larger in the cluster model. In other words, it is impossible to disorder further a completely disordered system. In this point string and cluster models differ significantly: while the former model produces an almost coherent system, the latter produces an almost disordered final state.

8.3 Aspects of intermittency analyses

In this section additional results from the above intermittency analyses are presented.
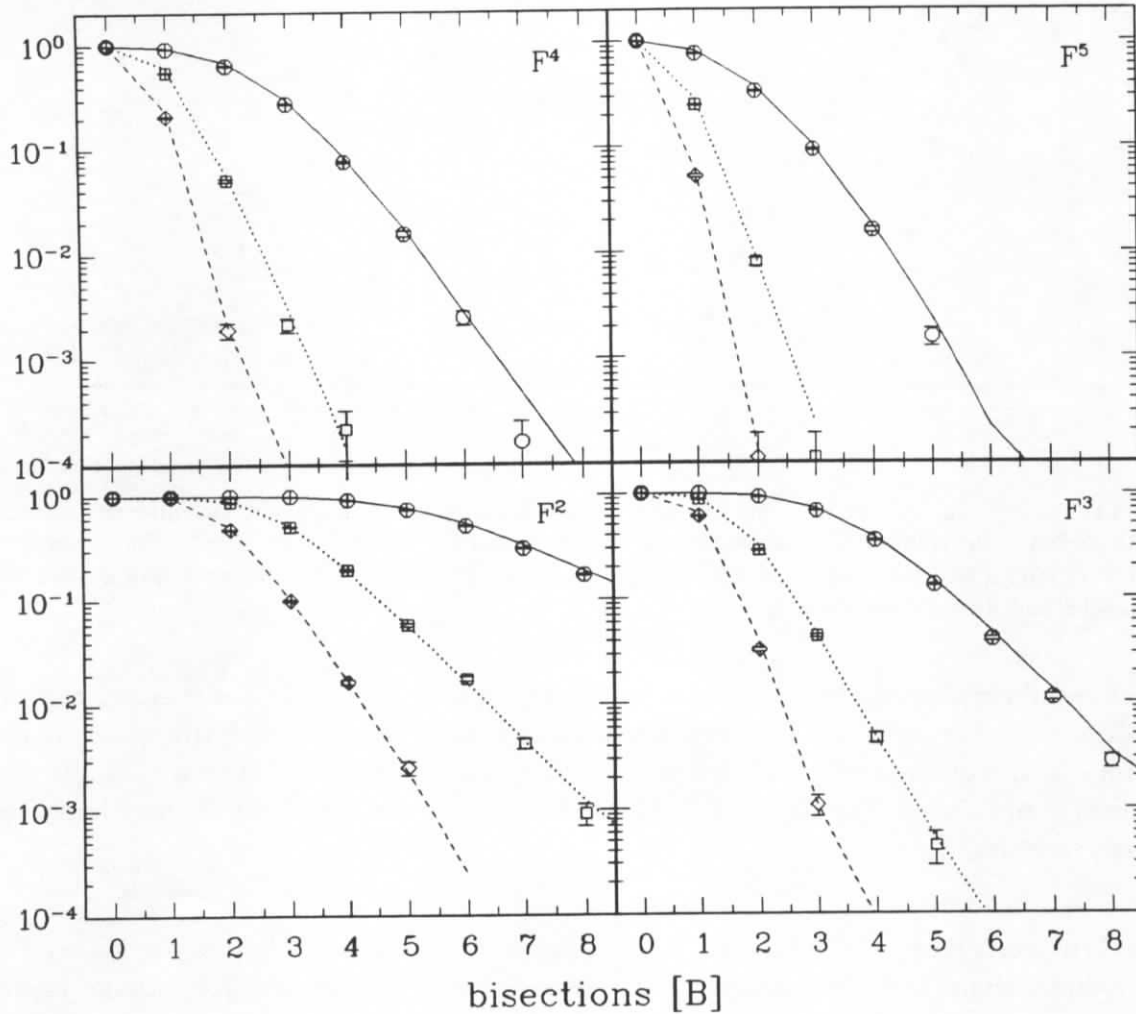
Figure 8.13: Fraction of events contributing to the factorial moment measurement according to Bialas and Gazdzicki. The open symbols represent the CELLO data and the curves show the Jetset 7.2 PS model. $D_T = 1$; y analysis $\mapsto$ open circles and solid lines: $D_T = 2$; y, ϕ analysis $\mapsto$ open squares and dotted lines: $D_T = 3$; $y, \phi, p_\perp^2$ analysis $\mapsto$ open diamonds and dashed lines.

Fraction of events: In figure 8.13 it is shown how the fraction of events, contributing to the measurement of factorial moments, varies with the resolution scale. This is done for different ranks q of the moments and different topological dimension D_T of the analysed phase space. A strong variation over four magnitudes is observed, making clear the need for a precise Monte Carlo simulation. The comparison with the Jetset 7.2 PS simulation shows excellent agreement in all dimensions and for all ranks.

Cluster multiplicity: The multiplicity distribution of clusters obtained during the factorial moment analysis is presented in KNO form in figure 8.14 (cf. section 6.1). The multiplicity distributions are shown for $B = 0, \ldots, 3$, corresponding to $m = 1, 2, 4, 8$ bins in the
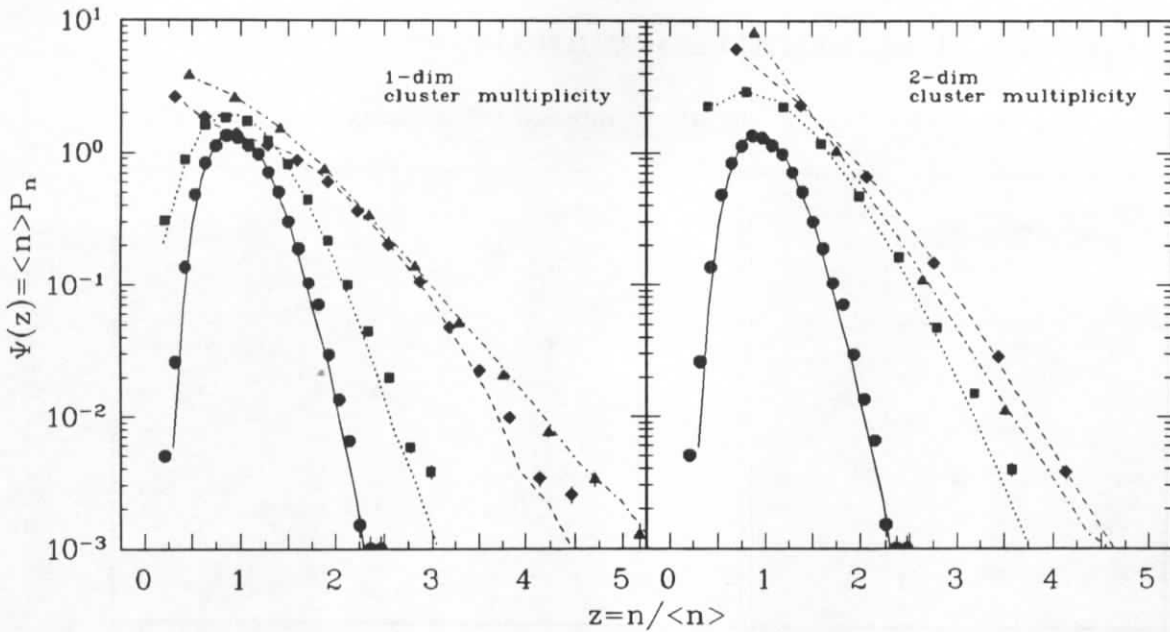
Figure 8.14: Cluster multiplicity from the one-dimensional rapidity analysis and the two-dimensional rapidity-azimuth analysis: the solid symbols show the CELLO data and the Jetset 7.2 PS result is indicated by the curves. $B = 0$; circles and solid lines: $B = 1$; squares and dotted lines: $B = 2$; diamonds and dashed lines: $B = 3$; triangles and dash-dotted lines.

one-dimensional rapidity analysis and to $m = 1, 4, 16, 64$ bins in the two-dimensional rapidity-azimuth analysis. For $m = 1$, of course, the ordinary multiplicity distribution is recovered; for two bins in the one-dimensional analysis e.g. the multiplicity distribution of single event hemispheres is obtained. The Jetset 7.2 PS model provides an excellent description also of these distributions.

Correlation matrices: In figure 8.15 the correlation matrices C^2 from the one-, two-, and three-dimensional factorial moment analyses are shown (see section 7.3). Large positive correlations are observed between all data points, showing that the same event contributes to factorial moments at different resolution scales. These correlations have to be taken into account if the data are compared to the Monte Carlo. The largest correlations, even between

Figure 8.15: Correlation matrices C^2 from one-, two- and three-dimensional analyses (left to right).

very distant data points, occur in the one-dimensional analysis. In the higher-dimensional analyses more information is available, reducing the correlations, however, they are still sizeable.

Inverse covariance matrices: The inverse covariance matrix $(V^2)^{-1}$ (see section 7.3) from the analysis of $\langle F^2 \rangle$ in one dimension is presented in table 8.2 and compared to the Jetset 7.2 PS+BE prediction. Apparently both matrices are very similar, again demonstrating the high quality of the Monte Carlo. Interestingly they have an approximate tridiagonal structure, which is, however, also true for the CELLO "toy" model without any genuine particle correlations. From this it can be concluded that the tridiagonal structure of the inverse covariance matrix is a general property of factorial moment analyses.

$$
\begin{pmatrix}
1.00 \\
-1.01 & 1.33 \\
0.04 & -0.27 & 0.38 \\
0.01 & -0.02 & -0.16 & 0.26 \\
0.00 & 0.00 & 0.00 & -0.10 & 0.15 \\
0.00 & 0.00 & 0.00 & 0.00 & -0.05 & 0.07 \\
0.00 & 0.00 & 0.00 & 0.00 & 0.00 & -0.02 & 0.04 \\
0.00 & 0.00 & 0.00 & 0.00 & 0.00 & 0.00 & -0.01 & 0.02 \\
0.00 & 0.00 & 0.00 & 0.00 & 0.00 & 0.00 & 0.00 & -0.01 & 0.01 \\
0.00 & 0.00 & 0.00 & 0.00 & 0.00 & 0.00 & 0.00 & 0.00 & 0.00 & 0.00
\end{pmatrix}
\begin{pmatrix}
1.00 \\
-1.00 & 1.30 \\
0.04 & -0.26 & 0.37 \\
0.00 & -0.01 & -0.16 & 0.25 \\
0.00 & 0.00 & 0.00 & -0.09 & 0.14 \\
0.00 & 0.00 & 0.00 & 0.00 & -0.05 & 0.07 \\
0.00 & 0.00 & 0.00 & 0.00 & 0.00 & -0.02 & 0.04 \\
0.00 & 0.00 & 0.00 & 0.00 & 0.00 & 0.00 & -0.01 & 0.02 \\
0.00 & 0.00 & 0.00 & 0.00 & 0.00 & 0.00 & 0.00 & -0.01 & 0.01 \\
0.00 & 0.00 & 0.00 & 0.00 & 0.00 & 0.00 & 0.00 & 0.00 & 0.00 & 0.00
\end{pmatrix}
$$

Table 8.2: Inverse covariance matrices: data (left) and Jetset 7.2 PS+BE (right). The matrix elements are normalized to $(V_{11}^2)^{-1}$.

8.4 Cartesian three-dimensional analysis

In this section a study of multiplicity fluctuations of charged particles in Lorentz invariant phase space is presented. For this the differential phase space element $dLips$ is decomposed according to (5.1). In contrast to the decomposition (5.2) this parameterization allows a unique definition of a resolution scale, since all variables are of the same dimensionality. A further advantage of this approach is the invariance of the factorial moments under rotational transformations of the analysed variables, thus making the definition of a preferred axis (such as the sphericity axis) unnecessary. The results presented below have been checked to be identical if the variables are defined in the laboratory frame or by the eigenvectors of the sphericity tensor.

The factorial moments of the charged multiplicity distribution are evaluated at different resolution scales according to the prescription given in section 7.1 on page 81. For reasons that will become clear later, the original phase space volume $\Delta Lips$ has been chosen to be thousand times larger than the volume actually occupied by our events, namely $1/(2\pi)^3 \cdot 1/2 \cdot 10^6$ GeV^2, corresponding to a range of ± 50 GeV$^{\frac{2}{3}}$ for the single variables $p_i/E^{\frac{1}{3}}$ (see figure 5.2). This arbitrary choice influences the absolute value of factorial moments at a given scale, implying a strong initial rise, but has no effect on the slopes at high resolution.

The analysis is performed with up to fourteen successive bisections B in every dimension, yielding a maximum of $m = 2^{42}$ three-dimensional phase space cells. The scale B can be related to the four-momentum transfer Q^2 by:

$$
B = \frac{\ln\left(\frac{\Delta^3 p/E}{Q^2}\right)}{D_T \ln 2} \tag{8.1}
$$

where $\Delta^3 p/E = 10^6$ GeV^2 is the initial size of the phase space volume. Typical Q^2 scales are also indicated in the figures to ease the comparison to physical processes.

For this analysis a special smoothing procedure is applied to remove fluctuations caused by the accidental setting of bin borders. This is accomplished by moving the complete event at random inside the large phase space volume, which for this purpose is continued periodically. The factorial moments from each event are calculated at ten different random positions and the average is taken. We have checked that the results are not influenced by this procedure, except that artificial fluctuations are damped.
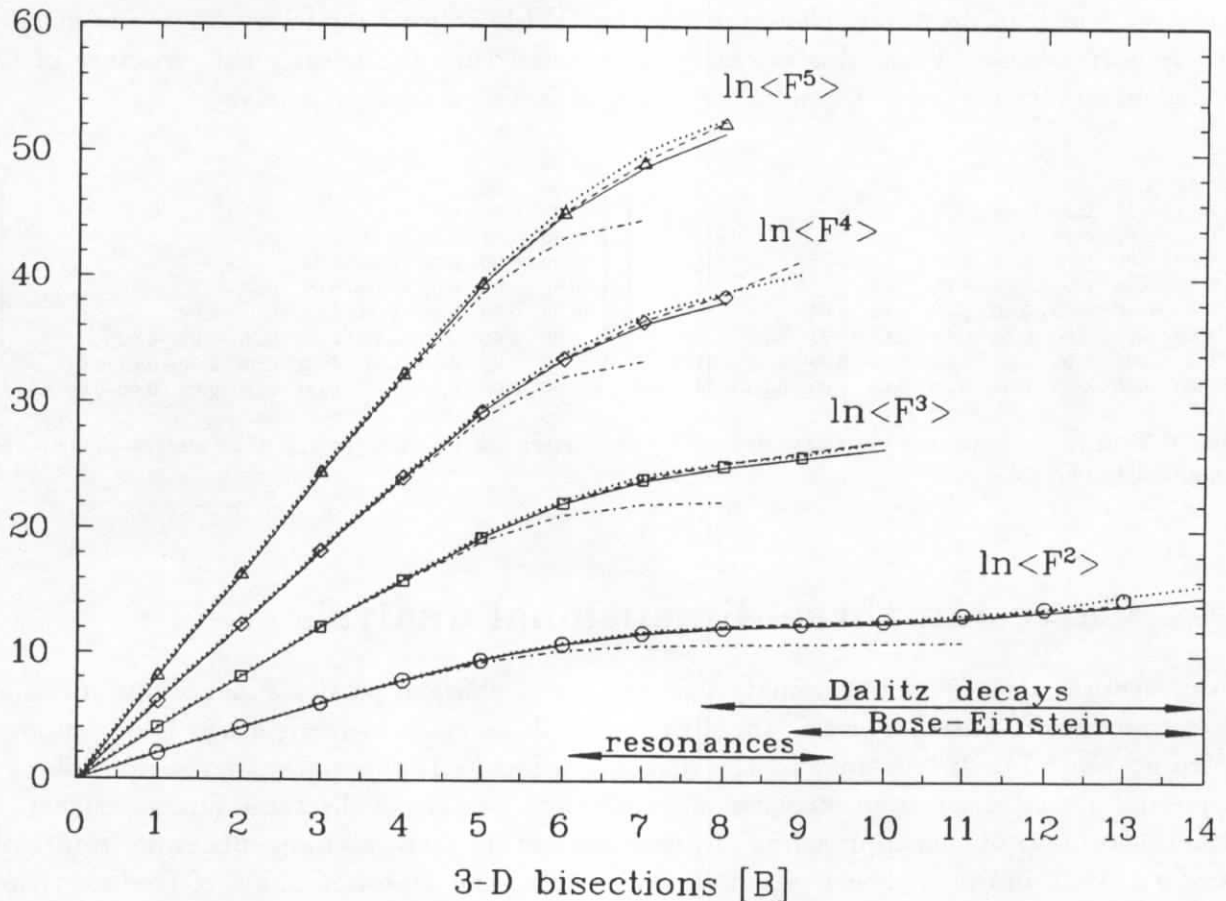
Figure 8.16: Factorial moments in three-dimensional phase space. The open symbols show the data (statistical errors are typically smaller than the symbol size and are omitted for clarity) and the dotted and solid curves correspond to the Jetset 7.2 PS simulation prior to and after detector simulation. The dashed curve indicates the Jetset 7.2 PS+BE model and the dash-dotted curve represents the CELLO "toy" model.

In figure 8.16 the factorial moments are displayed: different slopes are seen at different resolution scales. A very interesting behaviour is observed for $\langle F^2 \rangle$, which after a strong initial rise flattens out, but then starts to rise again. The results from a Monte Carlo simulation with the Jetset 7.2 parton shower model, with default parameters after inclusion of initial state radiation are seen to be in good agreement with the data. Including Bose-Einstein correlations in the simulation improves the description. Similarly the Jetset 7.2 ME model provides a good description of the data. It is also visible in figure 8.16 that detector effects are of minor importance in this analysis.

The comparison with the CELLO "toy" model (consult section 5.4 for a description of the model) shows that the fast initial rise of the moments is entirely due to the variation of the inclusive distribution, which is very strong due to the choice of the large initial phase

space volume. However, for $B \gtrsim 5$ the moments from the "toy" model are seen to bend over and saturate. This is in contrast to the experimental data and also to the Monte Carlo, both contain genuine particle correlations, which cause rising factorial moments at certain resolution scales.

8.4.1 Local fractal dimensions

Figure 8.17 shows the fractal dimension D_F^2 (cf. (7.16) on page 89) inferred from $\langle F^2 \rangle$ for increasing resolution. The errors shown are propagated from the measurement of $\langle F^2 \rangle$ using the covariance matrix (7.12).

On top of figure 8.17 the geometrical meaning of the fractal dimension is indicated. For very coarse resolutions the events appear point-like ($D_F^2 = 0$). This limit could only be reached with a very large initial value for $\Delta Lips$, which is the justification for this particular choice. With increasing resolution the structure begins to emerge: first along the jet-axis and then also transverse to the jet-axis. At very small scales all dimensions are fully resolved, and in the geometrical interpretation one expects $D_F^2 = 3$. The data, however, show a maximum dimension $D_F^2 \approx 2.5$ followed by a decrease to about $D_F^2 \approx 2.0$. This reduction of D_F^2 is the manifestation of the strong rise of $\langle F^2 \rangle$ at ultra-fine resolution. This complex behaviour is well reproduced by the Jetset 7.2 PS Monte Carlo simulation, both with and without detector simulation.

8.4.1.1 Multifractal objects

In the geometrical interpretation given above one would expect the fractal dimension derived from factorial moments to be independent of the rank q, i.e. one expects $\varphi^q/(q-1) = \text{const.}$ This relation does not apply to multifractal objects. To search for a possible multifractal behaviour the slopes φ^q obtained from $\langle F_m^q \rangle$ of rank q at a given resolution scale m are fitted to the expression:

$$\varphi^q = c\,(q-1)\left(\frac{q}{2}\right)^x \tag{8.2}$$

where $x = 0$ indicates geometrical scaling and $x = 1$ corresponds to the scaling law predicted by the α-model; i.e. a simple cascade model [75]. The fitted x values are shown in figure 8.18: a clear deviation from the simple geometrical scaling law is observed as the resolution increases. This behaviour is well described by the Monte Carlo expectation, both with and without detector simulation, again demonstrating the small influence of detector effects on this type of analysis. The reason for the observed multifractal behaviour is the interplay of processes with different correlation lengths, occuring e.g. in the resonance region.

8.4.2 Monte Carlo studies and discussion

Given the success of the Lund model in describing the data, we have undertaken some generator studies in order to isolate the effects contributing to the observed complex behaviour of the fractal dimension and the scaling law. The corresponding $\langle F^2 \rangle$ and D_F^2 curves are displayed in figures 8.19 and 8.20.

- The simplest case considered consists of primary particles produced in $q\bar{q}$ events with no transverse degrees of freedom. i.e. $\langle p_\perp^2 \rangle = 0$. These events exhibit a one-dimensional structure once the jet structure is resolved (solid line in figure 8.19). It is interesting
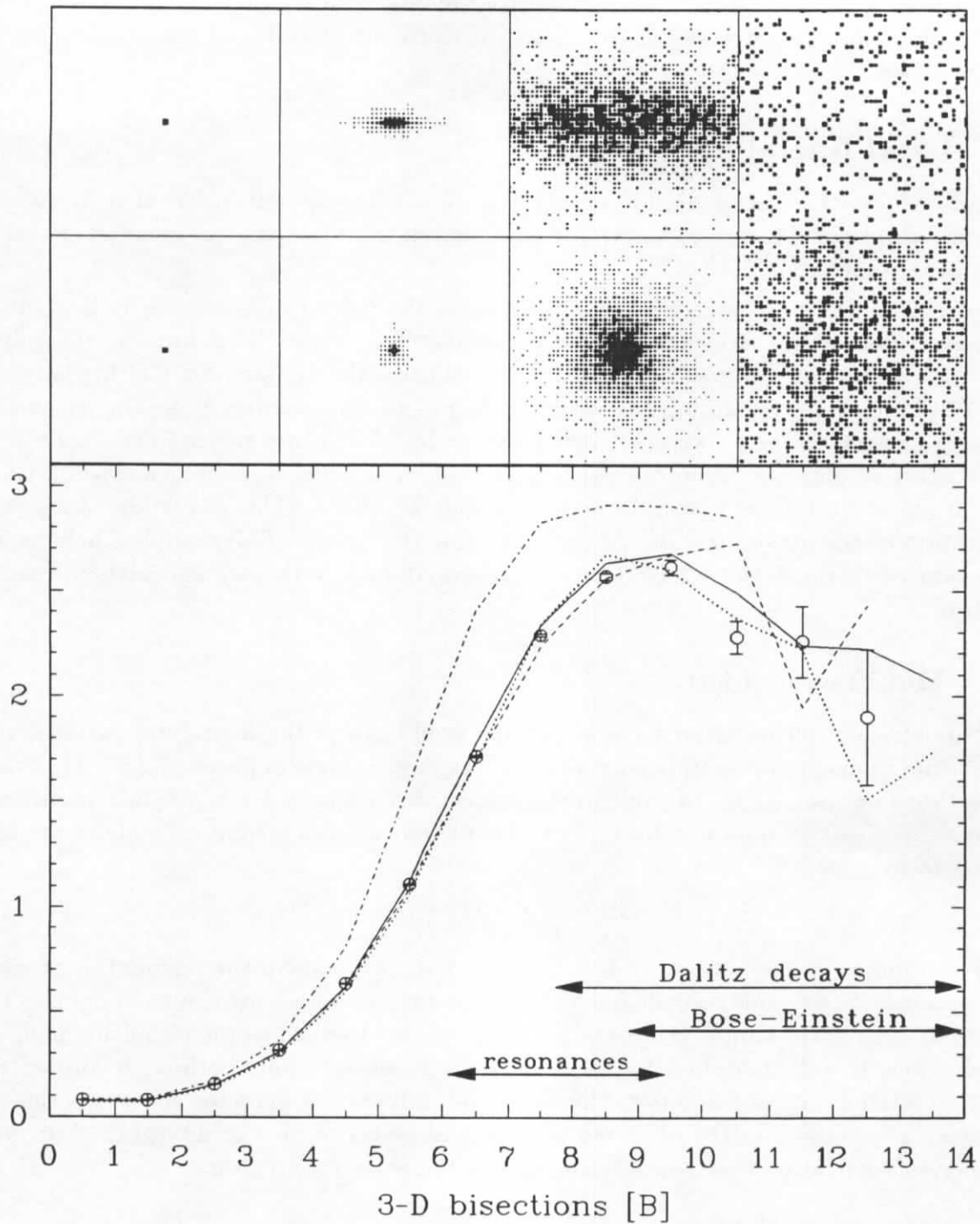
Figure 8.17: Fractal dimension D_F^2 as a function of B. The open symbols show the data with errors propagated from $\langle F^2 \rangle$. Superimposed, as the dotted and solid lines are the corresponding results from the Jetset 7.2 parton shower calculation prior to and after detector simulation. The dashed line shows the Jetset 7.2 PS+BE simulation, while the CELLO "toy" model is indicated by the dash-dotted line. Displayed above is a pictorial view of the fractal dimension at four typical scales. Upper row: plane along the sphericity axis. Lower row: plane perpendicular to the sphericity axis. This picture has been prepared using 400 Monte Carlo events.
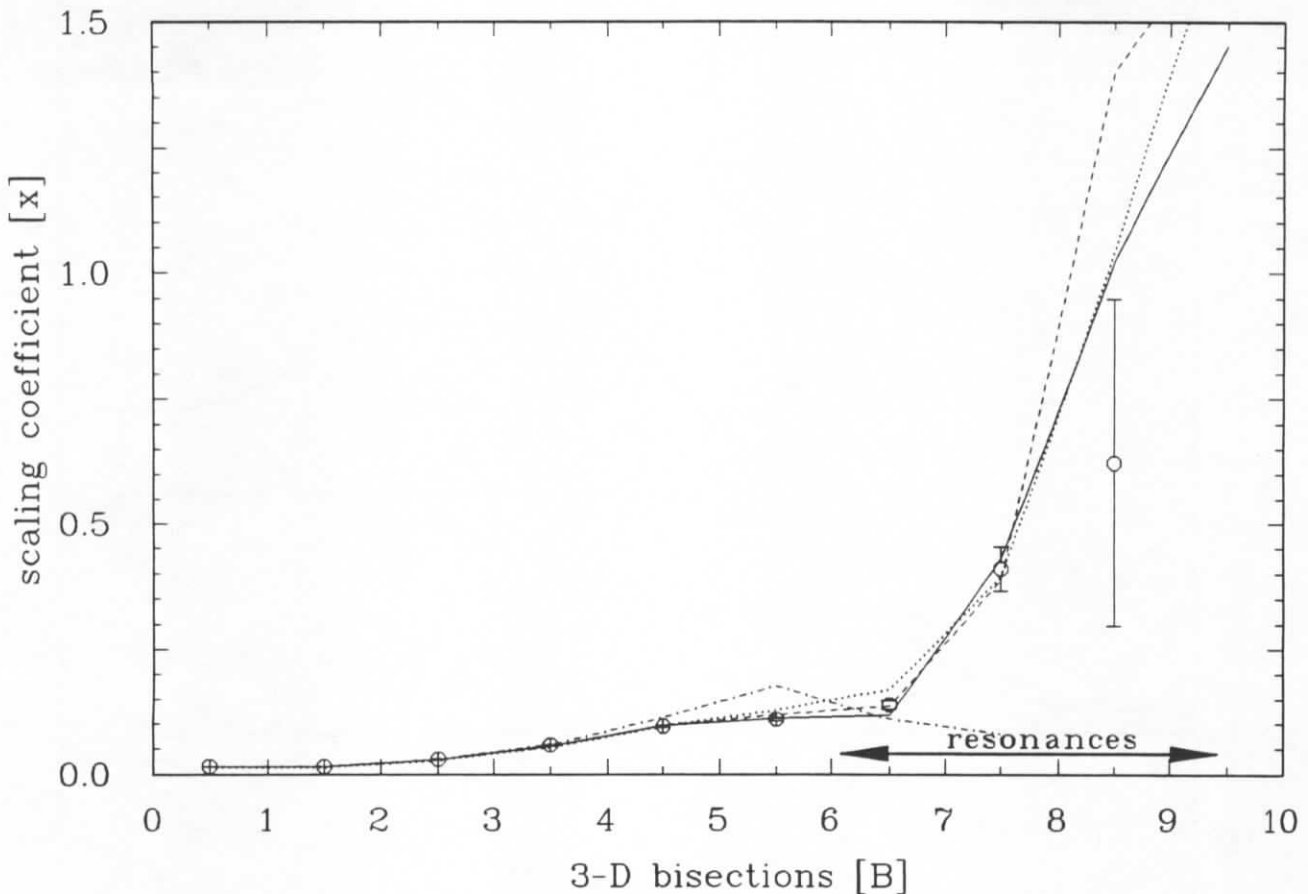
Figure 8.18: Anomalous scaling law. The open symbols show the data with errors propagated from the factorial moments. The dotted and solid curves correspond to the Jetset 7.2 PS simulation prior to and after detector simulation. The Jetset 7.2 PS+BE simulation is seen as the dashed line and the CELLO "toy" model is represented by the dash-dotted line. $x = 0$ indicates geometrical scaling.

to note that although the Lund string fragmentation mechanism is an iterative process no deviation from a one-dimensional object is seen in the high resolution limit, thus excluding it as a source of intermittency. In fact, since the Lund string is an almost *coherent* system the magnitude of fluctuations is even below that of Poissonian noise, as has been discussed in section 6.4.

• An important property of string fragmentation is its iterative character. To exhibit a fractal structure a further property is required; namely self-similarity. The latter property is absent in ordinary fragmentation mechanisms since different z values are used at each iteration. The self-similar character is rectified by the fragmentation function:

$$f(z) = \delta(z - a) ,$$ (8.3)

where the parameter a takes a fixed value in the range $m_\pi/E_{beam} \leq a \leq 1$. This treatment leads indeed to a fractal behaviour as is indicated by an increase of D_F^2 (dotted line in figure 8.19). It should be emphasized that the events, in the geometrical sense, are still one-dimensional without any transverse degree of freedom.
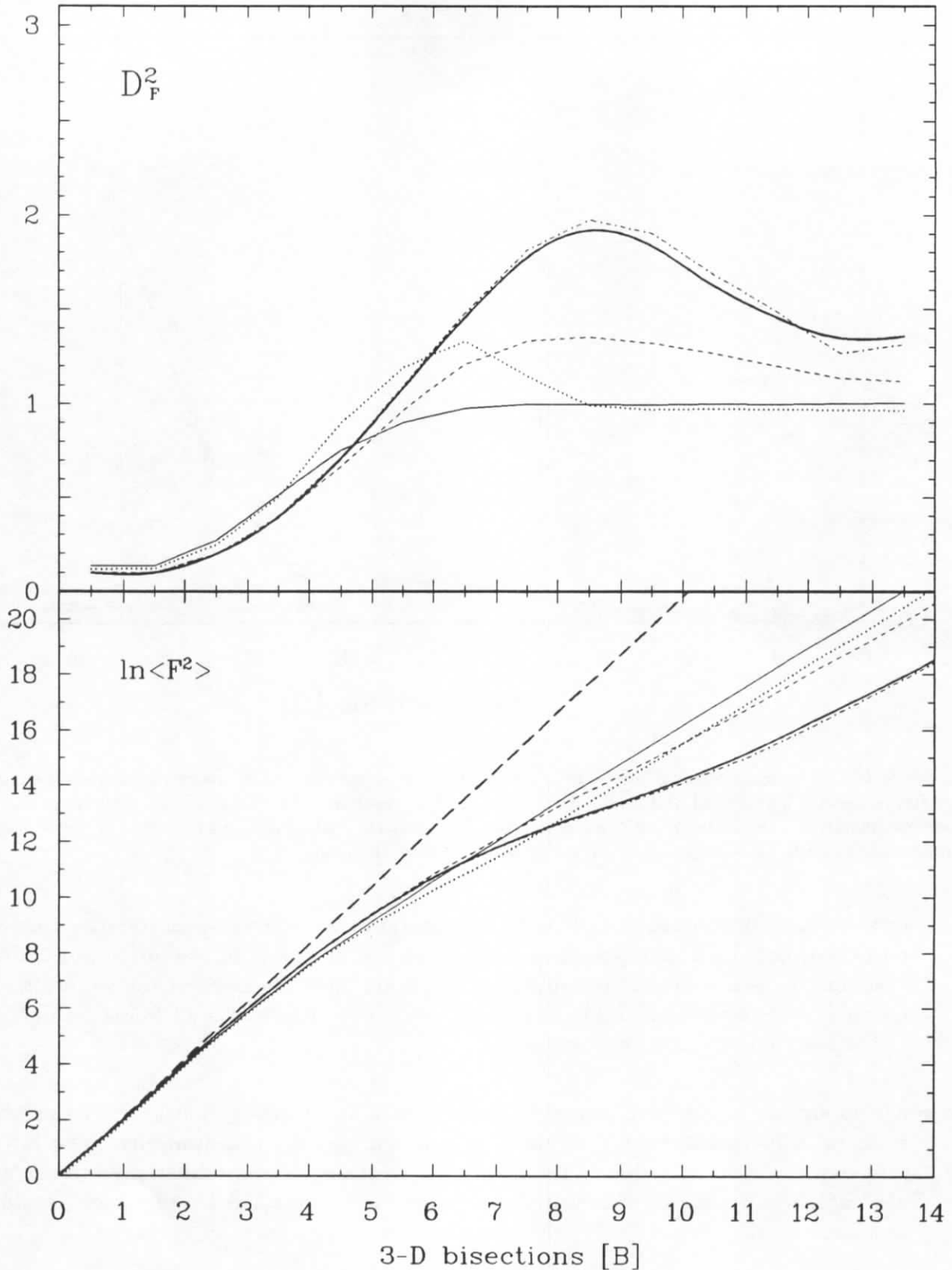
Figure 8.19: Jetset model generator studies of $\langle F^2 \rangle$ and D_F^2 with primary particles. If not stated otherwise, the Lund symmetric fragmentation function is used. Transverse string fragmentation is completely suppressed; i.e. $\langle p_\perp^2 \rangle = 0$. Solid line: primary particles from $q\bar{q}$ events: dotted line: ditto, but using a self-similar fragmentation function with $a = 0.45$: dashed line: primary particles from an $\mathcal{O}(\alpha_S^2)$ matrix element (ME) simulation: dash-dotted line: ditto, using the parton shower (PS) algorithm: thick solid line: ditto, using the colour dipole approximation (CD). The thick dashed line shows the behaviour of a point-like object.
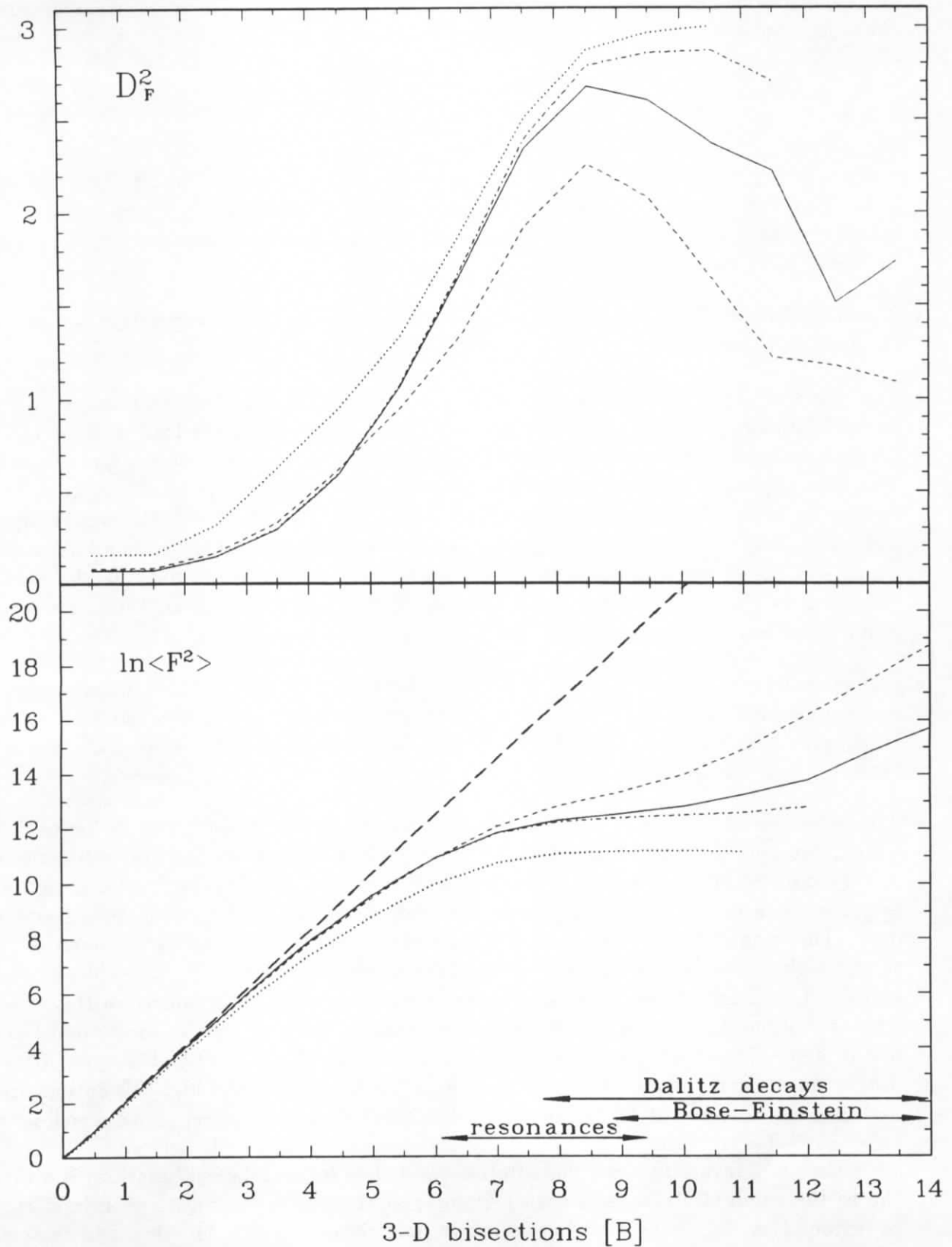
Figure 8.20: Jetset model generator studies of $\langle F^2 \rangle$ and D_F^2. Solid line: final stable particles in a default PS simulation: dash-dotted line: ditto, but neglecting e^+e^- pairs from the π^0 Dalitz decay: dotted line: primary particles from $q\bar{q}$ events with with $\langle p_\perp^2 \rangle = (0.35 \text{ GeV})^2$: dashed line: final stable particles from $q\bar{q}$ events with $\langle p_\perp^2 \rangle = (0 \text{ GeV})^2$. The thick dashed line shows the behaviour of a point-like object.

In case of the fragmentation function (8.3) the number of steps S in the fragmentation chain for a single jet is given by the following expression:

$$S = 1 + \frac{\ln\left(\frac{\varepsilon}{a}\right)}{\ln(1-a)} \tag{8.4}$$

where $\varepsilon = E_{min}/E_{beam}$ and E_{min} is the energy where the process stops. The multiplicity is given by $\langle N \rangle = 2S + 1$ and the variance of this distribution is strictly zero. The maximum fractal dimension D_F^2 obtained in this way does not depend on a, but occurs at higher resolution the smaller the a parameter is.

- The inclusion of initial state QED radiation was found to give a very slight increase of the fractal dimension.

- The effect of gluon emission is seen after inclusion of QCD radiation; (dashed line in figure 8.19) according to $\mathcal{O}(\alpha_S^2)$, (dash-dotted line) according to the leading log approximation (parton shower) and (thick line) according to the colour dipole approximation. The first approach leads to a maximum fractal dimension of $D_F^2 \approx 1.35$. The parton shower leads to a higher fractal dimension of $D_F^2 \approx 2$, very similar to the colour dipole approach. The reason for this behaviour is that every emitted gluon adds a kink to the string and thereby increases its "length". Comparing the matrix element to the parton shower, it is observed that the main increase of the fractal dimension comes from soft gluon radiation. This topic is also discussed by Andersson et al. in [67].

- Unfortunately, a straightforward distinction between the different perturbative QCD descriptions is hindered by transverse degrees of freedom, as is made clear after giving the quarks the standard $\langle p_\perp^2 \rangle$ of $(0.35 \text{ GeV})^2$, which leads to a fast rise of D_F^2 towards three (dotted line in figure 8.20).

- The influence of resonance decays is demonstrated by the dashed line in figure 8.20, which corresponds to $q\bar{q}$ events with $\langle p_\perp^2 \rangle = 0$, where resonances are allowed to decay. A very interesting structure is observed: at intermediate scales the fractal dimension appears much larger than one, almost reaching three, followed by a decrease towards one. This behaviour implies the existence of correlated two-particle production up to the highest resolution. This sounds rather interesting; however, the explanation is simple. The Dalitz decay $\pi^0 \to e^+e^-\gamma$ has been identified as the source of this effect. This is demonstrated by a comparison of the default parton shower simulation (solid line in figure 8.20) and the same simulation just neglecting the π^0 Dalitz decay (dash-dotted line). It is obvious that the rise of $\langle F^2 \rangle$ observed in the high resolution limit and thus the decrease of D_F^2 is caused by the Dalitz decay of neutral pions, which is the only source for correlated two-particle production in this limit. This is understandable since the e^+e^- invariant mass distribution (and thus its correlation function) is almost (up to the small electron mass scale) singular at threshold, leading to an intermittent behaviour (for the connection between two-particle correlation function and factorial moments see e.g. [83,76]). A similar effect is produced by photon conversion ($\gamma \to e^+e^-$) in the beam pipe.

- A study of Bose-Einstein correlations as implemented into the Jetset 7.2 program revealed a significant rise of the factorial moments at intermediate and high resolution

scales. The size of this effect is of the right order of magnitude to improve further the agreement of the data and the Monte Carlo concerning the factorial moments. Also the fractal dimension is reduced by Bose-Einstein correlations, since the pion phase space is effectively decreased. It is apparent in figure 8.17 that this effect is present in the data.

Finally, it is clear that these different effects do not simply add in the dimension, such that we cannot argue in favour of one or the other QCD approach. The parton shower and the matrix element ansatz with default parameters both describe our data.

Monte Carlo studies of the scaling coefficient x (cf. (8.2) and figure 8.18) indicate that the deviation from geometrical scaling at low resolution scales is due to the jet structure of the events. The strong violation of the geometrical scaling law at high resolution can be attributed to particle decays.

It may be criticized that the particular choice of variables (5.1), and more importantly the choice of a very large initial volume, lead to strong variations of the inclusive distribution and the large initial slopes are thus trivial. This particular choice has been made to reach the zero-dimensional limit, and does not invalidate the results derived in the high resolution limit, since for small bin sizes the inclusive distribution is constant to a good approximation. The sensitivity of this approach for genuine density fluctuations, as well as the quality of the data is demonstrated by the observation of a strong effect due to π^0 Dalitz decays and γ conversions in detector material. Moreover, a variation of the inclusive distribution at intermediate scales is inherent in e^+e^- annihilation, independent of the choice of variables. This is due to the mixture of events with different kinematics and topology, such as light and heavy quarks or hard and soft gluon radiation. In addition, the presentation of local slopes (or equivalently dimensions) as a function of the resolution scale clearly shows that there is a smooth transition, rather than a simple power law, as is implied by the usual straight line fits, whose results of course depend on the fit range chosen.

8.4.3 Transformed variables

In this section the three-dimensional analysis according to the phase space decomposition (5.1) is repeated: however, with variables transformed according to the recipe of Białas and Gazdzicki described in section 7.2. In this case the original phase space volume covers only the range actually occupied by the events. The results from this analysis are presented in figure 8.21. Compared to the analysis according to the decomposition (5.2), presented in figure 8.8, a much stronger rise of the factorial moments is seen. The influence of the non-constant inclusive distribution is completely removed as can be seen from the "toy" model result.

8.5 Summary on intermittency

In summary we have presented intermittency analyses in one- and two-dimensional projections of phase space and in three-dimensional phase space itself, using various methods to calculate the factorial moments. The significance of factorial moments in e^+e^- annihilation and their sensitivity to certain aspects of the complex hadronization process have been discussed in detail. The main results and conclusions are:
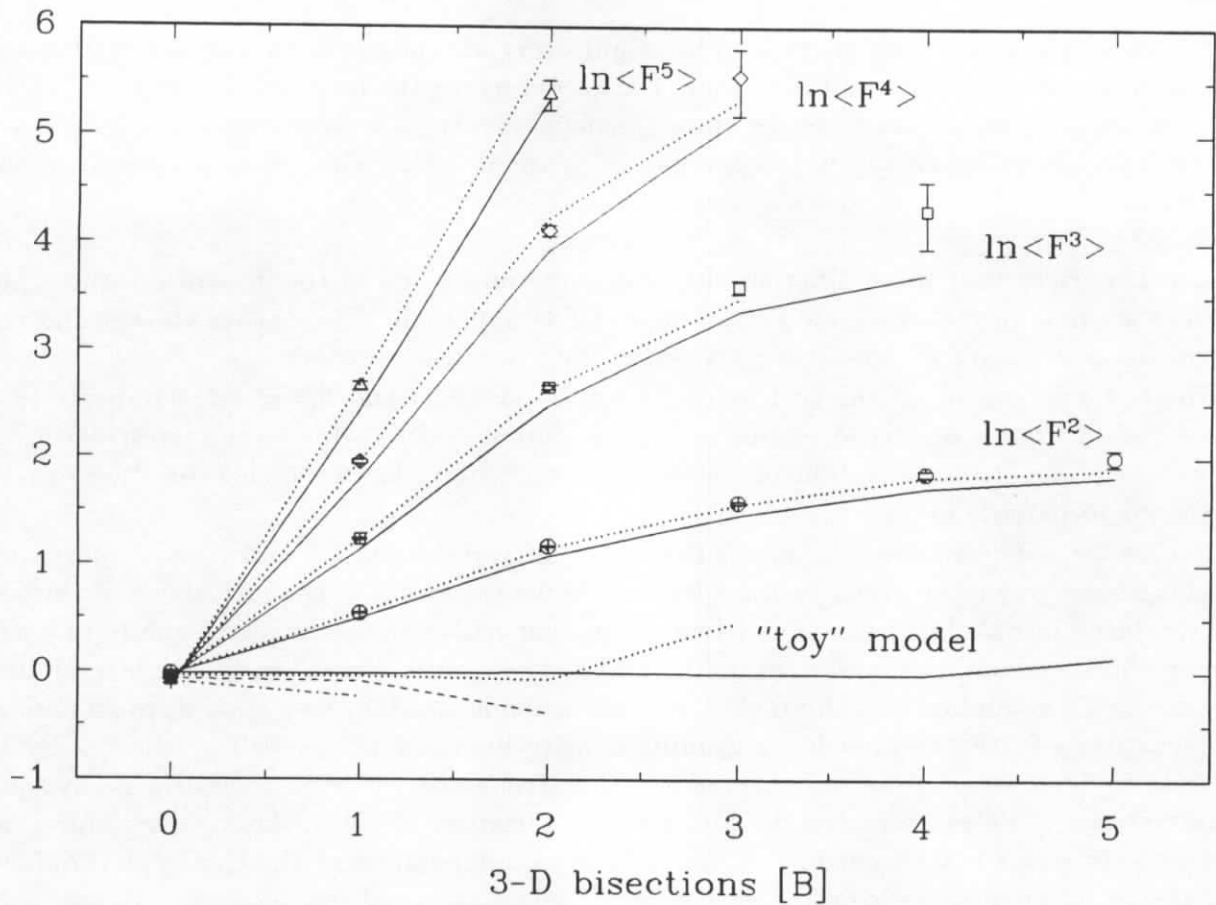
Figure 8.21: Transformed factorial moments in three-dimensional phase space. The open symbols show the data and the dotted and solid curves correspond to the Jetset 7.2 PS simulation with and without Bose-Einstein correlations. The lower curves indicate the results from the CELLO "toy" model (solid curve $\mapsto \langle F^2 \rangle$), (dotted curve $\mapsto \langle F^3 \rangle$), (dashed curve $\mapsto \langle F^4 \rangle$), (dash-dotted curve $\mapsto \langle F^5 \rangle$)).

- The factorial moment analysis of the total event sample is dominated by the occasional occurrence of hard bremsstrahlungs gluons, which populate a certain phase space region. Their contribution is so strong that it completely conceals the soft hadronization phase. For this reason various QCD inspired hadronization models all give the same result. The effect from hard gluons is seen in all dimensions and cannot be circumvented by a variable transformation.

- Two-jet events are ideal to test the non-perturbative hadronization phase. An important observation is the failure of the Lund string model to reproduce the rapidity correlations and fluctuations in these events. In line with the analysis of multiplicity distributions in chapter 6 the Herwig cluster model provides a good description of this property. The reason for this is the space-time structure underlying the string model, which leads to a regular pattern in rapidity space for hadrons produced off a string. In contrast to this the cluster model preserves, via its local hadronization mechanism, the fluctuations occuring during parton shower evolution. From this it is concluded that the non-perturbative hadronization process is really of a local nature, giving support the idea of local parton-hadron duality.

- Azimuthal anti-correlations, predicted by the string model due to local $p_\perp$ conservation are not observed with the same strength in the data. However, the inclusion of the Bose-

Einstein effect in the string model diminishes these anti-correlations and this model provides a good description of the data. The Herwig cluster model fails to describe the azimuthal correlations. The model behaviour is not rectified after inclusion of the Bose-Einstein effect. The reason for this difference between cluster and string models is the regular pattern of particle production in the latter, compared to a disordered particle state in the former. From this it is understandable that the Bose-Einstein effect has practically no influence on particle fluctuations in the cluster model.

- The importance of the phase space dimension is seen in the higher-dimensional analyses, which yield factorial moments growing as a power with the resolution scale. This is, however, only observed for the moments of rank two and three and has a rather trivial origin in Dalitz decays and other resonance decays. The moments of higher rank do not show this power law behaviour and it is also not expected that objects of that size should develop a fractal structure at the energy of this experiment.

Chapter 9

Two-particle correlations

9.1 Bose-Einstein correlations

In the previous discussion of multiparticle production the relevance of particle correlations has been pointed out. In this context the analysis of Bose-Einstein correlations is important, as it gives access to the space-time structure underlying particle production in e^+e^- annihilation. In addition, such an analysis allows us to determine the corresponding parameters of the Jetset model.

9.1.1 Introduction

It is a general belief that Bose-Einstein correlations in e^+e^- annihilation occur as a consequence of quantum-mechanical interference among identical bosons. This effect becomes visible as an enhancement in the correlation function

$$C_2(p_1, p_2) = \frac{\rho_2(p_1, p_2)}{\rho_1(p_1)\rho_1(p_2)} \tag{9.1}$$

of two identical pions with 4-momentum p_1 and p_2 respectively. The analysis is done as a function of the Lorentz invariant $Q = \sqrt{-(p_1 - p_2)^2}$, which is the momentum difference in the centre of mass of the pair, and is equal to $\sqrt{M^2 - 4m_\pi^2}$ if both particles are pions.

Neither the numerator nor the denominator of (9.1) can be determined directly from the data: $\rho_2(Q)$ receives unwanted contributions from non-identical particle pairs, such as pion-kaon pairs. Furthermore, a certain fraction of particle pairs consists of electro-weak decay products; e.g. from D^0, K_S^0 and η decays. It is not expected that particle pairs containing such electro-weak decay products experience Bose-Einstein correlations with an effective radius small enough to be observed experimentally [85]. These two effects result in a reduction of the original enhancement.

The denominator in (9.1) is not directly accessible, but can be approximated by $\rho_2^0(Q)$, i.e. by the density of oppositely charged particle pairs, with inherent problems.

In the case where the emission is completely incoherent and comes from a Gaussian shaped source the correlation function takes the form:

$$C_2(Q) = 1 + \lambda e^{-R^2 Q^2} . \tag{9.2}$$

The parameter λ allows for partial coherent emission and for other effects, causing an apparent reduction of the real enhancement. The parameter R is related to the mean square radius R_0 of the source; i.e. $R_0 = \hbar c R$.

9.1.2 Analysis

The basis for the present analysis is a sample of 18,543 multihadronic annihilation events, the selection of which has been described in section 4.1. In addition, V^0 pairs identified as secondary K_S^0 or Λ decays or photon conversion in detector material are rejected (see [23,33] for details of the V^0 identification).

Two different reference samples. determined entirely from the data, are used in this analysis:

I. *Neutral pairs from the same event:* these have the kinematical and topological features in common with the like-sign pairs. This reference sample is strongly affected by resonance production, requiring sizeable Monte Carlo corrections with their inherent uncertainties.

II. *Neutral pairs from mixed jets:* in this case correlations among particles of opposite charge (e.g. due to resonance decays) are circumvented by reflecting all positively (or negatively) charged particles at a plane perpendicular to the sphericity axis. By means of this *jet mixing*, correlations due to unlike-sign particle pairs are destroyed, while like-sign correlations are retained and moreover the event topology is preserved. This method has been developed in the course of the present work [61,62] and was recently applied by the ALEPH collaboration [87]. It works ideally for two-jet events, since hard gluon radiation tends to invalidate this reference sample, requiring a Monte Carlo correction. This correction is comparatively small and moreover does not depend on details of resonance production, the latter being modeled only crudely in the Monte Carlo. Therefore systematic uncertainties are reduced, and thus the results obtained from this method appear to be more reliable.
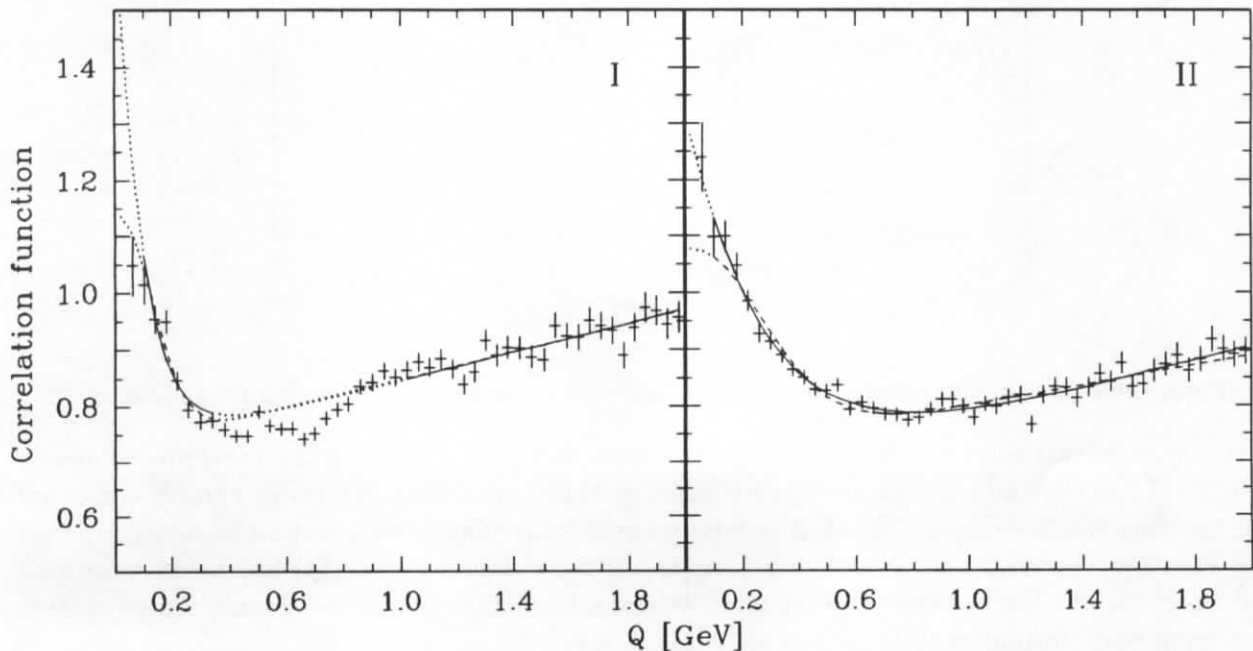
Figure 9.1: Raw correlation function: reference sample I (left) and reference sample II (right). The curves represent the fit results: Gaussian fit (dashed curve) and exponential fit (solid curve); the dotted range is excluded from the fit.

The correlation functions, using the two reference samples, are presented in figure 9.1. In extracting the parameters λ and R_0, imperfections of the reference sample can be accounted for by multiplying (9.2) with a linear function of Q:

$$\text{Gaussian} \qquad C(Q) = (a_1 + a_2 Q)(1 + \lambda e^{-R^2 Q^2}) , \qquad (9.3)$$

$$\text{Exponential} \qquad C(Q) = (a_1 + a_2 Q)(1 + \lambda e^{-RQ}) , \qquad (9.4)$$

where the a_i are free parameters. In addition to the Gaussian function (9.3) the exponential function (9.4) is used in this analysis – the fits to these functions are indicated in figure 9.1. Q values below 0.08 GeV are generally excluded from the fit to reduce systematic uncertainties, which may arise from the strong detector effects in this region. In addition, for reference sample I the Q region $0.3 - 1$ GeV, which is heavily affected by resonance decays, is excluded from the fit (figure 9.1). More importantly, just underneath the expected Bose-Einstein enhancement, strong contributions from η and η' decays occur, as is visible in figure 9.2.
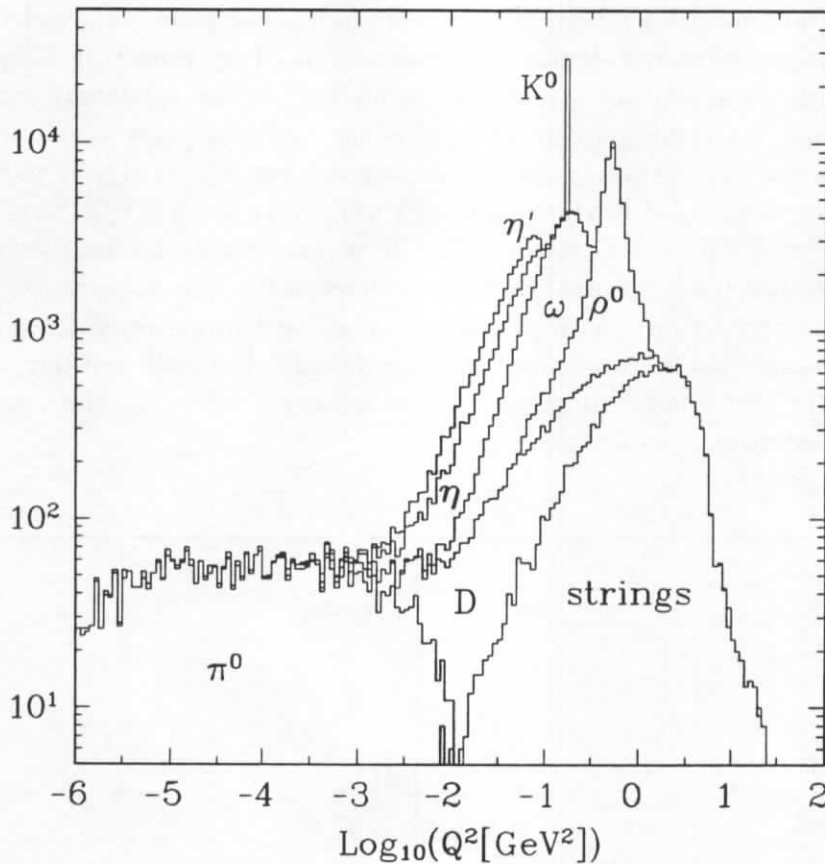
Figure 9.2: Q^2 distribution of e^+e^- and $\pi^+\pi^-$ pairs, obtained from the Jetset 7.3 PS simulation.

Detector effects tend to cancel in the correlation function, provided the tracking efficiency is identical for like- and unlike-sign particle pairs. The remaining difference can be corrected with the function $\varepsilon_1(Q) = C_{MC}^{gen}/C_{MC}^{det}$, where the Monte Carlo need not necessarily contain Bose-Einstein correlations. In this analysis the detector correction $\varepsilon_1(Q)$ has been computed from both Monte Carlo versions with and without Bose-Einstein correlations. As expected, these gave very similar results (see table 9.1).

Imperfections of the reference sample are unfolded by normalizing the corrected correlation function to the correlation function generated by the Monte Carlo with the Bose-Einstein effect switched off.

Correlation function	Fit	Reference sample I		Reference sample II	
		λ Strength	R_0 Radius [fm]	λ Strength	R_0 Radius [fm]
Data raw	Gauss.	0.55 ± 0.06	1.09 ± 0.09	0.52 ± 0.03	0.56 ± 0.03
	Exp.	1.32 ± 0.22	2.14 ± 0.27	1.05 ± 0.05	0.75 ± 0.02
Data corrected[a]	Gauss.	0.20 ± 0.04	0.75 ± 0.12	0.23 ± 0.02	0.55 ± 0.05
	Exp.	0.31 ± 0.08	1.13 ± 0.31	0.43 ± 0.04	0.66 ± 0.06
Data corrected[b]	Gauss.	0.21 ± 0.04	0.84 ± 0.17	0.25 ± 0.03	0.73 ± 0.09
	Exp.	0.38 ± 0.09	1.38 ± 0.27	0.41 ± 0.04	0.70 ± 0.16

Table 9.1: Bose-Einstein results: *a)* detector correction with Jetset 7.2 PS, *b)* detector correction with Jetset 7.2 PS+BE; the corrected correlation functions are normalized to Jetset 7.2 PS.

The corrected correlation function $C_2(Q)$ is presented in figure 9.3 and the fit results are summarized in table 9.1. In our case the fit slightly favours the exponential function (9.4) from the Gaussian function (9.3). For the final values of λ and R_0 the results from the two
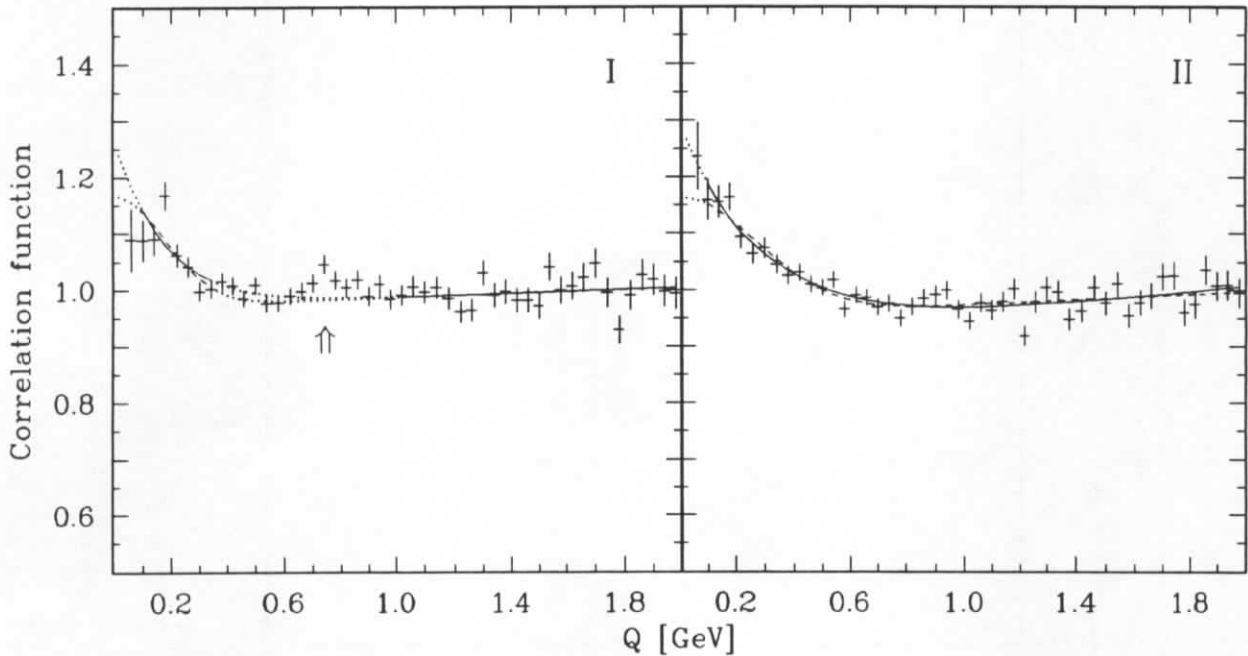
Figure 9.3: Corrected correlation function: reference sample I (left) and reference sample II (right). The curves represent fit results: Gaussian fit (dashed curve) and exponential fit (solid curve); the dotted range is excluded from the fit. The structure at $Q \approx 0.75$ GeV in the left hand plot is due to a ρ^0 mass shift of ≈ 20 MeV.

reference samples are combined. This yields:

Gaussian	$\lambda = 0.22 \pm 0.03$, $R_0 = 0.61 \pm 0.08$ fm
Exponential	$\lambda = 0.40 \pm 0.05$, $R_0 = 0.71 \pm 0.10$ fm

These results do not include Coulomb corrections nor non-pion corrections. Similar values of these parameters are reported by TASSO ($\lambda = 0.35 \pm 0.03$, $R_0 = 0.80 \pm 0.06$ fm) [86] and ALEPH ($\lambda = 0.28 \pm 0.01$, $R_0 = 0.51 \pm 0.02$ fm) [87].

Jetset Bose-Einstein model: The parameters required by the Jetset Bose-Einstein model to reproduce our data were determined to:

$$
\begin{array}{ll}
\lambda & = 2.4 \pm 0.3 \\
R_0 & = 0.60 \pm 0.08 \text{ fm}
\end{array}
$$

Here, the exponential function was used to describe the shape of the Bose-Einstein enhancement, which is slightly favoured by our data. These values are in good agreement with those obtained by the OPAL collaboration at LEP; i.e. $\lambda = 2.5$, $R_0 = 0.60$ fm [88]. This can be regarded as a success for the Bose-Einstein model of Sjöstrand [9], insofar as it provides a description of the effect, independent of the centre of mass energy. The radius of the pion source, inferred from Bose-Einstein correlations is in remarkable agreement with the transverse extension of the Lund string of 0.56 fm (see section 6.4.2.1). However, the large value required for λ (≈ 2.4), which is supposed to be smaller than one, indicates that Bose-Einstein correlations are still not understood in the scope of this model.
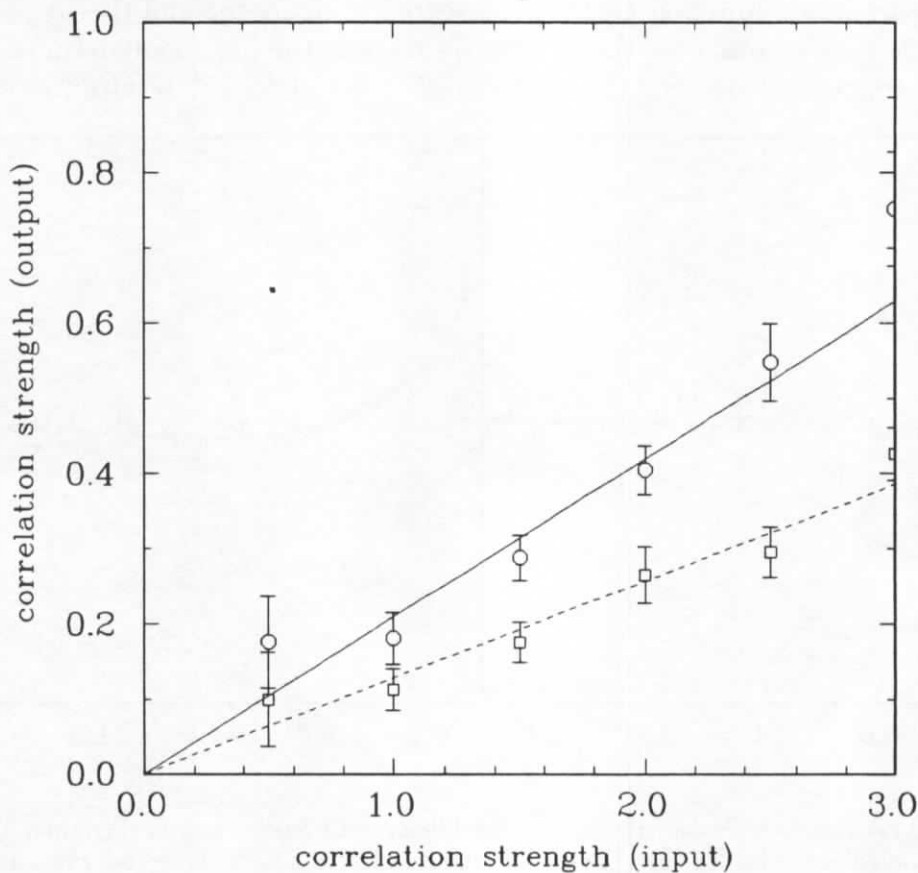
Figure 9.4: Comparison of input/output correlation strength in Herwig (squares) and Jetset (circles).

In this context, the relation between input and output correlation strength in the Jetset Bose-Einstein model is analysed. It is found that the output strength (using jet-mixing, and normalizing to the model prediction without Bose-Einstein correlations) is approximately 1/5 of the input strength in case of the Jetset 7.2 PS simulation, and even smaller (1/8) in the Herwig 5.0 PS simulation (see figure 9.4). The weaker response observed in Herwig is due to a lower rate of like-sign charged particle pairs within the effective Bose-Einstein radius.

9.2 ρ^0 meson mass shift

An interesting structure is seen in figure 9.3, where the two-particle correlation function obtained from the data is normalized to the corresponding function from the Monte Carlo simulation without Bose-Einstein correlations. At $Q \approx 0.75$, i.e. in the ρ^0 resonance region, a variation of the correlation function is observed, which can be attributed to an apparent shift of the ρ^0 meson mass of ≈ 20 MeV. This observation is supported by data from PETRA [86] and LEP [87], which all show the same structure (figure 9.5).
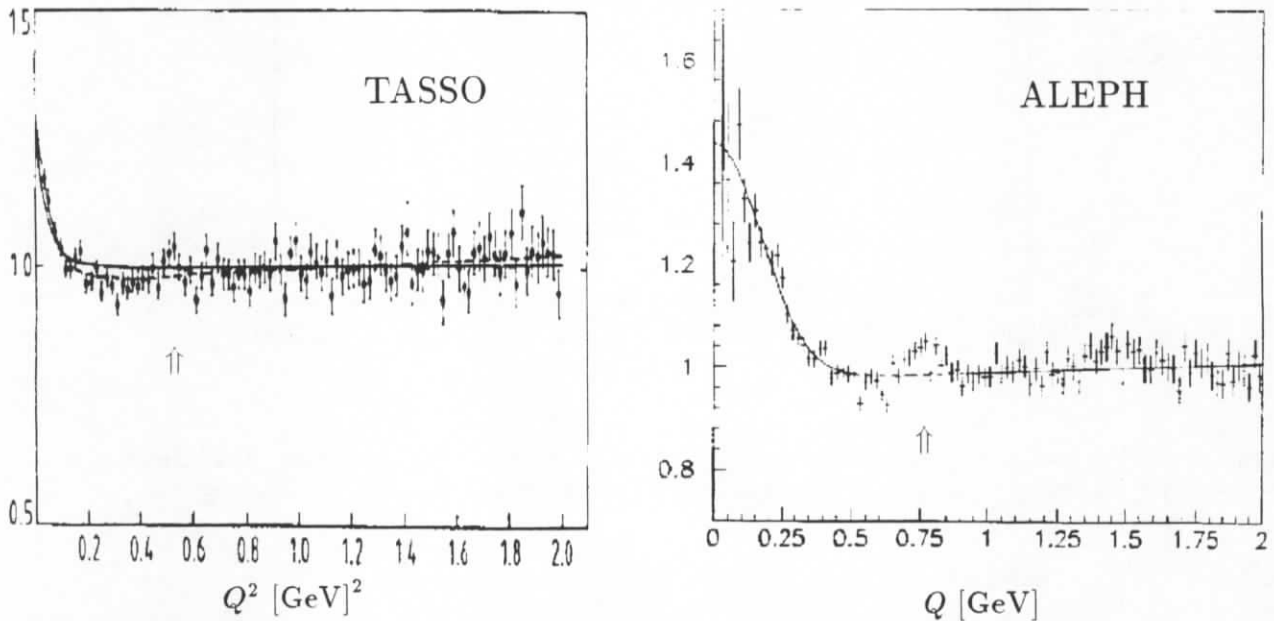
Figure 9.5: Two-particle correlation function $C_2(Q)$ from TASSO [86] at PETRA and ALEPH at LEP [87], normalized to the corresponding Monte Carlo prediction without Bose-Einstein correlations: a clear structure is seen at $Q^2 \approx 0.56$, $Q \approx 0.75$, which is attributed to an apparent shift of the ρ^0 meson mass of ≈ 20 MeV.

This effect is seen more directly if the Q distribution of $\pi^+\pi^-$ pairs from the Monte Carlo simulation is subtracted from the data. Since the Monte Carlo contains a standard ρ^0 Breit-Wigner, the mass shift is clearly revealed (figure 9.6).

Surprisingly, the Bose-Einstein model of Sjöstrand produces an effective ρ^0 meson mass shift of the same order of magnitude, as is indicated in figures 9.6 and 9.7. Since this model does not contain specific assumptions on the $\pi\pi$ strong interactions, but is rather a parameterization of the Bose-Einstein effect, the occurrence of a ρ^0 mass shift in this model is considered as the consequence of kinematical constraints.

In figure 9.7 the interference term:

$$\frac{m_{\pi^+\pi^-}^2 - m_\rho^2}{(m_{\pi^+\pi^-}^2 - m_\rho^2)^2 + m_\rho^2 \Gamma_\rho^2} \, , \tag{9.5}$$

is also indicated. This interference term provides an explanation for the ρ^0 meson mass shift observed in ρ^0 photoproduction [90]; however, it does not describe the effect observed in e^+e^- annihilation.
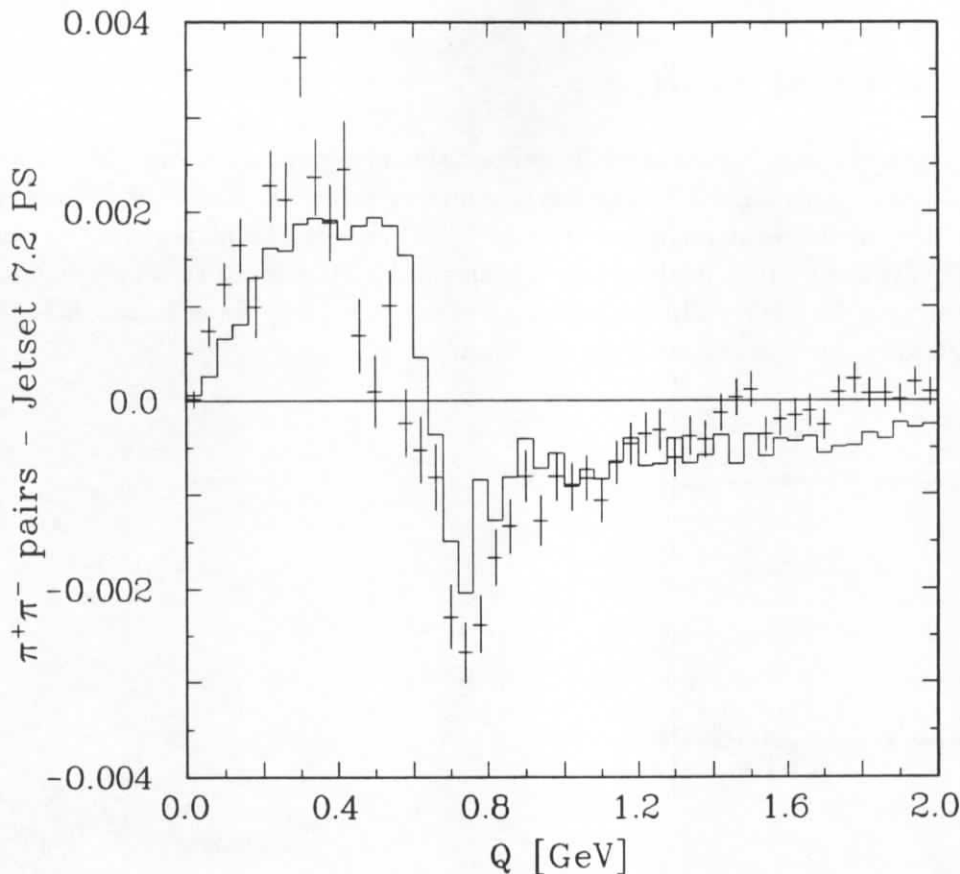
Figure 9.6: Q distribution of $\pi^+\pi^-$ pairs, with the Jetset 7.2 PS prediction subtracted. The histogram shows the Jetset 7.2 PS+BE simulation, with the Jetset 7.2 PS prediction subtracted.

9.2.1 $\rho^0\pi^+$ model

In the above analysis two different effects were identified in the data: the well-known Bose-Einstein effect – and a new effect, revealing itself as an apparent shift of the ρ^0 meson mass.

We note that in both cases charged pions are involved which take part in the strong interaction. In this section a simple model is presented, which demonstrates that the two effects are intimately connected and in fact have a common origin.

The simplest final states in e^+e^- annihilation, of relevance for the present investigation, are of the following type:

$$e^+e^- \rightarrow \pi_1^+\pi_2^+\pi_3^- X^- \ ,$$

where either the $\pi_1^+\pi_3^-$ or the $\pi_2^+\pi_3^-$ can form a ρ^0 meson.

To study this process three-pion phase space events are generated with a distribution in total energy according to $\rho^0\pi^+$ combinations in the Lund model. The events are produced with the following matrix elements:

$$\mathcal{M}_{non-sym} \ = \ BW(m_{13}) \ , \tag{9.6}$$

$$\mathcal{M}_{sym} \ = \ \frac{1}{\sqrt{2}}\left[BW(m_{13}) + BW(m_{23})\right] \ , \tag{9.7}$$

where $BW(m_{ij})$ is the ρ Breit-Wigner:

$$BW(m_{ij}) = \frac{m_\rho\Gamma_\rho}{m_\rho^2 - m_{ij}^2 - im_\rho\Gamma_\rho} \ . \tag{9.8}$$
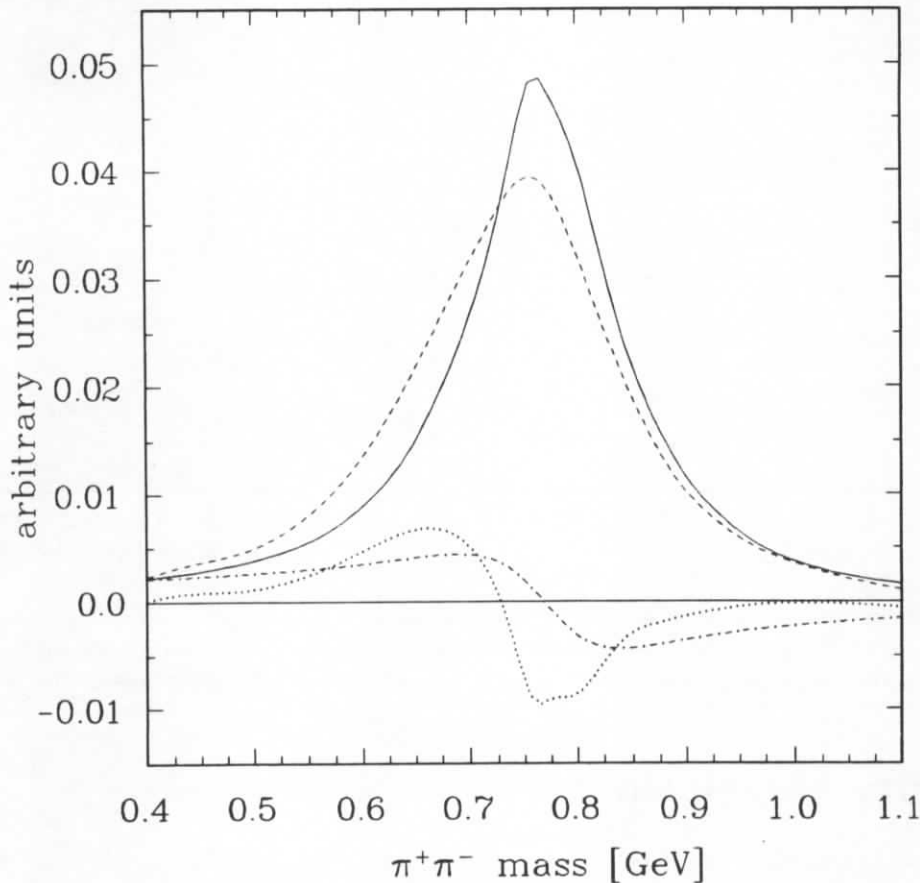
Figure 9.7: ρ^0 meson mass shift induced by Bose-Einstein correlations in the Jetset model: the solid curve shows the Breit-Wigner generated by Jetset 7.2 PS. After Bose-Einstein correlations are included as a classical force, acting on the final state pions, the dashed curve is obtained. The dotted curve shows the difference of the two and the dash-dotted curve indicates the interference term (9.5).

The matrix element $\mathcal{M}_{non-sym}$ corresponds to the situation in hadronization models, where particle production is described as a stochastic process, completely neglecting quantum mechanical interference. In contrast, the matrix element $\mathcal{M}_{sym}$ is symmetric under exchange of the identical pions π_1^+ and π_2^+, preserving the interference structure.

In figure 9.8 the two-particle correlation function $C_2(Q_{12}) = f^{sym}(Q_{12})/f^{non-sym}(Q_{12})$ of the two identical pions π_1^+ and π_2^+ is shown. A clear enhancement is seen at low Q values, corresponding to a strength $\lambda = 0.7$ and a radius $R_0 = 2.4$ fm. The enhancement is well described by the exponential form (9.4), with an additional quadratic term to describe the decrease at large Q values.

In addition, the $\pi^+\pi^-$ invariant mass distribution is modified by the symmetrized matrix element. This is indicated in figure 9.8, where the mass distributions $f^{non-sym}(m_{13}, m_{23})$ and $f^{sym}(m_{13}, m_{23})$ as well as the difference of the two are shown.

This model thus provides a qualitative description of both the Bose-Einstein effect and the ρ^0 meson mass shift, as observed in e^+e^- annihilation. These two effects have a common origin, namely the interference term in (9.7).

It did not escape our attention that the apparent ρ^0 meson mass shift must be taken into account, if the inclusive ρ^0 production cross section is to be determined.
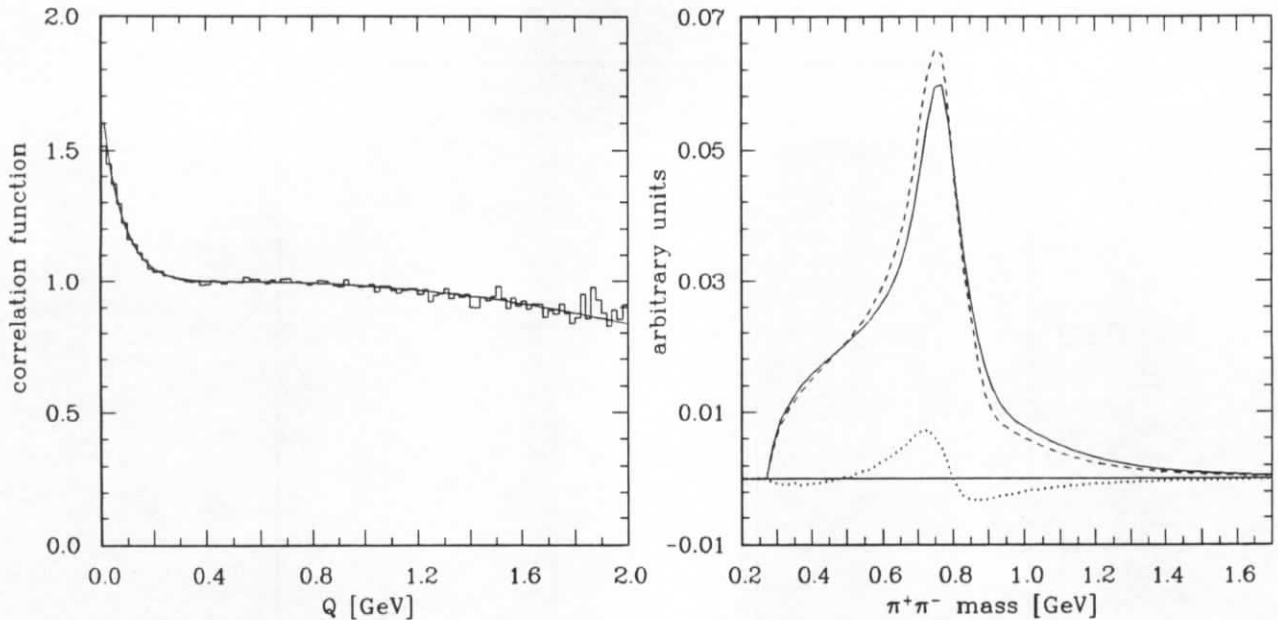
Figure 9.8: Correlation function and mass distribution, obtained from the $\rho^0\pi^+$ model (see text). The dashed curve in the right hand plot is obtained from the symmetrized matrix element (9.7) and the solid curve corresponds to the non-symmetric matrix element (9.6); the dotted curve is the difference of the two, i.e. the interference term.

9.3   Rapidity correlations

Complementing the analyses of the preceding sections, an analysis of rapidity correlations is presented. For this purpose, the rapidity correlation functions are defined as follows [83],

$$\rho_1(y_1) \;=\; \left\langle \sum_i \delta(y_1 - y_i) \right\rangle , \tag{9.9}$$

$$\rho_2(y_1, y_2) \;=\; \left\langle \sum_{i \neq j} \delta(y_1 - y_i)\delta(y_2 - y_j) \right\rangle , \tag{9.10}$$

where the square brackets indicate the average over all events, and the sum runs over all rapidity bins δ.

Here we present results in terms of the reduced cumulant:

$$k_2(y_1, y_2) = \frac{\rho_2(y_1, y_2)}{\rho_1(y_1)\rho_1(y_2)} - 1 . \tag{9.11}$$

Apparently $k_2(y_1, y_2)$ vanishes in the case where the two variables become statistically independent. In figure 9.9 the CELLO data on $k_2(y_1, y_2)$ are plotted for the total event sample and for selected two-jet events. Strong correlations with a range of one unit in rapidity are observed. These are seen to be much weaker in the two-jet sample, which indicates their origin due to hard gluon radiation. In addition strong long range correlations due to energy-momentum conservation are observed. The corresponding projections along the main diagonal are displayed in figure 9.10 and compared to the Lund model, which is seen to reproduce the data quite well. As in the factorial moment analysis the Monte Carlo including Bose-Einstein correlations gives a better description of the data at small δy. It is also seen that the correlations are larger for $y \leq 0$, i.e. in the event hemisphere opposite of the most energetic jet, which is likely to contain additional particles from gluon jets.
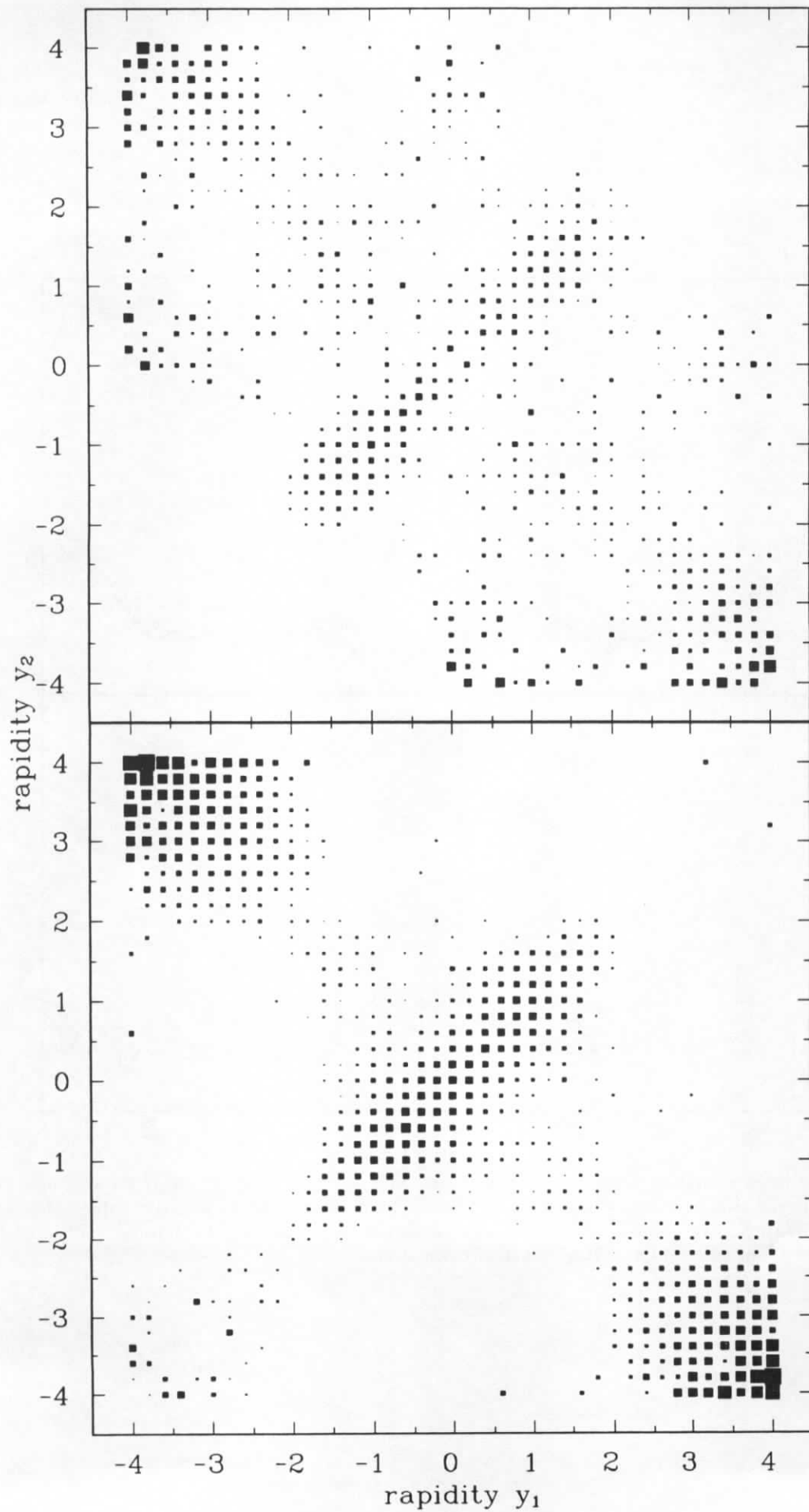
Figure 9.9: Reduced cumulant $k_2(y_1, y_2)$: total event sample (lower plot) and two-jet events (upper plot).
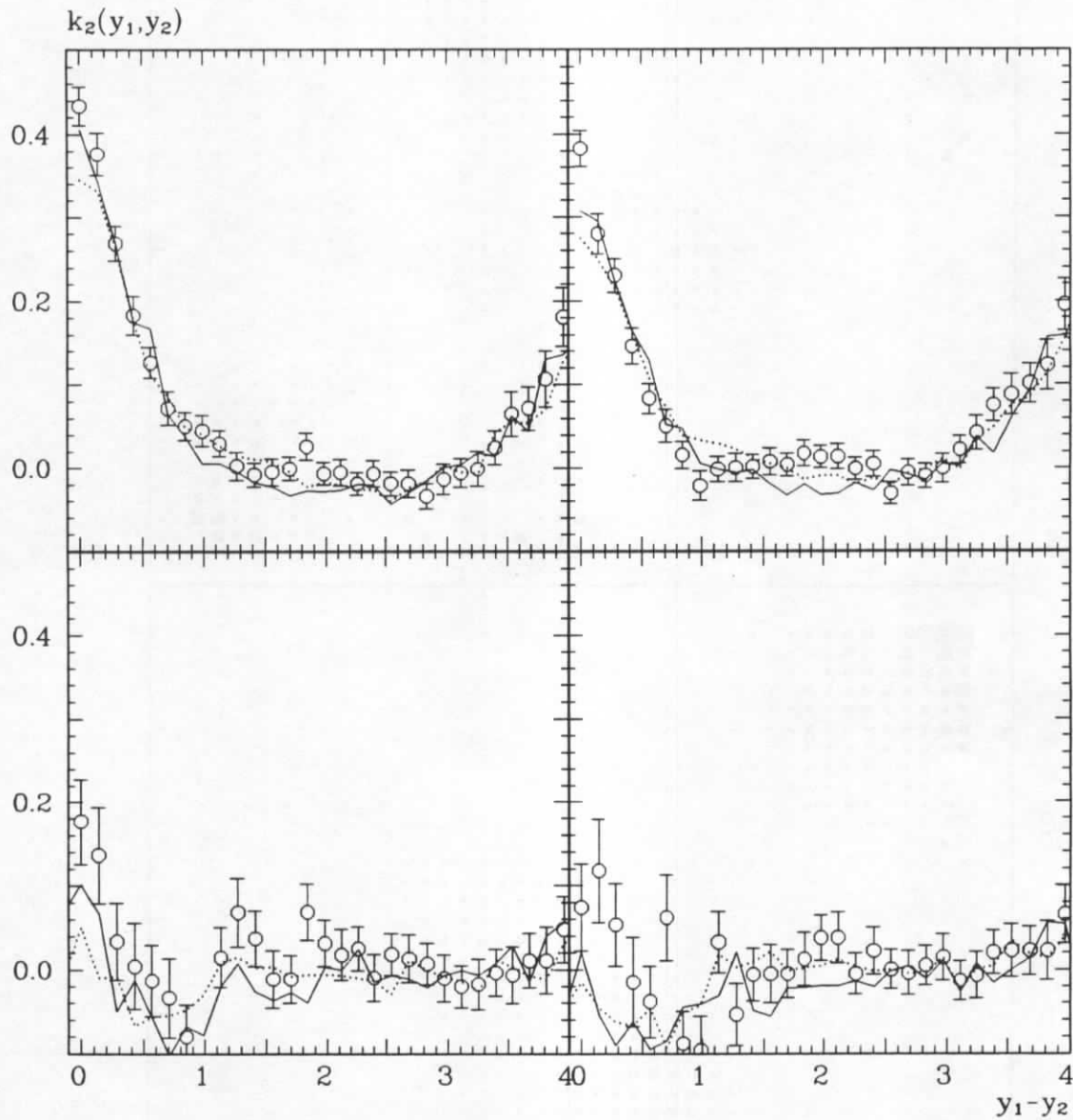
Figure 9.10: Reduced cumulant $k_2(y_1, y_2)$ averaged over $|y_1 + y_2| \leq 0.6$ for the entire data sample (upper plots) and for selected two-jet events (lower plots). The left plots correspond to negative values of y_1 and y_2 and the right plots to positive values. The data (open circles) are compared to the Jetset 7.2 PS model with (solid lines) and without (dotted lines) Bose-Einstein correlations.

Chapter 10

Summary on multiparticle production

We have presented detailed investigations of multiparticle production in e^+e^- annihilation. Correlations and fluctuations among the final state particles were used to give information on the perturbative and non-perturbative phase of e^+e^- annihilation. This procedure provided access to the underlying production mechanism and allowed us to distinguish between cluster and string fragmentation models. The basic results and conclusions are summarized here:

- Correlations and fluctuations depend strongly on rapidity: owing to phase space constraints and other conservation laws, fluctuations of the particle density are of binomial type (less than Poissonian) for $|y| > 2$. In contrast, the central rapidity region is characterized by gluon radiation and particle decays with negative binomial fluctuations (larger than Poissonian).

- In an analysis of the total event sample, multiplicity fluctuations are to a large extent caused by the occasional appearance of hard gluons, concealing other effects. For this reason, various QCD based hadronization models all give the same result, such that they cannot be distinguished by the experiment.

- Access to the non-perturbative phase is provided by a two-jet selection: here cluster and string fragmentation differs significantly, where the former is favoured by the experimental data.

    - The Lund symmetric fragmentation produces particles off the string with a regular pattern in rapidity and azimuth, such that density fluctuations occuring during parton shower evolution are smoothed and underestimate the data.

    - Owing to the local nature of particle production in the Herwig cluster model, density fluctuations from the parton shower are transferred to the cluster distribution. This model provides a good description of the data, which supports the hypothesis of local parton-hadron duality.

    - Further, it is noted that the mass spectrum of primary particles in the string model is considerably softer than the corresponding cluster mass spectrum. As this is no genuine property of the string model, but rather due to our limited knowledge of the higher resonances, it is suggested that the mass spectrum should be modified to reproduce the primordial resonance mass spectrum, as is the case in the cluster model. Still this does not guarantee larger correlations, since the Lund symmetric function would order heavier particles more strictly.

- Evidence for a string-like nature of particle production comes from the requirement of string-like fission of heavy clusters, without which the cluster model would also fail to describe the data.

- Azimuthal anti-correlations, predicted by the string model due to local $p_\perp$ conservation, are not observed with the same strength in the data. However, the inclusion of the Bose-Einstein effect as a classical force in the string model diminishes these anti-correlations and this model provides a good description of the data. The Herwig cluster model fails to describe the azimuthal correlations, indicating that isotropic two-body decays of clusters may be too poor an approximation of reality. The model behaviour is not rectified by inclusion of the Bose-Einstein effect.

- The significance of Bose-Einstein correlations is completely different in the Lund string and the Herwig cluster model. This is for two reasons: firstly, Herwig contains fewer like-sign particle pairs within the effective Bose-Einstein radius of the model. And secondly, particles are produced coherently off the string, while cluster fragments are in a disordered state. Therefore, the Bose-Einstein effect causes a strong disruption of the initial ordering of particles produced off the string. Since this ordering never existed, among cluster decay products, only a negligible effect results in this case.

- The importance of the phase space dimension is seen in the higher-dimensional intermittency analyses, which yield factorial moments growing as a power with the resolution scale. This is observed only for the moments of rank two and three, however, and has a rather trivial origin in Dalitz decays and other resonance decays. The moments of higher rank do not show this power law behaviour and it is also not expected that objects of that size should develop a fractal structure at the energy of this experiment.

- Bose-Einstein correlations are observed with a strength $\lambda = 0.2 - 0.4$ and an associated radius of $R_0 = 0.6 - 0.7$ fm, depending on the assumed shape of the correlation function.

- A new phenomenon is observed in the data, namely an apparent shift of the ρ^0 meson mass of approximately 20 MeV.

An explanation for both the Bose-Einstein effect and the ρ^0 meson mass shift is provided in terms of interference in a three pion system, where two ρ^0 meson combinations are possible.

Appendix A

Factorial moments in one dimension

The results tabulated here and in the following appendices are entirely written by a computer program. In addition to the CELLO data the corresponding results from Jetset 7.2 PS and Jetset 7.2 PS+BE are presented. The Monte Carlo results are given both on the generator level (indicated as g) and on the detector level (indicated as d).

| | | $\langle F^2 \rangle$ one-dimensional analysis (full y) | | | | |

Transformation:		None		Ochs		Białas
Normalization:		vertical	horizontal	vertical	horizontal	horizontal
CELLO	1	0.984 ± 0.005	0.984 ± 0.005	0.984 ± 0.005	0.984 ± 0.005	0.984 ± 0.005
J 7.2 PS+BE d	1	0.978 ± 0.004	0.978 ± 0.004	0.978 ± 0.004	0.978 ± 0.004	0.978 ± 0.004
J 7.2 PS+BE g	1	1.040 ± 0.003	1.040 ± 0.003	1.040 ± 0.003	1.040 ± 0.003	1.036 ± 0.003
J 7.2 PS d	1	0.979 ± 0.002	0.979 ± 0.002	0.979 ± 0.002	0.979 ± 0.002	0.979 ± 0.002
J 7.2 PS g	1	1.042 ± 0.006	1.042 ± 0.006	1.042 ± 0.006	1.042 ± 0.006	1.038 ± 0.006
CELLO	2	0.975 ± 0.005	0.981 ± 0.005	0.975 ± 0.005	0.975 ± 0.005	0.975 ± 0.005
J 7.2 PS+BE d	2	0.971 ± 0.004	0.975 ± 0.004	0.971 ± 0.004	0.971 ± 0.004	0.971 ± 0.004
J 7.2 PS+BE g	2	1.077 ± 0.003	1.077 ± 0.003	1.077 ± 0.003	1.077 ± 0.003	1.073 ± 0.003
J 7.2 PS d	2	0.966 ± 0.002	0.971 ± 0.002	0.966 ± 0.002	0.966 ± 0.002	0.966 ± 0.002
J 7.2 PS g	2	1.069 ± 0.006	1.070 ± 0.006	1.070 ± 0.006	1.070 ± 0.006	1.066 ± 0.006
CELLO	4	0.981 ± 0.007	1.542 ± 0.009	1.064 ± 0.006	1.064 ± 0.006	1.063 ± 0.006
J 7.2 PS+BE d	4	0.968 ± 0.006	1.544 ± 0.007	1.055 ± 0.005	1.055 ± 0.005	1.055 ± 0.005
J 7.2 PS+BE g	4	1.139 ± 0.005	1.772 ± 0.006	1.176 ± 0.004	1.176 ± 0.004	1.171 ± 0.004
J 7.2 PS d	4	0.963 ± 0.003	1.549 ± 0.004	1.044 ± 0.003	1.044 ± 0.003	1.044 ± 0.003
J 7.2 PS g	4	1.122 ± 0.008	1.763 ± 0.011	1.159 ± 0.007	1.159 ± 0.007	1.155 ± 0.007
CELLO	8	0.980 ± 0.050	1.674 ± 0.010	1.122 ± 0.007	1.122 ± 0.007	1.122 ± 0.007
J 7.2 PS+BE d	8	0.861 ± 0.023	1.673 ± 0.009	1.105 ± 0.006	1.105 ± 0.006	1.105 ± 0.006
J 7.2 PS+BE g	8	1.148 ± 0.027	1.948 ± 0.007	1.246 ± 0.004	1.246 ± 0.004	1.241 ± 0.004
J 7.2 PS d	8	0.886 ± 0.017	1.668 ± 0.005	1.089 ± 0.003	1.089 ± 0.003	1.089 ± 0.003
J 7.2 PS g	8	1.256 ± 0.057	1.930 ± 0.013	1.220 ± 0.007	1.220 ± 0.007	1.216 ± 0.007
CELLO	16	0.893 ± 0.024	1.793 ± 0.012	1.148 ± 0.008	1.148 ± 0.008	1.148 ± 0.008
J 7.2 PS+BE d	16	0.843 ± 0.015	1.783 ± 0.010	1.125 ± 0.006	1.125 ± 0.006	1.125 ± 0.006
J 7.2 PS+BE g	16	1.767 ± 0.261	2.069 ± 0.008	1.278 ± 0.005	1.278 ± 0.005	1.274 ± 0.005
J 7.2 PS d	16	0.843 ± 0.010	1.765 ± 0.006	1.107 ± 0.004	1.107 ± 0.004	1.107 ± 0.004
J 7.2 PS g	16	2.602 ± 0.865	2.036 ± 0.014	1.244 ± 0.008	1.244 ± 0.008	1.240 ± 0.008
CELLO	32	0.865 ± 0.022	1.834 ± 0.014	1.150 ± 0.009	1.150 ± 0.009	1.150 ± 0.009
J 7.2 PS+BE d	32	0.844 ± 0.015	1.821 ± 0.011	1.135 ± 0.007	1.135 ± 0.007	1.135 ± 0.007
J 7.2 PS+BE g	32	3.667 ± 1.379	2.124 ± 0.009	1.296 ± 0.005	1.296 ± 0.005	1.291 ± 0.005
J 7.2 PS d	32	0.841 ± 0.011	1.802 ± 0.006	1.116 ± 0.004	1.116 ± 0.004	1.116 ± 0.004
J 7.2 PS g	32	10.087 ± 8.454	2.080 ± 0.015	1.262 ± 0.009	1.262 ± 0.009	1.257 ± 0.009
CELLO	64	0.837 ± 0.017	1.848 ± 0.016	1.142 ± 0.011	1.142 ± 0.011	1.141 ± 0.011
J 7.2 PS+BE d	64	0.832 ± 0.016	1.827 ± 0.013	1.145 ± 0.009	1.145 ± 0.009	1.146 ± 0.009
J 7.2 PS+BE g	64	7.492 ± 4.352	2.147 ± 0.010	1.307 ± 0.006	1.307 ± 0.006	1.302 ± 0.006
J 7.2 PS d	64	0.833 ± 0.016	1.812 ± 0.008	1.121 ± 0.005	1.121 ± 0.005	1.121 ± 0.005
J 7.2 PS g	64	7.943 ± 6.319	2.102 ± 0.017	1.271 ± 0.011	1.271 ± 0.011	1.265 ± 0.010
CELLO	128	0.828 ± 0.019	1.848 ± 0.020	1.121 ± 0.015	1.121 ± 0.015	1.126 ± 0.015
J 7.2 PS+BE d	128	0.854 ± 0.028	1.847 ± 0.016	1.153 ± 0.012	1.153 ± 0.012	1.155 ± 0.012
J 7.2 PS+BE g	128	8.619 ± 6.016	2.168 ± 0.011	1.318 ± 0.007	1.318 ± 0.007	1.311 ± 0.007
J 7.2 PS d	128	0.839 ± 0.028	1.824 ± 0.009	1.125 ± 0.007	1.125 ± 0.007	1.125 ± 0.007
J 7.2 PS g	128	5.481 ± 4.008	2.114 ± 0.020	1.270 ± 0.013	1.270 ± 0.013	1.266 ± 0.013
CELLO	256	0.808 ± 0.026	1.815 ± 0.026	1.127 ± 0.020	1.127 ± 0.020	1.137 ± 0.020
J 7.2 PS+BE d	256	0.878 ± 0.046	1.849 ± 0.022	1.141 ± 0.016	1.141 ± 0.016	1.141 ± 0.016
J 7.2 PS+BE g	256	4.011 ± 2.523	2.191 ± 0.014	1.322 ± 0.010	1.322 ± 0.010	1.310 ± 0.009
J 7.2 PS d	256	0.801 ± 0.014	1.824 ± 0.012	1.111 ± 0.009	1.111 ± 0.009	1.114 ± 0.009
J 7.2 PS g	256	6.480 ± 5.115	2.135 ± 0.024	1.274 ± 0.017	1.274 ± 0.017	1.280 ± 0.017
CELLO	512	0.821 ± 0.039	1.840 ± 0.036	1.137 ± 0.028	1.137 ± 0.028	1.155 ± 0.028
J 7.2 PS+BE d	512	0.952 ± 0.103	1.851 ± 0.029	1.132 ± 0.022	1.132 ± 0.022	1.118 ± 0.022
J 7.2 PS+BE g	512	5.441 ± 4.285	2.213 ± 0.018	1.344 ± 0.013	1.344 ± 0.013	1.335 ± 0.013
J 7.2 PS d	512	0.803 ± 0.021	1.813 ± 0.016	1.106 ± 0.013	1.106 ± 0.013	1.108 ± 0.013
J 7.2 PS g	512	1.489 ± 0.334	2.170 ± 0.032	1.285 ± 0.023	1.285 ± 0.023	1.281 ± 0.023

Table A.1: $\langle F^2 \rangle$ one-dimensional analysis (full y).

$\langle F^3 \rangle$ one-dimensional analysis (full y)					
Transformation:	None		Ochs		Białas
Normalization:	vertical	horizontal	vertical	horizontal	horizontal
CELLO　　　1	0.960 ± 0.008	0.960 ± 0.008	0.960 ± 0.008	0.960 ± 0.008	0.959 ± 0.008
J 7.2 PS+BE d　1	0.942 ± 0.006	0.942 ± 0.006	0.942 ± 0.006	0.942 ± 0.006	0.942 ± 0.006
J 7.2 PS+BE g　1	1.116 ± 0.005	1.116 ± 0.005	1.116 ± 0.005	1.116 ± 0.005	1.107 ± 0.005
J 7.2 PS d　1	0.945 ± 0.003	0.945 ± 0.003	0.945 ± 0.003	0.945 ± 0.003	0.945 ± 0.003
J 7.2 PS g　1	1.120 ± 0.009	1.120 ± 0.009	1.120 ± 0.009	1.120 ± 0.009	1.112 ± 0.009
CELLO　　　2	0.942 ± 0.009	0.955 ± 0.008	0.942 ± 0.009	0.942 ± 0.009	0.941 ± 0.008
J 7.2 PS+BE d　2	0.928 ± 0.007	0.939 ± 0.007	0.927 ± 0.007	0.927 ± 0.007	0.927 ± 0.007
J 7.2 PS+BE g　2	1.206 ± 0.006	1.206 ± 0.006	1.207 ± 0.006	1.207 ± 0.006	1.197 ± 0.006
J 7.2 PS d　2	0.915 ± 0.004	0.926 ± 0.004	0.913 ± 0.004	0.913 ± 0.004	0.913 ± 0.004
J 7.2 PS g　2	1.174 ± 0.010	1.174 ± 0.010	1.174 ± 0.010	1.174 ± 0.010	1.166 ± 0.010
CELLO　　　4	0.866 ± 0.013	2.786 ± 0.030	1.243 ± 0.017	1.243 ± 0.017	1.241 ± 0.017
J 7.2 PS+BE d　4	0.851 ± 0.011	2.786 ± 0.025	1.223 ± 0.013	1.223 ± 0.013	1.222 ± 0.013
J 7.2 PS+BE g　4	1.277 ± 0.011	3.792 ± 0.023	1.603 ± 0.012	1.603 ± 0.012	1.590 ± 0.011
J 7.2 PS d　4	0.840 ± 0.007	2.770 ± 0.014	1.188 ± 0.007	1.188 ± 0.007	1.188 ± 0.007
J 7.2 PS g　4	1.236 ± 0.020	3.694 ± 0.039	1.522 ± 0.019	1.522 ± 0.019	1.512 ± 0.019
CELLO　　　8	0.887 ± 0.013	3.379 ± 0.048	1.428 ± 0.023	1.429 ± 0.023	1.426 ± 0.023
J 7.2 PS+BE d　8	0.875 ± 0.010	3.406 ± 0.039	1.380 ± 0.018	1.380 ± 0.018	1.380 ± 0.018
J 7.2 PS+BE g　8	1.711 ± 0.307	5.003 ± 0.041	1.840 ± 0.014	1.840 ± 0.014	1.825 ± 0.014
J 7.2 PS d　8	0.843 ± 0.006	3.370 ± 0.023	1.328 ± 0.010	1.328 ± 0.010	1.328 ± 0.010
J 7.2 PS g　8	1.110 ± 0.015	4.841 ± 0.069	1.714 ± 0.023	1.714 ± 0.023	1.701 ± 0.023
CELLO　　　16	0.954 ± 0.021	4.037 ± 0.067	1.503 ± 0.030	1.503 ± 0.030	1.501 ± 0.030
J 7.2 PS+BE d　16	0.934 ± 0.018	4.018 ± 0.055	1.463 ± 0.024	1.463 ± 0.024	1.463 ± 0.024
J 7.2 PS+BE g　16	1.386 ± 0.133	5.753 ± 0.051	1.971 ± 0.018	1.971 ± 0.018	1.955 ± 0.018
J 7.2 PS d　16	0.882 ± 0.010	3.879 ± 0.030	1.407 ± 0.013	1.407 ± 0.013	1.406 ± 0.013
J 7.2 PS g　16	1.183 ± 0.028	5.451 ± 0.083	1.809 ± 0.029	1.809 ± 0.029	1.795 ± 0.029
CELLO　　　32	1.031 ± 0.037	4.337 ± 0.104	1.543 ± 0.046	1.543 ± 0.046	1.536 ± 0.045
J 7.2 PS+BE d　32	0.943 ± 0.024	4.193 ± 0.072	1.515 ± 0.035	1.515 ± 0.035	1.512 ± 0.035
J 7.2 PS+BE g　32	1.472 ± 0.185	6.190 ± 0.064	2.049 ± 0.024	2.049 ± 0.024	2.037 ± 0.024
J 7.2 PS d　32	0.932 ± 0.014	4.158 ± 0.043	1.467 ± 0.020	1.467 ± 0.020	1.466 ± 0.020
J 7.2 PS g　32	1.230 ± 0.066	5.765 ± 0.105	1.907 ± 0.038	1.907 ± 0.038	1.890 ± 0.038
CELLO　　　64	1.017 ± 0.060	4.306 ± 0.134	1.503 ± 0.065	1.503 ± 0.065	1.497 ± 0.065
J 7.2 PS+BE d　64	0.934 ± 0.031	4.194 ± 0.104	1.569 ± 0.059	1.570 ± 0.059	1.571 ± 0.059
J 7.2 PS+BE g　64	1.272 ± 0.030	6.381 ± 0.083	2.088 ± 0.035	2.088 ± 0.035	2.073 ± 0.035
J 7.2 PS d　64	0.966 ± 0.037	4.182 ± 0.062	1.507 ± 0.033	1.507 ± 0.033	1.508 ± 0.033
J 7.2 PS g　64	1.323 ± 0.101	6.047 ± 0.138	1.958 ± 0.058	1.958 ± 0.058	1.942 ± 0.057
CELLO　　　128	1.166 ± 0.166	4.420 ± 0.222	1.436 ± 0.105	1.436 ± 0.105	1.415 ± 0.104
J 7.2 PS+BE d　128	0.925 ± 0.040	4.309 ± 0.167	1.649 ± 0.099	1.648 ± 0.099	1.672 ± 0.099
J 7.2 PS+BE g　128	1.301 ± 0.055	6.512 ± 0.116	2.170 ± 0.056	2.170 ± 0.056	2.126 ± 0.054
J 7.2 PS d　128	1.046 ± 0.069	4.330 ± 0.102	1.517 ± 0.054	1.517 ± 0.054	1.520 ± 0.054
J 7.2 PS g　128	1.325 ± 0.169	6.101 ± 0.205	1.932 ± 0.090	1.932 ± 0.090	1.887 ± 0.087
CELLO　　　256	1.431 ± 0.493	4.163 ± 0.366	1.392 ± 0.211	1.396 ± 0.212	1.421 ± 0.214
J 7.2 PS+BE d　256	1.065 ± 0.085	4.943 ± 0.362	1.536 ± 0.161	1.532 ± 0.160	1.565 ± 0.162
J 7.2 PS+BE g　256	1.293 ± 0.055	6.676 ± 0.188	2.110 ± 0.090	2.110 ± 0.090	2.084 ± 0.093
J 7.2 PS d　256	1.181 ± 0.253	4.310 ± 0.176	1.438 ± 0.093	1.437 ± 0.093	1.447 ± 0.093
J 7.2 PS g　256	1.252 ± 0.106	6.435 ± 0.336	1.956 ± 0.164	1.956 ± 0.164	2.025 ± 0.161
CELLO　　　512	0.810 ± 0.199	3.794 ± 0.816	1.265 ± 0.365	1.265 ± 0.365	1.264 ± 0.365
J 7.2 PS+BE d　512	0.981 ± 0.132	4.943 ± 0.614	1.523 ± 0.317	1.516 ± 0.316	1.384 ± 0.302
J 7.2 PS+BE g　512	1.285 ± 0.096	6.973 ± 0.335	2.562 ± 0.202	2.554 ± 0.201	2.318 ± 0.188
J 7.2 PS d　512	1.925 ± 1.024	4.310 ± 0.328	1.609 ± 0.201	1.606 ± 0.200	1.542 ± 0.197
J 7.2 PS g　512	1.352 ± 0.299	6.771 ± 0.588	2.145 ± 0.306	2.145 ± 0.306	2.171 ± 0.306

Table A.2: $\langle F^3 \rangle$ one-dimensional analysis (full y).

$\langle F^4 \rangle$ one-dimensional analysis (full y)					
Transformation:		None		Ochs		Białas
Normalization:		vertical	horizontal	vertical	horizontal	horizontal
CELLO	1	0.934 ± 0.011	0.934 ± 0.011	0.934 ± 0.011	0.934 ± 0.011	0.933 ± 0.011
J 7.2 PS+BE d	1	0.898 ± 0.009	0.898 ± 0.009	0.898 ± 0.009	0.898 ± 0.009	0.898 ± 0.009
J 7.2 PS+BE g	1	1.230 ± 0.008	1.230 ± 0.008	1.230 ± 0.008	1.230 ± 0.008	1.215 ± 0.008
J 7.2 PS d	1	0.905 ± 0.005	0.905 ± 0.005	0.905 ± 0.005	0.905 ± 0.005	0.905 ± 0.005
J 7.2 PS g	1	1.237 ± 0.015	1.237 ± 0.015	1.237 ± 0.015	1.237 ± 0.015	1.223 ± 0.015
CELLO	2	0.915 ± 0.014	0.933 ± 0.014	0.919 ± 0.015	0.919 ± 0.015	0.917 ± 0.015
J 7.2 PS+BE d	2	0.887 ± 0.011	0.902 ± 0.011	0.885 ± 0.011	0.885 ± 0.011	0.885 ± 0.011
J 7.2 PS+BE g	2	1.414 ± 0.011	1.411 ± 0.011	1.414 ± 0.011	1.414 ± 0.011	1.396 ± 0.011
J 7.2 PS d	2	0.862 ± 0.006	0.877 ± 0.006	0.859 ± 0.006	0.859 ± 0.006	0.859 ± 0.006
J 7.2 PS g	2	1.327 ± 0.018	1.327 ± 0.018	1.328 ± 0.018	1.328 ± 0.018	1.313 ± 0.018
CELLO	4	0.753 ± 0.019	5.382 ± 0.100	1.725 ± 0.057	1.725 ± 0.057	1.721 ± 0.057
J 7.2 PS+BE d	4	0.754 ± 0.016	5.341 ± 0.079	1.645 ± 0.036	1.645 ± 0.036	1.644 ± 0.036
J 7.2 PS+BE g	4	1.434 ± 0.023	8.928 ± 0.086	2.665 ± 0.039	2.665 ± 0.039	2.628 ± 0.039
J 7.2 PS d	4	0.737 ± 0.012	5.210 ± 0.043	1.559 ± 0.020	1.559 ± 0.020	1.559 ± 0.020
J 7.2 PS g	4	1.376 ± 0.045	8.366 ± 0.137	2.372 ± 0.059	2.372 ± 0.059	2.347 ± 0.059
CELLO	8	1.199 ± 0.044	8.067 ± 0.261	2.230 ± 0.093	2.230 ± 0.093	2.214 ± 0.091
J 7.2 PS+BE d	8	1.166 ± 0.032	8.125 ± 0.208	2.079 ± 0.064	2.079 ± 0.064	2.079 ± 0.064
J 7.2 PS+BE g	8	1.806 ± 0.027	16.436 ± 0.270	3.326 ± 0.057	3.326 ± 0.057	3.285 ± 0.057
J 7.2 PS d	8	1.084 ± 0.017	8.058 ± 0.120	1.953 ± 0.035	1.953 ± 0.035	1.953 ± 0.035
J 7.2 PS g	8	1.589 ± 0.042	15.213 ± 0.427	2.855 ± 0.089	2.855 ± 0.089	2.828 ± 0.089
CELLO	16	1.428 ± 0.062	10.977 ± 0.414	2.415 ± 0.139	2.415 ± 0.139	2.395 ± 0.136
J 7.2 PS+BE d	16	1.374 ± 0.052	10.892 ± 0.350	2.389 ± 0.111	2.390 ± 0.111	2.392 ± 0.111
J 7.2 PS+BE g	16	2.063 ± 0.054	20.570 ± 0.388	3.828 ± 0.088	3.827 ± 0.088	3.779 ± 0.087
J 7.2 PS d	16	1.251 ± 0.027	10.186 ± 0.185	2.248 ± 0.065	2.248 ± 0.065	2.248 ± 0.065
J 7.2 PS g	16	1.715 ± 0.057	18.240 ± 0.589	3.166 ± 0.126	3.166 ± 0.126	3.135 ± 0.125
CELLO	32	1.807 ± 0.153	13.528 ± 1.032	2.737 ± 0.319	2.736 ± 0.318	2.619 ± 0.298
J 7.2 PS+BE d	32	1.458 ± 0.082	11.491 ± 0.533	2.601 ± 0.216	2.600 ± 0.216	2.572 ± 0.214
J 7.2 PS+BE g	32	2.308 ± 0.073	23.799 ± 0.601	4.228 ± 0.146	4.227 ± 0.146	4.204 ± 0.146
J 7.2 PS d	32	1.550 ± 0.065	11.973 ± 0.369	2.619 ± 0.135	2.620 ± 0.135	2.614 ± 0.135
J 7.2 PS g	32	1.936 ± 0.102	20.336 ± 0.901	3.430 ± 0.197	3.430 ± 0.197	3.387 ± 0.196
CELLO	64	1.474 ± 0.160	11.919 ± 1.275	2.312 ± 0.382	2.311 ± 0.381	2.263 ± 0.378
J 7.2 PS+BE d	64	1.485 ± 0.152	11.232 ± 1.002	2.973 ± 0.638	2.976 ± 0.640	2.974 ± 0.640
J 7.2 PS+BE g	64	2.434 ± 0.164	25.370 ± 0.965	4.373 ± 0.320	4.374 ± 0.320	4.301 ± 0.313
J 7.2 PS d	64	1.604 ± 0.146	11.935 ± 0.697	2.784 ± 0.385	2.785 ± 0.385	2.784 ± 0.385
J 7.2 PS g	64	2.125 ± 0.170	22.458 ± 1.383	3.922 ± 0.416	3.920 ± 0.416	3.800 ± 0.405

Table A.3: $\langle F^4 \rangle$ one-dimensional analysis (full y).

$\langle F^5 \rangle$ one-dimensional analysis (full y)					

Transformation:		None		Ochs		Białas
Normalization:		vertical	horizontal	vertical	horizontal	horizontal
CELLO	1	0.911 ± 0.017	0.911 ± 0.017	0.911 ± 0.017	0.911 ± 0.017	0.909 ± 0.017
J 7.2 PS+BE d	1	0.850 ± 0.012	0.850 ± 0.012	0.850 ± 0.012	0.850 ± 0.012	0.850 ± 0.012
J 7.2 PS+BE g	1	1.391 ± 0.014	1.391 ± 0.014	1.391 ± 0.014	1.391 ± 0.014	1.368 ± 0.013
J 7.2 PS d	1	0.862 ± 0.007	0.862 ± 0.007	0.862 ± 0.007	0.862 ± 0.007	0.861 ± 0.007
J 7.2 PS g	1	1.400 ± 0.025	1.400 ± 0.025	1.400 ± 0.025	1.400 ± 0.025	1.379 ± 0.024
CELLO	2	0.906 ± 0.025	0.923 ± 0.023	0.922 ± 0.027	0.922 ± 0.027	0.920 ± 0.027
J 7.2 PS+BE d	2	0.857 ± 0.018	0.871 ± 0.017	0.854 ± 0.018	0.854 ± 0.018	0.854 ± 0.018
J 7.2 PS+BE g	2	1.741 ± 0.022	1.735 ± 0.022	1.742 ± 0.022	1.742 ± 0.022	1.711 ± 0.022
J 7.2 PS d	2	0.818 ± 0.011	0.831 ± 0.010	0.813 ± 0.010	0.813 ± 0.010	0.812 ± 0.010
J 7.2 PS g	2	1.548 ± 0.033	1.549 ± 0.033	1.549 ± 0.033	1.549 ± 0.033	1.525 ± 0.033
CELLO	4	0.787 ± 0.025	10.818 ± 0.333	2.976 ± 0.209	2.977 ± 0.209	2.965 ± 0.209
J 7.2 PS+BE d	4	0.766 ± 0.019	10.550 ± 0.257	2.576 ± 0.110	2.576 ± 0.110	2.575 ± 0.110
J 7.2 PS+BE g	4	1.705 ± 0.043	22.483 ± 0.334	5.398 ± 0.143	5.398 ± 0.143	5.293 ± 0.140
J 7.2 PS d	4	0.732 ± 0.018	10.046 ± 0.140	2.380 ± 0.061	2.380 ± 0.061	2.379 ± 0.061
J 7.2 PS g	4	1.565 ± 0.078	19.922 ± 0.496	4.412 ± 0.205	4.413 ± 0.205	4.352 ± 0.202
CELLO	8	2.197 ± 0.169	22.893 ± 1.540	4.399 ± 0.415	4.400 ± 0.415	4.300 ± 0.397
J 7.2 PS+BE d	8	1.989 ± 0.124	22.357 ± 1.336	3.746 ± 0.257	3.746 ± 0.257	3.743 ± 0.257
J 7.2 PS+BE g	8	3.453 ± 0.099	65.974 ± 1.945	7.333 ± 0.270	7.333 ± 0.270	7.221 ± 0.266
J 7.2 PS d	8	1.773 ± 0.064	22.509 ± 0.759	3.503 ± 0.144	3.503 ± 0.144	3.503 ± 0.144
J 7.2 PS g	8	2.693 ± 0.126	57.194 ± 2.974	5.692 ± 0.439	5.693 ± 0.439	5.649 ± 0.439
CELLO	16	2.724 ± 0.240	33.848 ± 2.549	4.726 ± 0.675	4.726 ± 0.675	4.596 ± 0.654
J 7.2 PS+BE d	16	2.627 ± 0.250	33.906 ± 2.359	4.824 ± 0.529	4.825 ± 0.529	4.828 ± 0.529
J 7.2 PS+BE g	16	4.288 ± 0.171	89.329 ± 3.394	9.261 ± 0.503	9.261 ± 0.503	9.110 ± 0.496
J 7.2 PS d	16	2.239 ± 0.110	30.596 ± 1.218	4.558 ± 0.392	4.558 ± 0.392	4.558 ± 0.392
J 7.2 PS g	16	3.346 ± 0.251	71.764 ± 5.078	6.635 ± 0.623	6.635 ± 0.624	6.590 ± 0.618
CELLO	32	4.839 ± 0.956	57.880 ± 11.173	7.123 ± 2.475	7.113 ± 2.470	6.127 ± 2.328
J 7.2 PS+BE d	32	2.869 ± 0.388	34.673 ± 3.786	5.620 ± 1.447	5.615 ± 1.445	5.502 ± 1.442
J 7.2 PS+BE g	32	5.170 ± 0.305	112.194 ± 6.993	11.084 ± 0.962	11.084 ± 0.962	11.074 ± 0.960
J 7.2 PS d	32	3.418 ± 0.330	42.455 ± 3.456	6.649 ± 0.963	6.650 ± 0.964	6.648 ± 0.964
J 7.2 PS g	32	3.972 ± 0.419	86.748 ± 8.589	7.037 ± 1.061	7.035 ± 1.061	7.024 ± 1.051

Table A.4: $\langle F^5 \rangle$ one-dimensional analysis (full y).

		None		Ochs		Białas
Transformation: Normalization:		vertical	horizontal	vertical	horizontal	horizontal
CELLO	1	1.047 ± 0.008	1.047 ± 0.008	1.047 ± 0.008	1.047 ± 0.008	1.047 ± 0.008
J 7.2 PS+BE d	1	1.049 ± 0.006	1.049 ± 0.006	1.049 ± 0.006	1.049 ± 0.006	1.049 ± 0.006
J 7.2 PS+BE g	1	1.114 ± 0.005	1.114 ± 0.005	1.114 ± 0.005	1.114 ± 0.005	1.114 ± 0.005
J 7.2 PS d	1	1.048 ± 0.004	1.048 ± 0.004	1.048 ± 0.004	1.048 ± 0.004	1.047 ± 0.004
J 7.2 PS g	1	1.113 ± 0.008	1.113 ± 0.008	1.113 ± 0.008	1.113 ± 0.008	1.113 ± 0.008
CELLO	2	1.094 ± 0.008	1.096 ± 0.008	1.095 ± 0.008	1.095 ± 0.008	1.095 ± 0.008
J 7.2 PS+BE d	2	1.104 ± 0.007	1.105 ± 0.007	1.104 ± 0.007	1.104 ± 0.007	1.104 ± 0.007
J 7.2 PS+BE g	2	1.204 ± 0.005	1.211 ± 0.005	1.206 ± 0.005	1.206 ± 0.005	1.206 ± 0.005
J 7.2 PS d	2	1.087 ± 0.004	1.089 ± 0.004	1.087 ± 0.004	1.087 ± 0.004	1.086 ± 0.005
J 7.2 PS g	2	1.182 ± 0.009	1.190 ± 0.009	1.186 ± 0.009	1.186 ± 0.009	1.186 ± 0.009
CELLO	4	1.166 ± 0.010	1.165 ± 0.009	1.156 ± 0.009	1.156 ± 0.009	1.156 ± 0.009
J 7.2 PS+BE d	4	1.171 ± 0.008	1.166 ± 0.008	1.158 ± 0.008	1.158 ± 0.008	1.158 ± 0.008
J 7.2 PS+BE g	4	1.272 ± 0.006	1.279 ± 0.006	1.275 ± 0.006	1.275 ± 0.006	1.275 ± 0.006
J 7.2 PS d	4	1.144 ± 0.004	1.138 ± 0.004	1.133 ± 0.004	1.133 ± 0.004	1.130 ± 0.005
J 7.2 PS g	4	1.237 ± 0.010	1.247 ± 0.010	1.245 ± 0.010	1.245 ± 0.010	1.245 ± 0.010
CELLO	8	1.215 ± 0.011	1.216 ± 0.010	1.198 ± 0.010	1.198 ± 0.010	1.198 ± 0.010
J 7.2 PS+BE d	8	1.215 ± 0.009	1.213 ± 0.008	1.196 ± 0.009	1.196 ± 0.009	1.196 ± 0.009
J 7.2 PS+BE g	8	1.314 ± 0.006	1.331 ± 0.006	1.318 ± 0.006	1.318 ± 0.006	1.317 ± 0.006
J 7.2 PS d	8	1.179 ± 0.005	1.177 ± 0.005	1.166 ± 0.005	1.166 ± 0.005	1.165 ± 0.006
J 7.2 PS g	8	1.272 ± 0.010	1.292 ± 0.011	1.279 ± 0.010	1.279 ± 0.010	1.280 ± 0.010
CELLO	16	1.238 ± 0.013	1.239 ± 0.012	1.215 ± 0.012	1.215 ± 0.012	1.215 ± 0.012
J 7.2 PS+BE d	16	1.234 ± 0.010	1.233 ± 0.010	1.214 ± 0.010	1.214 ± 0.010	1.214 ± 0.010
J 7.2 PS+BE g	16	1.331 ± 0.007	1.350 ± 0.007	1.340 ± 0.007	1.340 ± 0.007	1.339 ± 0.007
J 7.2 PS d	16	1.193 ± 0.006	1.193 ± 0.005	1.182 ± 0.005	1.182 ± 0.005	1.184 ± 0.007
J 7.2 PS g	16	1.285 ± 0.011	1.309 ± 0.012	1.295 ± 0.011	1.295 ± 0.011	1.295 ± 0.011
CELLO	32	1.246 ± 0.015	1.245 ± 0.014	1.219 ± 0.014	1.219 ± 0.014	1.220 ± 0.014
J 7.2 PS+BE d	32	1.253 ± 0.012	1.249 ± 0.011	1.227 ± 0.011	1.227 ± 0.011	1.227 ± 0.011
J 7.2 PS+BE g	32	1.340 ± 0.007	1.361 ± 0.007	1.350 ± 0.007	1.350 ± 0.007	1.350 ± 0.008
J 7.2 PS d	32	1.202 ± 0.007	1.202 ± 0.006	1.187 ± 0.006	1.187 ± 0.006	1.191 ± 0.008
J 7.2 PS g	32	1.299 ± 0.012	1.322 ± 0.013	1.302 ± 0.012	1.302 ± 0.012	1.302 ± 0.012
CELLO	64	1.235 ± 0.018	1.231 ± 0.017	1.221 ± 0.017	1.221 ± 0.017	1.220 ± 0.017
J 7.2 PS+BE d	64	1.257 ± 0.015	1.252 ± 0.014	1.248 ± 0.014	1.248 ± 0.014	1.248 ± 0.014
J 7.2 PS+BE g	64	1.354 ± 0.008	1.376 ± 0.009	1.357 ± 0.008	1.357 ± 0.008	1.356 ± 0.009
J 7.2 PS d	64	1.203 ± 0.008	1.203 ± 0.008	1.197 ± 0.008	1.197 ± 0.008	1.198 ± 0.010
J 7.2 PS g	64	1.305 ± 0.014	1.328 ± 0.015	1.310 ± 0.015	1.310 ± 0.015	1.311 ± 0.015
CELLO	128	1.252 ± 0.024	1.241 ± 0.022	1.203 ± 0.022	1.203 ± 0.022	1.203 ± 0.022
J 7.2 PS+BE d	128	1.243 ± 0.019	1.234 ± 0.018	1.245 ± 0.018	1.245 ± 0.018	1.244 ± 0.018
J 7.2 PS+BE g	128	1.364 ± 0.010	1.388 ± 0.010	1.368 ± 0.010	1.368 ± 0.010	1.366 ± 0.011
J 7.2 PS d	128	1.203 ± 0.010	1.203 ± 0.010	1.198 ± 0.010	1.198 ± 0.010	1.192 ± 0.012
J 7.2 PS g	128	1.315 ± 0.018	1.340 ± 0.018	1.320 ± 0.018	1.320 ± 0.018	1.321 ± 0.018
CELLO	256	1.284 ± 0.032	1.276 ± 0.030	1.233 ± 0.029	1.233 ± 0.029	1.245 ± 0.030
J 7.2 PS+BE d	256	1.226 ± 0.025	1.220 ± 0.024	1.232 ± 0.025	1.232 ± 0.025	1.229 ± 0.025
J 7.2 PS+BE g	256	1.374 ± 0.014	1.402 ± 0.014	1.377 ± 0.013	1.377 ± 0.013	1.361 ± 0.014
J 7.2 PS d	256	1.194 ± 0.014	1.194 ± 0.013	1.190 ± 0.013	1.190 ± 0.013	1.183 ± 0.017
J 7.2 PS g	256	1.321 ± 0.023	1.348 ± 0.023	1.311 ± 0.023	1.311 ± 0.023	1.310 ± 0.023
CELLO	512	1.271 ± 0.045	1.262 ± 0.042	1.219 ± 0.041	1.219 ± 0.041	1.257 ± 0.042
J 7.2 PS+BE d	512	1.252 ± 0.036	1.257 ± 0.034	1.258 ± 0.034	1.258 ± 0.034	1.222 ± 0.033
J 7.2 PS+BE g	512	1.386 ± 0.018	1.412 ± 0.018	1.414 ± 0.018	1.414 ± 0.018	1.405 ± 0.019
J 7.2 PS d	512	1.187 ± 0.019	1.183 ± 0.018	1.179 ± 0.018	1.179 ± 0.018	1.144 ± 0.022
J 7.2 PS g	512	1.309 ± 0.032	1.334 ± 0.032	1.316 ± 0.031	1.317 ± 0.031	1.310 ± 0.031

$\langle F^2 \rangle$ one-dimensional analysis (central y)

Table A.5: $\langle F^2 \rangle$ one-dimensional analysis (central y).

		None		Ochs		Białas
Transformation:		vertical	horizontal	vertical	horizontal	horizontal
Normalization:						
CELLO	1	1.164 ± 0.015	1.164 ± 0.015	1.164 ± 0.015	1.164 ± 0.015	1.164 ± 0.015
J 7.2 PS+BE d	1	1.162 ± 0.012	1.162 ± 0.012	1.162 ± 0.012	1.162 ± 0.012	1.162 ± 0.012
J 7.2 PS+BE g	1	1.372 ± 0.010	1.372 ± 0.010	1.372 ± 0.010	1.372 ± 0.010	1.370 ± 0.010
J 7.2 PS d	1	1.159 ± 0.007	1.159 ± 0.007	1.159 ± 0.007	1.159 ± 0.007	1.158 ± 0.008
J 7.2 PS g	1	1.364 ± 0.017	1.364 ± 0.017	1.364 ± 0.017	1.364 ± 0.017	1.364 ± 0.017
CELLO	2	1.317 ± 0.018	1.321 ± 0.018	1.320 ± 0.018	1.320 ± 0.018	1.320 ± 0.018
J 7.2 PS+BE d	2	1.344 ± 0.015	1.347 ± 0.015	1.343 ± 0.015	1.343 ± 0.015	1.343 ± 0.015
J 7.2 PS+BE g	2	1.664 ± 0.012	1.698 ± 0.013	1.673 ± 0.012	1.673 ± 0.012	1.673 ± 0.013
J 7.2 PS d	2	1.290 ± 0.008	1.292 ± 0.008	1.287 ± 0.008	1.287 ± 0.008	1.284 ± 0.010
J 7.2 PS g	2	1.571 ± 0.020	1.606 ± 0.020	1.584 ± 0.020	1.584 ± 0.020	1.584 ± 0.020
CELLO	4	1.619 ± 0.033	1.552 ± 0.026	1.581 ± 0.030	1.581 ± 0.030	1.581 ± 0.030
J 7.2 PS+BE d	4	1.632 ± 0.024	1.556 ± 0.020	1.585 ± 0.022	1.585 ± 0.022	1.585 ± 0.022
J 7.2 PS+BE g	4	1.978 ± 0.018	2.001 ± 0.018	1.990 ± 0.018	1.990 ± 0.018	1.986 ± 0.018
J 7.2 PS d	4	1.538 ± 0.013	1.464 ± 0.011	1.487 ± 0.012	1.487 ± 0.012	1.472 ± 0.014
J 7.2 PS g	4	1.798 ± 0.027	1.848 ± 0.028	1.832 ± 0.027	1.832 ± 0.027	1.832 ± 0.027
CELLO	8	1.814 ± 0.042	1.758 ± 0.037	1.732 ± 0.037	1.732 ± 0.037	1.732 ± 0.037
J 7.2 PS+BE d	8	1.813 ± 0.033	1.746 ± 0.028	1.737 ± 0.029	1.737 ± 0.029	1.737 ± 0.029
J 7.2 PS+BE g	8	2.170 ± 0.022	2.256 ± 0.022	2.181 ± 0.022	2.181 ± 0.022	2.175 ± 0.022
J 7.2 PS d	8	1.691 ± 0.018	1.635 ± 0.016	1.628 ± 0.016	1.628 ± 0.016	1.625 ± 0.019
J 7.2 PS g	8	1.941 ± 0.033	2.044 ± 0.035	1.985 ± 0.033	1.985 ± 0.033	1.985 ± 0.033
CELLO	16	1.911 ± 0.058	1.853 ± 0.051	1.799 ± 0.050	1.799 ± 0.050	1.802 ± 0.050
J 7.2 PS+BE d	16	1.885 ± 0.045	1.822 ± 0.039	1.814 ± 0.040	1.814 ± 0.040	1.813 ± 0.040
J 7.2 PS+BE g	16	2.244 ± 0.026	2.342 ± 0.027	2.296 ± 0.027	2.296 ± 0.027	2.289 ± 0.028
J 7.2 PS d	16	1.756 ± 0.024	1.709 ± 0.022	1.704 ± 0.022	1.704 ± 0.022	1.727 ± 0.027
J 7.2 PS g	16	2.035 ± 0.043	2.159 ± 0.045	2.074 ± 0.042	2.074 ± 0.042	2.073 ± 0.041
CELLO	32	1.907 ± 0.082	1.849 ± 0.073	1.783 ± 0.076	1.783 ± 0.076	1.785 ± 0.076
J 7.2 PS+BE d	32	2.031 ± 0.073	1.924 ± 0.059	1.860 ± 0.059	1.860 ± 0.059	1.858 ± 0.059
J 7.2 PS+BE g	32	2.257 ± 0.035	2.367 ± 0.036	2.350 ± 0.036	2.350 ± 0.036	2.351 ± 0.038
J 7.2 PS d	32	1.794 ± 0.039	1.741 ± 0.032	1.740 ± 0.033	1.740 ± 0.033	1.775 ± 0.041
J 7.2 PS g	32	2.125 ± 0.058	2.237 ± 0.060	2.136 ± 0.057	2.136 ± 0.057	2.135 ± 0.057
CELLO	64	2.067 ± 0.143	1.912 ± 0.116	1.859 ± 0.110	1.859 ± 0.110	1.839 ± 0.109
J 7.2 PS+BE d	64	1.992 ± 0.120	1.821 ± 0.090	1.936 ± 0.100	1.936 ± 0.100	1.936 ± 0.100
J 7.2 PS+BE g	64	2.290 ± 0.049	2.415 ± 0.051	2.342 ± 0.050	2.342 ± 0.050	2.345 ± 0.052
J 7.2 PS d	64	1.796 ± 0.061	1.739 ± 0.052	1.717 ± 0.051	1.717 ± 0.051	1.736 ± 0.064
J 7.2 PS g	64	2.130 ± 0.086	2.237 ± 0.085	2.148 ± 0.088	2.148 ± 0.088	2.151 ± 0.087
CELLO	128	1.842 ± 0.259	1.717 ± 0.206	1.523 ± 0.208	1.522 ± 0.208	1.522 ± 0.208
J 7.2 PS+BE d	128	2.232 ± 0.200	2.027 ± 0.173	2.160 ± 0.212	2.161 ± 0.212	2.161 ± 0.212
J 7.2 PS+BE g	128	2.311 ± 0.081	2.446 ± 0.083	2.317 ± 0.085	2.317 ± 0.085	2.306 ± 0.088
J 7.2 PS d	128	1.931 ± 0.128	1.782 ± 0.095	1.660 ± 0.088	1.660 ± 0.088	1.638 ± 0.112
J 7.2 PS g	128	2.206 ± 0.147	2.362 ± 0.150	2.259 ± 0.148	2.258 ± 0.148	2.252 ± 0.147
CELLO	256	1.513 ± 0.407	1.561 ± 0.441	0.858 ± 0.259	0.859 ± 0.259	1.249 ± 0.413
J 7.2 PS+BE d	256	1.509 ± 0.291	1.602 ± 0.279	2.090 ± 0.326	2.088 ± 0.325	2.088 ± 0.325
J 7.2 PS+BE g	256	2.612 ± 0.168	2.756 ± 0.169	2.522 ± 0.155	2.521 ± 0.155	2.413 ± 0.153
J 7.2 PS d	256	2.076 ± 0.225	1.819 ± 0.172	1.730 ± 0.168	1.730 ± 0.168	1.888 ± 0.248
J 7.2 PS g	256	2.015 ± 0.232	2.122 ± 0.234	2.252 ± 0.241	2.252 ± 0.241	2.278 ± 0.242

$\langle F^3 \rangle$ one-dimensional analysis (central y)

Table A.6: $\langle F^3 \rangle$ one-dimensional analysis (central y).

$\langle F^4 \rangle$ one-dimensional analysis (central y)						
Transformation:		None		Ochs		Białas
Normalization:		vertical	horizontal	vertical	horizontal	horizontal
CELLO	1	1.374 ± 0.029	1.374 ± 0.029	1.374 ± 0.029	1.374 ± 0.029	1.374 ± 0.029
J 7.2 PS+BE d	1	1.351 ± 0.021	1.351 ± 0.021	1.351 ± 0.021	1.351 ± 0.021	1.351 ± 0.021
J 7.2 PS+BE g	1	1.838 ± 0.020	1.838 ± 0.020	1.838 ± 0.020	1.838 ± 0.020	1.833 ± 0.020
J 7.2 PS d	1	1.347 ± 0.012	1.347 ± 0.012	1.347 ± 0.012	1.347 ± 0.012	1.345 ± 0.015
J 7.2 PS g	1	1.815 ± 0.035	1.815 ± 0.035	1.815 ± 0.035	1.815 ± 0.035	1.815 ± 0.035
CELLO	2	1.723 ± 0.042	1.731 ± 0.041	1.735 ± 0.043	1.735 ± 0.043	1.735 ± 0.043
J 7.2 PS+BE d	2	1.769 ± 0.033	1.775 ± 0.033	1.766 ± 0.033	1.766 ± 0.033	1.766 ± 0.033
J 7.2 PS+BE g	2	2.574 ± 0.030	2.679 ± 0.032	2.601 ± 0.031	2.601 ± 0.031	2.603 ± 0.032
J 7.2 PS d	2	1.639 ± 0.017	1.642 ± 0.017	1.630 ± 0.017	1.630 ± 0.017	1.622 ± 0.021
J 7.2 PS g	2	2.286 ± 0.045	2.389 ± 0.048	2.317 ± 0.046	2.317 ± 0.046	2.317 ± 0.046
CELLO	4	2.765 ± 0.148	2.351 ± 0.089	2.652 ± 0.123	2.652 ± 0.123	2.652 ± 0.123
J 7.2 PS+BE d	4	2.676 ± 0.088	2.303 ± 0.059	2.552 ± 0.080	2.552 ± 0.080	2.552 ± 0.080
J 7.2 PS+BE g	4	3.748 ± 0.071	3.794 ± 0.069	3.783 ± 0.070	3.783 ± 0.070	3.761 ± 0.070
J 7.2 PS d	4	2.463 ± 0.053	2.112 ± 0.036	2.283 ± 0.041	2.283 ± 0.041	2.223 ± 0.044
J 7.2 PS g	4	3.052 ± 0.086	3.220 ± 0.092	3.158 ± 0.088	3.158 ± 0.088	3.159 ± 0.088
CELLO	8	3.345 ± 0.199	3.049 ± 0.164	3.102 ± 0.162	3.102 ± 0.162	3.101 ± 0.162
J 7.2 PS+BE d	8	3.236 ± 0.141	2.880 ± 0.100	3.002 ± 0.112	3.002 ± 0.112	3.002 ± 0.112
J 7.2 PS+BE g	8	4.449 ± 0.103	4.752 ± 0.104	4.463 ± 0.097	4.463 ± 0.097	4.438 ± 0.100
J 7.2 PS d	8	3.009 ± 0.094	2.701 ± 0.076	2.748 ± 0.075	2.748 ± 0.075	2.729 ± 0.086
J 7.2 PS g	8	3.520 ± 0.144	3.872 ± 0.153	3.661 ± 0.127	3.661 ± 0.127	3.664 ± 0.127
CELLO	16	3.799 ± 0.315	3.528 ± 0.270	3.293 ± 0.254	3.292 ± 0.254	3.319 ± 0.258
J 7.2 PS+BE d	16	3.527 ± 0.236	3.194 ± 0.191	3.280 ± 0.203	3.280 ± 0.203	3.279 ± 0.203
J 7.2 PS+BE g	16	4.669 ± 0.132	5.003 ± 0.137	5.016 ± 0.150	5.016 ± 0.150	4.992 ± 0.153
J 7.2 PS d	16	3.229 ± 0.141	2.987 ± 0.128	2.999 ± 0.113	2.999 ± 0.113	3.121 ± 0.145
J 7.2 PS g	16	3.938 ± 0.232	4.357 ± 0.243	3.973 ± 0.190	3.973 ± 0.190	3.971 ± 0.189
CELLO	32	3.310 ± 0.580	3.179 ± 0.546	3.419 ± 0.634	3.418 ± 0.633	3.418 ± 0.633
J 7.2 PS+BE d	32	4.048 ± 0.703	3.370 ± 0.418	3.342 ± 0.385	3.342 ± 0.385	3.342 ± 0.385
J 7.2 PS+BE g	32	4.779 ± 0.247	5.129 ± 0.235	5.284 ± 0.246	5.285 ± 0.246	5.311 ± 0.256
J 7.2 PS d	32	3.617 ± 0.460	3.109 ± 0.243	3.273 ± 0.224	3.273 ± 0.224	3.362 ± 0.278
J 7.2 PS g	32	4.219 ± 0.342	4.537 ± 0.358	4.262 ± 0.348	4.263 ± 0.348	4.268 ± 0.348

Table A.7: $\langle F^4 \rangle$ one-dimensional analysis (central y).

$\langle F^5 \rangle$ one-dimensional analysis (central y)

Transformation:		None		Ochs		Białas
Normalization:		vertical	horizontal	vertical	horizontal	horizontal
CELLO	1	1.712 ± 0.063	1.712 ± 0.063	1.712 ± 0.063	1.712 ± 0.063	1.712 ± 0.063
J 7.2 PS+BE d	1	1.627 ± 0.038	1.627 ± 0.038	1.627 ± 0.038	1.627 ± 0.038	1.627 ± 0.038
J 7.2 PS+BE g	1	2.637 ± 0.042	2.637 ± 0.042	2.637 ± 0.042	2.637 ± 0.042	2.623 ± 0.043
J 7.2 PS d	1	1.625 ± 0.021	1.625 ± 0.021	1.625 ± 0.021	1.625 ± 0.021	1.623 ± 0.026
J 7.2 PS g	1	2.585 ± 0.074	2.585 ± 0.074	2.585 ± 0.074	2.585 ± 0.074	2.585 ± 0.074
CELLO	2	2.406 ± 0.099	2.412 ± 0.096	2.451 ± 0.103	2.451 ± 0.103	2.451 ± 0.103
J 7.2 PS+BE d	2	2.448 ± 0.078	2.458 ± 0.078	2.437 ± 0.074	2.437 ± 0.074	2.437 ± 0.074
J 7.2 PS+BE g	2	4.331 ± 0.079	4.605 ± 0.084	4.407 ± 0.085	4.407 ± 0.085	4.415 ± 0.089
J 7.2 PS d	2	2.184 ± 0.040	2.183 ± 0.039	2.157 ± 0.038	2.157 ± 0.038	2.141 ± 0.047
J 7.2 PS g	2	3.554 ± 0.107	3.804 ± 0.114	3.613 ± 0.106	3.612 ± 0.106	3.613 ± 0.106
CELLO	4	6.019 ± 0.773	4.108 ± 0.360	5.580 ± 0.600	5.580 ± 0.600	5.580 ± 0.600
J 7.2 PS+BE d	4	5.019 ± 0.354	3.676 ± 0.196	4.753 ± 0.345	4.753 ± 0.345	4.753 ± 0.345
J 7.2 PS+BE g	4	8.559 ± 0.338	8.571 ± 0.316	8.635 ± 0.333	8.635 ± 0.333	8.506 ± 0.319
J 7.2 PS d	4	4.735 ± 0.274	3.445 ± 0.156	4.101 ± 0.174	4.101 ± 0.174	3.820 ± 0.150
J 7.2 PS g	4	5.968 ± 0.311	6.478 ± 0.344	6.256 ± 0.311	6.256 ± 0.311	6.257 ± 0.311
CELLO	8	7.522 ± 1.002	6.496 ± 0.797	6.658 ± 0.710	6.658 ± 0.710	6.658 ± 0.710
J 7.2 PS+BE d	8	6.468 ± 0.675	5.101 ± 0.368	5.770 ± 0.438	5.770 ± 0.438	5.770 ± 0.438
J 7.2 PS+BE g	8	11.066 ± 0.605	11.975 ± 0.590	10.969 ± 0.512	10.970 ± 0.512	10.884 ± 0.533
J 7.2 PS d	8	6.829 ± 0.608	5.556 ± 0.490	5.705 ± 0.463	5.705 ± 0.463	5.498 ± 0.472
J 7.2 PS g	8	7.562 ± 0.873	8.612 ± 0.900	7.729 ± 0.555	7.729 ± 0.555	7.740 ± 0.556
CELLO	16	8.657 ± 1.460	8.161 ± 1.289	6.771 ± 1.316	6.770 ± 1.316	6.953 ± 1.334
J 7.2 PS+BE d	16	7.323 ± 1.121	6.184 ± 0.938	6.798 ± 1.009	6.798 ± 1.009	6.798 ± 1.009
J 7.2 PS+BE g	16	11.191 ± 0.766	12.225 ± 0.798	13.589 ± 0.884	13.590 ± 0.884	13.491 ± 0.892
J 7.2 PS d	16	7.202 ± 0.995	6.565 ± 0.990	6.250 ± 0.666	6.250 ± 0.666	6.783 ± 0.840
J 7.2 PS g	16	9.579 ± 1.562	10.742 ± 1.659	8.732 ± 0.897	8.731 ± 0.897	8.731 ± 0.897
CELLO	32	8.196 ± 3.404	8.783 ± 3.927	0.000 ± 0.000	0.000 ± 0.000	0.000 ± 0.000
J 7.2 PS+BE d	32	13.251 ± 6.620	7.535 ± 2.984	6.879 ± 2.339	6.880 ± 2.339	6.880 ± 2.339
J 7.2 PS+BE g	32	12.836 ± 1.975	13.276 ± 1.628	14.267 ± 1.742	14.268 ± 1.742	14.526 ± 1.834
J 7.2 PS d	32	13.623 ± 6.901	7.428 ± 2.309	7.524 ± 1.441	7.524 ± 1.441	7.616 ± 1.745
J 7.2 PS g	32	9.011 ± 1.972	9.917 ± 2.305	9.485 ± 2.296	9.486 ± 2.297	9.486 ± 2.297

Table A.8: $\langle F^5 \rangle$ one-dimensional analysis (central y).

Appendix B

Factorial moments in two dimensions

$\langle F^2 \rangle$ two-dimensional analysis (full y, ϕ)						

Transformation:		None		Ochs		Białas
Normalization:		vertical	horizontal	vertical	horizontal	horizontal
CELLO	1	0.984 ± 0.005	0.984 ± 0.005	0.984 ± 0.005	0.984 ± 0.005	0.984 ± 0.005
J 7.2 PS+BE d	1	0.978 ± 0.004	0.978 ± 0.004	0.978 ± 0.004	0.978 ± 0.004	0.978 ± 0.004
J 7.2 PS+BE g	1	1.040 ± 0.003	1.040 ± 0.003	1.040 ± 0.003	1.040 ± 0.003	1.036 ± 0.003
J 7.2 PS d	1	0.979 ± 0.002	0.979 ± 0.002	0.979 ± 0.002	0.979 ± 0.002	0.979 ± 0.002
J 7.2 PS g	1	1.042 ± 0.006	1.042 ± 0.006	1.042 ± 0.006	1.042 ± 0.006	1.038 ± 0.006
CELLO	4	0.933 ± 0.005	0.937 ± 0.005	0.932 ± 0.005	0.932 ± 0.005	0.931 ± 0.005
J 7.2 PS+BE d	4	0.933 ± 0.004	0.937 ± 0.004	0.933 ± 0.004	0.933 ± 0.004	0.932 ± 0.004
J 7.2 PS+BE g	4	1.037 ± 0.003	1.037 ± 0.003	1.037 ± 0.003	1.037 ± 0.003	1.033 ± 0.003
J 7.2 PS d	4	0.923 ± 0.002	0.927 ± 0.002	0.922 ± 0.002	0.922 ± 0.002	0.922 ± 0.002
J 7.2 PS g	4	1.022 ± 0.005	1.022 ± 0.005	1.022 ± 0.005	1.022 ± 0.005	1.019 ± 0.005
CELLO	16	0.888 ± 0.011	1.404 ± 0.010	1.012 ± 0.007	1.012 ± 0.007	1.011 ± 0.007
J 7.2 PS+BE d	16	0.889 ± 0.009	1.433 ± 0.008	1.026 ± 0.006	1.026 ± 0.006	1.025 ± 0.006
J 7.2 PS+BE g	16	1.075 ± 0.006	1.683 ± 0.006	1.179 ± 0.004	1.179 ± 0.004	1.174 ± 0.004
J 7.2 PS d	16	0.870 ± 0.005	1.399 ± 0.004	0.982 ± 0.003	0.982 ± 0.003	0.982 ± 0.003
J 7.2 PS g	16	1.031 ± 0.011	1.635 ± 0.011	1.125 ± 0.007	1.125 ± 0.007	1.122 ± 0.007
CELLO	64	1.107 ± 0.163	1.849 ± 0.017	1.176 ± 0.012	1.203 ± 0.012	1.179 ± 0.012
J 7.2 PS+BE d	64	0.819 ± 0.022	1.923 ± 0.015	1.178 ± 0.010	1.207 ± 0.010	1.187 ± 0.010
J 7.2 PS+BE g	64	1.472 ± 0.107	2.260 ± 0.011	1.369 ± 0.007	1.397 ± 0.007	1.372 ± 0.007
J 7.2 PS d	64	0.848 ± 0.051	1.800 ± 0.008	1.092 ± 0.005	1.114 ± 0.005	1.094 ± 0.005
J 7.2 PS g	64	2.295 ± 0.321	2.105 ± 0.018	1.249 ± 0.011	1.273 ± 0.011	1.250 ± 0.011
CELLO	256	0.941 ± 0.046	2.282 ± 0.032	1.333 ± 0.024	1.374 ± 0.023	1.348 ± 0.023
J 7.2 PS+BE d	256	0.875 ± 0.037	2.355 ± 0.027	1.310 ± 0.019	1.359 ± 0.019	1.315 ± 0.018
J 7.2 PS+BE g	256	7.342 ± 3.080	2.779 ± 0.018	1.532 ± 0.011	1.578 ± 0.011	1.536 ± 0.011
J 7.2 PS d	256	0.810 ± 0.019	2.151 ± 0.014	1.176 ± 0.010	1.212 ± 0.010	1.181 ± 0.010
J 7.2 PS g	256	26.373 ± 15.928	2.491 ± 0.029	1.353 ± 0.018	1.394 ± 0.018	1.357 ± 0.018
CELLO	1024	0.985 ± 0.061	2.683 ± 0.061	1.438 ± 0.046	1.506 ± 0.045	1.447 ± 0.044
J 7.2 PS+BE d	1024	0.874 ± 0.040	2.662 ± 0.052	1.401 ± 0.037	1.476 ± 0.037	1.421 ± 0.036
J 7.2 PS+BE g	1024	4.185 ± 1.491	3.225 ± 0.031	1.783 ± 0.021	1.836 ± 0.021	1.785 ± 0.021
J 7.2 PS d	1024	0.825 ± 0.027	2.369 ± 0.027	1.279 ± 0.020	1.311 ± 0.019	1.253 ± 0.019
J 7.2 PS g	1024	16.369 ± 8.839	2.859 ± 0.051	1.527 ± 0.036	1.577 ± 0.036	1.531 ± 0.035
CELLO	4096	1.058 ± 0.082	3.043 ± 0.126	1.599 ± 0.097	1.751 ± 0.097	1.710 ± 0.095
J 7.2 PS+BE d	4096	0.980 ± 0.091	3.038 ± 0.105	1.619 ± 0.080	1.722 ± 0.077	1.566 ± 0.074
J 7.2 PS+BE g	4096	6.730 ± 3.058	3.949 ± 0.062	2.278 ± 0.048	2.335 ± 0.047	2.300 ± 0.046
J 7.2 PS d	4096	0.904 ± 0.060	2.605 ± 0.054	1.341 ± 0.041	1.381 ± 0.039	1.364 ± 0.039
J 7.2 PS g	4096	6.629 ± 2.892	3.469 ± 0.102	2.002 ± 0.083	2.049 ± 0.078	2.005 ± 0.077
CELLO	16384	1.155 ± 0.174	3.452 ± 0.271	1.781 ± 0.218	2.145 ± 0.215	1.654 ± 0.190
J 7.2 PS+BE d	16384	0.939 ± 0.103	3.403 ± 0.217	1.774 ± 0.204	2.039 ± 0.172	1.647 ± 0.157
J 7.2 PS+BE g	16384	4.971 ± 1.709	5.293 ± 0.137	3.302 ± 0.116	3.399 ± 0.110	3.334 ± 0.108
J 7.2 PS d	16384	0.915 ± 0.093	2.817 ± 0.111	1.557 ± 0.091	1.607 ± 0.084	1.502 ± 0.081
J 7.2 PS g	16384	3.675 ± 0.933	4.768 ± 0.236	2.745 ± 0.209	3.001 ± 0.189	2.727 ± 0.179
CELLO	65536	0.895 ± 0.241	4.085 ± 0.577	0.903 ± 0.258	1.879 ± 0.392	1.388 ± 0.337
J 7.2 PS+BE d	65536	0.532 ± 0.089	3.187 ± 0.414	0.903 ± 0.240	1.729 ± 0.305	1.188 ± 0.253
J 7.2 PS+BE g	65536	3.814 ± 0.554	7.858 ± 0.333	5.198 ± 0.318	5.655 ± 0.282	4.977 ± 0.264
J 7.2 PS d	65536	1.006 ± 0.174	3.309 ± 0.240	1.587 ± 0.179	1.864 ± 0.180	1.620 ± 0.168
J 7.2 PS g	65536	1.974 ± 0.289	6.280 ± 0.540	2.178 ± 0.283	4.341 ± 0.451	3.084 ± 0.376

Table B.1: $\langle F^2 \rangle$ two-dimensional analysis (full y, ϕ).

$\langle F^3 \rangle$ two-dimensional analysis (full y, ϕ)					
Transformation:		None		Ochs		Białas
Normalization:		vertical	horizontal	vertical	horizontal	horizontal
CELLO	1	0.960 ± 0.008	0.960 ± 0.008	0.960 ± 0.008	0.960 ± 0.008	0.959 ± 0.008
J 7.2 PS+BE d	1	0.942 ± 0.006	0.942 ± 0.006	0.942 ± 0.006	0.942 ± 0.006	0.942 ± 0.006
J 7.2 PS+BE g	1	1.116 ± 0.005	1.116 ± 0.005	1.116 ± 0.005	1.116 ± 0.005	1.107 ± 0.005
J 7.2 PS d	1	0.945 ± 0.003	0.945 ± 0.003	0.945 ± 0.003	0.945 ± 0.003	0.945 ± 0.003
J 7.2 PS g	1	1.120 ± 0.009	1.120 ± 0.009	1.120 ± 0.009	1.120 ± 0.009	1.112 ± 0.009
CELLO	4	0.843 ± 0.009	0.850 ± 0.009	0.839 ± 0.009	0.839 ± 0.009	0.839 ± 0.009
J 7.2 PS+BE d	4	0.838 ± 0.007	0.844 ± 0.007	0.837 ± 0.007	0.837 ± 0.007	0.837 ± 0.007
J 7.2 PS+BE g	4	1.090 ± 0.006	1.089 ± 0.006	1.090 ± 0.006	1.090 ± 0.006	1.081 ± 0.006
J 7.2 PS d	4	0.808 ± 0.004	0.815 ± 0.004	0.808 ± 0.004	0.808 ± 0.004	0.808 ± 0.004
J 7.2 PS g	4	1.036 ± 0.010	1.036 ± 0.010	1.036 ± 0.010	1.036 ± 0.010	1.029 ± 0.010
CELLO	16	0.664 ± 0.035	2.147 ± 0.035	1.074 ± 0.023	1.075 ± 0.023	1.069 ± 0.023
J 7.2 PS+BE d	16	0.725 ± 0.030	2.304 ± 0.030	1.128 ± 0.018	1.128 ± 0.018	1.126 ± 0.018
J 7.2 PS+BE g	16	1.056 ± 0.023	3.318 ± 0.026	1.604 ± 0.015	1.604 ± 0.015	1.590 ± 0.015
J 7.2 PS d	16	0.633 ± 0.016	2.093 ± 0.015	0.999 ± 0.009	0.999 ± 0.009	0.998 ± 0.009
J 7.2 PS g	16	0.981 ± 0.044	3.004 ± 0.039	1.385 ± 0.022	1.385 ± 0.022	1.376 ± 0.022
CELLO	64	0.843 ± 0.046	4.415 ± 0.162	1.651 ± 0.082	1.747 ± 0.078	1.602 ± 0.068
J 7.2 PS+BE d	64	1.011 ± 0.046	5.250 ± 0.131	1.739 ± 0.064	1.888 ± 0.067	1.754 ± 0.063
J 7.2 PS+BE g	64	1.307 ± 0.028	7.900 ± 0.105	2.576 ± 0.046	2.738 ± 0.046	2.608 ± 0.044
J 7.2 PS d	64	0.770 ± 0.021	4.329 ± 0.065	1.402 ± 0.032	1.502 ± 0.031	1.450 ± 0.032
J 7.2 PS g	64	1.062 ± 0.052	6.356 ± 0.153	1.940 ± 0.069	2.081 ± 0.069	1.966 ± 0.065
CELLO	256	1.284 ± 0.191	8.089 ± 0.550	2.366 ± 0.389	2.371 ± 0.283	2.606 ± 0.327
J 7.2 PS+BE d	256	1.323 ± 0.140	10.463 ± 0.629	2.938 ± 0.262	3.493 ± 0.295	2.701 ± 0.266
J 7.2 PS+BE g	256	2.258 ± 0.246	15.829 ± 0.404	3.934 ± 0.192	4.323 ± 0.183	4.095 ± 0.187
J 7.2 PS d	256	1.134 ± 0.158	7.786 ± 0.262	1.992 ± 0.124	2.208 ± 0.127	2.044 ± 0.120
J 7.2 PS g	256	1.329 ± 0.110	11.555 ± 0.564	2.514 ± 0.195	2.881 ± 0.233	2.714 ± 0.204

Table B.2: $\langle F^3 \rangle$ two-dimensional analysis (full y, ϕ).

$\langle F^4 \rangle$ two-dimensional analysis (full y, ϕ)					

Transformation:		None		Ochs		Białas
Normalization:		vertical	horizontal	vertical	horizontal	horizontal
CELLO	1	0.934 ± 0.011	0.934 ± 0.011	0.934 ± 0.011	0.934 ± 0.011	0.933 ± 0.011
J 7.2 PS+BE d	1	0.898 ± 0.009	0.898 ± 0.009	0.898 ± 0.009	0.898 ± 0.009	0.898 ± 0.009
J 7.2 PS+BE g	1	1.230 ± 0.008	1.230 ± 0.008	1.230 ± 0.008	1.230 ± 0.008	1.215 ± 0.008
J 7.2 PS d	1	0.905 ± 0.005	0.905 ± 0.005	0.905 ± 0.005	0.905 ± 0.005	0.905 ± 0.005
J 7.2 PS g	1	1.237 ± 0.015	1.237 ± 0.015	1.237 ± 0.015	1.237 ± 0.015	1.223 ± 0.015
CELLO	4	0.771 ± 0.019	0.776 ± 0.018	0.766 ± 0.018	0.766 ± 0.018	0.764 ± 0.018
J 7.2 PS+BE d	4	0.741 ± 0.012	0.749 ± 0.012	0.747 ± 0.012	0.747 ± 0.012	0.748 ± 0.012
J 7.2 PS+BE g	4	1.186 ± 0.011	1.183 ± 0.011	1.186 ± 0.011	1.186 ± 0.011	1.171 ± 0.011
J 7.2 PS d	4	0.693 ± 0.007	0.699 ± 0.007	0.694 ± 0.007	0.694 ± 0.007	0.694 ± 0.007
J 7.2 PS g	4	1.052 ± 0.017	1.052 ± 0.017	1.052 ± 0.017	1.052 ± 0.017	1.040 ± 0.017
CELLO	16	0.417 ± 0.018	3.363 ± 0.138	1.320 ± 0.088	1.321 ± 0.088	1.310 ± 0.088
J 7.2 PS+BE d	16	0.484 ± 0.026	3.838 ± 0.118	1.400 ± 0.063	1.401 ± 0.063	1.393 ± 0.062
J 7.2 PS+BE g	16	1.114 ± 0.076	7.200 ± 0.129	2.668 ± 0.066	2.666 ± 0.066	2.629 ± 0.065
J 7.2 PS d	16	0.399 ± 0.017	3.119 ± 0.058	1.122 ± 0.034	1.123 ± 0.034	1.119 ± 0.034
J 7.2 PS g	16	0.972 ± 0.192	5.711 ± 0.154	1.923 ± 0.073	1.924 ± 0.073	1.917 ± 0.080
CELLO	64	1.223 ± 0.239	14.684 ± 3.392	3.140 ± 0.834	3.172 ± 0.785	2.172 ± 0.424
J 7.2 PS+BE d	64	1.618 ± 0.233	17.479 ± 1.416	3.355 ± 0.474	4.289 ± 0.563	3.483 ± 0.488
J 7.2 PS+BE g	64	2.523 ± 0.169	38.132 ± 1.399	7.350 ± 0.510	7.958 ± 0.436	7.458 ± 0.421
J 7.2 PS d	64	0.887 ± 0.072	12.763 ± 0.734	2.346 ± 0.219	2.589 ± 0.211	2.716 ± 0.252
J 7.2 PS g	64	1.699 ± 0.314	25.625 ± 1.929	4.877 ± 0.801	5.299 ± 0.711	4.797 ± 0.650

Table B.3: $\langle F^4 \rangle$ two-dimensional analysis (full y, ϕ).

$\langle F^5 \rangle$ two-dimensional analysis (full y, ϕ)					

Transformation:		None		Ochs		Białas
Normalization:		vertical	horizontal	vertical	horizontal	horizontal
CELLO	1	0.911 ± 0.017	0.911 ± 0.017	0.911 ± 0.017	0.911 ± 0.017	0.909 ± 0.017
J 7.2 PS+BE d	1	0.850 ± 0.012	0.850 ± 0.012	0.850 ± 0.012	0.850 ± 0.012	0.850 ± 0.012
J 7.2 PS+BE g	1	1.391 ± 0.014	1.391 ± 0.014	1.391 ± 0.014	1.391 ± 0.014	1.368 ± 0.013
J 7.2 PS d	1	0.862 ± 0.007	0.862 ± 0.007	0.862 ± 0.007	0.862 ± 0.007	0.861 ± 0.007
J 7.2 PS g	1	1.400 ± 0.025	1.400 ± 0.025	1.400 ± 0.025	1.400 ± 0.025	1.379 ± 0.024
CELLO	4	0.751 ± 0.046	0.746 ± 0.045	0.745 ± 0.041	0.745 ± 0.041	0.742 ± 0.041
J 7.2 PS+BE d	4	0.649 ± 0.020	0.656 ± 0.019	0.674 ± 0.022	0.674 ± 0.022	0.675 ± 0.022
J 7.2 PS+BE g	4	1.349 ± 0.023	1.344 ± 0.023	1.350 ± 0.023	1.350 ± 0.023	1.326 ± 0.023
J 7.2 PS d	4	0.597 ± 0.014	0.598 ± 0.013	0.604 ± 0.013	0.604 ± 0.013	0.605 ± 0.013
J 7.2 PS g	4	1.076 ± 0.029	1.076 ± 0.029	1.076 ± 0.029	1.076 ± 0.029	1.060 ± 0.029
CELLO	16	0.393 ± 0.048	5.213 ± 0.565	1.915 ± 0.419	1.912 ± 0.418	1.903 ± 0.417
J 7.2 PS+BE d	16	0.457 ± 0.037	6.392 ± 0.467	1.898 ± 0.222	1.905 ± 0.225	1.856 ± 0.215
J 7.2 PS+BE g	16	1.077 ± 0.056	17.434 ± 0.940	5.461 ± 0.384	5.452 ± 0.384	5.348 ± 0.377
J 7.2 PS d	16	0.318 ± 0.019	4.626 ± 0.254	1.461 ± 0.167	1.466 ± 0.170	1.451 ± 0.169
J 7.2 PS g	16	1.323 ± 0.653	11.081 ± 0.664	2.961 ± 0.270	2.964 ± 0.271	3.066 ± 0.376

Table B.4: $\langle F^5 \rangle$ two-dimensional analysis (full y, ϕ).

		None		Ochs		Białas
Transformation:		vertical	horizontal	vertical	horizontal	horizontal
Normalization:						
CELLO	1	1.047 ± 0.008	1.047 ± 0.008	1.047 ± 0.008	1.047 ± 0.008	1.047 ± 0.008
J 7.2 PS+BE d	1	1.049 ± 0.006	1.049 ± 0.006	1.049 ± 0.006	1.049 ± 0.006	1.049 ± 0.006
J 7.2 PS+BE g	1	1.114 ± 0.005	1.114 ± 0.005	1.114 ± 0.005	1.114 ± 0.005	1.114 ± 0.005
J 7.2 PS d	1	1.048 ± 0.004	1.048 ± 0.004	1.048 ± 0.004	1.048 ± 0.004	1.047 ± 0.004
J 7.2 PS g	1	1.113 ± 0.008	1.113 ± 0.008	1.113 ± 0.008	1.113 ± 0.008	1.113 ± 0.008
CELLO	4	1.065 ± 0.008	1.066 ± 0.008	1.065 ± 0.008	1.065 ± 0.008	1.065 ± 0.008
J 7.2 PS+BE d	4	1.080 ± 0.007	1.081 ± 0.007	1.080 ± 0.007	1.080 ± 0.007	1.080 ± 0.007
J 7.2 PS+BE g	4	1.173 ± 0.005	1.180 ± 0.005	1.175 ± 0.005	1.175 ± 0.005	1.175 ± 0.005
J 7.2 PS d	4	1.051 ± 0.004	1.052 ± 0.004	1.050 ± 0.004	1.050 ± 0.004	1.049 ± 0.005
J 7.2 PS g	4	1.140 ± 0.009	1.147 ± 0.009	1.144 ± 0.009	1.144 ± 0.009	1.144 ± 0.009
CELLO	16	1.167 ± 0.012	1.154 ± 0.011	1.145 ± 0.011	1.145 ± 0.011	1.146 ± 0.011
J 7.2 PS+BE d	16	1.204 ± 0.010	1.186 ± 0.009	1.180 ± 0.010	1.180 ± 0.010	1.180 ± 0.010
J 7.2 PS+BE g	16	1.317 ± 0.007	1.324 ± 0.007	1.320 ± 0.007	1.320 ± 0.007	1.319 ± 0.007
J 7.2 PS d	16	1.111 ± 0.005	1.100 ± 0.005	1.094 ± 0.005	1.095 ± 0.005	1.094 ± 0.006
J 7.2 PS g	16	1.223 ± 0.011	1.235 ± 0.011	1.231 ± 0.011	1.231 ± 0.011	1.232 ± 0.011
CELLO	64	1.347 ± 0.025	1.499 ± 0.020	1.327 ± 0.019	1.344 ± 0.019	1.339 ± 0.019
J 7.2 PS+BE d	64	1.383 ± 0.021	1.552 ± 0.017	1.363 ± 0.016	1.383 ± 0.016	1.370 ± 0.016
J 7.2 PS+BE g	64	1.481 ± 0.010	1.686 ± 0.011	1.513 ± 0.010	1.536 ± 0.010	1.516 ± 0.010
J 7.2 PS d	64	1.236 ± 0.010	1.383 ± 0.009	1.214 ± 0.008	1.230 ± 0.008	1.226 ± 0.010
J 7.2 PS g	64	1.305 ± 0.016	1.494 ± 0.017	1.345 ± 0.015	1.363 ± 0.015	1.350 ± 0.015
CELLO	256	1.481 ± 0.049	1.808 ± 0.038	1.505 ± 0.035	1.529 ± 0.034	1.509 ± 0.034
J 7.2 PS+BE d	256	1.451 ± 0.039	1.807 ± 0.032	1.527 ± 0.029	1.562 ± 0.029	1.543 ± 0.028
J 7.2 PS+BE g	256	1.656 ± 0.018	2.013 ± 0.018	1.711 ± 0.016	1.752 ± 0.016	1.725 ± 0.017
J 7.2 PS d	256	1.351 ± 0.020	1.605 ± 0.016	1.322 ± 0.015	1.343 ± 0.015	1.332 ± 0.018
J 7.2 PS g	256	1.406 ± 0.028	1.721 ± 0.029	1.475 ± 0.026	1.507 ± 0.026	1.480 ± 0.025
CELLO	1024	1.642 ± 0.108	2.058 ± 0.076	1.752 ± 0.072	1.835 ± 0.071	1.795 ± 0.070
J 7.2 PS+BE d	1024	1.511 ± 0.073	2.020 ± 0.062	1.691 ± 0.058	1.742 ± 0.057	1.663 ± 0.055
J 7.2 PS+BE g	1024	1.985 ± 0.036	2.376 ± 0.034	1.989 ± 0.031	2.031 ± 0.031	2.008 ± 0.032
J 7.2 PS d	1024	1.450 ± 0.040	1.760 ± 0.032	1.439 ± 0.029	1.458 ± 0.029	1.434 ± 0.035
J 7.2 PS g	1024	1.676 ± 0.056	2.042 ± 0.055	1.710 ± 0.051	1.754 ± 0.051	1.674 ± 0.050
CELLO	4096	1.734 ± 0.209	2.273 ± 0.157	2.015 ± 0.154	2.166 ± 0.152	2.198 ± 0.154
J 7.2 PS+BE d	4096	1.726 ± 0.147	2.369 ± 0.129	1.876 ± 0.118	2.048 ± 0.120	1.916 ± 0.118
J 7.2 PS+BE g	4096	2.646 ± 0.083	2.993 ± 0.072	2.549 ± 0.068	2.600 ± 0.067	2.549 ± 0.068
J 7.2 PS d	4096	1.603 ± 0.094	1.826 ± 0.063	1.544 ± 0.060	1.576 ± 0.059	1.573 ± 0.072
J 7.2 PS g	4096	2.321 ± 0.139	2.674 ± 0.122	2.302 ± 0.117	2.394 ± 0.114	2.315 ± 0.112
CELLO	16384	1.491 ± 0.351	2.506 ± 0.342	1.792 ± 0.293	2.379 ± 0.323	1.912 ± 0.285
J 7.2 PS+BE d	16384	1.676 ± 0.293	2.536 ± 0.265	2.127 ± 0.317	2.508 ± 0.264	2.006 ± 0.236
J 7.2 PS+BE g	16384	3.963 ± 0.221	4.400 ± 0.171	3.889 ± 0.175	4.019 ± 0.164	3.643 ± 0.161
J 7.2 PS d	16384	1.891 ± 0.184	2.085 ± 0.135	1.725 ± 0.127	1.876 ± 0.127	1.670 ± 0.149
J 7.2 PS g	16384	2.880 ± 0.328	3.509 ± 0.273	2.711 ± 0.255	3.298 ± 0.268	3.128 ± 0.266
CELLO	65536	0.721 ± 0.231	3.059 ± 0.721	0.906 ± 0.285	2.549 ± 0.658	0.000 ± 0.000
J 7.2 PS+BE d	65536	0.919 ± 0.312	2.118 ± 0.486	1.123 ± 0.330	2.564 ± 0.534	1.338 ± 0.386
J 7.2 PS+BE g	65536	5.639 ± 0.670	6.898 ± 0.426	5.199 ± 0.408	6.399 ± 0.409	5.665 ± 0.399
J 7.2 PS d	65536	2.268 ± 0.438	2.745 ± 0.309	2.006 ± 0.280	2.606 ± 0.301	1.817 ± 0.312
J 7.2 PS g	65536	2.096 ± 0.383	4.989 ± 0.648	2.350 ± 0.362	5.580 ± 0.686	3.213 ± 0.521

$\langle F^2 \rangle$ two-dimensional analysis (central y, full ϕ)

Table B.5: $\langle F^2 \rangle$ two-dimensional analysis (central y, full ϕ).

$\langle F^3 \rangle$ two-dimensional analysis (central y, full ϕ)						
Transformation:		None		Ochs		Białas
Normalization:		vertical	horizontal	vertical	horizontal	horizontal
CELLO	1	1.164 ± 0.015	1.164 ± 0.015	1.164 ± 0.015	1.164 ± 0.015	1.164 ± 0.015
J 7.2 PS+BE d	1	1.162 ± 0.012	1.162 ± 0.012	1.162 ± 0.012	1.162 ± 0.012	1.162 ± 0.012
J 7.2 PS+BE g	1	1.372 ± 0.010	1.372 ± 0.010	1.372 ± 0.010	1.372 ± 0.010	1.370 ± 0.010
J 7.2 PS d	1	1.159 ± 0.007	1.159 ± 0.007	1.159 ± 0.007	1.159 ± 0.007	1.158 ± 0.008
J 7.2 PS g	1	1.364 ± 0.017	1.364 ± 0.017	1.364 ± 0.017	1.364 ± 0.017	1.364 ± 0.017
CELLO	4	1.224 ± 0.020	1.227 ± 0.020	1.224 ± 0.020	1.224 ± 0.020	1.223 ± 0.020
J 7.2 PS+BE d	4	1.268 ± 0.016	1.270 ± 0.016	1.265 ± 0.016	1.264 ± 0.016	1.265 ± 0.016
J 7.2 PS+BE g	4	1.554 ± 0.012	1.584 ± 0.013	1.562 ± 0.012	1.562 ± 0.012	1.561 ± 0.013
J 7.2 PS d	4	1.172 ± 0.008	1.174 ± 0.008	1.170 ± 0.008	1.170 ± 0.008	1.165 ± 0.010
J 7.2 PS g	4	1.417 ± 0.019	1.447 ± 0.020	1.429 ± 0.019	1.429 ± 0.019	1.429 ± 0.019
CELLO	16	1.628 ± 0.054	1.497 ± 0.042	1.497 ± 0.043	1.496 ± 0.043	1.494 ± 0.043
J 7.2 PS+BE d	16	1.778 ± 0.041	1.647 ± 0.034	1.687 ± 0.037	1.687 ± 0.037	1.689 ± 0.037
J 7.2 PS+BE g	16	2.160 ± 0.026	2.182 ± 0.025	2.170 ± 0.025	2.171 ± 0.025	2.167 ± 0.026
J 7.2 PS d	16	1.420 ± 0.020	1.333 ± 0.017	1.348 ± 0.017	1.348 ± 0.017	1.343 ± 0.020
J 7.2 PS g	16	1.727 ± 0.034	1.770 ± 0.034	1.777 ± 0.037	1.776 ± 0.037	1.778 ± 0.037
CELLO	64	2.495 ± 0.402	2.971 ± 0.164	2.294 ± 0.166	2.351 ± 0.144	2.259 ± 0.139
J 7.2 PS+BE d	64	2.654 ± 0.220	3.284 ± 0.148	2.647 ± 0.129	2.771 ± 0.134	2.646 ± 0.134
J 7.2 PS+BE g	64	3.299 ± 0.101	4.570 ± 0.093	3.442 ± 0.079	3.586 ± 0.080	3.450 ± 0.081
J 7.2 PS d	64	1.957 ± 0.087	2.631 ± 0.071	1.867 ± 0.057	1.973 ± 0.060	1.888 ± 0.068
J 7.2 PS g	64	2.159 ± 0.105	3.252 ± 0.127	2.438 ± 0.111	2.525 ± 0.112	2.459 ± 0.108
CELLO	256	2.478 ± 0.498	5.620 ± 0.810	3.002 ± 0.559	3.122 ± 0.562	3.122 ± 0.493
J 7.2 PS+BE d	256	2.768 ± 0.642	5.438 ± 0.621	3.545 ± 0.480	3.787 ± 0.460	3.399 ± 0.439
J 7.2 PS+BE g	256	4.722 ± 0.364	8.334 ± 0.411	5.672 ± 0.352	6.113 ± 0.349	5.644 ± 0.385
J 7.2 PS d	256	2.400 ± 0.369	4.554 ± 0.317	2.482 ± 0.206	2.662 ± 0.211	2.456 ± 0.249
J 7.2 PS g	256	3.053 ± 0.461	5.875 ± 0.686	3.387 ± 0.388	3.675 ± 0.441	3.184 ± 0.325

Table B.6: $\langle F^3 \rangle$ two-dimensional analysis (central y, full ϕ).

$\langle F^4 \rangle$ two-dimensional analysis (central y, full ϕ)					
Transformation:		None		Ochs		Białas
Normalization:		vertical	horizontal	vertical	horizontal	horizontal
CELLO	1	1.374 ± 0.029	1.374 ± 0.029	1.374 ± 0.029	1.374 ± 0.029	1.374 ± 0.029
J 7.2 PS+BE d	1	1.351 ± 0.021	1.351 ± 0.021	1.351 ± 0.021	1.351 ± 0.021	1.351 ± 0.021
J 7.2 PS+BE g	1	1.838 ± 0.020	1.838 ± 0.020	1.838 ± 0.020	1.838 ± 0.020	1.833 ± 0.020
J 7.2 PS d	1	1.347 ± 0.012	1.347 ± 0.012	1.347 ± 0.012	1.347 ± 0.012	1.345 ± 0.015
J 7.2 PS g	1	1.815 ± 0.035	1.815 ± 0.035	1.815 ± 0.035	1.815 ± 0.035	1.815 ± 0.035
CELLO	4	1.547 ± 0.058	1.548 ± 0.057	1.547 ± 0.057	1.547 ± 0.057	1.545 ± 0.057
J 7.2 PS+BE d	4	1.572 ± 0.036	1.576 ± 0.036	1.569 ± 0.036	1.568 ± 0.036	1.571 ± 0.036
J 7.2 PS+BE g	4	2.275 ± 0.031	2.363 ± 0.032	2.295 ± 0.031	2.295 ± 0.031	2.293 ± 0.033
J 7.2 PS d	4	1.375 ± 0.020	1.375 ± 0.019	1.369 ± 0.019	1.369 ± 0.019	1.359 ± 0.023
J 7.2 PS g	4	1.877 ± 0.042	1.955 ± 0.044	1.904 ± 0.043	1.904 ± 0.043	1.904 ± 0.043
CELLO	16	2.879 ± 0.355	2.181 ± 0.207	2.295 ± 0.220	2.291 ± 0.219	2.277 ± 0.219
J 7.2 PS+BE d	16	2.959 ± 0.187	2.471 ± 0.138	2.695 ± 0.162	2.693 ± 0.161	2.714 ± 0.162
J 7.2 PS+BE g	16	4.320 ± 0.139	4.356 ± 0.142	4.342 ± 0.132	4.343 ± 0.132	4.309 ± 0.131
J 7.2 PS d	16	2.081 ± 0.106	1.756 ± 0.075	1.834 ± 0.076	1.836 ± 0.077	1.773 ± 0.081
J 7.2 PS g	16	2.713 ± 0.130	2.786 ± 0.125	3.019 ± 0.202	3.015 ± 0.202	3.019 ± 0.202

Table B.7: $\langle F^4 \rangle$ two-dimensional analysis (central y, full ϕ).

$\langle F^5 \rangle$ two-dimensional analysis (central y, full ϕ)					
Transformation:		None		Ochs		Białas
Normalization:		vertical	horizontal	vertical	horizontal	horizontal
CELLO	1	1.712 ± 0.063	1.712 ± 0.063	1.712 ± 0.063	1.712 ± 0.063	1.712 ± 0.063
J 7.2 PS+BE d	1	1.627 ± 0.038	1.627 ± 0.038	1.627 ± 0.038	1.627 ± 0.038	1.627 ± 0.038
J 7.2 PS+BE g	1	2.637 ± 0.042	2.637 ± 0.042	2.637 ± 0.042	2.637 ± 0.042	2.623 ± 0.043
J 7.2 PS d	1	1.625 ± 0.021	1.625 ± 0.021	1.625 ± 0.021	1.625 ± 0.021	1.623 ± 0.026
J 7.2 PS g	1	2.585 ± 0.074	2.585 ± 0.074	2.585 ± 0.074	2.585 ± 0.074	2.585 ± 0.074
CELLO	4	2.190 ± 0.199	2.173 ± 0.192	2.193 ± 0.195	2.191 ± 0.194	2.187 ± 0.194
J 7.2 PS+BE d	4	1.964 ± 0.082	1.974 ± 0.082	1.979 ± 0.084	1.978 ± 0.084	1.987 ± 0.085
J 7.2 PS+BE g	4	3.584 ± 0.083	3.794 ± 0.088	3.628 ± 0.086	3.628 ± 0.086	3.624 ± 0.089
J 7.2 PS d	4	1.670 ± 0.055	1.662 ± 0.051	1.660 ± 0.051	1.660 ± 0.051	1.634 ± 0.053
J 7.2 PS g	4	2.582 ± 0.096	2.746 ± 0.102	2.641 ± 0.100	2.642 ± 0.100	2.642 ± 0.100
CELLO	16	6.992 ± 2.502	3.733 ± 1.192	4.192 ± 1.229	4.172 ± 1.222	4.172 ± 1.222
J 7.2 PS+BE d	16	5.028 ± 0.726	3.665 ± 0.476	4.536 ± 0.690	4.525 ± 0.686	4.607 ± 0.687
J 7.2 PS+BE g	16	10.523 ± 1.041	10.622 ± 1.111	10.488 ± 0.866	10.494 ± 0.865	10.163 ± 0.793
J 7.2 PS d	16	3.822 ± 0.748	2.702 ± 0.438	2.808 ± 0.431	2.827 ± 0.442	2.380 ± 0.350
J 7.2 PS g	16	4.443 ± 0.493	4.425 ± 0.438	6.659 ± 1.509	6.629 ± 1.520	6.608 ± 1.518

Table B.8: $\langle F^5 \rangle$ two-dimensional analysis (central y, full ϕ).

Appendix C

Factorial moments in three dimensions

y, ϕ, $p_\perp^2$ analysis (Ochs method)					
Dataset	Bins	$\langle F^2 \rangle^h$	$\langle F^3 \rangle^h$	$\langle F^4 \rangle^h$	$\langle F^5 \rangle^h$
CELLO	2^0	0.984 ± 0.005	0.960 ± 0.008	0.934 ± 0.011	0.910 ± 0.017
J 7.2 PS+BE d	2^0	0.978 ± 0.004	0.942 ± 0.006	0.898 ± 0.009	0.850 ± 0.012
J 7.2 PS+BE g	2^0	1.040 ± 0.003	1.116 ± 0.005	1.230 ± 0.008	1.391 ± 0.014
J 7.2 PS d	2^0	0.979 ± 0.002	0.945 ± 0.003	0.905 ± 0.005	0.861 ± 0.007
J 7.2 PS g	2^0	1.041 ± 0.006	1.120 ± 0.009	1.237 ± 0.015	1.400 ± 0.025
CELLO	2^3	0.972 ± 0.006	0.964 ± 0.014	1.039 ± 0.048	1.361 ± 0.213
J 7.2 PS+BE d	2^3	0.966 ± 0.005	0.946 ± 0.011	0.971 ± 0.026	1.043 ± 0.064
J 7.2 PS+BE g	2^3	1.074 ± 0.003	1.231 ± 0.008	1.545 ± 0.022	2.135 ± 0.071
J 7.2 PS d	2^3	0.954 ± 0.003	0.903 ± 0.006	0.880 ± 0.013	0.894 ± 0.034
J 7.2 PS g	2^3	1.057 ± 0.006	1.158 ± 0.013	1.322 ± 0.029	1.543 ± 0.068
CELLO	2^6	1.121 ± 0.011	1.460 ± 0.067	2.446 ± 0.389	$-$
J 7.2 PS+BE d	2^6	1.131 ± 0.010	1.533 ± 0.052	2.064 ± 0.313	$-$
J 7.2 PS+BE g	2^6	1.307 ± 0.006	2.248 ± 0.039	5.563 ± 0.413	$-$
J 7.2 PS d	2^6	1.064 ± 0.005	1.353 ± 0.028	1.879 ± 0.175	$-$
J 7.2 PS g	2^6	1.230 ± 0.011	1.902 ± 0.055	3.498 ± 0.324	$-$
CELLO	2^9	1.542 ± 0.033	4.109 ± 0.752	$-$	$-$
J 7.2 PS+BE d	2^9	1.581 ± 0.028	5.404 ± 0.715	$-$	$-$
J 7.2 PS+BE g	2^9	1.928 ± 0.017	8.734 ± 0.474	$-$	$-$
J 7.2 PS d	2^9	1.413 ± 0.015	3.253 ± 0.272	$-$	$-$
J 7.2 PS g	2^9	1.701 ± 0.028	6.518 ± 0.670	$-$	$-$
CELLO	2^{12}	2.006 ± 0.103	$-$	$-$	$-$
J 7.2 PS+BE d	2^{12}	2.076 ± 0.087	$-$	$-$	$-$
J 7.2 PS+BE g	2^{12}	2.816 ± 0.052	$-$	$-$	$-$
J 7.2 PS d	2^{12}	1.786 ± 0.045	$-$	$-$	$-$
J 7.2 PS g	2^{12}	2.361 ± 0.087	$-$	$-$	$-$
CELLO	2^{15}	2.450 ± 0.316	$-$	$-$	$-$
J 7.2 PS+BE d	2^{15}	2.944 ± 0.286	$-$	$-$	$-$
J 7.2 PS+BE g	2^{15}	4.174 ± 0.174	$-$	$-$	$-$
J 7.2 PS d	2^{15}	2.325 ± 0.143	$-$	$-$	$-$
J 7.2 PS g	2^{15}	3.186 ± 0.274	$-$	$-$	$-$
CELLO	2^{18}	3.267 ± 1.033	$-$	$-$	$-$
J 7.2 PS+BE d	2^{18}	4.321 ± 0.966	$-$	$-$	$-$
J 7.2 PS+BE g	2^{18}	6.678 ± 0.612	$-$	$-$	$-$
J 7.2 PS d	2^{18}	3.413 ± 0.487	$-$	$-$	$-$
J 7.2 PS g	2^{18}	6.095 ± 1.060	$-$	$-$	$-$

Table C.1: y, ϕ, $p_\perp^2$ analysis (Ochs method).

y, ϕ, $p_\perp^2$ analysis (Białas method)					
Dataset	Bins	$\langle F^2 \rangle^h$	$\langle F^3 \rangle^h$	$\langle F^4 \rangle^h$	$\langle F^5 \rangle^h$
CELLO	2^0	0.984 ± 0.005	0.959 ± 0.008	0.933 ± 0.011	0.909 ± 0.017
J 7.2 PS+BE d	2^0	0.978 ± 0.004	0.942 ± 0.006	0.898 ± 0.009	0.850 ± 0.012
J 7.2 PS+BE g	2^0	1.036 ± 0.003	1.107 ± 0.005	1.215 ± 0.008	1.368 ± 0.013
J 7.2 PS d	2^0	0.979 ± 0.002	0.945 ± 0.003	0.905 ± 0.005	0.861 ± 0.007
J 7.2 PS g	2^0	1.038 ± 0.006	1.112 ± 0.009	1.223 ± 0.015	1.379 ± 0.024
CELLO	2^3	0.972 ± 0.006	0.965 ± 0.014	1.043 ± 0.048	1.378 ± 0.213
J 7.2 PS+BE d	2^3	0.965 ± 0.005	0.943 ± 0.011	0.969 ± 0.026	1.040 ± 0.063
J 7.2 PS+BE g	2^3	1.066 ± 0.003	1.202 ± 0.008	1.473 ± 0.021	1.988 ± 0.065
J 7.2 PS d	2^3	0.953 ± 0.003	0.903 ± 0.006	0.881 ± 0.014	0.899 ± 0.036
J 7.2 PS g	2^3	1.049 ± 0.006	1.132 ± 0.013	1.265 ± 0.028	1.437 ± 0.061
CELLO	2^6	1.062 ± 0.011	1.198 ± 0.060	1.991 ± 0.415	$-$
J 7.2 PS+BE d	2^6	1.075 ± 0.009	1.306 ± 0.049	1.902 ± 0.309	$-$
J 7.2 PS+BE g	2^6	1.277 ± 0.006	2.100 ± 0.038	5.212 ± 0.404	$-$
J 7.2 PS d	2^6	1.011 ± 0.005	1.146 ± 0.026	1.700 ± 0.170	$-$
J 7.2 PS g	2^6	1.192 ± 0.010	1.729 ± 0.053	3.169 ± 0.320	$-$
CELLO	2^9	1.286 ± 0.030	2.106 ± 0.471	$-$	$-$
J 7.2 PS+BE d	2^9	1.293 ± 0.025	2.504 ± 0.406	$-$	$-$
J 7.2 PS+BE g	2^9	1.656 ± 0.015	5.295 ± 0.330	$-$	$-$
J 7.2 PS d	2^9	1.162 ± 0.013	1.774 ± 0.207	$-$	$-$
J 7.2 PS g	2^9	1.417 ± 0.024	2.922 ± 0.429	$-$	$-$
CELLO	2^{12}	1.603 ± 0.091	$-$	$-$	$-$
J 7.2 PS+BE d	2^{12}	1.570 ± 0.074	$-$	$-$	$-$
J 7.2 PS+BE g	2^{12}	2.262 ± 0.047	$-$	$-$	$-$
J 7.2 PS d	2^{12}	1.414 ± 0.040	$-$	$-$	$-$
J 7.2 PS g	2^{12}	1.801 ± 0.074	$-$	$-$	$-$
CELLO	2^{15}	1.919 ± 0.280	$-$	$-$	$-$
J 7.2 PS+BE d	2^{15}	1.674 ± 0.212	$-$	$-$	$-$
J 7.2 PS+BE g	2^{15}	3.180 ± 0.153	$-$	$-$	$-$
J 7.2 PS d	2^{15}	1.524 ± 0.115	$-$	$-$	$-$
J 7.2 PS g	2^{15}	2.301 ± 0.229	$-$	$-$	$-$

Table C.2: y, ϕ, $p_\perp^2$ analysis (Białas method).

Cartesian three-dimensional analysis (Białas method)					
Dataset	Bins	$\langle F^2 \rangle^h$	$\langle F^3 \rangle^h$	$\langle F^4 \rangle^h$	$\langle F^5 \rangle^h$
CELLO	2^0	0.984 ± 0.005	0.959 ± 0.008	0.933 ± 0.011	0.909 ± 0.017
J 7.2 PS+BE d	2^0	0.978 ± 0.004	0.942 ± 0.006	0.898 ± 0.009	0.850 ± 0.012
J 7.2 PS+BE g	2^0	1.037 ± 0.005	1.109 ± 0.009	1.220 ± 0.015	1.378 ± 0.024
J 7.2 PS d	2^0	0.979 ± 0.002	0.945 ± 0.003	0.905 ± 0.005	0.861 ± 0.007
J 7.2 PS g	2^0	1.038 ± 0.005	1.110 ± 0.009	1.219 ± 0.015	1.372 ± 0.023
CELLO	2^3	1.715 ± 0.009	3.421 ± 0.037	7.002 ± 0.145	14.148 ± 0.580
J 7.2 PS+BE d	2^3	1.716 ± 0.008	3.422 ± 0.031	7.033 ± 0.123	14.519 ± 0.485
J 7.2 PS+BE g	2^3	1.737 ± 0.009	3.676 ± 0.037	8.376 ± 0.152	19.795 ± 0.647
J 7.2 PS d	2^3	1.637 ± 0.004	3.094 ± 0.016	5.946 ± 0.058	11.280 ± 0.222
J 7.2 PS g	2^3	1.693 ± 0.009	3.456 ± 0.034	7.495 ± 0.126	16.546 ± 0.474
CELLO	2^6	3.211 ± 0.022	14.042 ± 0.273	60.870 ± 3.131	216.309 ± 30.254
J 7.2 PS+BE d	2^6	3.157 ± 0.018	13.898 ± 0.241	68.483 ± 3.284	345.173 ± 42.983
J 7.2 PS+BE g	2^6	3.317 ± 0.021	16.556 ± 0.282	97.759 ± 4.673	670.729 ± 93.836
J 7.2 PS d	2^6	2.924 ± 0.010	11.804 ± 0.117	50.409 ± 1.400	205.541 ± 15.848
J 7.2 PS g	2^6	3.199 ± 0.020	15.379 ± 0.244	83.730 ± 3.181	462.511 ± 41.069
CELLO	2^9	4.813 ± 0.061	36.010 ± 2.287	254.886 ± 76.828	—
J 7.2 PS+BE d	2^9	4.710 ± 0.048	32.086 ± 1.695	205.770 ± 53.114	—
J 7.2 PS+BE g	2^9	5.288 ± 0.052	51.068 ± 2.207	684.786 ± 132.591	—
J 7.2 PS d	2^9	4.278 ± 0.026	28.623 ± 0.910	174.919 ± 33.867	—
J 7.2 PS g	2^9	5.092 ± 0.050	50.026 ± 2.094	647.135 ± 101.305	—
CELLO	2^{12}	6.313 ± 0.184	74.126 ± 22.343	—	—
J 7.2 PS+BE d	2^{12}	6.096 ± 0.143	0.000 ± 0.000	—	—
J 7.2 PS+BE g	2^{12}	7.281 ± 0.153	141.987 ± 26.532	—	—
J 7.2 PS d	2^{12}	5.512 ± 0.078	40.558 ± 7.403	—	—
J 7.2 PS g	2^{12}	7.100 ± 0.146	138.765 ± 24.045	—	—
CELLO	2^{15}	7.390 ± 0.553	—	—	—
J 7.2 PS+BE d	2^{15}	6.616 ± 0.422	—	—	—
J 7.2 PS+BE g	2^{15}	7.928 ± 0.420	—	—	—
J 7.2 PS d	2^{15}	6.174 ± 0.233	—	—	—
J 7.2 PS g	2^{15}	8.276 ± 0.425	—	—	—

Table C.3: Cartesian three-dimensional analysis (Białas method).

Cartesian three-dimensional analysis					
Dataset	Bins	$\langle F^2 \rangle^h$	$\langle F^3 \rangle^h$	$\langle F^4 \rangle^h$	$\langle F^5 \rangle^h$
CELLO	2^0	$0.98{\cdot}10^0 \pm 0.21{\cdot}10^{-2}$	$0.96{\cdot}10^0 \pm 0.34{\cdot}10^{-2}$	$0.93{\cdot}10^0 \pm 0.51{\cdot}10^{-2}$	$0.91{\cdot}10^0 \pm 0.76{\cdot}10^{-2}$
J 7.2 PS+BE d	2^0	$0.98{\cdot}10^0 \pm 0.17{\cdot}10^{-2}$	$0.94{\cdot}10^0 \pm 0.26{\cdot}10^{-2}$	$0.90{\cdot}10^0 \pm 0.38{\cdot}10^{-2}$	$0.85{\cdot}10^0 \pm 0.54{\cdot}10^{-2}$
J 7.2 PS+BE g	2^0	$1.04{\cdot}10^0 \pm 0.25{\cdot}10^{-2}$	$1.12{\cdot}10^0 \pm 0.42{\cdot}10^{-2}$	$1.24{\cdot}10^0 \pm 0.68{\cdot}10^{-2}$	$1.40{\cdot}10^0 \pm 0.11{\cdot}10^{-1}$
J 7.2 PS d	2^0	$0.98{\cdot}10^0 \pm 0.95{\cdot}10^{-3}$	$0.95{\cdot}10^0 \pm 0.15{\cdot}10^{-2}$	$0.90{\cdot}10^0 \pm 0.22{\cdot}10^{-2}$	$0.86{\cdot}10^0 \pm 0.31{\cdot}10^{-2}$
J 7.2 PS g	2^0	$1.04{\cdot}10^0 \pm 0.24{\cdot}10^{-2}$	$1.12{\cdot}10^0 \pm 0.41{\cdot}10^{-2}$	$1.23{\cdot}10^0 \pm 0.66{\cdot}10^{-2}$	$1.39{\cdot}10^0 \pm 0.11{\cdot}10^{-1}$
CELLO	2^3	$7.46{\cdot}10^0 \pm 0.16{\cdot}10^{-1}$	$5.67{\cdot}10^1 \pm 0.21{\cdot}10^0$	$4.35{\cdot}10^2 \pm 2.49{\cdot}10^0$	$3.36{\cdot}10^3 \pm 2.97{\cdot}10^1$
J 7.2 PS+BE d	2^3	$7.42{\cdot}10^0 \pm 0.13{\cdot}10^{-1}$	$5.58{\cdot}10^1 \pm 0.16{\cdot}10^0$	$4.19{\cdot}10^2 \pm 1.87{\cdot}10^0$	$3.14{\cdot}10^3 \pm 2.10{\cdot}10^1$
J 7.2 PS+BE g	2^3	$7.94{\cdot}10^0 \pm 0.20{\cdot}10^{-1}$	$6.68{\cdot}10^1 \pm 0.26{\cdot}10^0$	$5.83{\cdot}10^2 \pm 3.38{\cdot}10^0$	$5.25{\cdot}10^3 \pm 4.33{\cdot}10^1$
J 7.2 PS d	2^3	$7.44{\cdot}10^0 \pm 0.76{\cdot}10^{-2}$	$5.61{\cdot}10^1 \pm 0.94{\cdot}10^{-1}$	$4.23{\cdot}10^2 \pm 1.08{\cdot}10^0$	$3.20{\cdot}10^3 \pm 1.20{\cdot}10^1$
J 7.2 PS g	2^3	$7.94{\cdot}10^0 \pm 0.19{\cdot}10^{-1}$	$6.67{\cdot}10^1 \pm 0.25{\cdot}10^0$	$5.81{\cdot}10^2 \pm 3.24{\cdot}10^0$	$5.20{\cdot}10^3 \pm 4.12{\cdot}10^1$
CELLO	2^6	$5.65{\cdot}10^1 \pm 0.13{\cdot}10^0$	$3.35{\cdot}10^3 \pm 1.29{\cdot}10^1$	$2.02{\cdot}10^5 \pm 1.21{\cdot}10^3$	$1.23{\cdot}10^7 \pm 1.13{\cdot}10^5$
J 7.2 PS+BE d	2^6	$5.63{\cdot}10^1 \pm 0.10{\cdot}10^0$	$3.30{\cdot}10^3 \pm 1.02{\cdot}10^1$	$1.96{\cdot}10^5 \pm 9.21{\cdot}10^2$	$1.16{\cdot}10^7 \pm 8.26{\cdot}10^4$
J 7.2 PS+BE g	2^6	$6.05{\cdot}10^1 \pm 0.15{\cdot}10^0$	$3.97{\cdot}10^3 \pm 1.62{\cdot}10^1$	$2.73{\cdot}10^5 \pm 1.65{\cdot}10^3$	$1.95{\cdot}10^7 \pm 1.68{\cdot}10^5$
J 7.2 PS d	2^6	$5.64{\cdot}10^1 \pm 0.60{\cdot}10^{-1}$	$3.32{\cdot}10^3 \pm 5.87{\cdot}10^0$	$1.98{\cdot}10^5 \pm 5.30{\cdot}10^2$	$1.18{\cdot}10^7 \pm 4.67{\cdot}10^4$
J 7.2 PS g	2^6	$6.05{\cdot}10^1 \pm 0.15{\cdot}10^0$	$3.98{\cdot}10^3 \pm 1.57{\cdot}10^1$	$2.73{\cdot}10^5 \pm 1.59{\cdot}10^3$	$1.94{\cdot}10^7 \pm 1.60{\cdot}10^5$
CELLO	2^9	$4.06{\cdot}10^2 \pm 0.99{\cdot}10^0$	$1.82{\cdot}10^5 \pm 7.67{\cdot}10^2$	$8.51{\cdot}10^7 \pm 5.60{\cdot}10^5$	$4.07{\cdot}10^{10} \pm 4.15{\cdot}10^8$
J 7.2 PS+BE d	2^9	$4.05{\cdot}10^2 \pm 0.80{\cdot}10^0$	$1.80{\cdot}10^5 \pm 6.07{\cdot}10^2$	$8.25{\cdot}10^7 \pm 4.28{\cdot}10^5$	$3.83{\cdot}10^{10} \pm 3.02{\cdot}10^8$
J 7.2 PS+BE g	2^9	$4.39{\cdot}10^2 \pm 1.18{\cdot}10^0$	$2.20{\cdot}10^5 \pm 9.71{\cdot}10^2$	$1.18{\cdot}10^8 \pm 7.75{\cdot}10^5$	$6.58{\cdot}10^{10} \pm 6.24{\cdot}10^8$
J 7.2 PS d	2^9	$4.06{\cdot}10^2 \pm 0.46{\cdot}10^0$	$1.81{\cdot}10^5 \pm 3.49{\cdot}10^2$	$8.33{\cdot}10^7 \pm 2.45{\cdot}10^5$	$3.90{\cdot}10^{10} \pm 1.70{\cdot}10^8$
J 7.2 PS g	2^9	$4.39{\cdot}10^2 \pm 1.14{\cdot}10^0$	$2.20{\cdot}10^5 \pm 9.36{\cdot}10^2$	$1.17{\cdot}10^8 \pm 7.41{\cdot}10^5$	$6.51{\cdot}10^{10} \pm 5.91{\cdot}10^8$
CELLO	2^{12}	$2.60{\cdot}10^3 \pm 7.02{\cdot}10^0$	$8.25{\cdot}10^6 \pm 4.04{\cdot}10^4$	$2.84{\cdot}10^{10} \pm 2.25{\cdot}10^8$	$1.02{\cdot}10^{14} \pm 1.30{\cdot}10^{12}$
J 7.2 PS+BE d	2^{12}	$2.61{\cdot}10^3 \pm 5.71{\cdot}10^0$	$8.22{\cdot}10^6 \pm 3.21{\cdot}10^4$	$2.77{\cdot}10^{10} \pm 1.70{\cdot}10^8$	$9.69{\cdot}10^{13} \pm 9.04{\cdot}10^{11}$
J 7.2 PS+BE g	2^{12}	$2.88{\cdot}10^3 \pm 8.40{\cdot}10^0$	$1.04{\cdot}10^7 \pm 5.24{\cdot}10^4$	$4.13{\cdot}10^{10} \pm 3.22{\cdot}10^8$	$1.76{\cdot}10^{14} \pm 2.03{\cdot}10^{12}$
J 7.2 PS d	2^{12}	$2.62{\cdot}10^3 \pm 3.29{\cdot}10^0$	$8.26{\cdot}10^6 \pm 1.86{\cdot}10^4$	$2.80{\cdot}10^{10} \pm 9.94{\cdot}10^7$	$9.91{\cdot}10^{13} \pm 5.31{\cdot}10^{11}$
J 7.2 PS g	2^{12}	$2.88{\cdot}10^3 \pm 8.15{\cdot}10^0$	$1.03{\cdot}10^7 \pm 5.04{\cdot}10^4$	$4.10{\cdot}10^{10} \pm 3.05{\cdot}10^8$	$1.73{\cdot}10^{14} \pm 1.89{\cdot}10^{12}$
CELLO	2^{15}	$1.34{\cdot}10^4 \pm 3.98{\cdot}10^1$	$2.50{\cdot}10^8 \pm 1.51{\cdot}10^6$	$5.42{\cdot}10^{12} \pm 5.98{\cdot}10^{10}$	$1.30{\cdot}10^{17} \pm 2.70{\cdot}10^{15}$
J 7.2 PS+BE d	2^{15}	$1.36{\cdot}10^4 \pm 3.33{\cdot}10^1$	$2.57{\cdot}10^8 \pm 1.25{\cdot}10^6$	$5.58{\cdot}10^{12} \pm 4.64{\cdot}10^{10}$	$1.32{\cdot}10^{17} \pm 1.77{\cdot}10^{15}$
J 7.2 PS+BE g	2^{15}	$1.55{\cdot}10^4 \pm 4.95{\cdot}10^1$	$3.42{\cdot}10^8 \pm 2.11{\cdot}10^6$	$8.99{\cdot}10^{12} \pm 9.40{\cdot}10^{10}$	$2.65{\cdot}10^{17} \pm 4.47{\cdot}10^{15}$
J 7.2 PS d	2^{15}	$1.36{\cdot}10^4 \pm 1.90{\cdot}10^1$	$2.56{\cdot}10^8 \pm 7.14{\cdot}10^5$	$5.55{\cdot}10^{12} \pm 2.68{\cdot}10^{10}$	$1.32{\cdot}10^{17} \pm 1.05{\cdot}10^{15}$
J 7.2 PS g	2^{15}	$1.53{\cdot}10^4 \pm 4.74{\cdot}10^1$	$3.35{\cdot}10^8 \pm 1.98{\cdot}10^6$	$8.67{\cdot}10^{12} \pm 8.59{\cdot}10^{10}$	$2.50{\cdot}10^{17} \pm 3.95{\cdot}10^{15}$

Cartesian three-dimensional analysis (continued from previous page)

Dataset	Bins	$\langle F^2 \rangle^h$	$\langle F^3 \rangle^h$	$\langle F^4 \rangle^h$	$\langle F^5 \rangle^h$
CELLO	2^{16}	$4.97\cdot10^4 \pm 1.58\cdot10^2$	$3.89\cdot10^9 \pm 2.80\cdot10^7$	$3.75\cdot10^{14} \pm 5.58\cdot10^{12}$	$4.14\cdot10^{19} \pm 1.25\cdot10^{18}$
J 7.2 PS+BE d	2^{18}	$5.12\cdot10^4 \pm 1.35\cdot10^2$	$4.14\cdot10^9 \pm 2.47\cdot10^7$	$4.12\cdot10^{14} \pm 5.07\cdot10^{12}$	$4.73\cdot10^{19} \pm 1.16\cdot10^{18}$
J 7.2 PS+BE g	2^{18}	$6.06\cdot10^4 \pm 2.05\cdot10^2$	$6.09\cdot10^9 \pm 4.41\cdot10^7$	$7.87\cdot10^{14} \pm 1.09\cdot10^{13}$	$1.20\cdot10^{20} \pm 3.02\cdot10^{18}$
J 7.2 PS d	2^{18}	$4.99\cdot10^4 \pm 7.40\cdot10^1$	$3.89\cdot10^9 \pm 1.31\cdot10^7$	$3.72\cdot10^{14} \pm 2.55\cdot10^{12}$	$4.08\cdot10^{19} \pm 5.49\cdot10^{17}$
J 7.2 PS g	2^{18}	$5.91\cdot10^4 \pm 1.93\cdot10^2$	$5.76\cdot10^9 \pm 4.06\cdot10^7$	$7.23\cdot10^{14} \pm 9.84\cdot10^{12}$	$1.07\cdot10^{20} \pm 2.62\cdot10^{18}$
CELLO	2^{21}	$1.21\cdot10^5 \pm 4.44\cdot10^2$	$2.58\cdot10^{10} \pm 2.58\cdot10^8$	$7.09\cdot10^{15} \pm 1.74\cdot10^{14}$	$2.16\cdot10^{21} \pm 1.21\cdot10^{20}$
J 7.2 PS+BE d	2^{21}	$1.27\cdot10^5 \pm 3.81\cdot10^2$	$2.82\cdot10^{10} \pm 2.32\cdot10^8$	$8.07\cdot10^{15} \pm 1.76\cdot10^{14}$	$2.71\cdot10^{21} \pm 1.56\cdot10^{20}$
J 7.2 PS+BE g	2^{21}	$1.56\cdot10^5 \pm 5.72\cdot10^2$	$4.67\cdot10^{10} \pm 4.44\cdot10^8$	$1.99\cdot10^{16} \pm 4.92\cdot10^{14}$	$1.11\cdot10^{22} \pm 7.08\cdot10^{20}$
J 7.2 PS d	2^{21}	$1.16\cdot10^5 \pm 1.98\cdot10^2$	$2.31\cdot10^{10} \pm 1.09\cdot10^8$	$5.81\cdot10^{15} \pm 7.35\cdot10^{13}$	$1.69\cdot10^{21} \pm 5.80\cdot10^{19}$
J 7.2 PS g	2^{21}	$1.47\cdot10^5 \pm 5.14\cdot10^2$	$4.05\cdot10^{10} \pm 3.56\cdot10^8$	$1.55\cdot10^{16} \pm 3.18\cdot10^{14}$	$7.39\cdot10^{21} \pm 3.17\cdot10^{20}$
CELLO	2^{24}	$1.98\cdot10^5 \pm 1.12\cdot10^3$	$8.08\cdot10^{10} \pm 2.11\cdot10^9$	$5.39\cdot10^{16} \pm 5.88\cdot10^{15}$	$5.15\cdot10^{22} \pm 1.65\cdot10^{22}$
J 7.2 PS+BE d	2^{24}	$2.16\cdot10^5 \pm 9.74\cdot10^2$	$9.75\cdot10^{10} \pm 1.88\cdot10^9$	$6.59\cdot10^{16} \pm 5.60\cdot10^{15}$	$6.42\cdot10^{22} \pm 2.05\cdot10^{22}$
J 7.2 PS+BE g	2^{24}	$2.56\cdot10^5 \pm 1.22\cdot10^3$	$1.52\cdot10^{11} \pm 2.89\cdot10^9$	$1.59\cdot10^{17} \pm 1.51\cdot10^{16}$	$3.09\cdot10^{23} \pm 1.04\cdot10^{23}$
J 7.2 PS d	2^{24}	$1.84\cdot10^5 \pm 4.92\cdot10^2$	$6.93\cdot10^{10} \pm 8.21\cdot10^8$	$3.73\cdot10^{16} \pm 1.80\cdot10^{15}$	$2.40\cdot10^{22} \pm 3.80\cdot10^{21}$
J 7.2 PS g	2^{24}	$2.33\cdot10^5 \pm 1.08\cdot10^3$	$1.22\cdot10^{11} \pm 2.01\cdot10^9$	$9.71\cdot10^{16} \pm 5.85\cdot10^{15}$	$1.06\cdot10^{23} \pm 2.07\cdot10^{22}$
CELLO	2^{27}	$2.67\cdot10^5 \pm 3.13\cdot10^3$	$1.74\cdot10^{11} \pm 1.74\cdot10^{10}$	—	—
J 7.2 PS+BE d	2^{27}	$2.92\cdot10^5 \pm 2.73\cdot10^3$	$2.57\cdot10^{11} \pm 2.31\cdot10^{10}$	—	—
J 7.2 PS+BE g	2^{27}	$3.32\cdot10^5 \pm 2.82\cdot10^3$	$3.18\cdot10^{11} \pm 1.76\cdot10^{10}$	—	—
J 7.2 PS d	2^{27}	$2.38\cdot10^5 \pm 1.37\cdot10^3$	$1.50\cdot10^{11} \pm 7.24\cdot10^9$	—	—
J 7.2 PS g	2^{27}	$2.98\cdot10^5 \pm 2.60\cdot10^3$	$2.95\cdot10^{11} \pm 1.83\cdot10^{10}$	—	—
CELLO	2^{30}	$3.48\cdot10^5 \pm 9.70\cdot10^3$	—	—	—
J 7.2 PS+BE d	2^{30}	$3.66\cdot10^5 \pm 8.18\cdot10^3$	—	—	—
J 7.2 PS+BE g	2^{30}	$4.24\cdot10^5 \pm 8.13\cdot10^3$	—	—	—
J 7.2 PS d	2^{30}	$2.97\cdot10^5 \pm 4.16\cdot10^3$	—	—	—
J 7.2 PS g	2^{30}	$3.97\cdot10^5 \pm 7.96\cdot10^3$	—	—	—
CELLO	2^{33}	$5.74\cdot10^5 \pm 3.50\cdot10^4$	—	—	—
J 7.2 PS+BE d	2^{33}	$4.42\cdot10^5 \pm 2.52\cdot10^4$	—	—	—
J 7.2 PS+BE g	2^{33}	$6.18\cdot10^5 \pm 2.74\cdot10^4$	—	—	—
J 7.2 PS d	2^{33}	$4.22\cdot10^5 \pm 1.39\cdot10^4$	—	—	—
J 7.2 PS g	2^{33}	$6.60\cdot10^5 \pm 2.78\cdot10^4$	—	—	—
CELLO	2^{36}	$9.59\cdot10^5 \pm 1.28\cdot10^5$	—	—	—
J 7.2 PS+BE d	2^{36}	$9.17\cdot10^5 \pm 1.02\cdot10^5$	—	—	—
J 7.2 PS+BE g	2^{36}	$9.66\cdot10^5 \pm 9.60\cdot10^4$	—	—	—
J 7.2 PS d	2^{36}	$7.16\cdot10^5 \pm 5.11\cdot10^4$	—	—	—
J 7.2 PS g	2^{36}	$1.30\cdot10^6 \pm 1.09\cdot10^5$	—	—	—
CELLO	2^{39}	$2.06\cdot10^6 \pm 5.31\cdot10^5$	—	—	—
J 7.2 PS+BE d	2^{39}	$1.36\cdot10^6 \pm 3.51\cdot10^5$	—	—	—
J 7.2 PS+BE g	2^{39}	$1.30\cdot10^6 \pm 3.15\cdot10^5$	—	—	—
J 7.2 PS d	2^{39}	$1.23\cdot10^6 \pm 1.89\cdot10^5$	—	—	—
J 7.2 PS g	2^{39}	$2.12\cdot10^6 \pm 3.94\cdot10^5$	—	—	—

Table C.4: Cartesian three-dimensional analysis.

Bibliography

[1] G. Veneziano: A Topological Approach to the Dynamics of Quarks and Hadrons, preprint Ref.TH.2425-CERN (1977)
D. Amati and G. Veneziano: Preconfinement as a Property of Perturbative QCD, Phys. Lett. B 83 (1979) 87

[2] R.D. Field and R.P. Feynman: A Parametrization of the Properties of Quark Jets, Nucl. Phys. B 136 (1978) 1

[3] B. Andersson: On the Properties of the Colour Dipoles in QCD, Nucl. Phys. B 360 (1991) 109

[4] G. Gustafson and U. Pettersson: Dipole Formulation of QCD Cascades, Nucl. Phys. B 306 (1988) 746
B. Andersson, G. Gustafson and L. Lönnblad: Gluon Splitting in the Colour Dipole Cascades, Nucl. Phys. B 339 (1990) 393
L. Lönnblad: Ariadne 3 – a Monte Carlo for QCD Cascades in the Colour Dipole Formulation, Lund preprint LU TP 89-10 (1989)

[5] G. Marchesini and B.R. Webber: Simulation of QCD Jets Including Soft Gluon Interference, Nucl. Phys. B 238 (1984) 1
G. Marchesini and B.R. Webber: Monte Carlo Simulation of General Hard Processes with Coherent QCD Radiation, Nucl. Phys. B 310 (1988) 461

[6] B.R. Webber: A QCD Model for Jet Fragmentation Including Soft Gluon Interference, Nucl. Phys. B 238 (1984) 492

[7] B.R. Webber: Monte Carlo Simulation with QCD Coherence, preprint Cavendish-HEP-88/6 (1988)

[8] B. Andersson, G. Gustafson, G. Ingelman and T. Sjöstrand: Parton Fragmentation and String Dynamics, Phys. Rep. 97 (1983) 31

[9] T. Sjöstrand: The Lund Monte Carlo for e^+e^- Jet Physics, Comp. Phys. Commun. 28 (1983) 229
T. Sjöstrand and M. Bengtsson: The Lund Monte Carlo for Jet Fragmentation and e^+e^- Physics – Jetset version 6.3 – an update, Comp. Phys. Commun. 43 (1987) 367
T. Sjöstrand and M. Bengtsson: The Lund Monte Carlo for Jet Fragmentation and e^+e^- Physics – Jetset version 7.2/3, CERN long writeup

[10] C. Peterson, D. Schlatter, I. Schmitt and P. Zerwas: Scaling Violations in Inclusive e^+e^- Annihilation Spectra, Phys. Rev. D 27 (1983) 105

[11] TPC/Two Gamma Coll. H. Aihara et al.: Study of Baryon Correlations in e^+e^- Annihilation at 29 GeV, Phys. Rev. Lett. 57 (1986) 3140

[12] S.L. Wu: e^+e^- Physics at PETRA – The First Five Years, Phys. Rep. 107 (1984) 59 and references therein

[13] CELLO Coll. H.-J. Behrend et al.: CELLO – A New Detector at PETRA, Phys. Scr. 23 (1981) 610

[14] J. Harjes: Identifikation Niederenergetischer Elektronen, Myonen und Pionen mit dem Flüssigargon-Blei-Kalorimeter des CELLO Detektors, Diploma thesis, University of Hamburg, internal report (1987) DESY F14-87-06
Experimentelle Untersuchung der Reaktion $\gamma\gamma \to \pi^+\pi^-$ mit dem Detektor CELLO, Ph.D. thesis, University of Hamburg, internal report (1991) DESY FCE-91-01

[15] H. Fenner: Erzeugung von $\rho^0\omega$ in 2-Photon-Kollisionen, Ph.D. thesis, University of Hamburg, internal report (1992) DESY FCE-92-02

[16] J.H. Peters: Production of η, η' and $f_1(1285)$ Mesons in Tagged and Untagged Two-Photon Reactions, Ph.D. thesis, University of Hamburg, internal report (1990) DESY FCE-90-01

[17] B. Sack: Die Strahlrohrkammern des CELLO Detektors, Diploma thesis, University of Hamburg, (1984) unpublished

[18] U. Binder: Die Eigenschaften der zylindrischen Driftkammern des Detektors CELLO, Diploma thesis, University of Hamburg, preprint MPI-PAE/Exp.El. 125 (1983)

[19] H.-J. Behrend: The Fast Trackfinder for the CELLO Experiment at DESY, Comp. Phys. Commun. 22 (1981) 365

[20] J. Knapp: New Liquid Argon Trigger, CELLO note K081 (1984) unpublished
K. Gamerdinger et al.: Status of the New Liquid Argon Trigger, CELLO note K101 (1985) unpublished

[21] G. Franke: The CELLO Event Filter Program, CELLO note D035 (1985) unpublished

[22] J. Ahme: Untersuchung der Endzustände $K_S^0 K_S^0$ und $K_S^0 K\pi$ in Photon-Photon Reaktionen, Ph.D. thesis, University of Hamburg, internal report (1989) DESY FCE-89-01

[23] O. Podobrin: Erzeugung von strange und charm Mesonen in der e^+e^--Annihilation bei 35 GeV, Diploma thesis, University of Hamburg, internal report (1988) DESY F14-88-04

[24] M. Feindt: Criteria Applied in the 1986 DST Select Job, CELLO note D042 (1986) unpublished

[25] CELLO Coll. H.-J. Behrend et al.: An Analysis of Multihadronic Events Produced with Two Energetic Leptons in e^+e^- Annihilation, Phys. Lett. B 212 (1988) 515
An Experimental Study of e^+e^- Annihilation into Four Leptons, Z. Phys. C – Particles and Fields 43 (1989) 1

[26] W. de Boer and M. Iacovacci, Experiment 44 – Luminosity Determination, CELLO note R-02 (1988) unpublished

[27] V. Blobel: Unfolding Methods in High-Energy Physics Experiments, DESY preprint 84-118. lectures given at the CERN school of computing. Aiguablava, Spain, 1984

[28] V. Blobel: RUN – General Program for Regularized Unfolding, program description (1984). unpublished

[29] OPAL Coll. M.Z. Akrawy et al.: A Measurement of Global Event Shape Distributions in the Hadronic Decays of the Z^0, Z. Phys. C – Particles and Fields 47 (1990) 505

[30] F.A. Berends and R. Kleiss, Initial State Radiation for e^+e^- Annihilation into Jets, Nucl. Phys. B 178 (1981) 141

[31] TASSO Coll. W. Braunschweig et al.: Pion, Kaon and Proton Cross Sections in e^+e^- Annihilation at 34 GeV and 44 GeV CM Energy, Z. Phys. C – Particles and Fields 42 (1989) 189

[32] TPC/Two Gamma Coll. H. Aihara et al.: Charged Hadron Inclusive Cross Sections and Fractions in e^+e^- Annihilation at $\sqrt{s} = 29$ GeV, Phys. Rev. Lett. 61 (1988) 1263

[33] CELLO Coll. H.-J. Behrend et al.: Inclusive Strange Particle Production in e^+e^- Annihilation at 35 GeV, Z. Phys. C – Particles and Fields 46 (1990) 397

[34] CELLO Coll. H.-J. Behrend et al.: Measurement of Inclusive γ, π^0 and η Production in e^+e^- Annihilation at $\sqrt{s} = 35$ GeV, Z. Phys. C – Particles and Fields 47 (1990) 1

[35] O. Podobrin: $D^{*\pm}$ Production in e^+e^- Annihilation at 35 GeV, Procs. XXV. Rencontre de Moriond on High Energy Hadronic Interactions, Les Arcs, France, 1990, ed. J. Trân Thanh Vân (Editions Frontières, Gif-sur-Yvette, 1990) p. 217

[36] Procs. XXV. Int. Conf. on High Energy Physics, Singapore, Singapore, 1990, eds. K.K. Phua and Y. Yamaguchi (Phys. Soc. Japan, Tokyo, 1991)

[37] Procs. XX. Int. Symp. on Multiparticle Dynamics, Gut Holmecke, Germany, 1990, eds. R. Baier and D. Wegener (World Scientific, Singapore, 1991)

[38] Procs. XXVI. Rencontre de Moriond on High Energy Hadronic Interactions, Les Arcs, France, 1991, ed. J. Trân Thanh Vân (Editions Frontières, Gif-sur-Yvette, 1991)

[39] P. Carruthers and C.C. Shih: Correlations and Fluctuations in Hadronic Multiplicity Distributions – The Meaning of KNO Scaling, Phys. Lett. B 127 (1983) 242

[40] A. Giovannini and L. Van Hove: Negative Binomial Multiplicity distributions in High Energy Hadron Collisions, Z. Phys. C – Particles and Fields 30 (1986) 391

[41] A. Giovannini and L. Van Hove: Multihadron Production and QCD Parton Showers, preprint CERN-TH.5885/90, loc. cit. [36] p. 998

[42] Z. Koba, H.B. Nielsen and P. Olesen Scaling of Multiplicity distributions in High Energy Hadron Collisions, Nucl. Phys. B 40 (1972) 317

[43] E.D. Malaza and B.R. Webber: Multiplicity distribution in Quark and Gluon Jets, Nucl. Phys. B 267 (1986) 702

[44] B. Durand and I. Sarcevic: Multiplicities Without KNO – Parton Branching Versus Negative Binomial, Phys. Lett. B 172 (1986) 104

[45] TASSO Coll. W. Braunschweig et al.: Charged Multiplicity distributions and Correlations in e^+e^- Annihilation at PETRA Energies, Z. Phys. C – Particles and Fields 45 (1989) 193
HRS Coll. M. Derrick et al.: Rapidity Dependence of the Charged Particle Multiplicity Distributions in e^+e^- Annihilation at 29 GeV, Phys. Lett. B 168 (1986) 299
DELPHI Coll. P. Abreu et al.: Charged Particle Multiplicity distributions in Z^0 Hadronic Decays, Z. Phys. C – Particles and Fields 50 (1991) 185
OPAL Coll. P.D. Acton et al.: A Study of Charged Particle Multiplicities in Hadronic Decays of the Z^0, preprint CERN-PPE/91-176 (1991)
ALEPH Coll. D. Decamp et al.: Measurement of the Charged Particle Multiplicity distribution in Hadronic Z^0 Decays, preprint CERN-PPE/91-159 (1991)

[46] R. Szwed and G. Wrochna: Scaling Predictions for Multiplicity distributions at LEP, Z. Phys. C – Particles and Fields 47 (1990) 449

[47] T. Sjöstrand: Private communication

[48] T. Sjöstrand: Status of Fragmentation Models, Mod. Phys. Lett. A 3 (1988) 751

[49] T. Sjöstrand: QCD and Jets at LEP, preprint CERN-TH.5902/90 (1990)

[50] V. Blobel: VALLEY – A Program to Find Minima of Functions, program description (1982) unpublished

[51] M. Feindt: A Review of Two-Photon Physics, preprint CERN-PPE/91-90, loc. cit. [38] p. 409

[52] W. Kittel and R. Peschanski: Review on Intermittency in Particle Multiproduction, Procs. EPS-HEP '89, Madrid, Spain, 1989, eds. F. Barreiro, C. Lopez, R.F. Alvarez-Estrada and M. Quiros (North-Holland, Amsterdam, 1990) Nucl. Phys. B, Proc. Suppl. 16 (1990) 445
W. Kittel: Intermittency – A Review of Experimental Results, loc. cit. [37] p. 401
A. Bialas: Recent Theoretical Results on Intermittency, ibid. p. 669
B. Buschbeck: Intermittency – A Short Experimental Review, loc. cit. [38] p. 299
A. de Angelis, P. Lipa and W. Ochs: Fractal Structure and Intermittency in Multiparticle Production, preprint MPI-Ph/91-93 (1991), combined from three talks at the LP-HEP conference, Geneva, Suisse, 1991, to appear in the proceedings
N. Schmitz: A Review of Experimental Results on Intermittency, preprint MPI-PhE/91-09, to appear in Procs. XXI. Int. Symp. on Multiparticle Dynamics, Wuhan, China, 1991

[53] CELLO Coll. H.-J. Behrend et al.: Intermittency in Multihadronic e^+e^- Annihilation at 35 GeV, Contributed paper # 529, XXV. Int. Conf. on High Energy Physics, Singapore, 1990

[54] CELLO Coll. H.-J. Behrend et al.: Fractal Dimensions from a Three-Dimensional Intermittency Analysis in e^+e^- Annihilation, Phys. Lett. B 256 (1991) 97

[55] CELLO Coll. H.-J. Behrend et al.: Fluctuations and Correlations in Multihadronic e^+e^- Annihilation, in preparation

[56] TASSO Coll. W. Braunschweig et al.: Study of Intermittency in Electron-Positron Annihilation into Hadrons, Phys. Lett. B 231 (1989) 548

[57] DELPHI Coll. P. Abreu et al.: A Study for Intermittency in Hadronic Z^0 Decays, Phys. Lett. B 247 (1990) 137
A. de Angelis: Study of Intermittency in Hadronic Z^0 Decays, Mod. Phys. Lett. A 5 (1990) 2395

[58] OPAL Coll. M.Z. Akrawy et al.: Intermittency in Hadronic Decays of the Z^0, Phys. Lett. B 262 (1991) 351
N. Geddes: Intermittency in Electron-Positron Annihilation at 91 GeV, Rutherford preprint RAL-91-061 (1991)

[59] ALEPH Coll. D. Decamp et al.: An Investigation into Intermittency, Z. Phys. C – Particles and Fields 53 (1992) 21

[60] M. Feindt: Intermittency and Two-Particle Correlations in e^+e^- Annihilation, loc. cit. [36] p. 591

[61] O. Podobrin: Intermittency Fractal Dimensions and Correlation Phenomena in e^+e^- Annihilation at 35 GeV, loc. cit. [37] p. 417

[62] O. Podobrin: Intermittency and Bose-Einstein Correlations in e^+e^- Annihilation, DESY preprint 91-028, loc. cit. [38] p. 311

[63] O. Podobrin: CELLO Results on Multiparticle Production, DESY preprint 91-111, Procs. Workshop on Fluctuations and Fractal Structure, Ringberg Castle, Germany, 1991, eds. R.C. Hwa, W. Ochs and N. Schmitz (World Scientific, Singapore, 1992) p. 62

[64] A.K. Wróblewski: Soft Hadron Physics, Warsaw University preprint IFD/10/1990, loc. cit. [36] p. 125 and references therein

[65] G. Gustafson and C. Sjögren: Intermittency in e^+e^- Annihilation at PEP–PETRA Energies, Phys. Lett. B 248 (1990) 430

[66] G. Gustafson and C. Sjögren: Private communication

[67] B. Andersson, G. Gustafson, A. Nielsson and C. Sjögren: Fluctuations and Anomalous Dimensions in QCD Cascades, Z. Phys. C – Particles and Fields 49 (1991) 79

[68] W. Ochs: Scaling and Scale Breaking Phenomena in Multiparticle Production, loc. cit. [37] p. 434

[69] T. Sjöstrand: Multiple Interactions, Intermittency and Other Studies, Lund preprint LU TP 88-20 (1988), Procs. Workshop on Multiparticle Dynamics, Perugia, Italy, 1988, eds. R.C. Hwa, G. Pancheri and Y. Srivastava (World Scientific, Singapore, 1989) p. 327

[70] W. Ochs: Private communication

[71] Ya.I. Azimov, Yu.L. Dokshitzer, V.A. Khoze and S.I. Troyan, Hump-Backed QCD Plateau in Hadron Spectra, Z. Phys. C – Particles and Fields 31 (1986) 213

[72] CERN program library, ed. G. Benassi (1989)

[73] J.D. Bjorken: Properties of Hadron Distributions in Reactions Containing Very Heavy Quarks, Phys. Rev. D 17 (1978) 171

[74] S. Brodsky and J.F. Gunion: Hadron Multiplicity in Colour Gauge Theory Models, Phys. Rev. Lett. 37 (1976) 402

[75] A. Białas and R. Peschanski: Moments of Rapidity Distributions as a Measure of Short-Range Fluctuations in High-Energy Collisions, Nucl. Phys. B 273 (1986) 703
Intermittency in Multiparticle Production at High Energy, Nucl. Phys. B 308 (1988) 857

[76] P. Carruthers H.C. Eggers and I. Sarcevic: Analysis of Multiplicity Moments for Hadronic Multiparticle Data, Phys. Lett. B 254 (1991) 258

[77] W. Ochs: Multidimensional Intermittency Analyses, Z. Phys. C – Particles and Fields 50 (1991) 339

[78] W. Ochs: The Importance of Phase Space Dimension in the Intermittency Analysis of Multi Hadron Production, Phys. Lett. B 247 (1990) 101

[79] A. Białas and M. Gazdzicki: A New Variable to Study Intermittency, Phys. Lett. B 252 (1990) 483

[80] G. Ekspong, R. Peschanski and J. Wosiek: Bin-Size Correlations in the α-Model of Multi-Particle Fluctuations, Phys. Lett. B 251 (1990) 455

[81] B.B. Mandelbrot: The Fractal Geometry of Nature, (Freeman, San Fransisco, 1982)

[82] G. Paladin and A. Vulpiani: Anomalous Scaling Laws in Multifractal Objects, Phys. Rep. 156 (1987) 147

[83] P. Carruthers and I. Sarcevic: Short-Range Correlations and the Intermittency Phenomenon in Multihadron Rapidity Distributions, Phys. Rev. Lett. 63 (1989) 1562

[84] M.G. Bowler: e^+e^- Production of Heavy Quarks in the String Model, Z. Phys. C – Particles and Fields 11 (1981) 169

[85] TPC/Two Gamma Coll. H. Aihara et al.: Study of Bose-Einstein Correlations in e^+e^- Annihilation at 29 GeV, Phys. Rev. D 31 (1985) 996

[86] TASSO Coll. M. Althoff et al.: Bose-Einstein Correlations Observed in e^+e^- Annihilation at a Centre of Mass Energy of 34 GeV, Z. Phys. C – Particles and Fields 30 (1986) 355

[87] ALEPH Coll. D. Decamp et al.: A Study of Bose-Einstein Correlations in e^+e^- Annihilation at 91 GeV, preprint CERN-PPE/91-183 (1991)

[88] OPAL Coll. P.D. Acton et al.: A Study of Bose-Einstein Correlations in e^+e^- Annihilations at LEP, Phys. Lett. B 267 (1991) 143

[89] G. Bagliesi et al.: Top Quark Physics – Experimental Aspects, preprint CERN-PPE/92-05 (1992), to appear in Procs. of Workshop on Physics and Experiments with Linear Colliders, Hamburg, Germany and Saariselkä, Finland, 1991

[90] P. Söding: On the Apparent Shift of the Rho Meson Mass in Photoproduction, Phys. Lett. 19 (1966) 702

Acknowledgements

It is a pleasure to acknowledge the kind hospitality and financial assistance received from the DESY directorate in the course of this thesis.

Many thanks go to Michael Feindt for the advice and valuable discussions during the last three years.

I am grateful to my colleagues in CELLO for the most enjoyable collaboration. Special thanks go to the group of Hartwig Spitzer (Hartmut Fenner, Jens Harjes and Jan Hendrik Peters) and to Wim de Boer for numerous informative discussions.

It is a pleasure to acknowledge many valuable theoretical discussions with Torbjörn Sjöstrand.

Finally, thanks to Peter Bussey, Michael Feindt, Hartmut Fenner and Torbjörn Sjöstrand for carefully reading the manuscript.

And, last but not least, thanks to my sister Brigitta Podobrin for the front cover graphics.